A SEARCH FOR SUPERNOVA NEUTRINOS WITH THE SUDBURY NEUTRINO OBSERVATORY

By

Jaret Heise

B.Sc.(Hon), University of Saskatchewan, 1993

M.Sc., University of British Columbia, 1996

A THESIS SUBMITTED IN PARTIAL FULFILLMENT OF

THE REQUIREMENTS FOR THE DEGREE OF

DOCTOR OF PHILOSOPHY

in

THE FACULTY OF GRADUATE STUDIES

DEPARTMENT OF PHYSICS AND ASTRONOMY

We accept this thesis as conforming

to the required standard

.....

.....

.....

.....

.....

THE UNIVERSITY OF BRITISH COLUMBIA

December 2001

In presenting this thesis in partial fulfillment of the requirements for an advanced degree at the University of British Columbia, I agree that the Library shall make it freely available for reference and study. I further agree that permission for extensive copying of this thesis for scholarly purposes may be granted by the head of my department or by his or her representatives. It is understood that copying or publication of this thesis for financial gain shall not be allowed without my written permission.

Department of Physics and Astronomy
The University of British Columbia
6224 Agricultural Road
Vancouver, BC, Canada
V6T 1Z1

Date:

Abstract

The Sudbury Neutrino Observatory (SNO) is an underground Čerenkov detector designed to detect neutrinos from astrophysical sources. The fiducial mass of the detector consists of 1000 tonnes of D_2O, which provides sensitivity to all neutrino flavours. Since much of the energy released in the supernova burst is expected to be carried by the muon and tau neutrinos, the supernova signal recorded by the SNO detector is of particular importance. In addition, SNO is also sensitive to the prompt electron neutrino signal expected from capture processes during core collapse. Various supernova models are investigated and predictions of the SNO supernova signal are studied using simulated Monte Carlo data.

A data analysis program to identify neutrinos from a galactic supernova burst has been installed in the online system at SNO. The program automatically analyzes burst data and it is anticipated that a manual alert to the Supernova Early Warning System could be issued within 20–30 minutes with negligible possibility of a false alarm. The burst identification algorithm currently in use both online and offline provides detection sensitivity beyond the far edge of our galaxy.

A search for supernova neutrinos was performed using 241.0 days of data collected over the time period between November 2, 1999 and January 4, 2001. No candidate bursts were observed over this period, which places a 90% confidence level upper limit of < 3.5 galactic supernovae per year.

Table of Contents

List of Tables

List of Figures

Acknowledgments

From my first involvement with SNO in May 1996 to the final touches on my thesis in December 2001, a significant amount of time and effort has been invested both by myself and a host of others. As a result, I have many people to thank for their assistance, support and imparting of knowledge.

I want to start first by extending my deepest thanks to my supervisor Dr. Chris Waltham for guiding me through the Ph.D. journey from start to finish. Now that all has been said and done, I am better able to appreciate the direction I was given as well as the flexibility I was afforded. And I know I will miss his wry sense of humour.

The quality of this thesis has benefitted greatly from the contribution of the supervisory committee that has followed my progress throughout my term as a Ph.D. student. Members of this group include Dr. Douglas Beder, Dr. Douglas Scott and Dr. Chris Hearty. The university examiners Dr. Matthew Choptuik and Dr. Philip Loewen and the external examiner Dr. John Beacom also deserve my gratitude for their thorough reading of my thesis and for many useful comments.

Furthermore, this thesis would not have been possible without the work performed in conjunction with members of the SNO Supernova Working Group. My association with Dr. Clarence Virtue, Dr. Réda Tafirout and Mike Schwendener has been extremely rewarding, and I want to thank them for putting up with me. I want thank Réda in particular for his tireless work on the supernova monitoring system in general and for his help with the burst analysis.

I also want to express my appreciation for the privilege of being part of the SNO group at UBC, whose members include Dr. Rob Komar, Christian Nally, Dr. Thomas Kutter and

Siong Ng (as a summer student). Rob in particular deserves heaps of praise for the insight he has provided over the years and for the key role he played in my Ph.D. education. For all the computer know-how they passed along, I want to thank Rob, Christian and Doug Maas.

A large debt of gratitude must be paid to the members of the SNO collaboration, including not only the project scientists, but also members of the SNO site staff and the detector construction crew. I consider myself fortunate to have worked with the group of wonderful people who have been drawn to this project. In particular I wish to acknowledge the guidance of Dr. Richard van de Water, Dr. Hardy Seifert, Dr. Peter Doe, Dr. Davis Earle and Dr. Hugh Evans. I learned a great deal from each one of these people. Peter warrants special mention for the pain and suffering he endured while helping to edit my thesis.

Eddie Gorc of Eddie's Sports Bar in Sudbury and the members of his staff also deserve my heartfelt thanks for the friendship and hospitality (not to mention beer!) that they have provided over the years. While many names should be included, I want to be sure to recognize Kelly Morrison, Cyndi Dwyer, Vicky Brouillard, Joe (Guisseppe) Vocaturo and of course Randy Brunelle. They are some of the best ambassadors to Northern Ontario anyone could hope to know.

As with my M.Sc. thesis, I once again wish to acknowledge the hospitality of my relatives Don, Carol, Jonathan and Matthew Wilkie and my land people Ingrid Pinel and Terry Pask, and thank them for making Vancouver feel like home for the last 8 years. I know that I won't eat so well once I leave.

My parents have been supportive of all my endeavours, and for having that environment I consider myself very fortunate. It is my sincerest hope that this thesis will offer them comfort well into their old age. I also want to extend thanks to my two brothers: Brett, who never let me forget how little money I made as a graduate student; and Jordan, who

will probably read more of this thesis than anyone else in my family. Thanks also go to Charles the Cat for illuminating discussions on neutrino physics.

Last but not least, thanks go to my wife Kara for the support she was able to give and for the patience she was able to find.

Come quickly, I am tasting stars!

– Dom Perignon, upon discovering champagne.

Chapter 1

Introduction

The neutrino was first proposed in 1930 by Pauli [1] to account for the apparent missing energy and momentum in nuclear beta decay reactions. A series of experiments performed between 1950 and 1956 by Reines and Cowan [2] confirmed the existence of the neutrino by recording evidence of the electron antineutrino. To make the discovery, Reines and Cowan identified signatures of neutrinos from fission reactors using the inverse beta decay reaction

$$\overline{\nu}_e + p \rightarrow n + e^+. \tag{1.1}$$

In 1995, Reines was awarded the Nobel Prize in physics for this important work in the detection of the neutrino.

1.1 Neutrino Properties

Neutrinos are classified as leptons, which are fundamental particles in the Standard Model of particle physics. They come in 3 flavours, one associated with each of the three lepton families, as indicated in Table 1.1. As with the electron, muon and tau particles, neutrinos also have corresponding distinct antiparticles. Because they possess no electric charge, neutrinos only participate in weak and gravitational interactions, and have extremely low reaction cross sections as a result. This is the principal reason why neutrinos are so difficult to detect. As a neutral particle without a magnetic moment, neutrinos are not deflected in locally or globally distributed electric and magnetic fields. For a long time, the neutrino mass was assumed to be zero; however, recent evidence of neutrino oscillation indicates that

the neutrino mass is non-zero [3],[4]. The evidence for neutrino oscillation also constrains the sum of masses of neutrinos listed in Table 1.1 to be between 0.05 and 8.4 eV/c^2 [4]. Present upper limits for the masses of neutrinos as determined by direct measurement are found to be: $m_{\nu_e} < 3$ eV/c^2, $m_{\nu_\mu} < 0.19$ MeV/c^2 and $m_{\nu_\tau} < 18.2$ MeV/c^2 [5].

Generation	Lepton	Neutrino
First	electron, e^-	electron neutrino, ν_e
	positron, e^+	electron antineutrino, $\overline{\nu}_e$
Second	muon, μ^-	muon neutrino, ν_μ
	antimuon, μ^+	muon antineutrino, $\overline{\nu}_\mu$
Third	tau, τ^-	tau neutrino, ν_τ
	antitau, τ^+	tau antineutrino, $\overline{\nu}_\tau$

Table 1.1: The three generations of leptons and their associated neutrinos in the Standard Model of particle physics.

1.2 Neutrino Sources

Neutrinos are produced in a wide range of physical processes, and may constitute most of the normal matter that exists in the universe[1]. The recent neutrino oscillation evidence [4] indicates that the contribution to the critical density of the Universe is $0.001 < \Omega_\nu < 0.18$. From some of the most violent processes imaginable to radioactive decays observed on the Earth, neutrinos play a vital role. Various neutrino sources are briefly mentioned below, ordered according to the magnitude of the event that produces them.

1.2.1 Big Bang

When the temperature of the early universe was greater than 10^{10} K and matter densities were still very high, neutrinos remained in equilibrium with matter through weak interactions. The universe cooled quickly and 1 second after the Big Bang neutrinos decoupled

[1] Approximately 2/3 of the total matter in the universe is believed to be in the form of "dark energy" [6].

from the rest of the matter in the universe. As the universe expanded, the temperature of all the matter in it, including photons and neutrinos, decreased over time. The current temperature for the cosmic electromagnetic background radiation is measured to be T_{0_γ} = 2.725 ± 0.001 K [5]. Neutrinos decouple from matter before photons, and cool strictly due to the expansion of the Universe. However, photons cool more slowly. When temperatures in the early Universe fall below 6 $\times 10^9$ K ($T \sim m_e$), photons and electron/positron pairs that were once in equilibrium through the reaction $e^+e^- \leftrightarrow \gamma\gamma$ now only interact via the $e^+e^- \rightarrow \gamma\gamma$ reaction. This effectively heats photons compared to neutrinos, which means that the neutrino temperature for the current epoch, T_{0_ν}, is lower than the photon temperature and is given by [7]:

$$\frac{T_{0_\nu}}{T_{0_\gamma}} = \left(\frac{4}{11}\right)^{1/3}. \tag{1.2}$$

Therefore, the present temperature of neutrinos from the Big Bang is expected to be 1.9 K, and the average neutrino energy[2] is then $\langle E_\nu \rangle = 3.15\, kT_\nu = 5 \times 10^{-10}$ MeV. At these energies, the mean free path of neutrinos exceeds the size of the Universe. Therefore neutrinos remaining from the Big Bang cannot be detected with present technology. In the Universe today, the number density of neutrinos produced at the time of the Big Bang is approximately 100 cm^{-3} per neutrino species [7].

1.2.2 Gamma-Ray Bursts

Gamma-ray bursts (GRBs) are among the least understood phenomena in the universe. GRB events are characterized by a burst of 0.1 to 1 MeV photons with a duration ranging from ∼30 ms to ∼100 seconds [8]. Observations of GRBs imply that the photon events are due to the energy dissipation of a relativistically expanding "fireball", whose primal cause is not yet known. Two possible progenitors for GRB events are the merger of compact objects, such as neutron stars and black holes, and explosions of supermassive stars.

[2]The expression for the average energy $\langle E \rangle = 3.15\, kT$ is true for relativistic fermions that obey the Fermi-Dirac energy distribution. The corresponding expression for relativistic bosons is $\langle E \rangle = 2.7\, kT$.

The observed γ rays are thought to be produced by synchrotron emission of electrons accelerated by internal shocks within the expanding fireball. It has also been suggested that high energy neutrinos might be produced as a result of the dynamics within the fireball. In one scenario, high energy neutrinos are expected to be produced by the decay of charged pions created in interactions between photons and high energy protons, which are also accelerated by the shock. These photo-meson interactions are expected to convert a significant fraction of the fireball energy to neutrinos of energy $E_\nu > 10^{14}$ eV [9]. Neutrinos with lower energies of approximately 2–25 GeV or higher may be produced by inelastic nuclear collisions [10].

1.2.3 Supernovae

Supernovae resulting from gravitational collapse are prodigious sources of neutrinos. When a massive star depletes its supply of nuclear fuel, it collapses and the gravitational potential energy of the star is carried away by neutrinos of all flavours. Moreover, neutrino interactions with the infalling material are thought to help sustain the shock wave that ultimately ejects the outer layers of the star into space. The fundamental role that neutrinos play in the collapse of a massive star was confirmed in 1987 when neutrino events were observed from SN1987A. The average energy for supernova neutrinos is in the range between 13–20 MeV. However, the tails of the energy distribution can extend as high as 100 MeV.

1.2.3.1 Relic Supernovae

Throughout the evolution of the Universe, many supernova explosions have taken place. In fact, it is estimated that 1 supernova event occurs every second somewhere in the Universe[3]. Neutrinos from supernovae that occurred in other galaxies in the distant past are called

[3]There are on the order of 100 billion galaxies in the Universe. Assuming a conservative rate of 1 supernova every 500 years yields an overall rate of approximately 5 supernova per second occurring in the Universe.

relic neutrinos.

The flux of relic supernova neutrinos depends critically on the rate of supernovae as a function of time. Supernova rates that were either low in the past or high in the very distant past lead to a relic supernova signal that is difficult to measure today. For example, if the supernova rate should peak at redshifts[4] of order 2–3, the energies of the relic neutrinos would be redshifted below typical detector thresholds. Some information about the supernova rate over time is provided in studies performed by Pei and Fall [11], which indicate that the star formation rate was much higher at redshifts $z \sim 1$ than at the present epoch. The average energy for relic supernova neutrinos is approximately 5 MeV, with the high energy region of the energy distribution extending beyond 50 MeV [12].

1.2.4 Solar Fusion Reactions

The energy that powers main sequence stars like our Sun comes from the nuclear fusion reaction

$$4p \rightarrow {}^4\mathrm{He} + 2e^+ + 2\nu_e + 26.73 \text{ MeV}. \tag{1.3}$$

Protons are converted to α particles, positrons, neutrinos and a surplus of energy. This reaction can proceed through different channels and as a result neutrinos of different energies are produced. The primary source of neutrinos in the Sun is via the p-p reaction:

$$p + p \rightarrow d + e^+ + \nu_e. \tag{1.4}$$

However, these neutrinos are difficult to detect because they have relatively low energies ($E \leq 0.42$ MeV). The largest flux of high energy solar neutrinos comes from the ^{8}B reaction

$${}^8\mathrm{B} \rightarrow 2\,{}^4\mathrm{He} + e^+ + \nu_e. \tag{1.5}$$

[4]The phenomena of redshift is analogous to the Doppler shift in sound waves. Energies observed on Earth are lower than those measured at the distant source by a factor $(1 + z)$, where z is the redshift.

These neutrinos have an energy spectrum that extends to approximately 15 MeV. Detectors such as the Sudbury Neutrino Observatory and Super-Kamiokande have been designed to observe these ^{8}B neutrinos.

1.2.5 Cosmic Ray Interactions in the Atmosphere

Neutrinos are also produced in the Earth's upper atmosphere due to hadronic cascades originating from interactions with cosmic rays:

$$p \rightarrow X + \pi^- \rightarrow X + \mu^- + \overline{\nu}_\mu \rightarrow e^- + \overline{\nu}_e + \nu_\mu \tag{1.6}$$

$$p \rightarrow X + \pi^+ \rightarrow X + \mu^+ + \nu_\mu \rightarrow e^+ + \nu_e + \overline{\nu}_\mu. \tag{1.7}$$

Through the decay of pions and muons, high energy muon and electron neutrinos (and antineutrinos) are produced in the ratio of 2:1. In 1998, the Super-Kamiokande collaboration was able to demonstrate that atmospheric muon neutrinos oscillate into another flavour of neutrino [3]. The range of energies for atmospheric neutrinos is from approximately 100 MeV to 10 GeV [13].

1.2.6 Nuclear Reactors

Nuclear reactors generate power using the fission of radioactive elements such as ^{235}U, ^{238}U, ^{239}Pu and ^{241}Pu. Many of the fission products subsequently decay through beta emission, producing copious numbers of electron antineutrinos. The average energy of neutrinos produced in fission reactors is approximately 5 MeV, with the energy spectrum cutting off at roughly 8 MeV.

1.2.7 Radioactivity in the Earth

Radioactive decay of natural elements (mainly ^{238}U and ^{232}Th) in the interior of the Earth produces neutrinos as well as 40% of the observed outflow of heat from the Earth's surface [14]. The energy of these neutrinos falls in the range 1–2 MeV.

1.3 Study of Supernova Neutrinos

Neutrinos from supernovae are interesting for many important reasons. Unlike photons, neutrinos carry information about the physics processes that occur in the core of the collapsing star. Therefore, the supernova neutrino signal offers the best means of understanding the mechanism that governs supernova dynamics. With this understanding also comes a more refined understanding of the nucleosynthesis processes that occur in supernovae. Primordial nucleosynthesis is responsible for producing stable light elements such as hydrogen, helium and lithium, but the temperatures found in the cores of collapsing stars are required in order to overcome the Coulomb barrier associated with the higher mass elements. Therefore, the majority of the heavy elements in the Universe are the result of supernova explosions[5].

1.4 Study of Supernova Neutrinos at SNO

To study supernova neutrinos, it is necessary to construct a detector with a large volume of material in order to compensate for the low neutrino cross section. The Sudbury Neutrino Observatory (SNO) is such a detector, with 1700 tonnes of ultrapure light water (H_2O) surrounding 1000 tonnes of ultrapure heavy water (D_2O). The use of heavy water provides SNO a unique perspective on neutrinos in general. All other neutrino detectors that are currently in operation are mainly sensitive to electron neutrinos and antineutrinos during a supernova burst. However, neutrinos of all flavours are able to participate in reactions which breakup the deuterium atom, providing SNO with a sensitivity to neutrinos of all types. This is particularly important in the case of supernova neutrinos, because most of the energy is expected to be carried away from the collapsing star by ν_μ and ν_τ neutrinos and antineutrinos. One other feature of the supernova signal about which SNO is expected

[5]This includes us! The carbon and oxygen in our bodies was produced during the death of a massive star.

to provide insight is the prompt burst of electron neutrinos resulting from electron capture reactions in the core. Other currently existing detectors are not able to separate the electron neutrino signal from the electron antineutrino signal as well as SNO can.

In addition to information about the supernova mechanism, it is also possible to use supernova neutrinos to learn more about the properties of neutrinos. Analysis of the neutrino signal from a supernova explosion may provide the best means of directly measuring the muon and tau neutrino mass. Since SNO has a unique sensitivity to these neutrino flavours, it is expected to provide one of the best measurements of the muon and tau neutrino mass. Estimates suggest that analysis of the supernova signal observed in SNO might be able to limit the muon or tau neutrino mass to 30 eV/c^2 [15]. No other type of terrestrial experiment has the possibility of placing such a stringent limit.

In order to gain as much information as possible from the next galactic supernova, it is crucial to have a monitoring programme in place to detect the neutrino burst. The neutrino signal is expected to precede the visible signal by up to several hours, due to the time required for the shock wave to emerge from the envelope of the collapsed star. Therefore, the prompt detection of neutrinos from a supernova can be used to alert the astronomical community. Observations of the onset of the electromagnetic signal have never before been observed with modern instruments.

Chapter 2

Supernova Physics

2.1 Introduction

A supernova is defined as a highly energetic outburst resulting in the complete disruption of a star. Gravitational collapse refers to the inward collapse of the core of a massive star which has exhausted its nuclear fuel, and is expected to produce a very large number of neutrinos in the process. Only certain types of supernovae undergo gravitational collapse. However for most of this thesis, the term "supernova" is assumed to mean a supernova resulting from gravitational collapse that releases a large number of neutrinos.

2.2 Supernova Classifications

Astronomers classify supernovae according to their optically observed properties. The two main types of supernovae, Type I and Type II, are distinguished on the basis of their electromagnetic spectra and their "light curves", which describe the time variation of the optical luminosity values. Typical light curves for both Type I and Type II start with a rise in luminosity that lasts for approximately 10 days, followed by a decline which lasts on the order of a year. But there are differences in the spectra that distinguish them from one another, which are discussed in the sections below.

Type I supernovae are further subclassified as Types Ia, Ib and Ic, while Type II supernovae can be labelled as either Type II-L or II-P as indicated in Figure 2.1. This

classification scheme is purely phenomenological, so the classes do not necessarily correspond exactly to physical processes. The underlying processes that gives rise to Type I and Type II supernovae are quite different, however the explosion energies in both cases are remarkably similar.

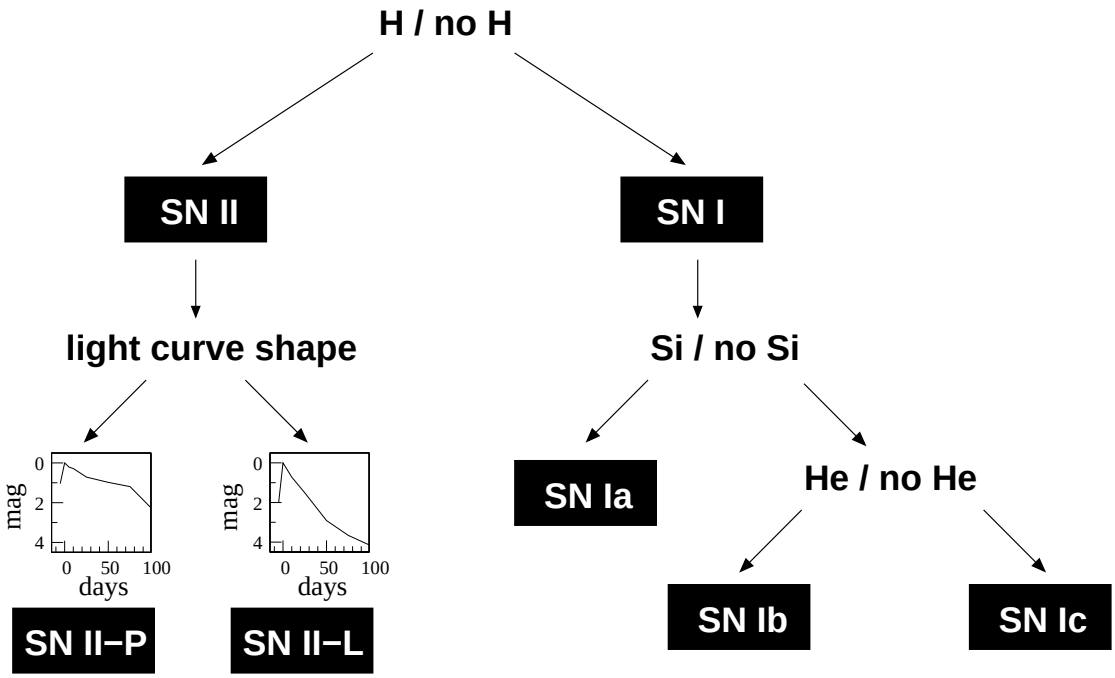

Figure 2.1: Supernova classification taxonomy, which is based on the observation of spectral lines and light curves. (After Cappellaro and Turatto [16])

2.2.1 Type I Supernovae

The primary feature used to classify a Type I supernova is the absence of hydrogen lines in its spectra at maximum light output. In general, the light curves of different Type I supernovae tend to be quite homogeneous, with similar luminosity and spectral evolution, and thus likely a consequence of uniform initial conditions.

A Type I supernova begins in an evolved binary system where one of the stars is a

white dwarf consisting mainly of carbon and oxygen[1]. To trigger the explosion, the white dwarf begins accreting matter from the companion star, which is possibly a supergiant or a main-sequence star. The hydrogen accreted from the companion star is quickly converted into helium before the explosion takes place, which explains its later absence in the absorption spectra of all Type I supernovae. When a sufficient amount of accreted mass has accumulated, a thermonuclear explosion is ignited, which is observed as a supernova explosion. Negligible neutrino emission is expected for supernovae arising from this type of physical process. Unlike Type II supernovae, the temperatures reached during nuclear burning are too low to support reactions that produce neutrinos (see Section 2.3.6).

In the model described above, the progenitor stars for Type I supernovae are not particularly massive since they evolve into white dwarfs, and additional mass is required to produce the instability that leads to an explosion. This characteristic appears to agree with observations, since the majority of Type I supernovae are found in elliptical galaxies, which contain very old populations of low-mass stars. Star formation in elliptical galaxies ended long ago. One possible reason for this might be that all of the interstellar gas in elliptical galaxies condensed into stars at the time the galaxy formed leaving no material for future star formation.

2.2.1.1 Type Ia

Type I supernovae are further subdivided according the appearance of the early-time spectrum. Type Ia supernovae are characterized by strong absorption near 6150 Å attributed to the presence of silicon. About 80% of Type I supernovae fall into the Type Ia category.

Due to their brightness and consistent light output, Type Ia supernovae are used in determining distance scales in the Universe[2].

[1]Low mass stars are unable to burn elements beyond carbon and oxygen. Our Sun, for instance, will end its life as a white dwarf.

[2]Recent analysis using Type Ia supernovae has indicated that the expansion of the Universe is accelerating! [17]

2.2.1.2 Type Ib, Ic

Type Ib supernovae lack the silicon spectral lines but instead show prominent helium lines in the spectrum, and Type Ic have neither the silicon or the helium lines. Supernovae exhibiting these features likely arise from gravitational collapse, but have previously lost their outer layers of hydrogen and possibly helium [18].

2.2.2 Type II Supernovae

Type II supernovae on the other hand are identified by the presence of hydrogen in their spectra at maximum light output. The luminosity peaks for Type II supernovae usually last for about 100 days, which is longer than for Type I. While the maxima tend to be less bright than Type I supernovae, the tails of the light curves for Type II supernovae often extend for longer periods of time.

The standard model for a Type II supernova is a massive star ($M \geq 8$ $M_\odot$), which has reached the end of $\leq$ 30 million years[3] of evolution on the main sequence when the pressure from fusion reactions can no longer support the gravitational pressure of the outer layers of gas. The star collapses inward, and when the density of the core reaches nuclear density the collapse "bounces" and a shock wave propagates outward. The interaction of this shock wave with the outer material is thought to contribute significantly to the explosion. According to prevailing theories, neutrinos originating from nuclear reactions in the collapsing core deposit sufficient energy behind the shock wave, enabling it to then completely eject the outer material. After bounce, the core continues to collapse until a neutron star, or possibly a black hole, is formed. In this model, 99% of the total binding energy of the star is carried away by neutrinos, leaving only 1% of the energy to be released in the kinetic energy of the ejecta and in electromagnetic radiation. An expanding shell of

[3]While our Sun is expected to live for a total of 10 billion years, massive stars have higher luminosities and burn their fuel faster. The stellar lifetime is roughly given by $T \propto 1/M^{2.5}$ [19]. For instance, a 20 $M_\odot$ star is expected to burn hydrogen for 10 million years [20].

gas continues to radiate radio waves and X rays for another ten thousand years.

What remains is an expanding nebula and a central neutron star which often appears in the form of a pulsar, a pulsating source of radiation in some or all electromagnetic wavelengths. The pulsed emission is due to the interplay between the fast rotation and strong magnetic fields (10^{12}–10^{13} G) in these objects.

Unlike Type I supernovae, which can be found in all types of galaxies (but mainly elliptical), Type II supernovae occur almost exclusively in the arms of spiral galaxies that are created in the process of star formation[4]. As such, spiral arms contain young stars which are more likely to be massive and therefore candidates for Type II supernovae.

2.2.2.1 Type II-P, II-L

Type II supernovae are subclassified according to their light curves. After the maximum peak, some Type II supernovae are observed to have almost constant luminosity values for periods up to 2–3 months. These are designated as Type II-P (plateau) supernovae, of which SN1987A is a prime example. Supernovae for which the light curve falls more rapidly are known as Type II-L (linear). The length of the plateau is thought to depend on the envelope mass of the progenitor star [16].

2.3 The Physics of Gravitational Collapse

This section describes a standard model for the gravitational collapse mechanism, which may result in a supernova of Type II or Ib/Ic. Various models exist to account for the processes involved in such a collapse, and they have many common features which are described below. References [21], [22], [23] and [24] provide an overview of this topic. A more detailed discussion of specific models can be found in Section 5.3.

[4]Supernova explosions are also thought to compress the surrounding interstellar medium and promote further star birth.

2.3.1 Standard Stellar Evolution

A star begins life when matter condenses from an interstellar cloud consisting of mainly hydrogen and helium with some small admixture of heavier elements. The protostar contracts under the influence of gravity and begins to heat up until the core temperature is high enough (10^7 K) to ignite hydrogen burning through nuclear fusion[5]. The thermal pressure from nuclear burning reactions provides a balancing force to counteract the inward gravitational attraction, resulting in a state of hydrostatic equilibrium.

Eventually, the supply of hydrogen in a star is reduced to a point where the pressure generated by its burning is no longer sufficient to support the overlying mass of material. When this happens, the stellar core starts to collapse, causing the temperature to increase until it is high enough to burn the helium that was produced in the first stage of the star's life. The unburned hydrogen forms an outer layer that surrounds the burning helium core.

The fusion of helium into carbon proceeds until the supply of helium is diminished and the star again contracts, heats up and a subsequent burning reaction involving the fusion of more massive atoms ignites. This process is repeated, producing progressively heavier elements in rapid succession. The products of successive nuclear burning stages are arranged in concentric shells, with the heaviest elements in the centre and hydrogen in the outer envelope. This is the well-known "onion skin" structure of a pre-supernova star.

By its nature, the fusion process creates fewer combustion products at each step of the burning process, such as during the fusion of hydrogen into helium where four hydrogen atoms are required to create one helium atom. Therefore each burning stage takes less time than the one preceding it. Hydrogen burning lasts for several million years; however, the last few stages last only a few years or months. The final burning stage of a pre-supernova star lasts only about a day.

[5]The minimum mass required to attain a core temperature of 10^7 K and begin hydrogen burning is about 0.08 $M_\odot$.

2.3.2 The Pre-Supernova Star

At the very end of their lives, massive stars are able to burn heavy elements such as oxygen and silicon to produce ^{56}Fe. This isotope of iron is the most strongly bound of all elements, which means that further fusion or fission reactions result in the absorption, rather than the production, of energy. Therefore, ^{56}Fe does not burn, but accumulates in the core of the star. The onion-skin structure of the star now has a relatively small iron core at the centre surrounded by shells of silicon, oxygen, neon, carbon, helium and an outer layer of hydrogen.

For objects with masses greater than the Chandrasekhar mass limit $M_{\rm Ch}$, the degeneracy pressure of the relativistic electron gas can no longer support the pressure being exerted due to gravity. The Chandrasekhar mass limit is given by [21]:

$$M_{\rm Ch} = 5.8\, Y_e^2\, {\rm M}_\odot, \tag{2.1}$$

where Y_e is the fraction of electrons per nucleon ($Y_e = Z/A$, where Z is the average charge and A is the average atomic number). For an iron-nickel core, the mass limit is $M_{\rm Ch}$ $\sim$1.2 M$_\odot$. Notice that this limit does not depend on the density of the star, but on the composition. When a mass of iron exceeds this limit, it will begin to compress under its own gravity.

2.3.3 Core Collapse

The electron degeneracy is unable to prevent the star from collapsing further once the mass of iron in the central core of the star exceeds the Chandrasekhar mass limit. For massive stars, the mass of the core is typically in the range $M_{\rm core} \simeq 1.4 - 2.0$ M$_\odot$. Two additional instabilities also contribute to core collapse. The most important of the two processes is *electron capture*. As the temperature and density in core rises, the rate of electron capture reactions also increases:

$$e^- + p \rightarrow n + \nu_e. \tag{2.2}$$

This stage of collapse is also referred to as *neutronization* because of the neutron produced in the final state. The electron neutrinos that result from this reaction are able to escape during this early stage of collapse because the neutrino mean free path is much greater than the size of the star. As a consequence, electron capture serves to decrease the energy and the number of particles in the core and therefore the pressure, which increases the rate of collapse.

A second process that contributes to core de-stabilization is called *photodisintegration*. Energetic photons are able to dissociate the stable iron nuclei through the reactions [24]:

$$\gamma + {}^{56}\mathrm{Fe} \rightarrow\ 13\,{}^{4}\mathrm{He} + 4n \tag{2.3}$$

$$\gamma + {}^{4}\mathrm{He} \rightarrow 2p + 2n. \tag{2.4}$$

Although these reactions increase the number of particles in the core, they are endothermic and therefore require energy in order to take place. The result is that the average kinetic energy of the particles decreases and so does the pressure. While photodisintegration also contributes to the de-stabilization of the core in lower mass stars, it is thought to be the dominant process in higher mass stars.

2.3.4 Neutrino Trapping

Core collapse continues and electron neutrinos are still able to diffuse out of the core until densities approaching $\rho \approx 10^{12}$ g/cm^3 are reached. At these densities not even neutrinos can escape as the mean free path for neutral current ν_e scattering becomes less than the size of the core for time scales on the order of milliseconds. At this point, all energy becomes trapped within a radius of approximately 30 km inside the core. The spherical shell at this radius, separating the inner region which is opaque to neutrinos and the outer region which is transparent to neutrinos, is known as the *neutrinosphere*. Neutrinos at a radius less than the neutrinosphere are considered to be trapped, whereas those beyond the neutrinosphere radius are free to propagate outward.

After neutrino trapping occurs, collapse continues and the core density continues to increase.

2.3.5 Core Bounce and Shock Breakout

Finally, the density in the core reaches the density of nuclear matter, $\rho = 2.7 \times 10^{14}$ g/cm^3. At this point matter cannot compress any further due to the nucleon degeneracy pressure. Unlike the electron degeneracy pressure which was overcome with sufficient mass ($M_{\rm core} > M_{\rm Ch}$), there is no possibility of further substantial collapse once regions are compressed to nuclear densities. There is however, a small amount of compressibility in this state and the momentum of the infalling material carries the collapse beyond the point of equilibrium, compressing the core to a density even higher than nuclear densities. When this happens, a "bounce" occurs. A shock wave is created inside the core and begins propagating outward and interacting with the outer layers of matter, which are still falling inward toward the core. The shock wave is a discontinuity in pressure, density and temperature, and its effect is to compress and heat the matter it passes through. The shock starts deep inside the core at a radius of approximately 10 km, and moves outward with a velocity of about 70 km/ms

2.3.6 Neutrino Breakout

At approximately 1 ms after bounce, the shock hits the neutrinosphere, and neutrinos created in the high-temperature wake are able to stream outward. This is called the "neutrino break-out" or "neutrino flash". The temperatures directly behind the shock wave are now sufficiently high to produce other flavours of neutrinos through a variety of

neutral current pair processes[6] including [25]:

- Pair annihilation: $\gamma + \gamma \rightleftharpoons e^+ + e^- \rightarrow \nu + \overline{\nu}$ (2.5)
- Plasmon decay: *plasma excitation* $\rightarrow e^+ + e^- \rightarrow \nu + \overline{\nu}$ (2.6)
- Photoneutrino: $\gamma + e^- \rightarrow e^- + \nu + \overline{\nu}$ (2.7)
- Bremsstrahlung: $e^- + (A, Z) \rightarrow (A, Z) + e^- + \nu + \overline{\nu}$. (2.8)

Photoneutrino processes dominate at lower temperatures (10^8–10^9 K), while the main contributions at higher temperatures (10^9–10^{10} K) are due to pair annihilation. The plasma processes dominate at high densities over the full range of temperatures [26].

2.3.7 Explosion

The next necessary stage in this evolution is the "explosion", in which the outer material of the star is completely ejected. However, when the shock wave reaches a distance of a few hundred kilometers from the centre of the star both it and the explosion are stalled. Part of the reason that the supernova fails to explode promptly is due to the energy lost as the shock wave passes through regions of high temperature with high densities of heavy nuclei in the vicinity of the core. Photodisintegration reactions (Equation 2.3) can occur in these regions and require large amounts of energy ($kT \sim 9$ MeV per nucleon in heavy nuclei), which removes energy from behind the shock.

The slow-down of the shock wave is further aggravated by the emission of neutrinos. Protons resulting from the photodisintegration reactions above readily capture electrons. Since these reactions take place above the neutrinosphere, the neutrino emitted in this process can escape, thereby removing energy from the star. Additional energy is carried away by neutrinos that are created in pair production reactions in the high temperature

[6]The temperatures are not sufficiently high to create muon and tau particles via the charged-current process. Therefore, muon and tau neutrinos and antineutrino are created via neutral current processes. However, $\nu_e\overline{\nu}_e$ pairs can be created through both neutral- and charged-current reactions.

environment. The net result is that both temperature and pressure are sharply reduced in the shock wave causing it to stall, while matter continues to fall through it.

Failure or success of the prompt shock depends primarily on the amount of material the shock has to traverse before it emerges from the iron core. Relatively low mass stars have correspondingly small iron cores, and may explode via the prompt shock mechanism. Once the shock has emerged relatively easily from the small core, the lower core temperature of smaller stars will also favour the prompt explosion. At low temperatures, electron capture processes no longer decrease the pressure and reduce the energy in the core, therefore the mass of the inner core increases and expands to energize the outgoing shock wave.

A different mechanism is necessary for more massive stars. While many of these neutrinos were described in earlier sections as being "trapped", they do diffuse out of the core on longer time scales. Neutrons and protons behind the shock absorb a small fraction of this $\sim 10^{53}$ erg/s neutrino luminosity diffusing out from the newly forming neutron star. This addition of energy from neutrinos effectively revives the shock wave, which will then expel the outer material from the star [27]. Since only a small fraction of the neutrinos interact, the material in the vicinity of the shock wave does not suffer greatly from diminishing energy reserves or pressure. Therefore, neutrino heating is most effective at a radius of about 150 km, where the probability of neutrino absorption is not too low and yet the temperature is not so high that the matter there emits a large number of neutrinos. As a result, the value of 150 km becomes the bifurcation radius: all the matter within this boundary ultimately falls into the core, while the matter outside is expelled.

The neutrinos that re-heat the shock wave diffuse out of the core over several hundred milliseconds, therefore this mechanism is referred to as the "delayed" explosion.

2.3.8 Cooling

The neutron star that remains behind after the explosion cools by emitting neutrinos over a timescale of tens of seconds. Neutrinos of all flavours are emitted as $\nu\overline{\nu}$ pairs through reactions such as those mentioned in Equations 2.5, 2.6, 2.7 and 2.8. In fact most of the neutrinos are emitted during this phase as the star sheds its binding energy almost completely in the form of neutrinos, each carrying approximately 15 MeV.

However, if the progenitor star is particularly massive, the flux of neutrinos emitted during the cooling stage may be truncated due to the formation of a black hole.

2.3.9 Aftermath

After the explosion, the shock wave continues to move outward through the outer envelope. Various kinds of electromagnetic radiation result from the interaction of the shock with the outer material. Large amounts of ^{56}Ni are created as the shock wave moves through the shell of silicon that surrounds the iron core. The ^{56}Ni isotope is unstable and decays via electron capture with a half life of 6.1 days:

$$^{56}\mathrm{Ni} + e^- \rightarrow {}^{56}\mathrm{Co} + \gamma + \nu_e, \qquad E_\gamma = 0.2 - 1.6 \text{ MeV}. \tag{2.9}$$

The cobalt nucleus decays to iron by electron capture with a half life of 77.3 days:

$$^{56}\mathrm{Co} + e^- \rightarrow {}^{56}\mathrm{Fe} + \gamma + \nu_e, \qquad E_\gamma = 0.2 - 3.6 \text{ MeV} \tag{2.10}$$

and, less often, by positron emission:

$$^{56}\mathrm{Co} \rightarrow {}^{56}\mathrm{Fe} + \gamma + e^+ + \nu_e. \tag{2.11}$$

At late times, the supernova light curve is powered by the decay of ^{56}Co. The gamma rays from the decay can begin to escape as the ejecta expands and thins.

2.4 Expected Frequency of Supernovae

2.4.1 Relative Frequency of Supernova Types

Some techniques for estimating the frequency of galactic supernovae only predict the total number for all types. Supernova data from other galaxies can also be used to estimate the ratio of the different types within our own galaxy. Since only supernovae of Type II and Ib/c are expected to generate a substantial neutrino signal, knowing which types of supernovae are more likely is useful information.

Galaxies are classified into three general types based on their shapes: elliptical, spiral and irregular. A fourth type of galaxy has been observed to share both elliptical and spiral attributes and is called a "lenticular" galaxy. The Milky Way galaxy is classified as spiral Sbc galaxy.

According to Tammann *et al.* [28], most supernovae occur in spiral and irregular galaxies because of the large population of massive stars in those types of galaxies. Of the few that do occur in elliptical galaxies, essentially all are of Type Ia with no contribution from any of the other types. Therefore, a neutrino burst due to gravitational collapse is not expected from elliptical galaxies.

Narrowing the study to spiral galaxies similar to the Milky Way indicates that Type II/Ib supernovae are between 5 and 6 times more frequent than those of Type Ia [28], [16]. In other words, 83–86% of the supernovae in spiral Sbc galaxies belong to the Type II/Ib designation. For other types of spiral galaxies, the fraction of Type II/Ib supernovae is estimated to be as high as 91%.

2.4.2 Galactic Supernovae

There are a number of different techniques that can be used to estimate the frequency of supernovae within the Milky Way. However, the results of these studies vary quite widely.

2.4.2.1 Historical Supernovae

One method for determining the supernova rate in our galaxy is to rely on observations of supernovae in the past. Over the last one thousand years, 6 supernovae have been observed by early astronomers, which likely constitutes the complete set of supernova events that occurred within 3 kpc of the Sun[7] [29]. However, these observations represent only about 20% of the expected total, since it is likely that many were obscured by dust, especially toward the centre of the galaxy. This is one of the reasons why all of the historically observed supernovae are limited to a sector of the galactic plane which spans only 60°, and in the last millennium, all but the closest one are in the direction away from the galactic centre [30]. The recent known supernovae in our galaxy are listed in Table 2.1.

Using historical supernova events, the supernova rate can be calculated in two ways. The most direct way involves assuming that the supernova rate in the entire galaxy is the same as that in the historically observable region. Estimates using this method suggest a galactic supernova mean interval of $\tau \leq$30 yr [30] and 14–25 yr [31]. If the type of supernova in the historical events can be determined accurately then a supernova rate can be determined using detailed models of the population distribution in the galaxy. Calculations performed using this approach estimate one supernova every 6–17 yr [29]. The Crab is almost certainly a Type II supernova based on the observation of the hydrogen spectral lines and of the pulsar remnant. As well, data collected by Tycho Brahe indicates that the supernova of 1572 is of Type I. Unfortunately, the type assignments of other historical supernovae are not as straightforward. Where possible, the type designation for the set of historically observed supernova is also specified in Table 2.1. Distance information[8] is compiled from

[7]The parsec (pc) is defined as the distance at which 1 astronomical unit (AU) perpendicular to an observer's line of sight subtends an angle of 1 arc second. 1 pc = 3.09×10^{13} km = 3.26 light years.

[8]There are several conflicting reports on the distances to historical supernovae. For instance, in reference [32] the distance to Kepler's supernova of 1604 is quoted as $D = 3.4 \pm 0.3$ kpc, while in reference [33] the distance is $D = 10.0$ kpc. The author suspects a confusion in units between kpc and kly (3 kpc $\approx$ 10 kly).

van den Bergh [29], Schaeffer [32] and Reed [34].

Name	**Year**	**Distance (kpc)**	**Type**
Lupus	1006	1.6	Ia
Crab	1054	2.0	II
SN1181	1181	3.2	II?
Tycho	1572	2.4	I?
Kepler	1604	3.4	I/II?
Cas A	∼1680	3.4	Ib

Table 2.1: Recent observed galactic supernovae. The Cas A supernova seems to have gone unnoticed in the records of early astronomers, except possibly by Flamsteed [35].

2.4.2.2 Supernovae in Other Galaxies

Another technique that is useful in estimating the supernova rate in our galaxy is to measure the supernova rates in other galaxies. However, a number of considerations are required in order to make this comparison.

First, the number of supernovae in a given galaxy depends significantly on the type of galaxy and in particular on the luminosity of the galaxy. Therefore, in order to use data from other galaxies to predict the supernova rate in the Milky Way, it is necessary to know both the type and size of our galaxy. Another consideration is the orientation of the galaxy with respect to our own. Due to absorption, supernovae are more difficult to detect when their parent galaxies are viewed "edge-on" rather than from "above". Finally, determination of galactic sizes and therefore luminosity involves determining the distance to the galaxy. Large uncertainties in the Hubble constant mean that these factors are not very well known.

Adopting $H_0 = 50$ km s^{-1} Mpc^{-1} for the Hubble constant and assuming that the Milky Way can be classified as a Sbc type galaxy with luminosity $L = 2.3 \times 10^{10}$ L$_\odot$, Tammann *et al.* [28] estimate a total of 2.0 galactic supernovae per century (or 1 supernova every 49

years) with a possible range of 1.6–3.2 supernovae per century (or 1 supernova every 31– 63 years). Roughly 85% of these events are due to supernovae of Type II/Ib (see Section 2.4.1, from which a substantial neutrino signal is expected. In that case, the best estimate of the rate is 1 every 57 years.

Lower values for the galactic supernova rate are obtained by a more recent study. Using the same luminosity as above but a higher value for the Hubble constant ($H_0 = 65$ km s^{-1} Mpc^{-1}), Cappellaro and Turatto [16] suggest that the Type II+Ib/c supernova rate is (1.5 $\pm$ 1.0) per century, or one Type II+Ib/c supernova every (67 $\pm$ 44) years. Considering all supernova types, the predicted rate is approximately 1/53 yr. Taking into account the uncertainty in the Hubble constant contributes an additional range of 15–20 years.

Tammann *et al.* [28] also report a combined estimate of 1/40 years using both extra-galactic and historical observations.

2.4.2.3 Supernova Remnants

Searching for the remains of a supernova explosion is also a crude method used for estimating the supernova rate. After a supernova explosion the expanding shell of ejected material interacts with the interstellar medium, producing radio emission and possibly other types of radiation. Based on the counts and ages of these remnants, an estimate of the supernova rate can be made. However, characteristics of the supernova remnant such as the lifetime depend to a large extent on the interstellar medium surrounding the supernova, which affects the number of observable remnants in different regions of the galaxy.

Leahy and Wu [36] provide an estimate of supernova rates based on radio supernova remnant surveys of 1 per $f \times (18 - 42)$ yr, where f is some factor less than or of order unity.

A different remnant considered by Hartmann *et al.* [37] is the γ-ray signal from the decay ^{44}Ti $\rightarrow$ ^{44}Sc $\rightarrow$ ^{44}Ca with a mean life of 78.2 years. The decay of ^{44}Ti generates

a number of gamma-ray photons, of which 1.16 MeV is the highest energy and therefore the easiest to detect. The relatively short mean life implies that this method is sensitive to only very recent or very near supernovae[9]. In the initial application of this method, no emission was detected after searching almost ten years of data, which when combined with historical supernovae yields a mean interval of $\tau = 10$–40 years. The lower end of the estimate range is due to constraints imposed by the γ-ray search.

Another type of remnant used to estimate Type II/Ib supernova rates is the pulsar. Pulsars are thought to be associated only with gravitational collapse supernovae, and are strong sources of highly periodic radio signals which are thought to be rotating magnetic neutron stars. Several pulsars have been associated with supernova remnants (the Crab pulsar, for instance). However, since no conclusive evidence for a pulsar has been found in the remnant of SN1987A, it is possible that not all gravitational collapse events give rise to a pulsar. Therefore, the birthrate of pulsars may represent a lower limit on the Type II/Ib supernova rate.

In order to calculate the supernova rate, it is necessary to know both the number of pulsars in a region and the age of those pulsars. Observations indicate that the rotation period of a pulsar radio signal increases with time as the pulsar "spins down" after the formation of a neutron star. Therefore careful measurements of the rotation period can be used to indicate the age of the pulsar, and from that the rate of formation of pulsars in the galaxy.

Sophisticated simulations of pulsars with observational input from from astronomical data suggest a wide range of pulsar birthrates. The lowest estimates are for mean interval times in the range of 1 per 4.4–14 yr [41], while other studies predict a less frequent pulsar

[9]In fact, according to the authors, none of the known historical supernovae is either close or young enough to produce a detectable signal. However, γ rays from ^{44}Ti have been observed in the Cas A remnant [38] and in the recently discovered young supernova remnant RX J0852.0-4622 / GRO J0852-4642 [39]. There has also been an initial report of observed ^{44}Ti emissions associated with a previously unknown galactic supernova [40], but there are some indications that this claim has been withdrawn.

birthrate: 1 per 100 years [42] and 1 per 125–250 years [43].

2.4.2.4 Iron Abundances

Using estimates of the composition and the age of the universe, predictions of the average supernova rate can be obtained by assuming that a large fraction of the iron in the universe was manufactured and dispersed by supernova explosions [44]. Tammann *et al.* [28] use this information to argue that the average supernova rate for all types must be 6 supernovae per century. Since approximately 85% of all supernovae are Type II/Ib, the mean interval time between Type II/Ib supernovae is ∼20 years. However, the present rate of iron production is likely smaller than in earlier epochs, therefore the above rate is an upper limit on current supernova rates.

2.4.2.5 Stellar Evolution Rates

The death rate of stars can also be calculated using models of the galaxy that describe the distribution of types of stars and their masses in conjunction with observational data. Ratnatunga and van den Bergh [45] report a supernova mean interval time of 40–250 yr for progenitor masses $M > 8$ $M_\odot$. A more recent application of this methods yields a lower mean interval time of between 28–40 yr for all supernova types [28].

2.4.2.6 Neutrinos

Data from neutrino detectors also places a limit on the rate of supernovae in the galaxy. Early detectors including Baksan, Mont Blanc, IMB and Kamiokande combine to give an effective search time that is at least 10 years. Using Poisson statistics, the mean interval between Type II and Ib supernovae is more than 12 yr at the $1\,\sigma$ level [28].

2.4.2.7 Summary

In the preceding sections, various methods are described that attempt to estimate the supernova rate in our galaxy. From this survey, a wide range of values are suggested

for the mean interval between supernovae in the Milky Way galaxy. These methods and their associated estimates are summarized in Table 2.2. From these data, Tammann *et al.* suggest that the combined best estimate for the total galactic supernova rate is $2.5^{+0.8}_{-0.5}$ supernovae per century. As 85% of these are expected to result from Type II/Ib supernovae, one neutrino burst is expected every ∼47 years. A widely accepted range is 1 supernova per 30–50 years [33].

Method	**Mean Interval (yr)**	
	Type II + Ib	**All Types**
Historical Galactic SN		14–25 [31]
		6–17 [29]
		≤30 [30]
Extragalactic events	34–76 [28]	31–63 [28]
	23–111 [16]	20–86 [16]
Radio remnants		12–46 [29]
		≤18–42 [36]
Gamma ray remnants		≥10–20 [37]
Pulsar remnants	4–14 [41]	
	100 [42]	
	125–250 [43]	
Iron abundance	>20 [28]	>17 [44]
Stellar death rates		28–40 [28]
	40–250 [45]	
Neutrinos	>12 [28]	

Table 2.2: Estimates of the mean interval between supernovae in the Milky Way galaxy by various methods. A widely accepted range is 1 supernova per 30–50 years.

2.4.3 Local Group Supernovae

Current neutrino detectors are sensitive to a burst of neutrinos from beyond the far edge of the Milky Way galaxy. Therefore, the expected supernova rates for galaxies near to the Milky Way are also of interest.

Compared to the massive Milky Way galaxy, the expected frequency of Type II/Ib

supernovae in our nearest satellite galaxies, the Large (LMC) and Small (SMC) Magellanic Clouds, is much smaller. The supernova rate in the LMC (where SN1987A originated from) is one supernova on order of every 200 years on average. In the SMC, the supernova rate is even lower at one supernova every 900 years on average [28].

The nearest massive galaxy is Andromeda at a distance of 800 kpc. Studies of Hα line emission and far-infrared fluxes[10] in this galaxy indicate that the Type II/Ib supernova rate is roughly 1/120 years. This is somewhat surprising since this rate is lower than that expected for the Milky Way and yet and the Andromeda galaxy contains more mass. Table 2.3 summarizes the expected supernova rates in nearby galaxies. These estimates agree with recorded observations. Only one supernova has been observed in the Large Magellanic Cloud (SN1987A) during ~300 years of surveillance, while none has been observed in the Small Magellanic Cloud. Furthermore, roughly 100 years of observation has yielded one supernova in the Andromeda galaxy (SN1885A).

Galaxy	**Mean Interval (yr)**	
	Type II + Ib	**All Types**
Large Magellanic Cloud (LMC)	222	204
Small Magellanic Cloud (SMC)	909	833
Andromeda (M31)	120	83
Triangulum (M33)	161	147

Table 2.3: Estimates of the mean interval between supernovae in nearby galaxies.

Combining the Milky Way together with the Large and Small Magellanic Clouds, Tammann *et al.* [28] estimate that current neutrino detectors are sensitive to 2.7 Type II and Ib supernovae per century, or one burst every 37 years.

In order to obtain a detection rate on the order of one supernova per year, neutrino

[10] Hα line emission has been correlated with Type II/Ib progenitors, since only hot stars with $M \geq 10\,M_{\odot}$ contribute to the ionization of hydrogen [46]. Similarly, the far-infrared radiation is produced when dust is heated by hot massive stars [28].

detectors would need to be sensitive to a much larger volume of space than the current generation, possibly extending as far as the Virgo cluster of galaxies at 15 Mpc, which contains roughly 2000 galaxies and has a total estimated mass of 1.2×10^{15} $M_{\odot}$ [47].

Chapter 3

Supernova Neutrinos

3.1 Introduction

The first direct evidence of the role of neutrinos in supernova explosions came on February 23, 1987 with the signal of the brightest supernova in 383 years. Information gathered from that event was sufficient to confirm general aspects of supernova explosion theory, but many details will not be resolved until the next galactic supernova is observed. In the sections that follow, the supernova neutrino signal is described in some detail, from the small number of events recorded in 1987 to general predictions from contemporary supernova models.

3.2 Supernova 1987A

Supernova 1987A (SN1987A) was first identified by Ian Shelton at the Las Campanas Observatory in Chile on February 24, 1987 [48]. Shelton had taken a 3-hour exposure photograph starting at 01:20 UT, which later showed the appearance of an extraordinarily bright star in the Large Magellanic Cloud. After the discovery, other observations were used to further define the onset of the optical signal. New Zealand amateur astronomer Albert Jones made a number of observations of SN1987A but perhaps most importantly he did not observe the supernova when monitoring the LMC at 9:22 UT. Later at 10:38 UT, McNaught obtained a photograph of the LMC that showed the supernova at approximately magnitude = 6.0 (barely visible to the naked eye). These two observations would later be

used to constrain the arrival time of the optical signal.

The SN1987A explosion actually took place approximately 165 000 years ago in the Large Magellanic Cloud, an irregular satellite galaxy approximately 51 kpc away from our Sun. The progenitor star was called Sanduleak -69° 202 and had an estimated mass M = 20 $M_\odot$ [20]. Somewhat surprisingly, the progenitor was a blue supergiant rather than a red one, and had a lower metallicity and smaller radius than was expected for a typical pre-supernova star. However, the properties of Sanduleak -69° 202 are not inconsistent with models of gravitational collapse. It is assumed that the progenitor star lost several solar masses from its surface during its red giant stage, but still retained much of its hydrogen envelope. There has been recent evidence that a pulsar has been detected in the supernova location. Even though early reports [49] that identified a pulsar associated with SN1987A were withdrawn, new observations [50] suggest that a 2.14 ms pulsar may have been discovered. However, these findings are not yet widely accepted by the astronomical community.

3.2.1 Detected Supernova Neutrinos

After the initial discovery of the supernova by optical astronomers, data from various neutrino detectors operating at the time were searched for signs of neutrinos that could be related to the supernova explosion. The results of this intensive search showed that a number of detectors recorded neutrino events in the time preceding the measurements by optical astronomers. These detectors included the Kamiokande II, IMB, Baksan and LSD detectors.

3.2.1.1 KII Detector

The Kamiokande II (KII) detector [51] consisted of 3000 tonnes of purified water (2140 tonnes fiducial volume) surrounded by 948 50-cm diameter photomultiplier tubes capable of detecting Čerenkov radiation. The detection efficiency at the 7.5-MeV energy threshold

used for analysis was approximately 40% [52]. Unfortunately, little effort was made to synchronize the experiment clock to Universal Coordinated Time (UTC), which contributes a 1 minute error on the time of the first event.

The KII detector was sensitive to Čerenkov light from recoil electrons produced by neutrino electron scattering

$$\nu + e^- \rightarrow \nu + e^-, \tag{3.1}$$

and to Čerenkov light from recoil positrons produced by antineutrino absorption on free protons in the water molecules

$$\overline{\nu}_e + p \rightarrow n + e^+. \tag{3.2}$$

Eleven events were recorded in the KII detector[1] in the energy range of 7.5–50 MeV. The times and energies of these events are shown in Figure 3.1. In the plot, time is taken to be relative to the first event, which was recorded February 23, 1987 at 7:35:35 UT ($\pm$ 1 min). Since the cross section for the antineutrino reaction is roughly two orders of magnitude higher than for the elastic scattering reaction (see Section 5.4), most, if not all, of the observed events are associated with electron antineutrinos.

3.2.1.2 IMB Detector

Similar to the KII detector, the Irvine-Michigan-Brookhaven (IMB) detector [53] was also a water Čerenkov detector. It consisted of 7000 tonnes of purified water (5000 tonnes fiducial volume) surrounded by 2048 20-cm diameter photomultiplier tubes. For a 7-hour period that included the search for neutrinos from SN1987A, one-quarter of the IMB photomultiplier tubes were inoperative, reducing its detection efficiency to 14% at the 20-MeV energy threshold. However, of the four detectors that reported neutrino events from SN1987A, IMB was one of two detectors that was able to specify the absolute time of their events with an accuracy of less than about 1 minute. The absolute time of each event recorded in

[1] An additional event was also recorded below the nominal analysis threshold. The energy of this event was 6.3 MeV.

the detector was accurate to 50 ms, whereas the relative time between events was known to better than 1 ms.

The IMB detector was also sensitive to Čerenkov light from recoil electrons and positrons and was able to identify 8 events in the energy range of 20–40 MeV, the first of which was recorded at 7:35:41.37 UT (± 50 ms). The energies and times for these events are shown in Figure 3.1, where the times for the IMB data are relative to the first IMB neutrino event. Taking into account the large error associated with the time of the first KII event, the IMB and KII bursts are essentially simultaneous.

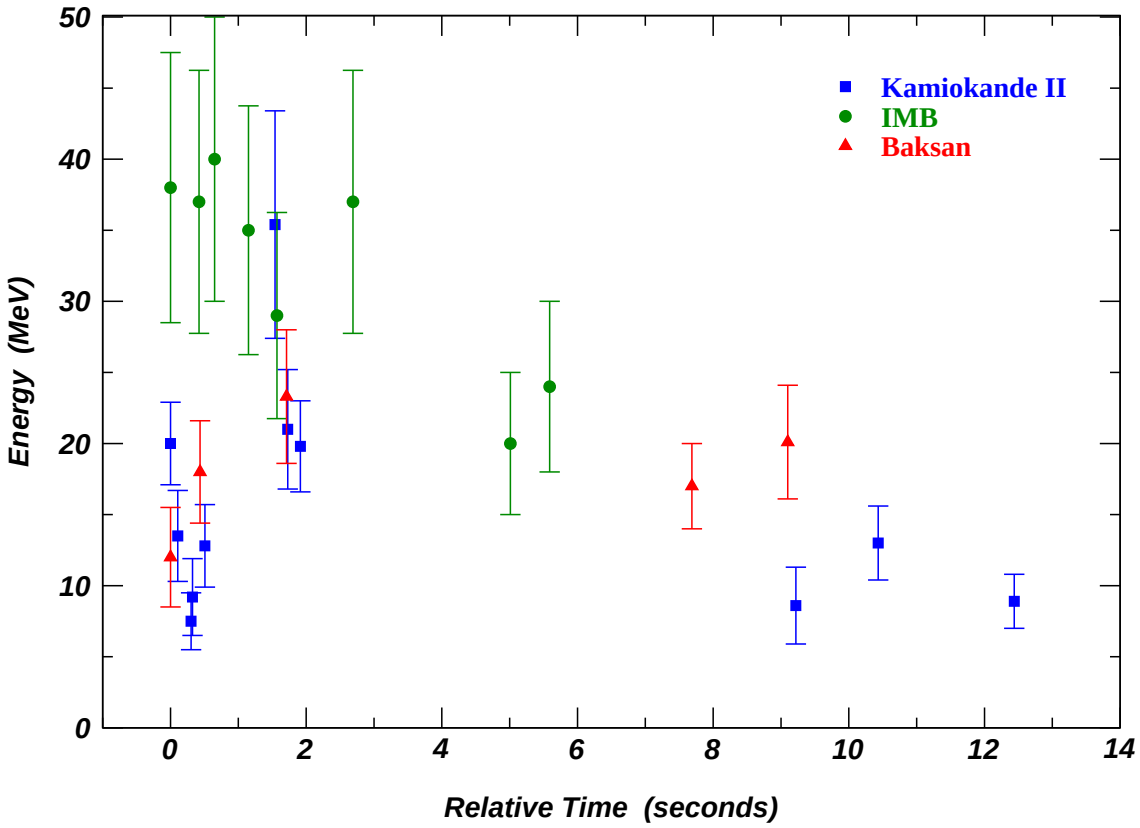

Figure 3.1: Electron/positron energies and relative times for the events identified by the Kamiokande II, IMB and Baksan detectors during SN1987A. Eleven events were recorded by Kamiokande II, 8 events by IMB and 5 by Baksan. The time of events recorded by each detector is relative to the first event in that detector.

3.2.1.3 Baksan Detector

The Baksan detector consisted of 330 tonnes of oil-based liquid scintillator (200 tonnes fiducial volume) separated into 3150 units, each of which is viewed by a photomultiplier tube capable of detecting scintillation light. The detection efficiency was approximately 50% for 10 MeV electrons. Initially, the absolute time of each event recorded in the detector was reported to be 2 s [54], but subsequent studies a few weeks after the supernova event showed that the detector clock had shifted forward by 54 seconds [55]. The relative time between events is quoted as being accurate to 1 ms.

Scintillator detectors are mainly sensitive to electron antineutrinos through the same reaction that the KII and IMB water Čerenkov detectors used. Five neutrino events were observed between 11 MeV and 50 MeV in the time range suggested by the KII and IMB data, with the first event recorded at 7:36:11.818 UT ($^{+2}_{-54}$ s). An additional event is often listed, but is generally attributed to background. The time difference between the first IMB event and the first Baksan event is 31 seconds. Taking the likely time shift into account, it is not unreasonable to consider the neutrino events recorded in the Baksan detector as belonging to the same burst that was seen in the KII and IMB detectors. The time and energy data are shown in Figure 3.1, where the times for the Baksan data are relative to the first Baksan event.

3.2.1.4 LSD Detector

Another detector that reported observation of neutrino events believed to possibly be associated with SN1987A is the Liquid Scintillator Detector (LSD) in the Mont Blanc Laboratory [56]. Instead of water, the LSD detector consisted of 90 tonnes of liquid scintillator as the target material, which was contained in 72 separate counters, each of which was observed by 3 photomultiplier tubes. Different layers of the detector had different energy thresholds. The inner layer had an energy threshold of 5 MeV, while the outer layer was

less sensitive, having an energy threshold of 7 MeV [57].

As with the other three detectors, LSD was sensitive to electron antineutrinos through the reaction $\overline{\nu}_e + p \rightarrow n + e^+$. The positron was detected through the annihilation $e^+ + e^- \rightarrow \gamma$ and the neutron was detected through the neutron capture reaction $n + p \rightarrow d + \gamma$. While the positron detection efficiency is not mentioned, 40–60% of the neutrons are detected in the same counter as the positron.

Event Time (UT) (±2 s)	**Event Energy (MeV) (±20%)**
2:52:36.79	7
40.65	8
41.01	11
42.70	7
43.80	9

Table 3.1: Time and energy information for the events recorded at LSD, possibly associated with SN1987A.

While first to announce the detection of neutrinos associated with SN1987A, the results from LSD are the most controversial. The LSD detector recorded 5 events starting at 2:52:36.792 UT (± 2 ms), almost 5 hours earlier than the events observed at the other neutrino detectors [57]. Table 3.1 list the events with their measured time and energy values. Three of the events were observed in the inner layer and 2 were observed in the outer layer. None of the larger water Čerenkov detectors observed a signal near the time of the LSD signal, and the Baksan detector only found a single 11-MeV event, which is near their energy threshold for analysis. As well, based on the signal observed in the KII and IMB detectors, the most probable signal was less than or of order 1 event in the LSD detector [20], whereas 5 events were recorded. Some also argue [58] that detailed light curve models favour the later time and that the early burst from LSD is not well fit by the standard collapse assumptions. For these reasons, many astrophysicists are skeptical

of the LSD results.

3.2.1.5 Homestake Detector

The Homestake ^{37}Cl detector was also operational immediately preceding SN1987A. The Homestake detector has a fiducial mass consisting of 615 tonnes of C_2Cl_4 and is only sensitive to ν_e neutrinos. Neutrino interactions are observed using the reaction

$$\nu_e + {}^{37}\mathrm{Cl} \rightarrow e^- + {}^{37}\mathrm{Ar}. \tag{3.3}$$

No events were observed that were correlated with SN1987A [20], which is consistent with the number of expected events.

3.2.1.6 Summary

A summary of the detectors that reported neutrino events from SN1987A is presented in Table 3.2. A total of 24 events were observed near 7:36 UT on February 23, 1987. An additional signal is claimed by the LSD group near 2:53, but remains unsubstantiated by the other detectors. Although the LSD detector is sensitive to lower energy neutrinos than either the IMB and Baksan detectors, the KII detector should have registered a significant signal, which it did not.

Detector	**Target**	**Mass (ktonne)**		**Energy**	**#**	**UT Time**
		Total	**Fid.**	**(MeV)**	**Events**	**Feb 23, 1987**
KII	H_2O	3	2.1	7.5–50	11	7:35:35 ($\pm$ 1 min)
IMB	H_2O	6.9	5.0	20–40	8	7:35:41 ($\pm$ 50 ms)
Baksan	$(CH_2)_n$	0.33	0.20	10–50	5	7:36:12 ($^{+2}_{-54}$ s)
LSD	$(CH_2)_n$		0.09	>5,7	5	2:52:37 ($\pm$ 2 ms)
Homestake	C_2Cl_4		0.62	0.8	0	

Table 3.2: Summary of detectors that recorded neutrino events from SN1987A.

The exact time of the onset of optical brightening is not known, but constraints from the earliest observations imply that neutrino signal from SN1987A preceded the optical

signal by at most 3.0 hours. This time delay between the neutrino and optical signals is consistent with predictions from supernova explosion theory.

The energies and times of the events observed by the KII, IMB and Baksan detectors are consistent with the predictions of a simplistic gravitational collapse model. Not only are the neutrino energies in the expected range, but the decrease with time of the average energies and the decrease in event rate with time also agree with general predictions.

All of the neutrinos observed from SN1987A are believed to be $\overline{\nu}_e$ neutrinos, so very little information was gathered regarding the roles that neutrino flavours have in the collapse mechanism.

3.3 Neutrino Signal

Having established the general importance of neutrinos to gravitation collapse supernovae through the observation of neutrinos from SN1987A, it is timely to review the current predictions for a more significant neutrino signal.

As discussed in Chapter 2, nearly all of the gravitational binding energy in a core collapse supernova is emitted in the form of neutrinos. The gravitational binding energy carried by neutrinos, E_b, is estimated to be:

$$E_b \sim \frac{GM_{\rm core}^2}{R_{\rm core}} \sim 3 \times 10^{53} \text{ergs}, \tag{3.4}$$

where G is the gravitational constant, $M_{\rm core} \sim 1$ M$_\odot$ is the mass of the core that collapses (also the mass of the resulting neutron star) and $R_{\rm core} \sim 10$ km is the radius of the proto-neutron star. Of the large amount of energy released, approximately 1% is expected to be carried by electron neutrinos in the prompt neutronization burst, while the remaining energy is imparted equally to the six neutrino flavours through thermal cooling reactions. The properties of supernova neutrinos from various models are discussed at length in Chapter 5, but a few general statements can be made at this point.

3.3.1 Core Infall and Neutrino Trapping

At the onset of collapse, as the temperatures and densities in the core begin to rise, electron neutrinos are produced via electron capture reactions in the neutronization stage. The core is not yet too dense for neutrinos to escape on short time scales. The electron neutrino luminosity (energy radiated per unit time) continues to increase over a period of approximately 100 ms until it reaches its maximum value near the time of core bounce.

3.3.2 Core Bounce and Neutrino Breakout

The shock wave that is produced after core bounce takes 1 ms to reach the neutrinospheres located between 50 and 100 km for the various neutrino species, where neutrinos can escape the collapsing star. In the region behind the shock wave, the temperature is sufficiently high that neutrino pairs of all flavours are produced.

Neutrinos produced in the core have a hierarchy of energies depending on their type. Electron neutrinos and antineutrinos thermally couple with matter primarily by the following charged current processes:

$$\nu_e + n \rightleftharpoons p + e^-, \quad \overline{\nu}_e + p \rightleftharpoons n + e^+. \tag{3.5}$$

The large neutron-to-proton ratio in the core means that for a given neutrino energy, matter has a higher ν_e opacity than $\overline{\nu}_e$ opacity. Hence, electron antineutrinos will tend to thermally decouple from matter deeper in the core where the temperature is hotter. Compared to electron-type neutrinos, muon and tau neutrinos have fewer reaction channels available to them, since they do not possess energy sufficient to interact via charged current reactions. As a consequence, muon and tau neutrinos decouple from the surrounding material earlier than the electron neutrinos and antineutrinos, placing them deepest in the core of the collapsing star and therefore at the highest temperature. Hence, on average, electron neutrinos will have the lowest temperatures, electron antineutrinos will have slightly higher temperatures and ν_μ and ν_τ neutrinos will have the highest temperatures.

3.3.3 Explosion

The next phase of the neutrino signal depends on whether or not the "prompt" or "delayed" explosion mechanism occurs. If the shock wave is able to propel through the outer layers of material without losing too much energy in the process, a "prompt" explosion may take place. In that case, a relatively small amount of material will fall back onto the core and the neutrino luminosities will decrease as less gravitational energy is available for release. Furthermore, with less mass to traverse, neutrinos tend to emerge from deeper and hotter regions in the core, which is reflected in higher neutrino energies.

On the other hand, if the prompt explosion fails, then the luminosity of all neutrino flavours remains high as matter continues to accrete onto the core, contributing more mass to the gravitational energy. With the explosion delayed, additional electron neutrinos are released through electron capture processes behind the shock front. It might also be possible to have subsequent smaller magnitude bounces called "core-ringing". In such a scenario, the changing density and therefore neutrino opacities may be reflected in the emerging neutrino luminosities (for instance, see Figure 5.3). Neutrino heating in the delayed explosion mechanism is expected to cause the neutrino energies to increase suddenly at the time of explosion, similar to the energy increase in the prompt mechanism.

3.3.4 Cooling

After the explosion, the newly formed neutron star cools by releasing neutrinos according to the processes described in Section 2.3.6. The cooling phase lasts for some tens of seconds, during which time on the order of 99% of the star's energy is dissipated. Eventually, the densities and temperatures in the core decrease to the point that cooling reactions which produce neutrinos are no longer possible. For the neutrinos that remain trapped, the core will become transparent to neutrinos of different flavours at different times according to the relative opacities. Muon and tau neutrinos and antineutrinos will decouple from the

material in the core first, followed by the electron neutrinos and antineutrinos.

There is also the possibility that a black hole will be formed in the cooling stage. Exceptionally high rates of accretion onto the core may occur in stars with a relatively large amount of mass in the envelope. In such cases, core collapse may proceed beyond the point where nucleon degeneracy pressure is able maintain stability and a black hole may form as a result. Black hole formation is expected to occur 1–2 seconds after core bounce (for example, see the Bruenn 25 $M_{\odot}$ model in Section 5.3.5.2).

3.3.5 Supernova Neutrino Summary

The supernova neutrino signal is expected to last for tens of seconds. Typical average energies are 12 MeV for electron neutrinos, 15 MeV for electron antineutrinos and 18 MeV for the muon and tau neutrinos and antineutrinos.

All of the models in Chapter 5 are intended to represent the "delayed" explosion mechanism.

3.4 Potential Physics

The detection of the next galactic supernova will yield important information about the supernova collapse mechanism as well as convey information about the properties of neutrinos.

3.4.1 Constraints on Supernova Models

Electromagnetic waves are unable to convey information about the dense region of the core relevant to the explosion mechanism. Therefore one of the only means to study the inner workings of a supernova explosion is by using the observation of neutrinos. The fundamental role of the neutrino in the process of gravitational collapse was confirmed by the set of neutrinos detected from SN1987A. However, a larger number of events is required

in order to establish the details of the explosion mechanism and distinguish between the predictions of various supernova models.

Many of the signatures of the explosion mechanism are expected to be seen in the time evolution of the neutrino luminosity and energy spectrum. Evidence supporting either the "prompt" or "delayed" explosion hypotheses may be found in a large neutrino data set. In the prompt supernova models, the envelope of the progenitor star is expelled on the timescale of 10 ms, whereas in the delayed scenario, this time is on the order of seconds. Additional support for the delayed explosion hypothesis would be provided were a gradual increase in neutrino energies to be observed during the time before the explosion. It is thought that this corresponds to the gradual decay of mass accretion before the delayed explosion commences [59].

Neutrino flavour information is also extremely valuable. A prompt signal of electron neutrinos provides insight into the neutronization processes in the core of the collapsing star. There is also some indication that the ν_e neutrinos in the neutronization phase have higher energies in the delayed mechanism as opposed to the prompt mechanism [60]. As well, it remains to be shown that the six neutrino flavours carry off the binding energy of the collapsing star in equal parts. Furthermore, using energy information from the different neutrino flavours, it should be possible to confirm the expected neutrino energy hierarchy.

The progression of the neutrino signal over time may also indicate a flux cutoff possibly due to the formation of a black hole. Correlating this observation with information about the progenitor star will provide a more complete picture of the evolution of massive stars.

3.4.2 Neutrino Physics

With only the 24 events from SN1987A it was possible to place limits on many properties of the neutrino, including the neutrino mass and lifetime. The number of neutrino events detected in the next galactic supernova should increase this total by more than two orders

of magnitude. The analysis of such a data set could place limits on neutrino characteristics that could not be achieved any other way.

3.4.2.1 Neutrino Mass Measurement

Massive neutrinos arriving from a supernova explosion will have a spread in arrival times based on their energies. That is, higher energy neutrinos will arrive sooner than lower energy neutrinos. The extra time, Δt, that a neutrino of mass m_ν and energy E_ν requires to travel a distance D compared to a massless neutrino of the same energy is given by:

$$\begin{aligned} \Delta t(E_\nu) &= D\left(\frac{1}{v}-\frac{1}{c}\right) \\ &= \frac{D}{c}\left[\frac{1}{2}\left(\frac{m_\nu c^2}{E_\nu}\right)^2 - \frac{3}{8}\left(\frac{m_\nu c^2}{E_\nu}\right)^4 + \frac{15}{96}\left(\frac{m_\nu c^2}{E_\nu}\right)^6 - \cdots\right] \\ &\approx \frac{D}{2c}\left(\frac{m_\nu c^2}{E_\nu}\right)^2 \end{aligned} \tag{3.6}$$

in the relativistic limit $E_\nu \gg m_\nu$, where v is the speed of the neutrino and c is the speed of light. Therefore, even if all neutrinos are emitted simultaneously, the dispersion experienced by massive neutrinos of different energies is expected to stretch the burst in time.

In order for a detection signal to be sensitive to neutrino mass in this prescription, it is necessary to make certain assumptions. The most important assumption is that the neutrinos are all emitted from the supernova at the same time, or at least in a much shorter time than the spread of arrival times. Assuming that the electron antineutrinos detected from SN1987A were emitted simultaneously, a conservative upper limit for the mass of the neutrino results in $m_{\overline{\nu}_e} < 30$ eV/c^2 [58].

As discussed in Chapter 2, neutrino diffusion from the core is a relatively slow process, lasting on the order of seconds. Therefore, current understanding suggests that neutrinos produced during core collapse are not emitted simultaneously. However, by making reasonable assumptions about the spread in emission times, slightly lower limits can be obtained using data from SN1987A ($m_{\overline{\nu}_e} <$ 10–20 eV/c^2 [61]). Recently, Totani [62] has

suggested that analysis of the initial steep rise in neutrino luminosity may be sensitive to an electron antineutrino mass around 3 eV/c^2. Unfortunately, even with a nearby supernova, limits of the electron neutrino mass obtained using supernova neutrinos are higher than current estimates obtained using other methods. The current limit on the mass of the electron antineutrino is inferred from studies of the endpoint region of the tritium beta decay spectrum to be $m_{\overline{\nu}_e} < 3$ eV/c^2 [5] ([63], [64]).

The masses of the muon and tau neutrinos are not so well constrained. The current mass limits for the muon and tau neutrinos are $m_{\nu_\mu} < 0.19$ MeV/c^2 and $m_{\nu_\tau} < 18.2$ MeV/c^2, respectively [5]. Therefore the time-of-flight method for determining these neutrino masses may prove useful provided a model-independent method of defining a reference time can be found. Two approaches to this problem have been suggested recently, and are described below.

Beacom and Vogel [15] propose that a measurement or limit on the mass of $\nu_{\mu,\tau}$ neutrinos could be obtained by considering the time delay relative to $\overline{\nu}_e$ neutrinos. They predict that average delays on the order of 0.1 s could be resolved using the relatively large neutrino data set from a future galactic supernova. The SNO detector (see Chapter 4) is ideal for this measurement because of the high sensitivity to muon and tau neutrinos. Beacom and Vogel determine that the SNO detector would be sensitive to a 35 eV/c^2 muon or tau neutrino in the event of a galactic supernova. Using $\overline{\nu}_e$ neutrino data from the SuperKamiokande detector, the upper limit that SNO could place is slightly less at 30 eV/c^2.

Another possible way of defining a reference time is to consider the possibility that a black hole forms after core collapse, as suggested by Beacom *et al.* [65]. If the rate measured in neutrino detectors remains high at the time of black hole formation, then the neutrino signal will appear to be terminated sharply in time. Time for neutrinos that arrive after the cutoff can then be measured relative to the cutoff time. The expected sensitivity to the mass of the heaviest neutrino using the SNO detector is between 8 and 24 eV/c^2.

3.4.2.2 Neutrino Lifetime

The fact that neutrinos reached the Earth after having traveled roughly 165 000 light years from the site of SN1987A places a limit on the neutrino lifetime. If neutrinos from SN1987A had decayed in flight, then the flux observed on Earth would have been reduced. Since the measured neutrino luminosity roughly agrees with the expected luminosity based on the binding energy of a neutron star, the minimum neutrino lifetime, τ_ν can be estimated as [58]:

$$\gamma\tau_\nu > D/c = 1.7 \times 10^5 \text{ yr}, \tag{3.7}$$

where D is the distance the neutrinos traveled from the supernova and γ is the relativistic factor. Before evidence was found for solar neutrino oscillations [4], it was thought that neutrinos might decay while en route from the Sun to the Earth. Analysis of the SN1987A data indicated that this was not likely. Note that this limit will likely not be improved for a long time to come.

3.4.3 Early Alert

Since neutrinos emerge from the collapsing core of a star sooner than any form of electromagnetic radiation, their detection can be used to warn the astronomical community. In the case of SN1987A, the neutrino signal preceded the optical signal by at most 3 hours. For a given supernova event, the time for the shock wave to emerge from the collapsing star depends on the nature of the envelope surrounding the progenitor star. Estimates based on theoretical model calculations indicate that the shock propagation time to the surface of a bare helium core is about 1 minute [66]. According to Shigeyama *et al.*, the propagation time for a standard compact supernova is 35 minutes [67]. For other stars, the propagation time, t_{prop}, is given approximately by:

$$t_{prop} = 35 \text{ min } \frac{R}{21.5R_\odot}\sqrt{\frac{M/7M_\odot}{E/2.5 \times 10^{51} \text{ erg}}}, \tag{3.8}$$

where R is the radius of the progenitor, M is the amount of mass ejected and E is the explosion energy. For a supergiant star like Betelgeuse, characteristic parameters of $R \approx 500\ \mathrm{R}_\odot$, $M \approx 15\ \mathrm{M}_\odot$, $E \approx 10^{53}$ ergs yield a shock propagation time of 2 hours. The largest supergiant stars ($R \approx 1500\ \mathrm{R}_\odot$) may experience shock propagation times on the order of 8 hours according to the Shigeyama *et al.* prescription. Other estimates [68] suggest that the shock wave traversal time in red supergiants may be significantly higher at 17–25 hours for a 15 $\mathrm{M}_\odot$ star and 58 hours for a 25 $\mathrm{M}_\odot$ star.

Chapter 4

The SNO Detector

4.1 Introduction

The Sudbury Neutrino Observatory (SNO) is a heavy water Čerenkov detector situated 2072 m (5996 metres water equivalent) underground in INCO's Creighton Mine near Sudbury, Ontario, Canada. The cavity that houses the detector is shaped like a barrel with a height of 34 m and a width of 22 m at the widest point. The detector consists of 1000 tonnes of heavy water on loan from Atomic Energy of Canada Limited (AECL), and is contained within a spherical acrylic vessel. The D_2O volume is efficiently viewed by an array of almost 10000 photomultiplier tubes (PMTs). Between the acrylic vessel and the PMT support structure (PSUP) is approximately 1700 tonnes of ultra-pure light water. The volume beyond the support structure contains 5300 tonnes of light water, and is used primarily as a background shield for gamma rays and neutrons originating in the rock and as an anti-coincidence veto. A schematic picture of the Sudbury Neutrino Observatory is provided in Figure 4.1. More specifications and a detailed description of the SNO detector can be found in [69].

4.2 Detection Mechanisms

The SNO detector is able to detect Čerenkov radiation resulting from the passage of charged particles and from the interactions of gamma rays and neutrons. Signatures from each of these particles constitute an important part of the supernova neutrino signal and are

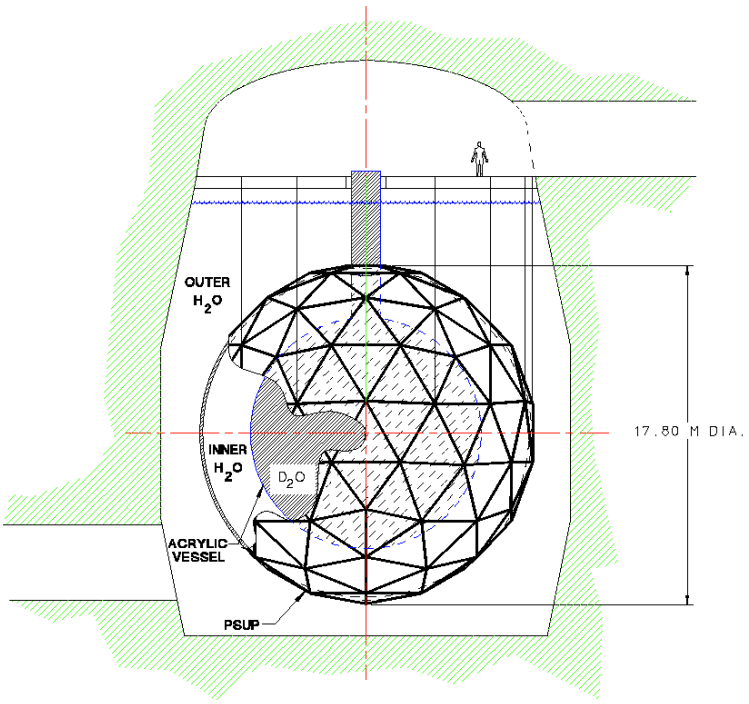

Figure 4.1: Cross section schematic of the SNO detector.

discussed in the sections that follow.

4.2.1 Charged Particle Detection

To detect charged particles that are produced by neutrino interactions, the SNO detector relies on the generation of Čerenkov light. The speed of light in a medium of refractive index n is c/n, where c is the speed of light in vacuum. When a charged particle traverses a medium with a speed greater than the speed of light in that medium, a "shock" wave is created and Čerenkov light is emitted as a result. The minimum energy needed to produce Čerenkov light is summarized for various particles in Table 4.1. For the relevant analysis energy thresholds in SNO, all electrons and positrons produce Čerenkov light in both the light- and heavy-water regions. On the other hand, only protons with kinetic energies above ~500 MeV will generate Čerenkov light.

Charged Particle	**Particle Mass (MeV/c^2)**	**Particle Total Energy Čerenkov Threshold (MeV)**	
		H_2O	**D_2O**
electron/positron, $e^{\pm}$	0.511	0.766	0.770
muon, $\mu^{\pm}$	105.658	158	159
pion, $\pi^{\pm}$	139.570	209	210
proton, p^{+}	938.272	1407	1414

Table 4.1: Čerenkov radiation energy threshold values in H_2O and D_2O for various charged particles.

Čerenkov light is emitted in a cone of half angle $\theta_{\check{C}}$ with respect to the trajectory of the charged particle:

$$\cos\theta_{\check{C}} = \frac{1}{n\beta}, \tag{4.1}$$

where $\beta = v/c$ is the particle speed expressed in terms of the speed of light in vacuum. Electrons or positrons that have kinetic energies of 2 MeV have speeds which are already very close to the speed of light, $\beta \approx 1$. In the case of heavy water ($\overline{n}_{D_2O} = 1.337$), charged particles traveling with $\beta \approx 1$ produce a Čerenkov cone which has an opening angle of $\theta_{\check{C}} = 41.6°$. The corresponding angle in light water ($\overline{n}_{H_2O} = 1.342$) is very similar at $\theta_{\check{C}} = 41.8°$. Therefore, the angle $\theta_{\check{C}} \approx 42°$ is characteristic of all charged particle events in SNO, and does not distinguish between particle energies or between interactions in either the H_2O or D_2O volumes. The primary difference between low energy particles and high energy particles lies in the path length. The spectrum of Čerenkov light is a function of both wavelength, λ, and path length, x, and is given as [5]:

$$\frac{d^2N}{dx\,d\lambda} = \frac{2\pi\alpha}{\lambda^2}\left(1 - \frac{1}{\beta^2 n^2(\lambda)}\right), \tag{4.2}$$

where $\alpha \approx 1/137$ is the fine structure constant. In water, the amount of light that a charged particle emits per unit track length is roughly constant over particle energy and

corresponds to approximately 360 Čerenkov photons for every 1 cm path length in the spectral range to which SNO PMTs are sensitive (λ = 300–650 nm) [70]. However, the electron or positron path length depends linearly on energy and is approximately 0.45 cm per MeV [70]. Charged particles with higher energies have longer path lengths and therefore produce more Čerenkov photons, which trigger a larger number of photomultiplier tubes in the detector. The number of PMTs that are hit during a given event is referred to as the "NHIT" of the event and is used in characterizing the energy of the event. Figure 4.2 shows a Monte Carlo simulation of the Čerenkov ring detected when a 10 MeV electron is produced in the SNO detector. For this event, a total of ∼1600 Čerenkov photons are produced with wavelengths between 300–650 nm, but only about 6% of those photons are detected due to the low quantum efficiency of the PMTs (17%), attenuation in detector materials (65%) and photocathode coverage (54%). The image of the Čerenkov ring is not filled in because of the short range of 10 MeV electrons and positrons.

Due to the $1/\lambda^2$ dependence in Equation 4.2, more Čerenkov photons are produced at shorter wavelengths than at longer wavelengths. The SNO photomultiplier tubes are able to detect photons with wavelengths between 300–650 nm, and are therefore mostly sensitive to the blue and ultraviolet end of the Čerenkov spectrum.

4.2.2 Gamma Ray Detection

Gamma rays are detected indirectly through the process of Compton scattering, in which a photon scatters from an atomic electron producing a less energetic photon and a scattered electron:

$$\gamma + e^- \rightarrow \gamma' + e^-. \tag{4.3}$$

In order to be detected, the scattered electron must have enough energy to produce Čerenkov light. In general, because the scattered electron has less energy than the incoming gamma ray, fewer Čerenkov photons are generated for a gamma ray event compared to

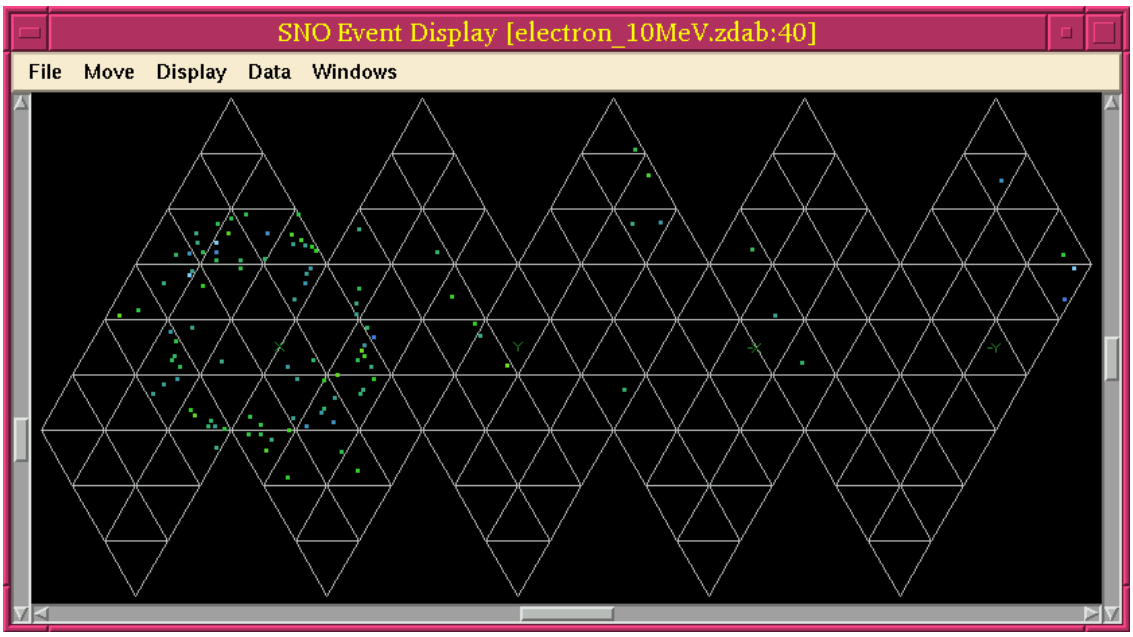

Figure 4.2: Ring of Čerenkov light detected from a 10 MeV electron event simulated in the SNO detector. A total of 100 PMTs register a hit in this event, of which about 10 are from reflected light. In this view, the spherical array of PMTs is unfolded to form a flat map.

a charged particle event, and therefore fewer PMTs are hit.

4.2.3 Neutron Detection

Since neutron detection is a crucial aspect of the SNO experiment, three separate running phases are planned. The first phase with pure D_2O offers limited sensitivity to neutrons, so two additional methods will also be used to increase the sensitivity. For the ongoing physics programs, the use of these different methods will allow for a comparison of results in which the systematic errors are significantly different.

The first phase of running with pure D_2O extended from November 2, 1999 to May 28, 2001.

4.2.3.1 Pure D_2O Phase

During the initial running stage, no enhanced neutron detection technique is employed, and SNO relies on neutron capture in pure D_2O:

$$\boldsymbol{n} + d \rightarrow t + \gamma \ \cdots \rightarrow e^-, \qquad E_\gamma = 6.3 \text{ MeV}. \tag{4.4}$$

Free neutrons thermalize and can subsequently capture on a deuteron in the heavy water region to produce an energetic 6.3 MeV gamma ray. The gamma ray then undergoes Compton scattering and the resulting electron often has enough energy to produce Čerenkov light. However, due to the small capture cross section on deuterium, the neutron detection efficiency is relatively low at roughly 37%[1]. The mean neutron capture time in the pure D_2O phase is 40 ms.

4.2.3.2 Salt Phase

During the first enhancement phase, NaCl salt is added to the heavy water up to a concentration of 0.2%. The sensitivity to neutrons is increased because of the high cross section for neutron capture on ^{35}Cl. Neutron capture in ^{35}Cl results in a cascade of gamma rays of energy totaling 8.6 MeV, which are detectable from Čerenkov light produced by Compton scattered electrons:

$$\boldsymbol{n} + {}^{35}\text{Cl} \rightarrow {}^{36}\text{Cl} + \Sigma\gamma \ \cdots \rightarrow e^-, \qquad E_{\Sigma\gamma} = 8.6 \text{ MeV}. \tag{4.5}$$

Due to the high neutron capture cross section associated with ^{35}Cl, the 83% detection efficiency is significantly higher than for the pure D_2O phase. SNO Monte Carlo simulations indicate that it should also be possible to distinguish charged particle events from neutron and gamma-ray events based on the event topology. The distribution of light from Čerenkov light produced by charged particle events is different from that generated during Compton

[1]For an analysis energy threshold of 5 MeV, the detection efficiency using the only the pure D_2O method is even less at approximately 24%.

scattering interactions in which multiple Čerenkov cones may be produced. Compared to the capture time of 40 ms in the pure D_2O phase, the mean neutron capture time with salt in the heavy water is much less at 4 ms. At the end of the salt operation phase, a reverse osmosis filtration system will be used to remove the salt from the heavy water.

4.2.3.3 NCD Phase

A second enhancement technique that is planned for the measurement of neutrons involves the introduction of an array of 96 strings of ^{3}He gas-filled proportional counters into the heavy-water region. The counters have been constructed using ultra pure nickel tubing fabricated by a chemical vapour deposition process. Neutrons are detected through energetic protons and tritons produced by the neutron capture on ^{3}He:

$$\boldsymbol{n} + {}^3\mathrm{He} \rightarrow p + t, \qquad E_{thres} = 0.764 \text{ MeV}. \tag{4.6}$$

The neutron detection efficiency using the neutral current detectors is 37%. However, an additional 18% of neutrons capture on deuterium, bringing the total efficiency during this phase to 55% [69]. With the proposed 1-m spacing of the strings, the mean time to neutron capture in the NCD phase is 16 ms.

The NCD neutron signal, which does not depend on Čerenkov light, makes it possible to distinguish neutron events from the charged particle and gamma ray events on an event-by-event basis. During the pure D_2O and salt phases, the neutron signature is obtained from Čerenkov radiation just as with electrons, positrons and γ rays. However, it is possible to distinguish the different types of events based on the event topology. For instance, the distribution of light arising from a single energetic electron is different from a neutron event resulting from a gamma-ray cascade in the salt phase. While the NCD detector array is not as efficient at capturing neutrons as ^{35}Cl, it provides a more straightforward means of separating signals from the different event types. Furthermore, the pulse shape of the ^{3}He capture events will enable them to be distinguished from any alpha particle radioactivity

from the walls of the ultra pure nickel tubes used as the bodies of the proportional counters.

4.2.3.4 Neutrons in the H_2O Region

There is also some sensitivity to neutrons present in the H_2O region through the capture reaction with hydrogen:

$$\boldsymbol{n} + p \rightarrow d + \gamma, \qquad E_\gamma = 2.2 \text{ MeV}. \tag{4.7}$$

The 2.2 MeV γ ray is below the nominal solar neutrino analysis threshold at 5 MeV, but might be observed in the analysis of a supernova signal, where the analysis threshold could be set lower.

4.3 Neutrino Interactions

Through the use of both D_2O and H_2O, the SNO detector is able to rely on a number of reactions in order to observe neutrino interactions. Moreover, the supernova neutrino signal is expected to have significant contributions from all neutrino types, and those neutrinos are expected to have higher energies than solar neutrinos, which further increases the number of available interactions.

Reactions in the SNO detector are classified into three groups according to the type of interaction: charged current, neutral current and elastic scattering. In the sections that follow, the relevant reactions from each of these categories are introduced. Further details describing the reaction kinematics and cross sections are provided in Chapter 5.

4.3.1 Charged Current

Charged current reactions are identified as such because a charged boson, $W^\pm$, is exchanged between the interacting particles. Supernova neutrinos, which have energies in the range $\sim$0–100 MeV (see Section 5.3), are unable to produce muon and tau particles in the final state. Therefore, only ν_e and $\overline{\nu}_e$ neutrinos participate in charged current reactions.

4.3.1.1 $\overline{\nu}_e + p \rightarrow n + e^+$ Reaction

The $\overline{\nu}_e$ inverse beta decay reaction[2] is the dominant supernova neutrino reaction in any water Čerenkov detector, including SNO:

$$\overline{\nu}_e + p \rightarrow n + e^+ \quad (E_{thres} = 1.806 \text{ MeV}) \quad [\text{H}_2\text{O}]. \tag{4.8}$$

The Feynman diagram for this process showing the exchange of a charged W^+ boson is illustrated in Figure 4.3. The result of the W exchange is that a u quark is converted to a d quark creating a neutron and a positron in the final state.

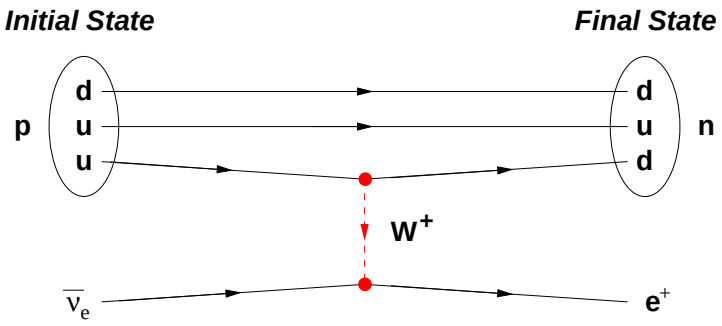

Figure 4.3: Feynman diagram for the $\overline{\nu}_e + p \rightarrow n + e^+$ charged current reaction. Exchange of a W^+ boson allows one of the u quarks in the proton to change into a d quark, creating a neutron and a positron in the final state.

This reaction only occurs in the light water volume, therefore only the relativistic positron in the final state is detected. In principle, it is possible to observe both the positron and the neutron, however the 2.2 MeV γ ray due to neutron capture on hydrogen is difficult to detect. Therefore, the contribution from the neutron in this reaction is ignored in the studies that follow.

Applying weak magnetism and recoil corrections [71], the angle at which the positron is emitted tends to favour the direction of the incoming neutrino (slightly forward peaked),

[2]The reaction $\nu_e + n \rightarrow e^- + p$ will not be directly observed since there are no free neutron targets.

while the neutron is strongly forward peaked. However, even if the analysis threshold is set low enough to observe the neutron signature in the light water region, the directional information of the neutron is lost during the thermalization process.

4.3.1.2 $\nu_e + d$ Reactions

Other important charged current reactions involve neutrino interactions with the deuteron in the heavy water region of the detector:

$$\nu_e + d \rightarrow p + p + e^- \quad (E_{thres} = 1.442 \text{ MeV}) \quad [\text{D}_2\text{O}] \tag{4.9}$$

$$\overline{\nu}_e + d \rightarrow n + n + e^+ \quad (E_{thres} = 4.033 \text{ MeV}) \quad [\text{D}_2\text{O}]. \tag{4.10}$$

In both reactions, the neutrino interacts with a deuteron through the charged-current exchange of a W boson producing a relativistic charged lepton. Two protons remain in the final state for the reaction in Equation 4.9, while the final state for the reaction in Equation 4.10 has two neutrons. The details of both interactions are illustrated in Figure 4.4.

The protons in Equation 4.9 are not detected in SNO because their energies do not exceed the Čerenkov radiation threshold, but Čerenkov radiation from the electron is detected. However, it is possible to detect all three final state particles from the $\overline{\nu}_e + d \rightarrow n + n + e^+$ reaction. The positron is sufficiently energetic to emit Čerenkov radiation, and the two neutrons produce a signal due to the neutron capture mechanisms discussed in Section 4.2.3. With three detectable particles in the final state, the signature for this reaction is unique in the SNO detector: the prompt detection of the positron followed by a time-delayed coincidence of the two neutrons. In both reactions, the angular distribution is slightly backward peaked, with the neutrino reaction more so than the antineutrino reaction.

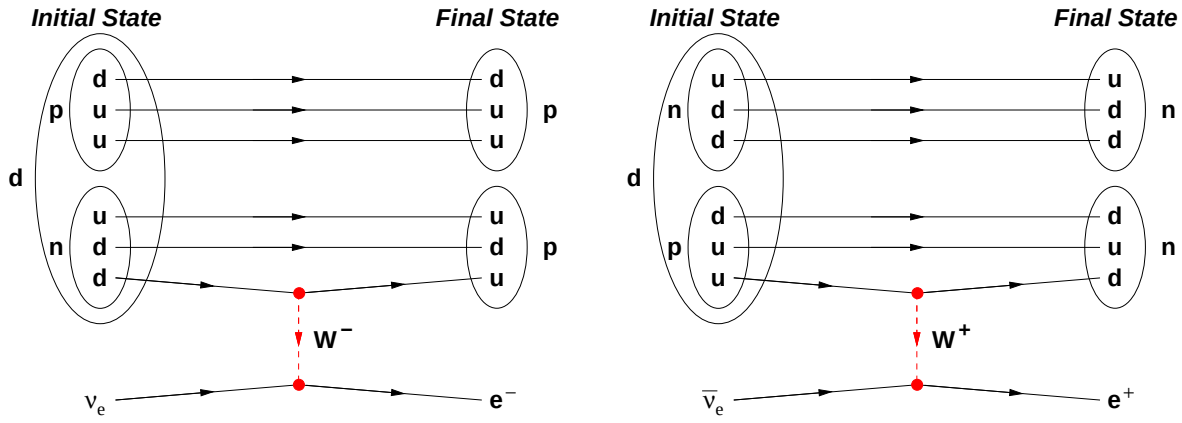

Figure 4.4: Feynman diagrams for the $\nu_e + d \rightarrow p + p + e^-$ and $\overline{\nu}_e + d \rightarrow n + n + e^+$ charged current reactions. In the case of the electron neutrino, exchange of a W boson allows one of the d quarks in the neutron to change into a u quark, creating a proton and an electron in the final state. For the electron antineutrino, one of the u quarks is changed into a d quark, creating a neutron and a positron in the final state.

4.3.1.3 ν_e + O Reactions

Electron neutrinos and antineutrinos also participate in charged current interactions with oxygen in the SNO detector. The principal isotope involved is ^{16}O:

$$\nu_e + {}^{16}\mathrm{O} \rightarrow {}^{16}\mathrm{F} + e^- \quad (E_{thres} = 15.4 \text{ MeV}) \quad [\mathrm{D_2O}, \mathrm{H_2O}] \tag{4.11}$$

$$\overline{\nu}_e + {}^{16}\mathrm{O} \rightarrow {}^{16}\mathrm{N} + e^+ \quad (E_{thres} = 11.4 \text{ MeV}) \quad [\mathrm{D_2O}, \mathrm{H_2O}] \tag{4.12}$$

$$\tag{4.13}$$

but the ^{18}O isotope also contributes, especially at lower energies:

$$\nu_e + {}^{18}\mathrm{O} \rightarrow {}^{18}\mathrm{N} + e^+ \quad (E_{thres} = 1.66 \text{ MeV}) \quad [\mathrm{D_2O}, \mathrm{H_2O}]. \tag{4.14}$$

In all cases, Čerenkov light from the charged lepton constitutes the detection signal. However, for the energy regime relevant for supernova neutrinos, interactions involving ν_e tend to have angular distributions that are slightly backward peaked, while the $\overline{\nu}_e$ reactions involving oxygen are essentially isotropic [72].

4.3.2 Neutral Current

Instead of a charged boson mediating the process, particles interacting via the neutral current exchange a neutral Z^0 boson. As a result, neutrinos of all types are able to participate in neutral current reactions. While both the charged current and neutral current reactions will provide substantial contributions to the total number of neutrinos observed with SNO, the neutral current channels are particularly important because all neutrino types are able to participate in these interactions. This sensitivity is especially important since the majority of the energy in a supernova explosion is carried by the muon and tau neutrino types. No other detector that is currently in operation has the level of sensitivity to ν_μ and ν_τ neutrinos that SNO offers.

4.3.2.1 $\nu_x + d$ Reactions

The main set of neutral current reactions are those involving deuterium:

$$\nu_x + d \rightarrow \nu_x + p + n \quad (E_{thres} = 2.225 \text{ MeV}) \quad [\text{D}_2\text{O}], \tag{4.15}$$

where ν_x represents all active neutrino flavours ($x = e, \mu, \tau$). Exchange of a Z boson means that the deuteron is simply broken apart and the constituent proton and neutron are free particles in the final state. Figure 4.5 shows the details of the interaction.

As with previous reactions, the proton does not have sufficient energy to generate Čerenkov radiation, so the neutron is the only particle that is detected. Due to the neutron capture processes, no directional information can be obtained from the final state particles that participate in these interactions.

4.3.2.2 $\nu_{\mu,\tau}$ + ^{16}O Reactions

Other neutral current reactions include interactions with oxygen. It is possible that the highest energy supernova neutrinos ($\nu_{\mu,\tau}$ neutrinos) will excite resonances in ^{16}O, which then mainly decay by proton and neutron emission. Although the proton and neutron

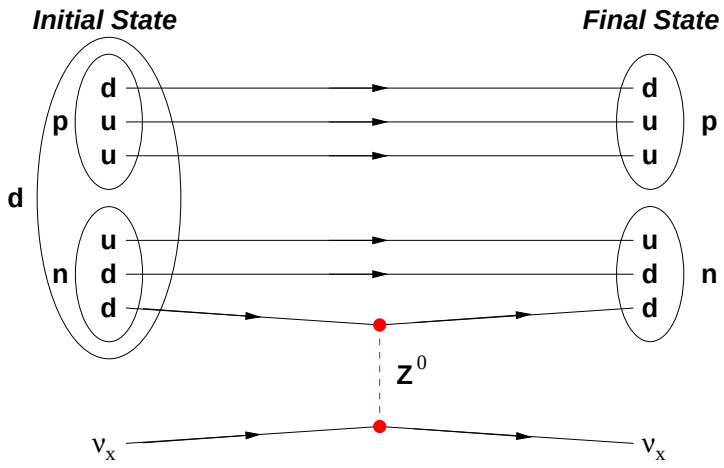

Figure 4.5: Feynman diagram for the $\nu_x + d \rightarrow \nu_x + p + n$ neutral current reaction. Exchange of a Z^0 boson means that the deuteron is simply broken apart and the constituent proton and neutron are free particles in the final state.

decays are mainly to the ground states of ^{15}N and ^{16}O, respectively, in some cases the decays will go to excited states in these nuclei. These excited states will often decay by emitting a γ ray with energies between 5–10 MeV [73]. The possible reactions are summarized as follows:

$$\nu_{\mu,\tau} + {}^{16}\mathrm{O} \rightarrow \nu_{\mu,\tau} + {}^{15}\mathrm{O} + n \qquad (E_{thres} = 15.0 \text{ MeV}) \quad [\mathrm{D_2O}] \tag{4.16}$$

$$\nu_{\mu,\tau} + {}^{16}\mathrm{O} \rightarrow \nu_{\mu,\tau} + {}^{15}\mathrm{O} + n + \gamma \quad (E_{thres} = 15.0 \text{ MeV}) \quad [\mathrm{D_2O}, \mathrm{H_2O}] \tag{4.17}$$

$$\nu_{\mu,\tau} + {}^{16}\mathrm{O} \rightarrow \nu_{\mu,\tau} + {}^{15}\mathrm{N} + p + \gamma \quad (E_{thres} = 15.0 \text{ MeV}) \quad [\mathrm{D_2O}, \mathrm{H_2O}]. \tag{4.18}$$

The detection signal for these reactions arises from either a neutron (Equation 4.16), both a neutron and a γ ray (Equation 4.17) or a single γ ray (Equation 4.18). As with the other neutral current reactions, there is no information available concerning the initial neutrino direction.

4.3.3 Elastic Scattering

The elastic scattering process is actually a combination of the charged- and neutral-current processes. The electron neutrino (or antineutrino) and the electron can interact through the exchange of either a charged W boson or a neutral Z^0 boson. Other neutrino types can only interact through the neutral current channel, which means that their cross sections are lower than those of the ν_e and $\overline{\nu}_e$ neutrinos.

4.3.3.1 $\nu + e^- \rightarrow \nu + e^-$ Reactions

Because of the neutral current component, supernova neutrinos of all flavours can also interact via the neutrino-electron elastic scattering process:

$$\nu_e + e^- \rightarrow \nu_e + e^- \qquad (E_{thres} = 0 \text{ MeV}) \quad [\mathrm{D_2O}, \mathrm{H_2O}] \tag{4.19}$$

$$\overline{\nu}_e + e^- \rightarrow \overline{\nu}_e + e^- \qquad (E_{thres} = 0 \text{ MeV}) \quad [\mathrm{D_2O}, \mathrm{H_2O}] \tag{4.20}$$

$$\nu_{\mu,\tau} + e^- \rightarrow \nu_{\mu,\tau} + e^- \quad (E_{thres} = 0 \text{ MeV}) \quad [\mathrm{D_2O}, \mathrm{H_2O}] \tag{4.21}$$

$$\overline{\nu}_{\mu,\tau} + e^- \rightarrow \overline{\nu}_{\mu,\tau} + e^- \quad (E_{thres} = 0 \text{ MeV}) \quad [\mathrm{D_2O}, \mathrm{H_2O}]. \tag{4.22}$$

Figure 4.6 shows both the charged current and neutral current contributions to the elastic scattering reactions involving electron neutrinos (and antineutrinos). Muon and tau neutrinos from a supernova only interact via the neutral current component.

Neutrino-electron elastic scattering interactions are important in all water Čerenkov detectors. In the case of SNO, elastic scattering reactions take place in both the D_2O and H_2O volumes of the detector, and in either region, SNO measures the Čerenkov light emitted by the relativistic recoil electrons.

4.3.3.2 Interaction Summary

Table 4.2 lists the interactions that are relevant for supernova neutrinos. Notice that a number of reactions involving oxygen have relatively high interaction energy threshold

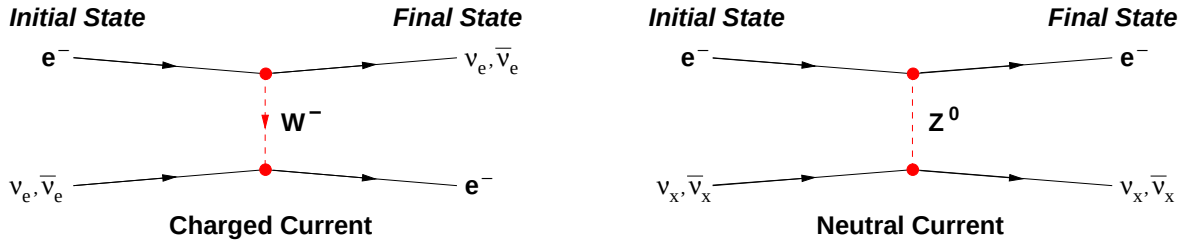

Figure 4.6: Feynman diagrams for the $\nu + e^- \rightarrow \nu + e^-$ elastic scattering reaction. All neutrino flavours ν_x $(x = e, \mu, \tau)$ can interact via the neutral current channel, but only ν_e and $\overline{\nu}_e$ neutrino reactions have contributions from both the charged current and neutral current channels.

values compared to the others. The significance of this aspect is discussed in detail in Chapters 5 and 6. SNO observes neutrinos indirectly by detecting final state particles that produce Čerenkov radiation. These particles are listed in Table 4.2 for each interaction, along with any asymmetry in the angular distribution that might be exploited when trying to locate the source of the supernova neutrino signal.

4.4 Detector Backgrounds

The SNO detector is designed to provide very low levels of radioactive background for the reactions that are used to detect neutrinos. The entire detector is constructed from materials which have been carefully selected for low ^{238}U and ^{232}Th content, since gamma rays from the decay of daughter particles from these decay chains can mimic neutrino signals. The most problematic of these daughters are ^{208}Tl from the thorium chain and ^{214}Bi from the uranium chain, which in both cases contribute γ rays during fission processes that have energies $E_\gamma > 2.2$ MeV. Gamma rays with such energy are able to photodisintegrate the deuteron and contribute neutrons that are indistinguishable from those produced in neutrino interactions. This is why extraordinary efforts have been made to reduce these backgrounds in the fiducial volume of the detector. Limits on the radiopurity of both the

Reaction	**Region**	**Energy Threshold (MeV)**	**Detectable Particles**	**Lepton Angle Asym**
Charged Current:				
$\overline{\nu}_e + p \rightarrow n + e^+$	H_2O	1.806	e^+, n?	∼forward
$\nu_e + d \rightarrow p + p + e^-$	D_2O	1.442	e^-	∼forward
$\overline{\nu}_e + d \rightarrow n + n + e^+$	D_2O	4.033	$2n, e^-$	∼backward
$\nu_e + O \rightarrow F + e^-$	D_2O	15.4	e^-	∼backward
$\overline{\nu}_e + O \rightarrow N + e^+$	D_2O	11.4	e^+	none
$\nu_e + O \rightarrow F + e^-$	H_2O	15.4	e^-	∼backward
$\overline{\nu}_e + O \rightarrow N + e^+$	H_2O	11.4	e^+	none
Neutral Current:				
$\nu_e + d \rightarrow \nu_e + p + n$	D_2O	2.225	n	N/A
$\overline{\nu}_e + d \rightarrow \overline{\nu}_e + p + n$	D_2O	2.225	n	N/A
$\nu_{\mu,\tau} + d \rightarrow \nu_{\mu,\tau} + p + n$	D_2O	2.225	n	N/A
$\overline{\nu}_{\mu,\tau} + d \rightarrow \overline{\nu}_{\mu,\tau} + p + n$	D_2O	2.225	n	N/A
$\nu_{\mu,\tau} + {}^{16}O \rightarrow \nu_{\mu,\tau} + {}^{15}O + n + \gamma$	D_2O	15.0	n, γ	N/A
$\overline{\nu}_{\mu,\tau} + {}^{16}O \rightarrow \overline{\nu}_{\mu,\tau} + {}^{15}O + n + \gamma$	D_2O	15.0	n, γ	N/A
$\nu_{\mu,\tau} + {}^{16}O \rightarrow \nu_{\mu,\tau} + {}^{15}N + p + \gamma$	D_2O	15.0	γ	N/A
$\overline{\nu}_{\mu,\tau} + {}^{16}O \rightarrow \overline{\nu}_{\mu,\tau} + {}^{15}N + p + \gamma$	D_2O	15.0	γ	N/A
$\nu_{\mu,\tau} + {}^{16}O \rightarrow \nu_{\mu,\tau} + {}^{15}O + n$	D_2O	15.0	n	N/A
$\overline{\nu}_{\mu,\tau} + {}^{16}O \rightarrow \overline{\nu}_{\mu,\tau} + {}^{15}O + n$	D_2O	15.0	n	N/A
$\nu_{\mu,\tau} + {}^{16}O \rightarrow \nu_{\mu,\tau} + {}^{15}O + n + \gamma$	H_2O	15.0	n?, γ	N/A
$\overline{\nu}_{\mu,\tau} + {}^{16}O \rightarrow \overline{\nu}_{\mu,\tau} + {}^{15}O + n + \gamma$	H_2O	15.0	n?, γ	N/A
$\nu_{\mu,\tau} + {}^{16}O \rightarrow \nu_{\mu,\tau} + {}^{15}N + p + \gamma$	H_2O	15.0	γ	N/A
$\overline{\nu}_{\mu,\tau} + {}^{16}O \rightarrow \overline{\nu}_{\mu,\tau} + {}^{15}N + p + \gamma$	H_2O	15.0	γ	N/A
Elastic Scattering:				
$\nu_e + e^- \rightarrow \nu_e + e^-$	D_2O	0.0	e^-	forward
$\overline{\nu}_e + e^- \rightarrow \overline{\nu}_e + e^-$	D_2O	0.0	e^-	forward
$\nu_{\mu,\tau} + e^- \rightarrow \nu_{\mu,\tau} + e^-$	D_2O	0.0	e^-	forward
$\overline{\nu}_{\mu,\tau} + e^- \rightarrow \overline{\nu}_{\mu,\tau} + e^-$	D_2O	0.0	e^-	forward
$\nu_e + e^- \rightarrow \nu_e + e^-$	H_2O	0.0	e^-	forward
$\overline{\nu}_e + e^- \rightarrow \overline{\nu}_e + e^-$	H_2O	0.0	e^-	forward
$\nu_{\mu,\tau} + e^- \rightarrow \nu_{\mu,\tau} + e^-$	H_2O	0.0	e^-	forward
$\overline{\nu}_{\mu,\tau} + e^- \rightarrow \overline{\nu}_{\mu,\tau} + e^-$	H_2O	0.0	e^-	forward

Table 4.2: Summary of supernova neutrino interactions in the SNO detector, including the energy threshold, the final state detectable particles and whether or not there is any asymmetry in the charged lepton angular distribution. It may be possible to detect some of the neutrons in the H_2O volume (labeled as "n?") with a sufficiently low analysis threshold.

light water volume and the heavy water volume are set such that the neutron production rates due to photodisintegration do not exceed one-tenth that of the standard solar model neutral current rate (approximately 1 per day).

Sensitive techniques [74] have been developed for the measurement of the principal daughter particles from the ^{238}U and ^{232}Th decay chains. These techniques include degassing (ZnS Lucas cells) and chemical extraction (MnO_x, HTiO) from recirculated water to determine the effective levels of ^{238}U and ^{232}Th. The isotopes ^{222}Rn and ^{226}Ra are monitored in the case of the uranium chain, while ^{224}Ra and ^{212}Pb are used to indicate the levels of thorium daughters. Information on background radiation in the detector can also be gathered from observations of the Čerenkov light patterns on the PMTs. In the case of the ^{3}He neutron detectors, the materials used in construction have been carefully selected to minimize levels of uranium and thorium and their daughters. Techniques have been developed for the measurement of inherent radioactivity in these detectors which might lead to photodisintegration of the deuteron.

Table 4.3 highlights the radioactivity levels in a number of key areas, starting in the surrounding host rock and moving inward to the heavy water region. These limits have been achieved by use of very pure materials and careful manufacture. Furthermore, the detector was constructed under clean-room conditions and continues to be operated in the same manner. The air is filtered using HEPA filters and all personnel wear clean-room clothing to maintain an air quality on the order of Class 2500. An extensive water purification/recirculation system is used to reduce the radioactivity in both the heavy and light water volumes.

The PMT support structure is 99.99% impermeable to water, enabling water flow to be directed outwards from the region between the acrylic vessel and the PMTs into the outer region where it is removed, purified, stripped of radon and radium and re-injected in the inner region. This process maintains a lower level of radioactivity in the light water in the

Region	**Radioactivity Goal (10^{-12} g/g)**		**Radioactivity Level (10^{-12} g/g)**	
	^{232}Th	**^{238}U**	**^{232}Th**	**^{238}U**
Norite rock	N/A	N/A	5.5×10^6	1.1×10^6
PMT Support Structure	15000	15000	4000	4000
PMTs	90000	120000	6000	9000
Acrylic Vessel	1.1	1.1	< 1.1	< 1.1
H_2O (inner)	0.037	0.45	0.0891	0.00233
D_2O	0.037	0.45	0.00448	0.00157

Table 4.3: Radioactivity levels in various regions of the SNO detector, where the most crucial areas are the heavy water and inner light water regions. In those volumes, the equivalent concentrations of ^{238}U and ^{232}Th are below the design goals for cleanliness in almost all cases.

inner region than in the less critical outer region.

4.5 Detector Components

A number of distinct components and systems make up the SNO detector, including the acrylic vessel, the water systems, the PMT array, the readout electronics, the data acquisition and the various calibration devices. Each of these components is briefly described in the sections that follow.

4.5.1 Acrylic Vessel

The acrylic vessel, which holds the heavy water, is 12 m in diameter and was constructed from 122 ultraviolet-transmitting acrylic panels that were transported underground and bonded together *in situ*[3]. These panels are 5.5 cm thick, except for a special set of ten at the equator that are 11.4 cm thick and were machined to accommodate suspension ropes that support the vessel.

[3]The author participated extensively in the construction of the acrylic vessel.

An acrylic chimney is attached to the top of the sphere and is made using ultraviolet absorbing acrylic to reduce the "piping" of unwanted Čerenkov light, which could be misreconstructed into the fiducial volume. Calibration sources are inserted into the heavy water through the chimney and pipes for the water systems are mounted there as well. Eventually, the ^{3}He proportional counters will also be deployed through the chimney.

4.5.2 Water Systems

The SNO water system consists of three separate systems: the ultrapure light water (H_2O) system, the heavy water (D_2O) system and the N_2 cover gas system.

4.5.2.1 Light Water System

Light water is supplied from a surface purification plant that produces potable water for the entire mine. The water reaches the 6800-foot level of the mine through a series of pipes and open holding tanks, during which time the water is saturated with air. Before being processed, the incoming water contains sand and silt particles, bacteria, algae, inorganic salts, organic molecules and many gases (for example, N_2, O_2, CO_2, Rn). Just outside the lab, the light water is de-aerated (removing O_2 and N_2) and passed through a multimedia filter consisting of a bed of sand and charcoal to remove large particles. At this stage, a 10 μm filter is also used to remove finer particles. The water then enters the laboratory, where the water first passes through a pair of activated charcoal filters that convert chlorine into chloride, a form which is easier to remove at later stages. A similar function is performed by the addition of EDTA, which reacts mainly with aluminum leaving it in a form that is more easily removed by reverse osmosis. Zeolite softener is used to remove heavy elements that are present in the water, such as iron, calcium, magnesium and aluminum. In the final stage of pretreatment, the incoming water is passed through a reverse osmosis unit, which removes 99% of ionized salts and organics by using high pressure across a semipermeable membrane. The water is now suitable for injection into the main purification loop.

The main light water circulation loop continually removes water from outside the PSUP for purification and monitoring and then returns the clean water to the H_2O volume inside the PSUP. In the main purification loop, water passes through a 185 nm UV mercury lamp to break up large organic molecules into constituent ions, 12 ion exchange columns, a 1 μm filter, a second 254 nm UV lamp to kill any bacteria and a custom process degasser that removes O_2 and N_2 and Rn gases. Finally, a chiller cools the water to 10°C in order to inhibit organic growth and cool the photomultiplier tubes, and the water is returned to the cavity at 150 litres/minute.

4.5.2.2 Heavy Water System

As with the light water system, the heavy water system is used to maintain the high purity levels of the D_2O. However, the heavy water system is also responsible for introducing and removing the NaCl salt used during the second phase of detector operation. The D_2O is supplied by the Ontario Hydro Bruce heavy water plant and shipped underground in specially designed rail cars. Heavy water delivered to the lab was first passed through ion-exchange columns to reduce the ionic content.

The main heavy water circulation loop removes water from the top of the acrylic vessel for purification and monitoring and returns it to the bottom. While the systems are completely separate, many of the same types of purification methods used with the light water are also used with the heavy water. These include a series of reverse osmosis filters, ultrafiltration units and a process degasser. Absorption columns with MnO_x beads are also used to remove radium from the recirculated water.

Addition of the NaCl salt into the D_2O is done by making a high concentration brine solution that is slowly added to the heavy water volume. Later desalination will be performed with two dedicated reverse osmosis units.

4.5.2.3 Cover Gas System

Both the light- and heavy-water volumes are isolated from the laboratory air to prevent radon contamination by using a layer of N_2 gas. The measured concentration of radon in the nitrogen gas is 10^{-5} pCi/litre compared with 3 pCi/litre in the laboratory air.

4.5.3 Photomultiplier Tube Array

Surrounding the acrylic vessel is a geodesic support structure (PSUP) 18 m in diameter, which houses a total of 9529 Hamamatsu R1408 20 cm photomultiplier tubes (PMTs). A photomultiplier tube works by converting photons to electrons at an interface called the photocathode. The photoelectron that is produced is accelerated using a set of plates called dynodes, which have voltage applied such that there is a potential difference at each step. Electrons striking the dynode liberate more electrons, and after several such multiplication steps, the resulting number of electrons constitutes an electronic signal that is measurable. Of the total number of PMTs that make up the detector, 9438 PMTs face inward to the heavy water region. A small subset (49 PMTs) called "low gain" PMTs have a dynode tap and a second signal cable to extend the dynamic range of the charge measurement by a factor of 100. Another 91 PMTs are mounted facing outward to detect light from events such as muon interactions in the outer light water region. It is very likely that the outward looking (OWL) PMTs will also detect events during a burst of supernova neutrinos. An additional 4 PMTs are installed in the AV chimney to veto light from static electric discharge in that area. Finally, a set of 23 PMTs are available for diagnostic studies and are mounted on a sled placed outside the PSUP and facing toward the detector.

By itself, the inward facing array of PMTs provides a photocathode coverage of 31%. However, each inward-looking PMT is equipped with a light concentrator to improve the light collection efficiency and increase the effective geometric coverage of the entire array to 54% of 4π. The outward-looking PMTs do not have concentrators.

The electron cascade in the PMT becomes less efficient in the presence of a magnetic field, as electrons from one dynode are deflected while en route to the successive dynode. Therefore, magnetic field-compensation coils are embedded in the cavity wall that surrounds the detector in order to counteract the effect of the Earth's magnetic field. The maximum residual field at the PMT array is 19 μT and the average overall improvement in the gain is 8.6% [75].

The PMTs are operated at high voltages in the range 1700–2100 V, resulting in a gain of 2×10^7 (except for the low gain PMTs). As specified by the manufacturer, the measured RMS timing resolution of the photomultiplier tubes is 1.5 ns. Average noise rates in the PMTs are relatively low at approximately 500 Hz due in part to the cool 10°C water that surrounds them.

4.6 SNO Electronics

The SNO electronics acts as the interface to the PMT array. Each PMT is supplied high voltage and has its signal read out through a single 32 m waterproof coaxial cable that is connected to one channel in an eight channel paddle card. Four paddle cards are seated into one 32-channel PMT interface card (PMTIC), which in turn is connected to both a high voltage distribution plane and a front-end card (FEC), where the PMT signal is processed. One FEC has 4 daughterboards, each of which is responsible for processing the signal from 8 channels for a total of 32 channels per FEC. Signal information is stored in the SNO CMOS chip, which contains a 4 MB on-board memory buffer. There is enough combined memory in all of the FECs to store $\sim 10^6$ supernova events[4]. The PMTICs and FECs are combined in groups of 16 to form a crate and in total there are 9728 possible electronics channels in 19 SNO crates. Each crate also contains a translator card and a crate trigger

[4]The entire system of readout electronics contains 4 MB $\times$ (19 crates $\times$ 16 FECs) = 1.2 GB of memory. The average supernova event contains 100 PMT hits, of which each hit requires 12 bytes. Therefore, the event capacity is 1.2 GB / 1.2 kB = 1 million supernova events.

card. The translator card communicates with a similar card in the data acquisition VME crate, while the trigger card performs the analog sum the individual channel triggers for a particular crate and sends the sum to a central Master Trigger Card (MTC). The MTC is responsible for processing the all of the signal sums in the detector and deciding when a set of PMT hits constitutes an interesting event.

The SNO electronics is also responsible for measuring PMT time and charge information. There are three distinct charge values available in the SNO data stream:

- QHS: high gain, short integration time (70 ns)
- QHL: high gain, long integration time (400 ns)
- QLX: low gain, short or long integration time (the default is 400 ns)

The current from each PMT is split into two branches (approximately in the ratio 1:16) and fed into two separate channels of a charge integrator. Low gain charge is measured in the channel with less current, while high gain charge is measured by the channel with more current. Compared to the high gain signal, the QLX charge is roughly a factor of 10 lower in gain. The low gain charge is useful for events that produce large amounts of light (muon events, for example) where the PMT response is no longer linear in the high gain setting and the associated analog-to-digital converters (ADCs) become saturated and provide no resolution in the measurement. Different charge integration times make it possible to separate charge measured in the prompt signal from the total charge, which may have some contribution from reflected light.

Each daughterboard contains level-crossing discriminators[5] and charge measurement capacitors. When the discriminator is triggered, the daughterboards begin recording the three charge quantities QHS, QHL and QLX. The triggering of the discriminator also starts a time-to-amplitude converter (TAC) to measure the charge integration time.

[5]These thresholds are adjustable in the SNO Data Acquisition software. On average, the discriminator threshold for each electronics channel is set to 0.25 of the mean charge for a single photoelectron.

4.7 SNO Trigger

The trigger for the SNO detector is used to determine which events are interesting and should constitute the data set. Design of the trigger system is dictated by a broad range of physics goals, from observing solar neutrinos to detecting muons and possibly receiving bursts neutrinos originating in supernovae. Other aspects that also need to be considered include a wide range of calibration devices and being able to perform studies of the detector background.

After having gathered PMT information from all of the PMTs in the detector, the global trigger is formed at the Master Trigger Card. The primary SNO event trigger uses the number of phototube hits and is called the "NHIT" trigger. SNO PMT hits are counted by performing an analog sum of the signals from the SNO CMOS chips. If the sum is above a programmable threshold, a global trigger causes the data stored on the FECs to be collected by the data acquisition system and built into events. When the global trigger is created, an additional lockout signal prevents any other signal from creating a global trigger while the current trigger cycle is active. The lockout period is set to 400 ns, during which time the MTC writes the trigger related information to its on-board memory. At the end of the lockout period, if any trigger is still above threshold, a new global trigger is generated immediately. Otherwise, the system waits for the next discriminator threshold crossing or external trigger signal to start the cycle again. Therefore, the deadtime per PMT is 400 ns, and the overall trigger deadtime is less than 10 ns. The electronics system is capable of handling trigger rates above 1 MHz and a sustained low energy event rate of better than 1 kHz [76].

The NHIT trigger requires a certain number of photomuliplier tubes (PMTs) to register a Čerenkov photon hit within a certain time window. The nominal setting for the NHIT trigger time window is 100 ns, which is slightly longer than the largest possible difference

in photon arrival times for an interaction in the D_2O (66 ns). A 20 ns NHIT trigger is also available for studies involving a smaller selected fiducial volume of the detector. These two types of NHIT triggers are referred to as the NHIT100 and NHIT20 triggers, respectively. In addition to these discrete analog sums, the SNO detector can also trigger on the analog sum of the 9438 shaped PMT signals, called the "ESUM" trigger. The ESUM trigger is a measure of the total charge in an event (or energy). The NHIT and ESUM triggers complement each other well. An event can have many PMTs hit causing the detector to trigger on NHIT, but the total charge may not be sufficiently high to cause an ESUM trigger. On the other hand, if only a few PMTs are hit in one event, the detector will not trigger on NHIT, but if those few PMTs have very high charge, ESUM will be triggered. It is also possible for the OWL PMTs to generate both an NHIT trigger and an ESUM trigger. To study the PMT noise rates, a built-in pulser is used to provide a global trigger at set intervals. This trigger is called the "pulse-gt" trigger. The pulser rate is programmable, and is typically set to 5 Hz.

The trigger system is also responsible for maintaining and recording relative event timing, absolute event time, the global trigger ID number and information regarding which trigger types were satisfied for each event. Two oscillators are used to keep a record of absolute and relative time. Relative timing between events is recording using a 50 MHz counter that relies on a 100 MHz oscillator. The 50 MHz clock resolution allows events times to be latched at 20 ns intervals. Absolute time is maintained for the purpose of correlating events in the SNO data to other experiments by a 10 MHz clock that is synchronized by a commercial GPS unit. Ticks from the 10 MHz clock provide a time resolution of 100 ns, while the absolute accuracy is dictated by the GPS receiver and possible degradation by the military and is thought to be roughly 300 ns[6].

[6]Effective midnight on May 1, 2000, the "selective availability" (or degradation) of commercial GPS signals ended. It is unclear how much the absolute timing accuracy is affected.

4.8 SNO Data Acquisition

The SNO data acquisition (DAQ) is designed to read out the PMT data stored in the SNO electronics and sort the individual PMT hits into events. The principal hardware component of the SNO DAQ system is a single VME crate containing a Motorola 68040 embedded CPU (or eCPU) with 32 MB of on-board memory. Front-end cards in each crate are read out sequentially by the eCPU as is the MTC, and a Sun workstation is responsible for sorting the FEC and MTC data and building them into events. The readout of the electronics is controlled and monitored via a user interface program called "SNO Hardware Acquisition and Readout Control" (SHaRC) running on a Power Computing 250 MHz PPC Macintosh that communicates with the eCPU using a PCIbus-VME interface.

The burst capability of the SNO DAQ has not yet been fully investigated. However, the SNO data acquisition system has demonstrated the ability to process data at 450–500 kB/s, which corresponds to an event rate of 38–42 kHz. Real-time processes that subscribe to the data stream, such as the SNO online burst monitor, are able to receive events at a rate of 25–33 kHz with very little loss of information.

4.9 SNO Calibration

Accurate measurement of the physics processes in SNO requires a set of calibrations to properly interpret the raw PMT time and charge information. A number of calibration devices are employed to this end, and can be divided into three categories: low level calibration of the detector electronics and photomultipliers, detector optical and energy response and the detector physics response.

4.9.1 Low Level Calibrations

An electronic charge pulser is used in conjunction with a light source at a known position to convert digitized PMT charge and time values to photoelectrons and nanoseconds. These calibration activities are referred to as electronics calibration (ECA) and the phototube calibration (PCA).

4.9.2 Optical and Energy Calibrations

Optical sources are used to measure absorption, scattering and timing, whereas the energy calibration sources are used to determine the correspondence between the energy of a particle and the number of PMTs that receive Čerenkov radiation.

The primary optical source employed in SNO is a nitrogen laser connected through fibre optic cable to a diffuser ball (the combined system is referred to as the "laserball"), which produces photons at several discrete wavelengths in the range $\lambda = 360$–700 nm. The laser generates sharp pulses (600 ps wide) up to a rate of 45 Hz at various intensities and at various locations within both the H_2O and D_2O volumes. Pulse width is increased slightly by the diffuser ball to about 2 ns.

Another optical source that was used during the commissioning of the SNO detector is the sonoluminescence source. This source offers very short pulses (< 100 ps) at a rate of 25 kHz, over a range of frequencies corresponding to a blackbody at a temperature of over 20 000 K, which is similar to the Čerenkov spectrum.

Energy calibrations are performed using a variety of sources that cover a range of energies. At low energies, the energy response of the SNO detector is determined using a ^{16}N gamma ray source [77]. The ^{16}N is produced in the reaction:

$$n + {}^{16}\mathrm{O} \rightarrow p + {}^{16}\mathrm{N}^{*}, \tag{4.23}$$

where 66% of the time the nitrogen excited state decays by beta emission to an excited

state of oxygen, which returns to the ground state by emitting a gamma ray:

$$^{16}\mathrm{N}^{*} \rightarrow {}^{16}\mathrm{O}^{*} + e^{-},\ {}^{16}\mathrm{O}^{*} \rightarrow {}^{16}\mathrm{O} + \gamma, \quad E_{\gamma} = 6.13\ \mathrm{MeV}. \tag{4.24}$$

It is the detector response to the 6.13 MeV gamma ray that is used in the energy calibration. There is no external trigger for this source, so a 3-mm thick scintillator viewed by a 5-cm PMT tags the initial decay electron and is used in the analysis to indicate that a decay took place. The short-lived ($\tau_{1/2} = 7.13$ s) $^{16}\mathrm{N}^{*}$ is delivered to the detector fiducial volume through capillary tubes using a gas transport system, during which time some fraction of the isotopes decay in the detector before reaching the decay chamber that houses the scintillator and PMT. Therefore, in addition to the $^{16}\mathrm{N}$ source events that have an associated e^{-} tag, many events in the data do not, and appear as genuine physics events.

To reach energies above 6 MeV, a miniature accelerator [78] is used to produce high energy gamma rays through the proton-tritium (or pt) reaction:

$$p + {}^{3}\mathrm{H} \rightarrow {}^{4}\mathrm{He} + \gamma, \quad E_{\gamma} = 19.82\ \mathrm{MeV}. \tag{4.25}$$

The monoenergetic 19.8 MeV gamma ray is used as the calibration signal, however neutrons are also produced by side reactions $^{2}\mathrm{H}(t,n)^{4}\mathrm{He}$, $^{3}\mathrm{H}(d,n)^{4}\mathrm{He}$ and $^{3}\mathrm{H}(t,nn)^{4}\mathrm{He}$ due to impurities in the beam and other effects. These events are not tagged in the data.

4.9.3 Physics Calibrations

Physics calibrations involve measuring the detector response to various particles that produce Čerenkov light and often have characteristics similar to the principal neutrino interactions being measured. An example of this is the $^{8}\mathrm{Li}$ beta source. The short-lived ($\tau_{1/2} = 0.84$ s) $^{8}\mathrm{Li}$ isotope is produced through the reaction:

$$n + {}^{11}\mathrm{B} \rightarrow \alpha + {}^{8}\mathrm{Li}, \tag{4.26}$$

and is used to calibrate the detector through the subsequent decay:

$$^{8}\mathrm{Li} \rightarrow e^{-} + {}^{8}\mathrm{Be}^{*},\ {}^{8}\mathrm{Be}^{*} \rightarrow 2\alpha. \tag{4.27}$$

Unlike the gamma sources which provide monoenergetic particles, the electrons from the ^{8}Li source have a spectrum of energies similar to that of the ^{8}B solar neutrino spectrum. As such, it is also possible to use the 13 MeV endpoint energy to study the energy response of the detector.

As with the ^{16}N source, a small PMT is installed in the ^{8}Li decay chamber in order to tag the α particles. However, unlike the ^{16}N source, the scintillation is provided by the He gas that is also used in the transport.

The detector response to neutrons is studied using the fission of ^{252}Cf, which produces on average 4 neutrons and 20 low energy gamma rays. Two ^{252}Cf sources of different activities are available: the weak source is 0.001 μCi and the strong source is 0.01 μCi.

Also in this category are calibration sources used to simulate the radioactive backgrounds in the detector, such as ^{238}U and ^{232}Th. To date, three sources have been used to study these backgrounds in SNO: an encapsulated uranium source, an encapsulated thorium source and a proportional counter (PC) source which has thorium plated on the anode wire. As mentioned in Section 4.4, the most serious detector radioactive backgrounds are due to gamma rays produced in the U and Th decay chains that have sufficient energy to photodisintegrate the deuteron.

A summary of the calibration sources in use within SNO is provided in Table 4.4. Those sources which are not externally triggered or tagged in the data require special handling by the online burst monitor described in Chapter 9.

4.10 The SNO Monte Carlo Package

The official SNO Monte Carlo analysis package is called SNOMAN (SNO Monte Carlo and Analysis) [69] and is written in the FORTRAN 77 programming language. SNOMAN simulates e, γ, n and μ physics in the detector as well as Čerenkov photon propagation to the PMTs. The full geometry and optical properties that are included in the simulation

Calibration Source	**Calibration Type**	**Triggered/ Tagged?**
Low Level Calibration:		
ECA	charge	triggered
PCA	discrete λ, 360–700 nm	triggered
Optical Calibration:		
Laser	discrete λ, 360–700 nm	triggered
Sonoluminescence	γ, Č spectrum	none
Energy Calibration:		
^{16}N	γ, $E_\gamma = 6.13$ MeV	some tagged
pt	γ, $E_\gamma = 19.8$ MeV	none
Physics Calibration:		
^{8}Li	e^-, ^{8}B spectrum	some tagged
^{252}Cf (strong)	n	none
^{252}Cf (weak)	n	none
U	$\gamma \rightarrow n$	none
Th	$\gamma \rightarrow n$	none
PC	$\gamma \rightarrow n$	some tagged

Table 4.4: Summary of sources used to calibrate the SNO detector.

package are the result of detailed studies and measurements of the various components and detector calibration.

SNOMAN relies on several external software packages. Interactions of the γ and $e^{\pm}$ particles are simulated in SNO using routines from the EGS4 package [79], while routines adopted from MCNP [80] are used to describe the propagation of neutrons.

The CERNLIB software package ZEBRA is used to manage the SNO data structure (and to overcome the lack of dynamic memory allocation in FORTRAN 77). As well, data from the detector are written to tape in the form of packed ZEBRA banks. A central database (SNODB), which is based on the CERNLIB package HEPDB, is used to keep track of all constants and time-varying parameters in the SNO detector.

Chapter 5

SNO Supernova Monte Carlo

5.1 Introduction

Development of the SNO supernova Monte Carlo draws on many different areas of physics—from the description of the supernova signal as it emerges from the collapsing star to the neutrino interactions with the particles in the heavy- and light-water volumes and the many parameters that characterize the SNO detector. These various aspects are described in some detail in the sections that follow. Further details relating to specific calculations are provided in Appendix B.

Within the SNO collaboration, the author has been responsible for the development of the current incarnation of the SNO supernova simulation software and for performing Monte Carlo simulations in order to characterize the signal in the detector. Preliminary software developed by Ng [81] for simulating supernova neutrinos in the SNO detector was entirely re-written by the author.

5.2 Supernova Signal Formalism

For a given neutrino species, the number of neutrinos emitted at the source of the supernova per unit energy per unit time can be written as the product of two components:

$$\frac{d^2N_{src}}{dE_\nu dt_i} = F(t_i)f(E_\nu, t_i), \tag{5.1}$$

where t_i is the time of neutrino emission from the supernova for a given neutrino species and E_ν is the specific neutrino energy at time t_i.

The $F(t_i)$ factor in Equation 5.1 represents the number of neutrinos emitted per unit time, and has the following general form:

$$F(t_i) = \frac{L_\nu(t_i)}{\epsilon_\nu(t_i)}, \tag{5.2}$$

where $L_\nu(t_i)$ is the time-dependent neutrino luminosity, or neutrino energy flux per unit time, and $\epsilon_\nu(t_i)$ is the time-dependent average neutrino energy. While the details of the luminosity and average energy functions vary between models, there are robust features predicted for the supernova signal. The luminosity spectrum is expected to be sharply peaked at early emission times and the average energy spectrum is expected to exhibit a hierarchical structure in which muon and tau neutrinos have the highest average energies followed by the electron antineutrino and finally the electron neutrino. These two features are discussed further in Section 5.3.2.

The total energy carried away by a given neutrino species during a supernova explosion is determined by integrating the source luminosity over all neutrino emission times:

$$E_{\nu,total} = \int_0^\infty L_\nu(t_i) dt_i \tag{5.3}$$

and the total number of neutrinos of a given species emitted during the collapse is given by:

$$N_{\nu,total} = \int_0^\infty \frac{L_\nu(t_i)}{\epsilon_\nu(t_i)} dt_i. \tag{5.4}$$

Therefore, the average neutrino energy for a given species is calculated as:

$$\langle E_\nu \rangle = \frac{E_{\nu,total}}{N_{\nu,total}}. \tag{5.5}$$

The $f(E_\nu, t_i)$ factor in Equation 5.1 specifies the shape of the neutrino energy distribution. In the case of supernova neutrinos, this shape is given by a Fermi-Dirac thermal distribution[1]:

$$f(E_\nu, t_i) = \frac{1}{N_{FD}(t_i)} \left[\frac{E_\nu^2}{1 + e^{E_\nu / T_\nu(t_i)}} \right], \tag{5.6}$$

[1]While many papers refer to the Fermi-Dirac distribution in the context of supernova neutrino energy spectra, few present the actual form, and those that do are often conflicting.

where E_ν is the specific neutrino energy (not average), $T_\nu(t_i)$ is the time-dependent neutrino temperature and $N_{FD}(t_i)$ is the normalization factor such that:

$$\int_0^\infty f(E_\nu, t_i)\, dE_\nu = 1. \tag{5.7}$$

Written explicitly, the expression for the normalization becomes:

$$N_{FD}(t_i) = \int_0^\infty \frac{E_\nu^2}{1 + e^{E_\nu/T_\nu(t_i)}}\, dE_\nu. \tag{5.8}$$

For constant neutrino temperatures, the normalization factor simplifies to the following form:

$$\begin{aligned} N_{FD} &= \int_0^\infty \left(\frac{E_\nu}{T_\nu}\right)^2 T_\nu^2 \left[\frac{1}{1 + e^{E_\nu/T_\nu}}\right] dE_\nu \\ &= T_\nu^3 \int_0^\infty \frac{x^2}{1 + e^x}\, dx \\ &= 1.803\, T_\nu^3, \end{aligned} \tag{5.9}$$

where the substitution $x = (E_\nu/T_\nu)$ is used to obtain a standard integral form.

Monte Carlo studies of neutrino transport within the collapsing star [82] have indicated that the instantaneous neutrino spectra are "pinched", meaning that the low- and high-energy tails of the emergent distribution are suppressed relative to a Maxwell-Boltzmann spectrum of the same average energy. The deficit in low-energy neutrinos is due to the fact that there are fewer low energy neutrinos produced in the core of the proto-neutron star than high energy neutrinos (emission $\propto E_\nu^4$). On the other hand, the lack of high energy neutrinos is a consequence of the energy dependence in the neutrino interaction cross sections (interaction probability $\propto E_\nu^2$). High energy neutrinos are more likely to scatter than low energy neutrinos, so the high energy tail of the number distribution is shifted to lower energies as higher energy neutrinos are preferentially scattered and lose energy.

To address these effects, some models introduce a "degeneracy" or "effective chemical potential" parameter, $\eta_\nu(t_i)$, to better describe the thermal spectrum. Incorporating $\eta_\nu(t_i)$

into Equation 5.6, $f(E_\nu, t_i)$ then becomes:

$$f(E_\nu, t_i) = \frac{1}{N_{FD}} \left[\frac{E_\nu^2}{1 + e^{E_\nu / T_\nu(t_i) - \eta_\nu(t_i)}} \right] \tag{5.10}$$

with the corresponding normalization factor modified in the same manner.

The neutrinos from the supernova then propagate a distance D to Earth, where they interact in a neutrino detector at time t. The number of such interactions per unit energy per unit time depends on the number of target particles in the detector, N_t, and the interaction cross section, $\sigma(E_\nu)$:

$$\frac{d^2 N_{det}}{dE_\nu dt} = N_t \, \sigma(E_\nu) \frac{1}{4\pi D^2} \frac{d^2 N_{src}}{dE_\nu dt_i}. \tag{5.11}$$

Therefore, the number of neutrino interactions that take place in a detector is obtained by integration:

$$N_{det} = N_t \frac{1}{4\pi D^2} \int_0^\infty \int_0^\infty \sigma(E_\nu) \frac{d^2 N_{src}}{dE_\nu dt_i} \, dE_\nu \, dt_i. \tag{5.12}$$

Including the neutrino mass, m_ν, in the above treatment, means that the neutrino signal will be delayed relative to its massless counterpart, which travels at the speed of light. The arrival time of a massive neutrino at the detector is $t = t_i + D/c + \Delta t(E_\nu)$, where (D/c) is the time offset due to the distance traveled by the neutrino, which is usually dropped for convenience. Formally, the supernova neutrino signal at the detector becomes:

$$\frac{d^2 N_{det}}{dE_\nu dt} = N_t \, \sigma(E_\nu) \frac{1}{4\pi D^2} \int \frac{d^2 N_{src}}{dE_\nu dt_i} \delta(t - t_i - \Delta t(E_\nu)) \, dt_i, \tag{5.13}$$

where the energy-dependent delay, $\Delta t(E_\nu)$, is given by Equation 3.6:

$$\begin{aligned} \Delta t(E_\nu) &= D \left(\frac{1}{v} - \frac{1}{c} \right) \\ &= \frac{D}{c} \left[\frac{1}{2} \left(\frac{m_\nu c^2}{E_\nu} \right)^2 - \frac{3}{8} \left(\frac{m_\nu c^2}{E_\nu} \right)^4 + \frac{15}{96} \left(\frac{m_\nu c^2}{E_\nu} \right)^6 - \cdots \right] \\ &\approx \frac{D}{2c} \left(\frac{m_\nu c^2}{E_\nu} \right)^2 \end{aligned} \tag{5.14}$$

in the relativistic limit $E_\nu \gg m_\nu$, where v is the speed of the particle and c is the speed of light.

5.3 Supernova Models

5.3.1 Introduction

Beginning with the first numerical simulations performed by Colgate and White [83] in the 1960s, there has been significant progress in the modeling of supernovae. The problem requires understanding the behaviour of matter over extremes of temperature and density that are impossible to reproduce in a laboratory. Failure of the "prompt" mechanism to generate a sustainable shock wave gave way to the "delayed" mechanism, in which the shock wave is reenergized by the intense neutrino flux that is carrying the binding energy of the proto-neutron star. Despite including general relativity in the transport and hydrodynamical equations, simulations of spherically symmetric (1-d) models have so far not resulted in a supernova explosion. The next frontier is to construct axis-symmetric (2-d) models in which it is possible to study the role of convection[2], rotation and magnetic fields in the evolution of a collapsing star. Many aspects of the latest two-dimensional models are currently under investigation, and some elements of three-dimensional models are currently being developed [84] to provide even greater insight.

A number of supernova models appear in the literature, and are used to predict the expected signal in various neutrino detectors. Some of these models offer a very general supernova signal, glossing over many of the details of the predicted core collapse mechanism, in favour of concentrating on some of the more robust features. Meanwhile, other more sophisticated models are based on the results of detailed calculations over limited regions of the supernova time spectrum. Since there still remains much uncertainty in the supernova community, a survey of five models is presented below for discussion. Descriptions of the most generic models are covered first, followed by the models based on more detailed calculations. In the chapters that follow, these same models will be used to make predictions

[2]One of the main motivations for considering convection comes from observations of SN1987A, which indicate that extensive mixing occurred throughout much of the ejected material.

about the supernova neutrino signal in SNO.

5.3.2 General Predictions

According to the description presented in Chapter 3, a number of general features of the supernova neutrino signal are predicted. The first prediction is for a significant enhancement in the neutrino signal at the onset of the burst due to electron capture reactions in the core. Only ν_e neutrinos participate in these interactions, therefore the signal enhancement should be predominantly from ν_e neutrinos.

The second prediction describes the relative energies of the various neutrino species. Neutrinos produced in a supernova explosion are expected to have a hierarchy of temperatures depending on their type. Because different neutrinos interact through different reactions, electron neutrinos are thought to have the lowest temperatures, electron antineutrinos to have slightly higher temperatures and "ν_μ" neutrinos are predicted to have the highest temperatures.

A further prediction of all "delayed" explosion supernova models is that the neutrino luminosity remains fairly high before the explosion. This period of enhanced luminosity may last for hundreds of milliseconds.

5.3.3 Beacom and Vogel Model

The most generic supernova model under consideration is one that was recently introduced by Beacom and Vogel [85]. As a basis for their model, Beacom and Vogel use the timing information from the SN1987A data set and cite the numerical simulations of Janka [86] and Woosley *et al.* [87] for neutrino energy properties. The Beacom and Vogel model has the gravitational binding energy of the star, $E_B = 3 \times 10^{53}$ ergs, released and carried away in equal parts by the 6 neutrino flavours (ν_e, $\overline{\nu}_e$, ν_μ, $\overline{\nu}_\mu$, ν_τ, $\overline{\nu}_\tau$). In this scenario, the ν_e neutrinos are responsible for carrying 17% of the energy, the $\overline{\nu}_e$ neutrinos for 17% and the

ν_μ and ν_τ (and their antiparticles), collectively called "ν_μ", account for 66%. The Beacom and Vogel model was initially constructed for use in supernova signal timing studies, and as such the detailed shape of the luminosity and average neutrino energy spectra was less important than the general shape of the signal and characteristic durations. Therefore, this model ignores even robust features such as the predicted enhancement to the electron neutrino signal due to the neutronization of the core.

The Beacom and Vogel neutrino luminosity is described by two exponential functions[3] and is the same for all neutrino species. After core bounce, when the temperature in the core of the proto-neutron star is very high, the luminosity of all neutrino species begins to increase exponentially:

$$L_\nu(t) = \frac{E_B}{6}\left(\frac{1}{\tau_1+\tau_2}\right)\exp\left[+\frac{(t-t_0)}{\tau_1}\right], t \le t_0, \tag{5.15}$$

where the rise is characterized by the time constant $\tau_1 = 0.030$ s and extends to $t_0 = 0.090$ s. The choice of time constant is related to the shock propagation time across the core of the proto-neutron star. Immediately after the exponential increase phase, a cooling phase begins where the luminosity is described by exponential decay:

$$L_\nu(t) = \frac{E_B}{6}\left(\frac{1}{\tau_1+\tau_2}\right)\exp\left[-\frac{(t-t_0)}{\tau_2}\right], t > t_0. \tag{5.16}$$

The decay time constant governing the cooling regime is given as $\tau_2 = 3$ s. Figure 5.1 shows the neutrino luminosity as a function of time. Notice that the neutrino luminosity extends out to a time around 10 s, which is consistent with neutrino data from SN1987A. It should also be noted that the luminosity in the cooling period falls off very slowly compared with other supernova models.

In the Beacom and Vogel model, electron neutrinos have the lowest temperature $T_{\nu_e} = 3.5$ MeV, while electron antineutrinos have a slightly higher temperature $T_{\overline{\nu}_e} = 5.0$ MeV

[3] In reference [15], the same authors advocate a slightly different model. Instead of an exponential rise, a one-sided Gaussian function is used, which has the same width as the exponential described in the text. The exponential function is used here because it is likely closer in shape to the expected signal and is also easier to normalize.

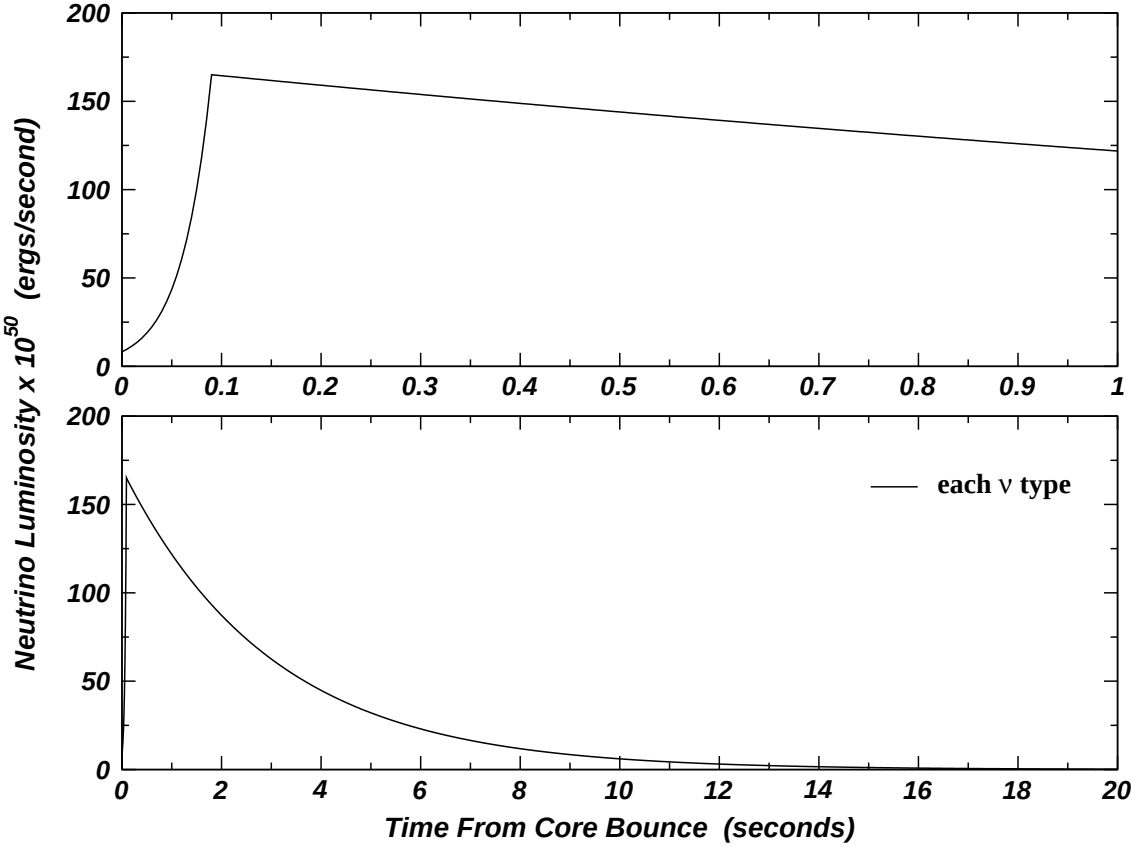

Figure 5.1: Supernova neutrino luminosity as a function of time in the Beacom and Vogel model [85]. The top plot highlights the first 1 s of the burst luminosity signal, showing both the initial exponential rise and the subsequent exponential decay periods. The bottom plot demonstrates that the luminosity spectrum extends out to ∼10 s, which is consistent with neutrino observations from SN1987A. In this model, all neutrino species are assumed to have the same luminosity, and no special features relating to the collapse mechanism are included. For the sake of comparison, the "ν_μ" luminosity (sum of the ν_μ, $\overline{\nu}_\mu$, ν_τ and $\overline{\nu}_\tau$ components) would be four times greater than the individual neutrino signal shown.

and "ν_μ" neutrinos have the highest temperature $T_{\text{“}\nu_\mu\text{”}} = 8.0$ MeV. Even though the neutrino flux is decreasing, simulations by Woosley *et al.* [87] suggest that the average neutrino energies remain high and nearly constant. Beacom and Vogel use this information to argue that there is no compelling reason to introduce a time-dependent temperature, and so they use the temperature values listed above for all times. The average neutrino

energies for this model are related to the spectrum temperatures by $\langle E_\nu \rangle = 3.15\, kT_\nu$. Since the neutrino temperatures do not vary with time in this model, the average neutrino energies are calculated in a straightforward manner: 11.0 MeV for ν_e neutrinos, 15.8 MeV for $\overline{\nu}_e$ neutrinos and 25.2 MeV for "ν_μ" neutrinos.

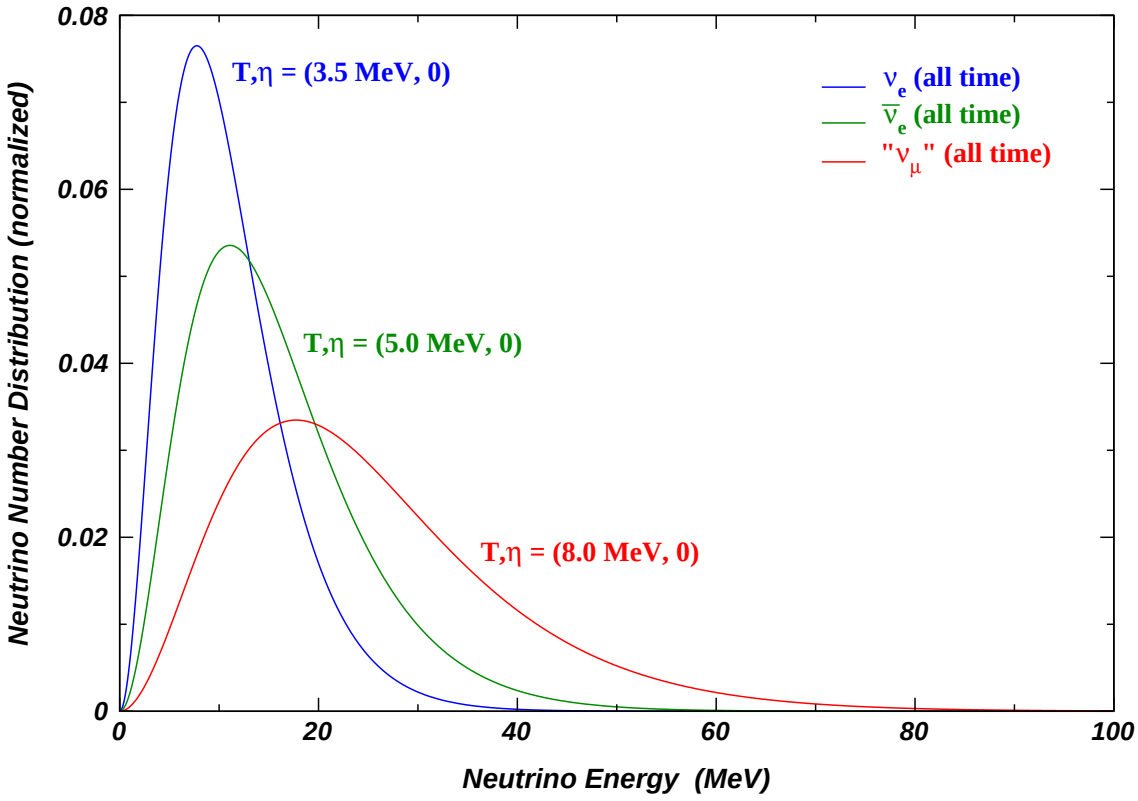

Figure 5.2: Fermi-Dirac neutrino energy distribution in the Beacom and Vogel model [85]. Because of the generic nature of this model, the neutrino temperatures are taken to be constant in time and no chemical potential factor is used to modify the distribution. Note that "ν_μ" represents any of the following neutrino types: ν_μ, $\overline{\nu}_\mu$, ν_τ or $\overline{\nu}_\tau$, not the sum.

The neutrino energy spectra are governed by the Fermi-Dirac distribution, where for this model all neutrino flavours have an associated chemical potential parameter, $\eta_\nu = 0$. The resulting Fermi-Dirac spectrum for the various neutrino species is determined using Equations 5.6 and 5.9 with the neutrino temperature values listed above. The energy

distributions shown in Figure 5.2 also confirm the relative energies of the different neutrino species. Compared to the other neutrino types, the energy distribution for "ν_μ" neutrinos has a peak at higher energies, and also has a long tail extending to nearly 100 MeV.

5.3.4 Burrows *et al.* Model

Although still generic, Burrows *et al.* [60] provide a model that examines possible structure in the neutrino signal based on details of the core collapse mechanism. The resulting model makes predictions beyond what was identified in the 24 events studied from SN1987A. To construct their model, Burrows *et al.* draw on the work of several groups who were doing detailed supernova model calculations in the early 1990s, namely Wilson [27], Bruenn [88], Myra and Burrows [89] and Burrows [90]. The total neutrino energy radiated in this model is 2.90×10^{53} ergs, of which 20% is carried by the ν_e neutrinos, 18% is carried by the $\overline{\nu}_e$ neutrinos and 62% is carried collectively by the "ν_μ" neutrinos, which is quite similar to that of the Beacom and Vogel model discussed in the previous section. The most relevant features of the model are discussed below.

The Burrows neutrino luminosity spectrum has a number of features that reflect various stages of the collapse mechanism, which are highlighted in Figure 5.3. The initial ramp of the ν_e neutrino signal is the result of neutronization in the core. As the temperature in the core increases, protons and electrons combine to produce ν_e neutrinos through the $p + e^- \rightarrow n + \nu_e$ reaction. This prompt electron neutrino signal is the first signature of collapse and accounts for luminosity values reaching $L_\nu \sim 3 \times 10^{53}$ ergs/s. Core collapse continues for the first 0.1 s until nuclear density is reached, and the inner core rebounds once further collapse is no longer possible. The shock wave resulting from core bounce is accompanied by both a ν_e flash as electron capture takes place behind the shock wave front and by the rapid turnon of the $\overline{\nu}_e$ and "ν_μ" signals made possible by the high temperature of the shock. Figure 5.3 shows the associated contributions to the luminosity spectra shortly

after time $t_i = 0$. Superimposed on the luminosity peak due to neutronization, the ν_e flash brings the luminosity to its highest value, $L_\nu = 6 \times 10^{53}$ ergs/s, after which it then decays over 5 ms. Within ~80 ms of the luminosity peak, the ν_e and $\overline{\nu}_e$ luminosity signals merge. The explosion that ultimately destroys the outer envelopes of the star occurs 460 ms after core bounce, with the potential of a significant increase in the ν_e and $\overline{\nu}_e$ luminosities. In the time between the shock wave breakout and the explosion, Burrows *et al.* predict that a delayed explosion mechanism may result in modulations to the luminosity spectrum due to pulsations of the outer mantle of the proto-neutron star, possibly lasting for hundreds of milliseconds. A period of cooling follows the explosion for almost 1 minute until the point of transparency where the neutrino luminosities fall dramatically.

Unlike Beacom and Vogel, Burrows *et al.* use a time-dependent spectrum of average neutrino energies for the different neutrino flavours. At the shock breakout, there is a sudden change in the energy spectrum followed by a hardening of the spectrum that culminates in the explosion of the star. From that point on, the energy spectra gradually soften. Figure 5.4 shows the average neutrino energy spectrum as a function of time for the various neutrino types. The average energies used in the Burrows *et al.* model are $\langle E_{\nu_e} \rangle = 9.9$ MeV, $\left\langle E_{\overline{\nu}_e} \right\rangle = 11.6$ MeV and $\left\langle E_{\text{“}\nu_\mu\text{”}} \right\rangle = 15.4$ MeV. Compared to the average neutrino energies found in the Beacom and Vogel model, the values used by Burrows *et al.* are lower. In particular, the average energy for the $\overline{\nu}_e$ and “ν_μ” neutrinos is significantly lower, and this will have a noticeable effect on the supernova signal.

In this model, the energy distributions are assumed to have a Fermi-Dirac shape with a time dependent neutrino temperature and a set of non-zero degeneracy parameters. For the prompt ν_e signal a temperature $T_{\nu_e} = 1.7$ MeV is used for emission times up until 2 ms after core bounce. A corresponding degeneracy parameter, $\eta_{\nu_e} = 11.0$ is used to significantly pinch the tails of the burst ν_e neutrino thermal spectrum. For all other times, the following degeneracy parameters are used: $\eta_{\nu_e} = 1.2$, $\eta_{\overline{\nu}_e} = 2.0$, $\eta_{\text{“}\nu_\mu\text{”}} = 3.0$ (the $\overline{\nu}_e$ and

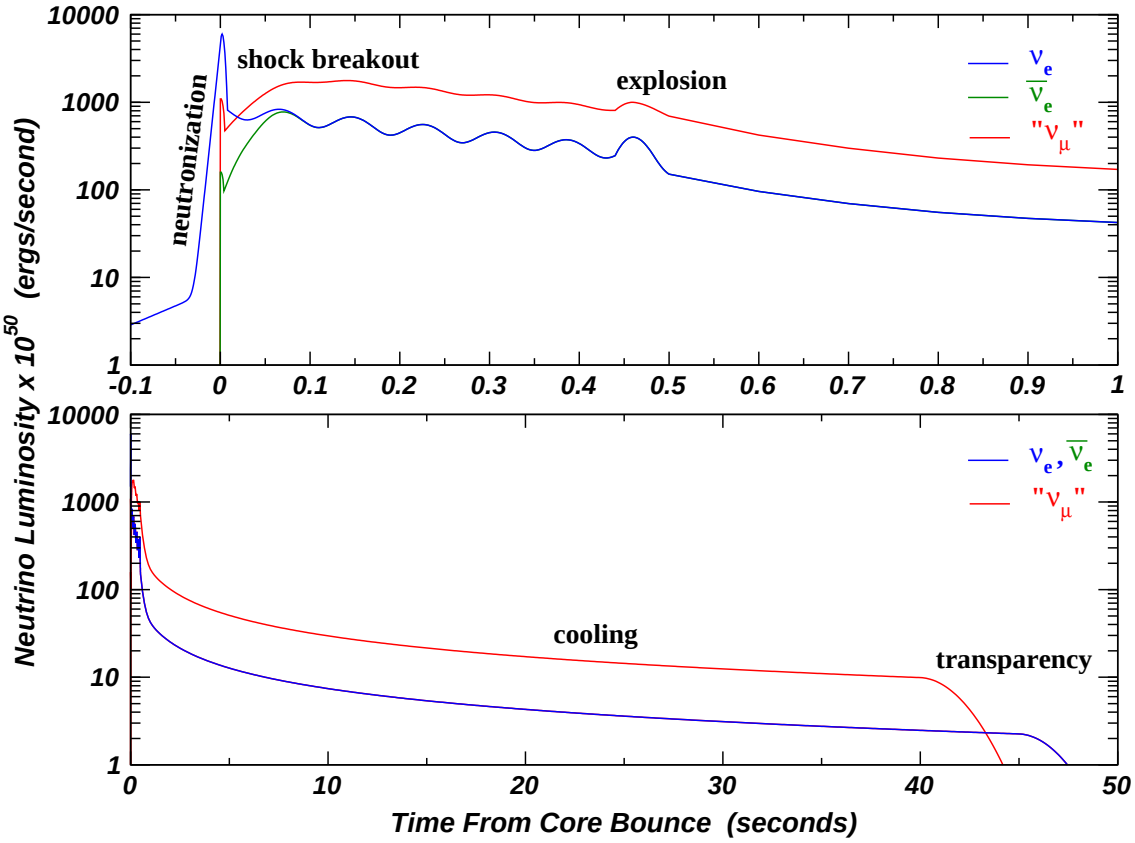

Figure 5.3: Supernova neutrino luminosity as a function of time in the Burrows *et al.* model [60]. The top figure shows the burst evolution in the first second of the neutrino burst, including a sharp prompt peak due to neutronization in the core followed by pulsations leading to an explosion at 460 ms. The bottom figure shows the cooling phase that takes over after the explosion extending to almost 50 seconds. Note that here the "ν_μ" luminosity is the sum of the ν_μ, $\overline{\nu}_\mu$, ν_τ and $\overline{\nu}_\tau$ contributions and is therefore a factor of four times greater than either the ν_e or $\overline{\nu}_e$ luminosity signals.

"ν_μ" signals are not present prior to $t_i = 2$ ms). The use of non-zero degeneracy parameters means that the neutrino temperature is no longer related to the average neutrino energy by $\langle E_\nu \rangle = 3.15\, kT_\nu$. Instead, the conversion factors listed in Table 5.1 apply [91]. Using Equation 5.10, the Fermi-Dirac spectra for the various neutrino species are computed and the resulting distributions are shown in Figure 5.5.

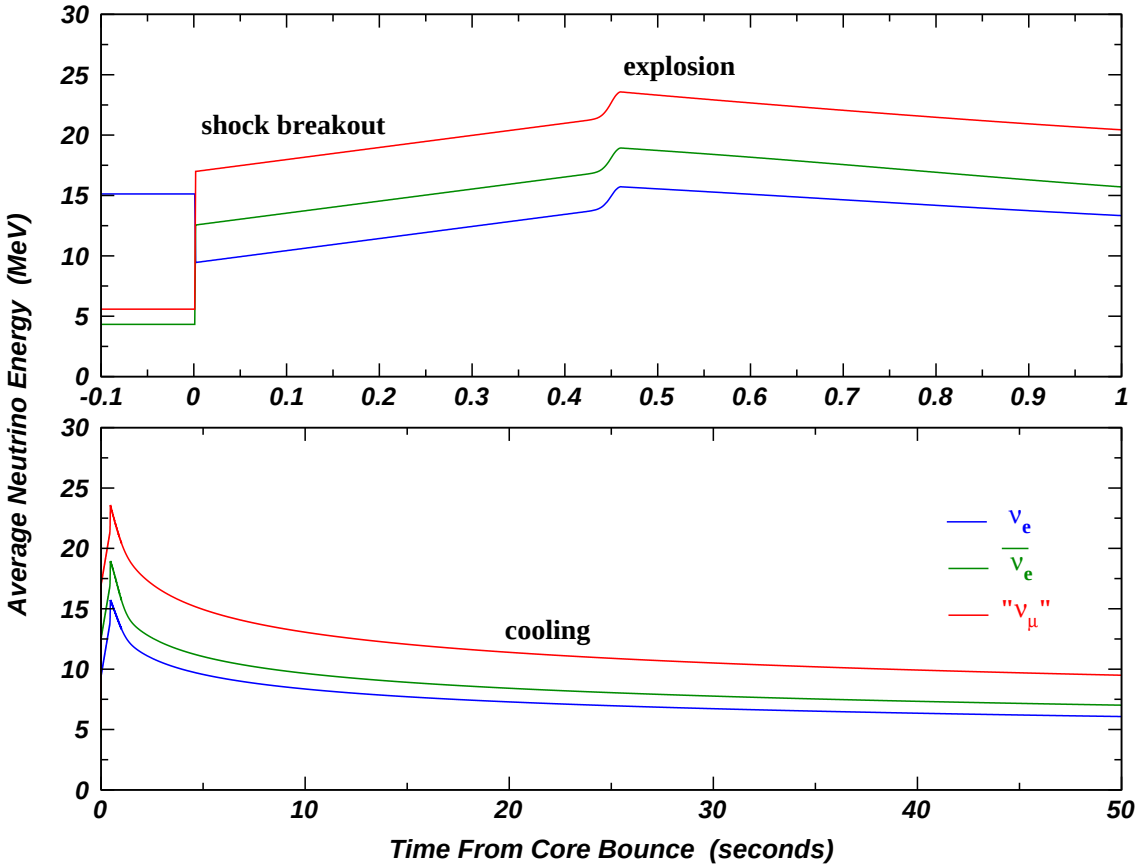

Figure 5.4: Supernova neutrino average energy as a function of time using the Burrows *et al.* model [60]. According to the top plot, the average energies for all neutrino species rise from the time of core bounce until the explosion. The bottom plot shows that after the explosion, the average energies gradually decrease. "ν_μ" represents any of the following neutrino types: ν_μ, $\overline{\nu}_\mu$, ν_τ or $\overline{\nu}_\tau$.

Neutrino Type	Time Regime	Degeneracy Parameter, η	Conversion $kT_\nu \rightarrow \langle E_\nu \rangle$
ν_e	$t_i \leq 1$ ms	11.0	8.90
	$t_i > 1$ ms	1.2	3.37
$\overline{\nu}_e$	$t_i > 1$ ms	2.0	3.61
"ν_μ"	$t_i > 1$ ms	3.0	3.99

Table 5.1: Specifications relating to the degeneracy parameter, η, for the Burrows *et al.* model.

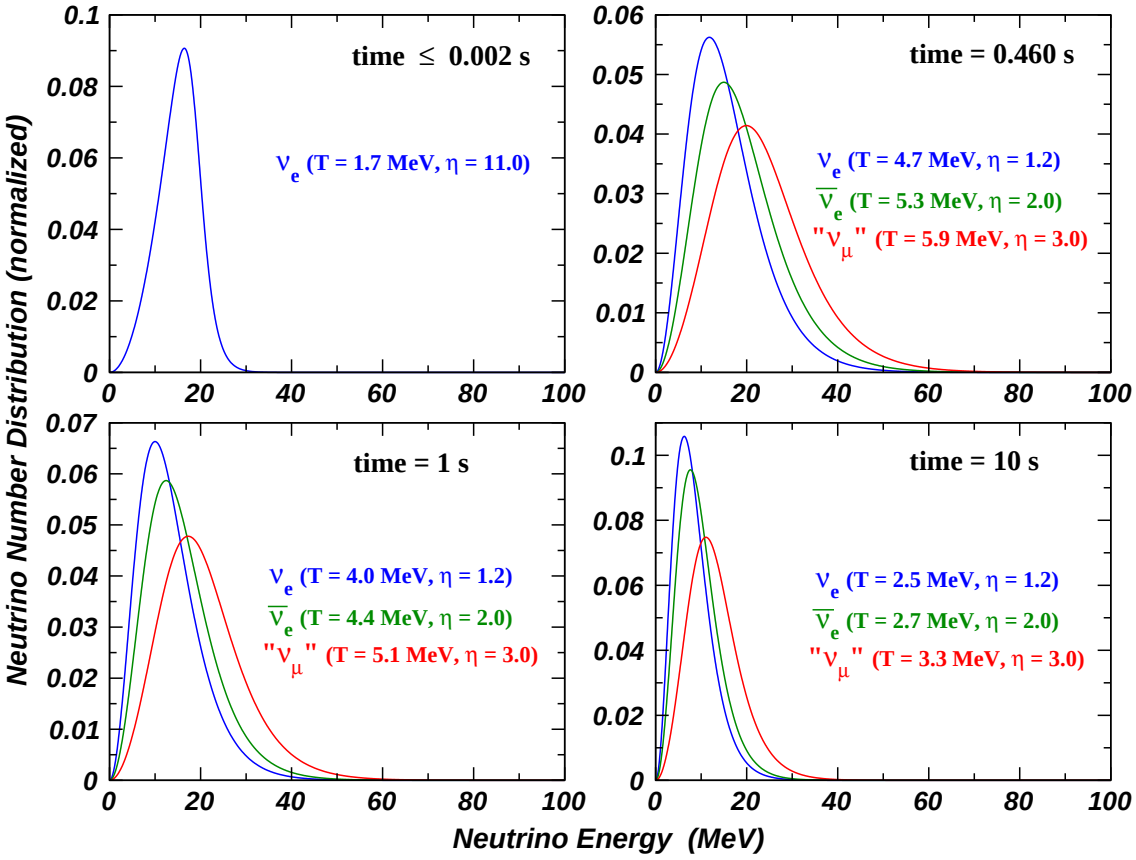

Figure 5.5: Fermi-Dirac neutrino energy distribution in the Burrows *et al.* model [60]. Since the neutrino temperatures and degeneracy parameters are a function of time, so are the Fermi-Dirac energy distributions. Four representative times are used to show how the spectral distributions evolve. Notice at $t \leq 0.002$ s how the energy distribution at low energies appears shifted toward the peak value, while the high-energy tail of the distribution does not extend as far as the ν_e distributions at other times. This is due to the relatively large value of η_ν used to modify the thermal spectrum. "ν_μ" represents any of the following neutrino types: ν_μ, $\overline{\nu}_\mu$, ν_τ or $\overline{\nu}_\tau$.

5.3.5 Bruenn Models

In a recent publication [92], Bruenn *et al.* describe a set of sophisticated calculations used to simulate the supernova collapse mechanism. They consider two sizes of progenitor star,

15 $M_\odot$ and 25 $M_\odot$, to be representative of small-iron-core and large-iron-core stars, respectively. When the core begins to collapse, the iron core mass is 1.278 $M_\odot$ for the 15 $M_\odot$ model and 1.770 $M_\odot$ for the 25 $M_\odot$ model. The computer code developed for these simulations is called MGFLD-TRANS, and it couples the general relativistic multigroup flux-limited diffusion (MGFLD) approximation to the Boltzmann transport equation to Lagrangian general relativistic hydrodynamics. A general relativistic approach is important because of the strong gravitational fields present during core collapse. Compared to Newtonian transport and hydrodynamics, Bruenn *et al.* find that in most cases the combined effect of including general relativity results in an increase in both the luminosities and average energies of all neutrino flavours during the shock reheating epoch. Some shortcomings of using the MGFLD approximation are discussed by Janka [93].

This model together with the one presented in Section 5.3.6 represent some of the leading edge of supernova collapse modeling to date. However, no group to date has successfully modeled a supernova to the point of explosion. Another drawback of these detailed model calculations is the limited time over which they are performed. However, with faster computers becoming available, many groups are working to add the necessary physics as well as extend the time range in the calculations.

5.3.5.1 Bruenn 15 $M_\odot$ Model

In the case of the 15 $M_\odot$ model, core bounce occurs 0.1829 s after the initial collapse. The peak in the ν_e luminosity shown in Figure 5.6 is due to electron capture in the wake of the shock wave. While the magnitude of the peak is roughly half the value the Burrows *et al.* use in their generic model, it is still the most striking feature of the distribution. Beginning at 0.4 s after bounce, the electron neutrino and antineutrino luminosities drop abruptly due to a change in the rate of accretion when the interface between the silicon and oxygen shells pass through the neutrinospheres. The drop in density reduces the mass accretion

rate and has a significant effect on the ν_e and $\overline{\nu}_e$ luminosities. The "ν_μ" luminosity is unaffected by the drop in the mass accretion rate because those neutrinos are produced (and decouple from matter) deeper in the core, where accretion effects are minimal.

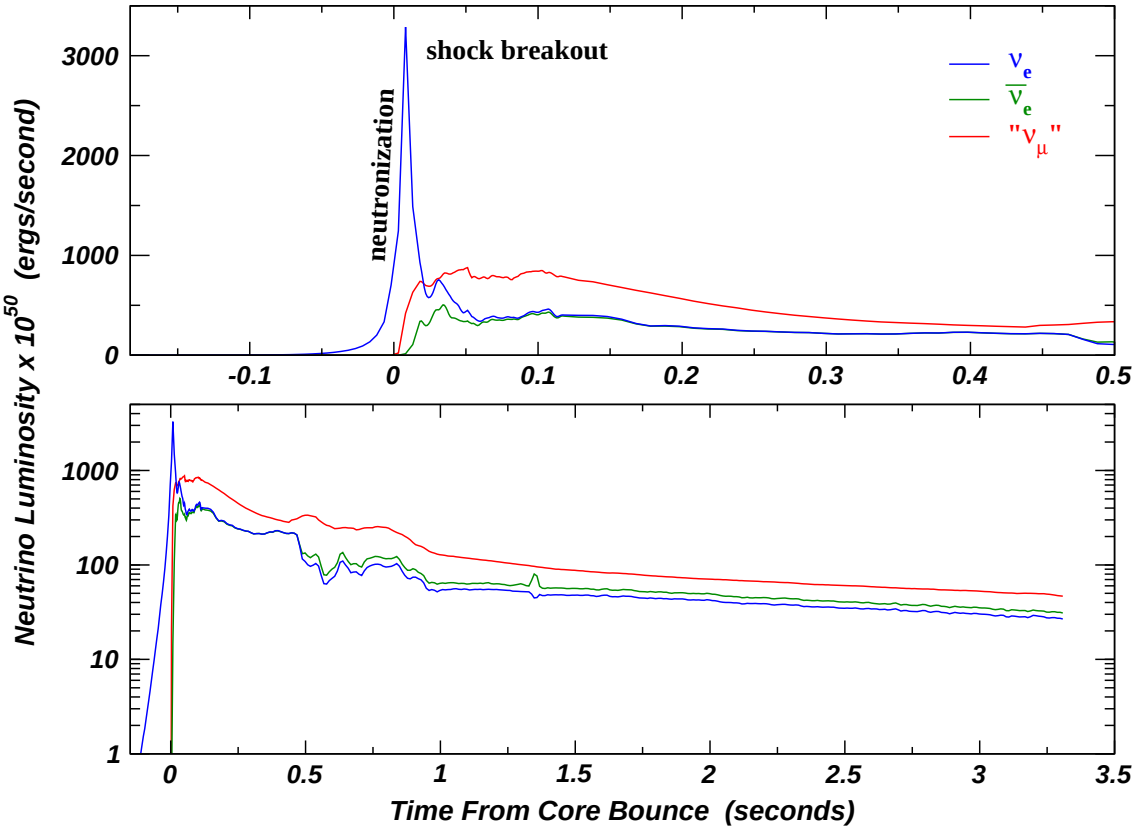

Figure 5.6: Supernova neutrino luminosity spectrum in the Bruenn 15 $M_\odot$ model [92]. The prompt peak due to neutronization is clearly visible. The calculation ends at 3.3 s after core bounce. Note that here the "ν_μ" luminosity is the sum of the ν_μ, $\overline{\nu}_\mu$, ν_τ and $\overline{\nu}_\tau$ contributions.

As with the other models investigated, the hierarchy of neutrino energies exists, in which the ν_e neutrinos have the lowest average energy and the "ν_μ" neutrinos have the highest average energy. Figure 5.7 presents the average energy spectra for ν_e, $\overline{\nu}_e$ and "ν_μ" neutrinos. Starting around 1 s after core bounce, the average energy values for all neutrino types stay roughly constant for the remainder of the burst. This behaviour appears to

support the approach adopted by Beacom and Vogel in their model.

The data presented in Figure 5.7 differ slightly from those shown by Bruenn *et al.* in reference [92]. In their paper, Bruenn *et al.* note that there is a spike in the "ν_μ" average energy at the time of core bounce due to a numerical artifact, and represents an unphysical energy. The data that were made available to the author have the highest energy "ν_μ" neutrinos removed from the calculation of the luminosity and average energy values. Therefore, there is very little evidence of the unphysical energy spike in Figure 5.7.

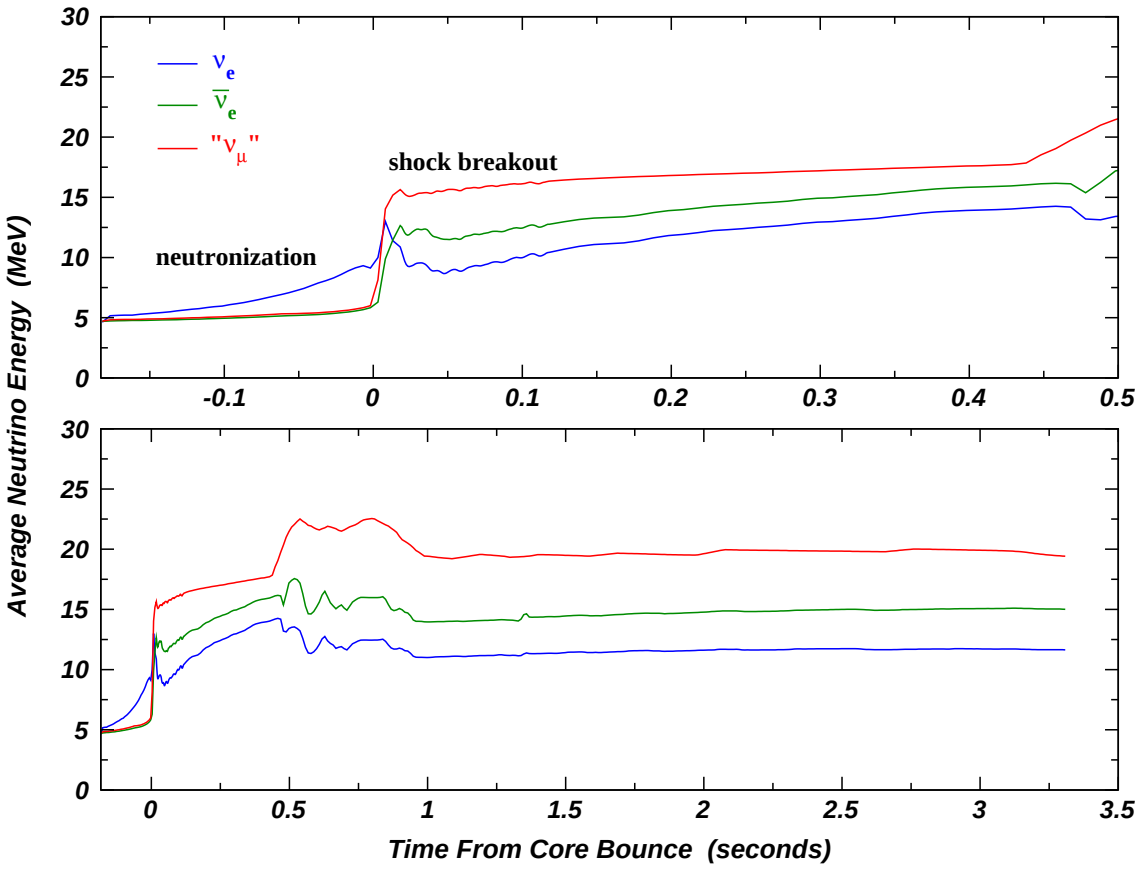

Figure 5.7: Supernova neutrino average energy spectrum using the Bruenn 15 $M_\odot$ model [92]. From the time of core bounce, the average energies for all neutrino species rise until the onset of accretion effects at 0.42 s. From that point on, the average energies remain relatively constant. The calculation ends at 3.3 s after core bounce.

5.3.5.2 Bruenn 25 $M_\odot$ Model

Core bounce for the 25 $M_\odot$ model occurs 0.2723 s after the initial collapse. Figure 5.8 shows the neutrino luminosity spectrum for ν_e, $\overline{\nu}_e$ and "ν_μ" neutrinos. Except for the neutronization peak, the luminosities for all neutrino types in the 25 $M_\odot$ model are almost twice as large as those in the 15 $M_\odot$ calculation. The sizable contribution from the combined "ν_μ" neutrinos immediately following the shock breakout is particularly striking. The difference in the prompt electron neutrino luminosity peak heights in the 15 $M_\odot$ and 25 $M_\odot$ models is relatively modest at 9%. One other difference between the two models is that there is a small secondary peak in the 25 $M_\odot$ model luminosity spectrum for the ν_e and $\overline{\nu}_e$ neutrinos. In each case, the spike occurs 15 ms after core bounce and is caused by recollapse of material that in turn heats the ν_e and $\overline{\nu}_e$ neutrinospheres increasing the average energy and luminosity for those species.

The average energy spectra shown in Figure 5.9 generally resemble the early evolution of the curves shown in Figure 5.7 for the 15 $M_\odot$ model. One feature that is different in the 25 $M_\odot$ model is the spike in the "ν_μ" average energy at the time of core bounce. Bruenn *et al.* suggest that this feature is a numerical artifact and represents an unphysical energy increase. While this artifact was removed for the 15 $M_\odot$ model, it remains for the 25 $M_\odot$ model. However, relatively few "ν_μ" neutrinos exist at that time, so the overall effect is small. Another difference is that the average energies in the heavier progenitor model are higher than those in the lighter progenitor model.

5.3.6 Liebendörfer Model

Seeking to improve upon previous approaches which use approximations to the transport equations, Liebendörfer *et al.* [94] developed an exact three-flavour Boltzmann neutrino

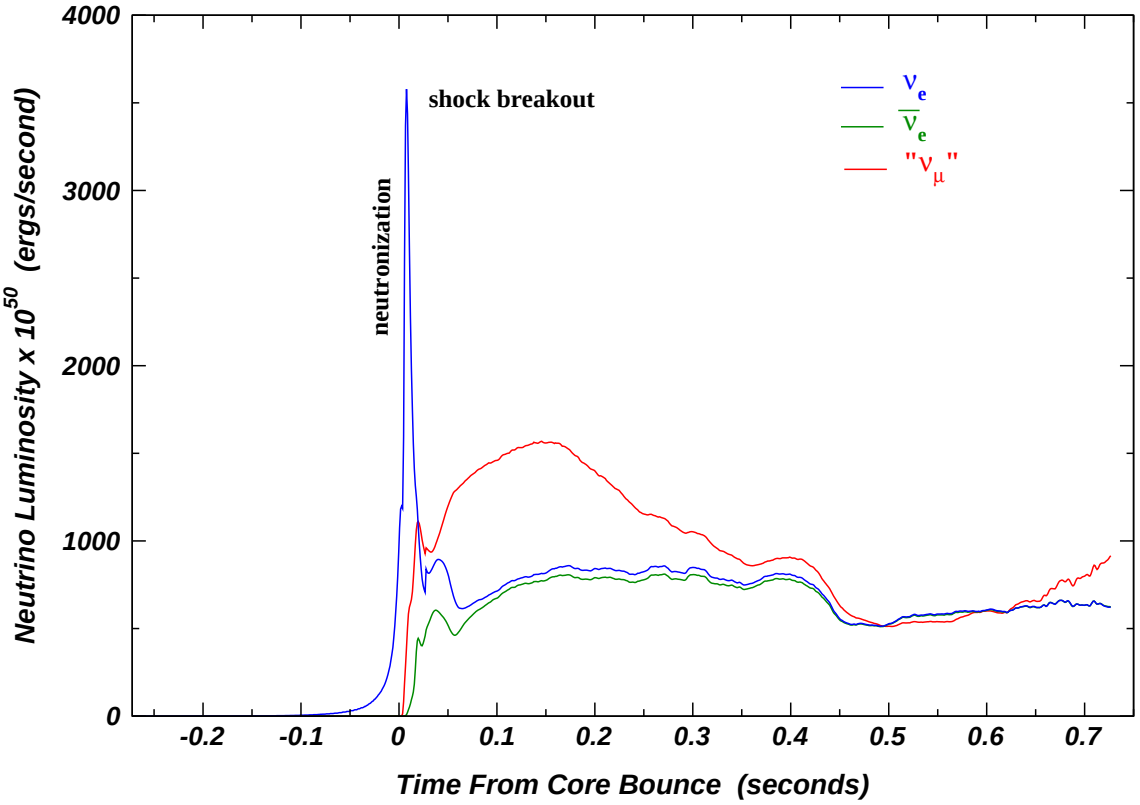

Figure 5.8: Supernova neutrino luminosity spectrum in the Bruenn 25 $M_\odot$ model [92]. The luminosity is truncated at 0.73 s after core bounce when a black hole forms.

transport program called AGILE-BOLTZTRAN. The effect of using a more accurate neutrino transport is to essentially increase the overall heating efficiency during the core collapse. As in the model of Bruenn *et al.*, general relativity is also included in all transport and hydrodynamics equations. While this approach is more rigorous, it did not yield a supernova explosion[4].

The results of this model are shown in Figures 5.10 and 5.11. The electron neutrino luminosity rises slowly during the initial period of collapse and infall, and decreases as the core reaches maximum density. It remains suppressed for another ~4 ms while the shock

[4]A. Mezzacappa originally reported evidence for a simulated supernova explosion at the Neutrino 2000 conference in Sudbury, ON. This was later found to be an artifact of the computer code.

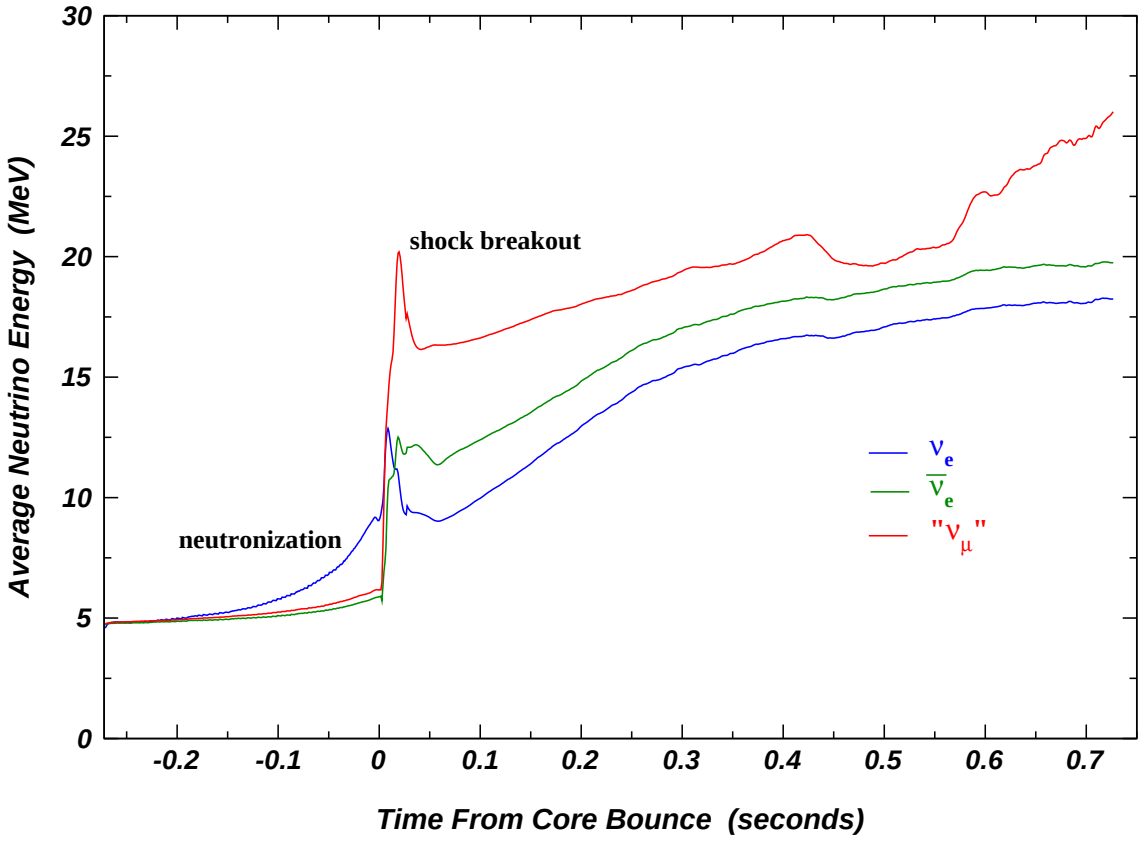

Figure 5.9: Supernova neutrino average energy spectrum using the Bruenn 25 $M_\odot$ model [92]. From the time of core bounce, the average energies for all neutrino species rise until the flux is completely cut off at 0.73 s and a black hole forms.

wave propagates to the electron neutrinosphere. At that point, the ν_e luminosity is greatly enhanced due to electron capture behind the shock front. Peak values for the ν_e luminosity reach 3.5×10^{53} ergs/s at the shock breakout. Generally, the luminosity curves for this 13 $M_\odot$ model agree quite well with those from the Bruenn 15 $M_\odot$ model over the same time range.

As with the previous four models, the well-established hierarchy of neutrino energies, in which the ν_e neutrinos have the lowest average energy and the "ν_μ" neutrinos have the highest average energy, also exists in this model. Figure 5.11 presents the average

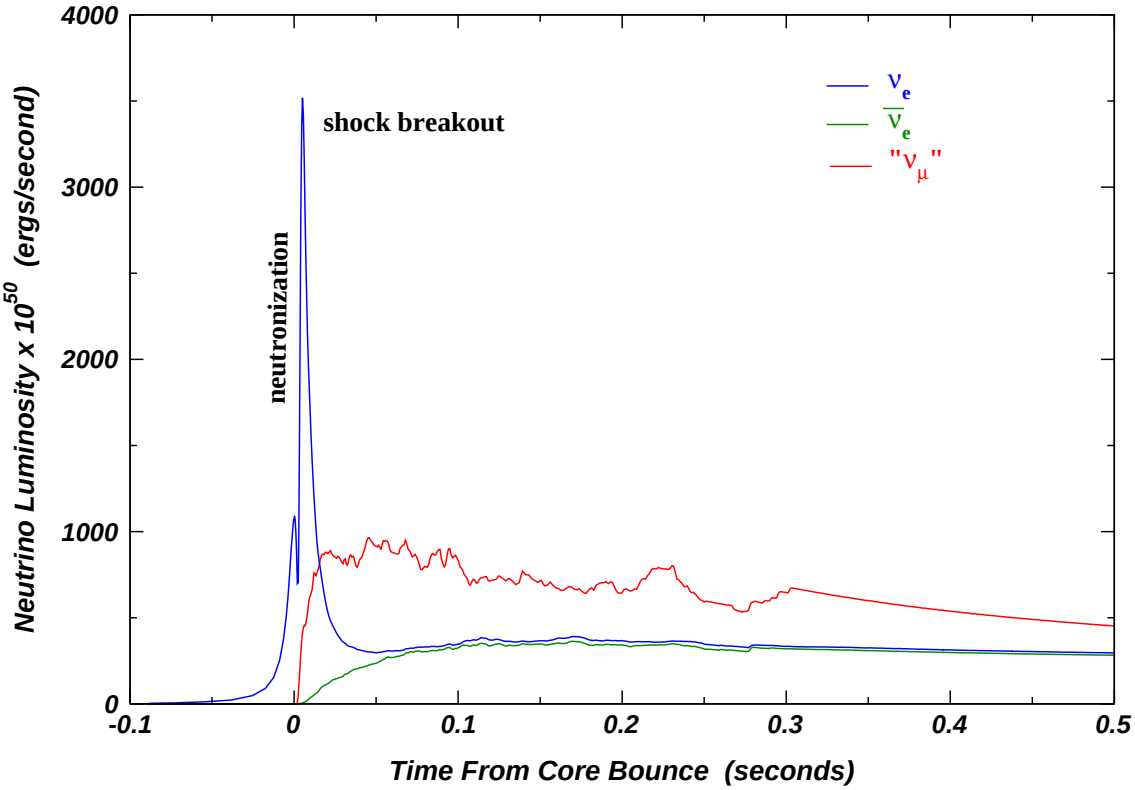

Figure 5.10: Supernova neutrino luminosity spectrum in the Liebendörfer 13 $M_\odot$ model [94]. The prompt peak due to electron capture in the neutronization phase is clearly visible. The calculation ends at 500 ms after core bounce. Note that the "ν_μ" luminosity is the sum of the ν_μ, $\overline{\nu}_\mu$, ν_τ and $\overline{\nu}_\tau$ contributions.

energy spectra for ν_e, $\overline{\nu}_e$ and "ν_μ" neutrinos. In many ways these curves are very similar to those found in the Bruenn 25 $M_\odot$ model and not the Bruenn 15 $M_\odot$ model, which is more comparable in size.

5.3.7 Supernova Model Summary

A general overview of the five models presented in the preceding sections points out a number of robust features. For a supernova explosion that does not result in a black hole, the neutrino signal is predicted to last for several tens of seconds. The formation of a

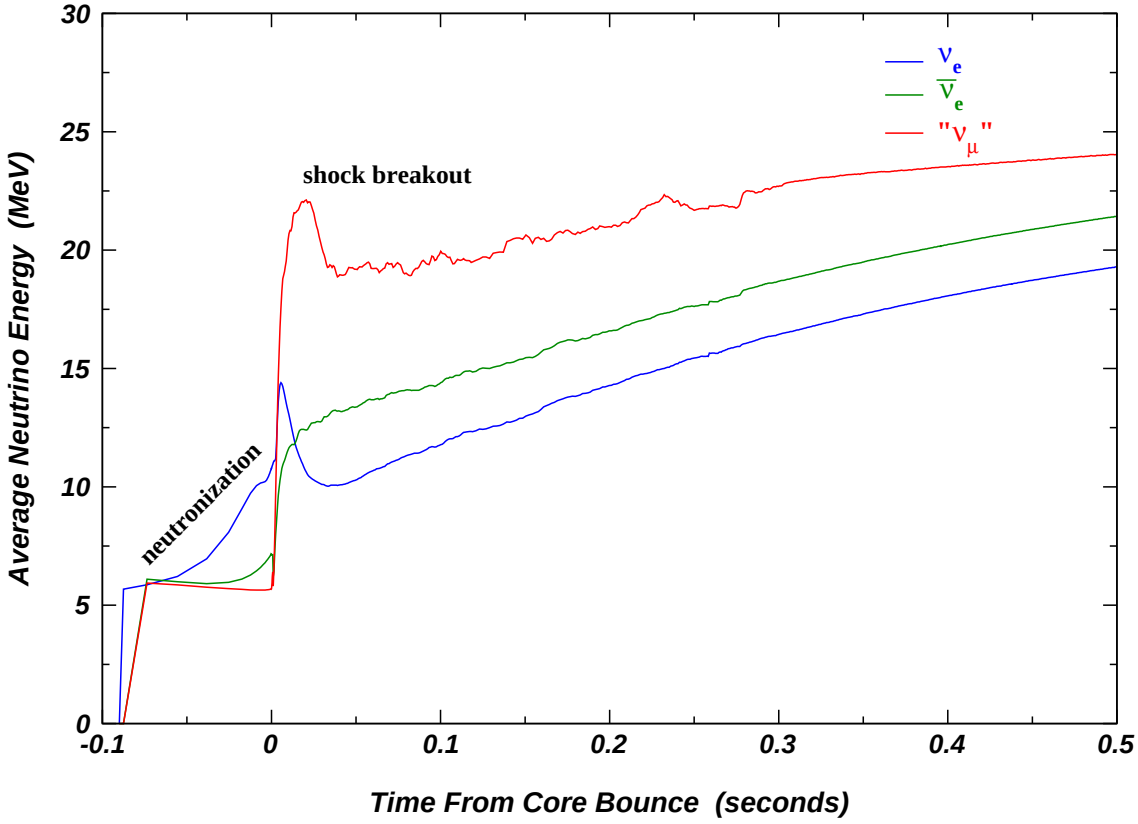

Figure 5.11: Supernova neutrino average energy spectrum using the Liebendörfer 13 $M_\odot$ model [94]. After the initial peak, the average energies for all neutrino species rise until until the calculation ends at 500 ms after core bounce.

black hole might limit the flux to only 1–2 seconds. According to the energy distributions specified in the two generic models, supernova neutrinos are expected to have energies in the range 0–100 MeV, with the largest fraction having energies below 50 MeV. Equivalent descriptions of the energy distribution are not available for the detailed model calculations.

As expected, the most universal feature that is present in all of the models reviewed is the hierarchy of neutrino energies. Electron neutrinos have the lowest energies, electron antineutrinos have slightly higher energies and muon and tau neutrino and antineutrinos have the highest energies. The exact ratios between these values may differ, but the order

SN Model Parameter	**Beacom Model**	**Burrows Model**	**Bruenn Models**		**Liebendörfer Model**
Progenitor Mass ($M_\odot$)	N/A	N/A	15	25	13
Burst Duration	full	full	limited	full	limited
L_{peak} ($\times 10^{53}$ ergs/s)	0.17	6.00	3.29	3.58	3.52
$E_{\nu,total}$ ($\times 10^{53}$ ergs)	3.00	2.90	1.14	1.70	0.68
ν_e fraction	16.7%	20.2%	27.7%	32.2%	29.5%
$\overline{\nu}_e$ fraction	16.7%	17.9%	25.6%	27.8%	21.9%
"ν_μ" fraction	66.7%	61.9%	46.7%	40.0%	48.6%
$N_{\nu,total}$ ($\times 10^{52}$)	1.56	2.21	0.77	1.05	0.38
ν_e fraction	29.0%	26.8%	36.0%	38.1%	37.6%
$\overline{\nu}_e$ fraction	20.3%	20.2%	26.4%	27.7%	22.7%
"ν_μ" fraction	50.7%	53.0%	37.5%	34.2%	39.8%
$\langle E_\nu \rangle$ (MeV)	19.2	13.1	14.8	16.2	17.8
$\langle E_{\nu_e} \rangle$	11.0	9.9	11.4	13.7	14.0
$\langle E_{\overline{\nu}_e} \rangle$	15.8	11.6	14.4	16.3	17.2
$\langle E_{\text{"}\nu_\mu\text{"}} \rangle$	25.2	15.4	18.5	18.9	21.8
Ratio (ν_e:$\overline{\nu}_e$:"ν_μ")	1:1.4:2.3	1:1.2:1.6	1:1.3:1.6	1:1.2:1.4	1:1.2:1.6
Comments	generic	generic with details	1-d GR ~trans	1-d GR ~trans	1-d GR exact trans

Table 5.2: Summary statistics for various supernova models.

is consistently the same. A second feature that appears in all of the models (with the exception of the Beacom and Vogel model) is the enhancement at the onset of the signal due to electron capture in the neutronization phase of collapse. It should be emphasized that the Beacom and Vogel model cannot be used to study features beyond the general time and energy properties of the supernova signal.

Of the models under consideration, the Beacom and Vogel model and the Burrows *et al.* model appear to represent the two extreme cases in supernova models. Comparing average energy values, it is evident that the Beacom and Vogel model uses higher values for all neutrino energies than is found in the Burrows *et al.* model. The largest difference

is in the $\left\langle E_{\text{“}\nu_\mu\text{”}} \right\rangle$ values, where the values from the two models are separated by nearly 10 MeV. Higher neutrino energies will lead to a corresponding higher number of counts in certain reaction channels. In some of the studies that follow, results from these two models will be used to indicate the range of possible values.

It is difficult to compare values from the generic models, which describe the full duration of the burst, to values from the detailed models because of the limited time over which the calculations for the detailed models are performed. For instance, the fraction of "ν_μ" neutrinos is considerably lower for the detailed calculations than for the two generic models. In the case of the Bruenn 25 $M_\odot$ model, this is due to the formation of a black hole. However, in the Bruenn 15 $M_\odot$ model and the Liebendörfer 13 $M_\odot$ model, the deficiency is due to the artificially short burst duration. For a full burst, the fraction of "ν_μ" neutrinos in these two models would be higher. The relevant parameters from the five models discussed in the preceding sections are summarized in Table 5.2.

For much of the discussion of the neutrino signal in Chapter 6 and for all of the subsequent analysis, only the two generic models are considered. These models reflect the robust characteristics established from the neutrino events recorded during SN1987A and also contain features predicted from current studies of the core collapse mechanism. As well, both generic models describe the full duration of the neutrino signal, making them more complete examples of potential supernovae. The general predictions offered by the Beacom and Vogel model and the Burrows model make them the most useful models for understanding the detection possibilities of the next galactic supernova.

5.4 SNO Supernova Neutrino Kinematics and Cross Sections

5.4.1 Introduction

In addition to having more available interactions with heavy water, the interaction cross sections are also higher compared to light water. In the sections that follow, kinematics and cross sections for the main supernova neutrino interactions are presented in some detail. These interactions are grouped into three categories based on the interaction type: charged current, neutral current and elastic scattering.

5.4.2 Charged Current

Recall from discussions in Section 4.3 that only ν_e and $\overline{\nu}_e$ neutrinos participate in charged current reactions. Isolating the ν_e component of the supernova signal is especially important when trying to identify the prompt neutronization peak in the supernova burst. In addition to having higher interaction cross sections than the other interaction types, charged current reactions involving the electron neutrino will give SNO a unique measurement of the neutronization contribution to the supernova signal.

5.4.2.1 $\overline{\nu}_e + p \rightarrow n + e^+$ Reaction

A discussion of the kinematics for this reaction begins with the total positron energy E_e. In the laboratory reference frame, E_e can be expressed as:

$$E_e = E_\nu + \frac{q^2}{2m_p} + \frac{m_p^2 - m_n^2}{2m_p}, \tag{5.17}$$

where $q^2 = (p_\nu - p_e)^2$ is the four-momentum transfer, m_n is the neutron mass and m_p is the proton mass. The range of positron energies allowed by kinematics is obtained by solving the following quadratic equation:

$$0 \;=\; \left\{[2(E_\nu + m_p)]^2 - 4E_\nu^2\right\} E_e^2$$

$$+4(E_\nu + m_p)(m_n^2 - m_p^2 - m_e^2 - 2m_p E_\nu)E_e$$
$$+(m_n^2 - m_p^2 - m_e^2 - 2m_p E_\nu)^2 + (2E_\nu m_e)^2. \quad (5.18)$$

The laboratory angle of the positron with respect to the incoming neutrino direction is given by:

$$\cos\theta_e = \frac{m_n^2 - m_p^2 - 2m_p(E_\nu - E_e) + 2E_\nu E_e - m_e^2}{2E_\nu\sqrt{E_e^2 - m_e^2}} \quad (5.19)$$

In a recent study [71], Vogel and Beacom investigate this reaction and recommend using the Llewellyn Smith cross section formalism [95] in conjunction with modifications they calculate that provide weak magnetism and recoil corrections to order $\mathcal{O}\ (1/M)$, where $M = (m_n + m_p)/2$ is the nucleon mass. The resulting differential cross section is somewhat reduced, and the formula with corrections is given by:

$$\frac{d\sigma}{d|q^2|} = \frac{\sigma_0^{\overline{\nu}p}}{E_\nu^2}\left[A(q^2) + B(q^2)\frac{(s-u)}{M^2} + \frac{C(q^2)(s-u)^2 - C(q^2)4M^2(m_n - m_p)^2}{M^4}\right], \quad (5.20)$$

where the terms $A(q^2), B(q^2)$ and $C(q^2)$ represent the following expressions:

$$\begin{aligned} A(q^2) &= \frac{(m_e^2 - q^2)}{4M^2}\left[\left(4 - \frac{q^2}{M^2}\right)|F_A|^2 - \left(4 + \frac{q^2}{M^2}\right)\left|F_V^1\right|^2\right. \\ &\quad - \frac{q^2}{M^2}\left|\xi F_V^2\right|^2\left(1 + \frac{q^2}{M^2}\right) - \frac{4q^2 F_V^1 \xi F_V^2}{M^2} \\ &\quad \left. - \frac{m_e^2}{M^2}\left(\left|F_V^1 + \xi F_V^2\right|^2 + |F_A|^2\right)\right] \quad (5.21) \\ B(q^2) &= -\frac{q^2}{M^2}F_A(F_V^1 + \xi F_V^2) \quad (5.22) \\ C(q^2) &= \frac{1}{4}\left(|F_A|^2 + \left|F_V^1\right|^2 - \frac{q^2}{M^2}\left|\frac{\xi F_V^2}{2}\right|^2\right). \quad (5.23) \end{aligned}$$

The form factors used in Equations 5.21, 5.22, 5.23 are assumed to be real in all cases and are given as follows:

$$\begin{aligned} F_V^1(q^2) &= \left(1 - \frac{q^2}{4M^2}\right)^{-1}\left[G_E^V(q^2) - \frac{q^2}{4M^2}G_M^V(q^2)\right] \quad (5.24) \\ \xi F_V^2(q^2) &= \left(1 - \frac{q^2}{4M^2}\right)^{-1}\left[G_M^V(q^2) - G_E^V(q^2)\right] \quad (5.25) \end{aligned}$$

$$F_A(q^2) = -1.26\left(1 - \frac{q^2}{(1032\ \text{MeV})^2}\right)^{-2}, \tag{5.26}$$

and

$$G_E^V(q^2) = \left(1 - \frac{q^2}{(840\ \text{MeV})^2}\right)^{-2} \tag{5.27}$$

$$G_M^V(q^2) = (1+\xi)G_E^V. \tag{5.28}$$

Updated constants used by Llewellyn Smith in Equations 5.24, 5.25, 5.26, 5.27 and 5.28 are provided by Ahrens *et al.* [96]. In Equation 5.20, $s = (p_\nu + p_p)^2$ and $u = (p_\nu - p_n)^2$ are Mandelstam variables and the expression $(s-u)$ is given by:

$$(s-u) = 4m_p E_\nu + q^2 - m_e^2 - m_n^2 + m_p^2 \tag{5.29}$$

and $\sigma_0^{\overline{\nu}p}$ is the normalizing constant defined explicitly as:

$$\begin{aligned}\sigma_0^{\overline{\nu}p} &= \frac{M^2\cos^2\theta_C}{8\pi}\left[\frac{G_F}{(\hbar c)^3}\right]^2 (\hbar c)^2(1+\Delta^R_{\text{inner}}) \\ &= 1.805\times 10^{-39}\ \text{cm}^2,\end{aligned} \tag{5.30}$$

where G_F is the weak coupling constant, θ_C is the Cabibbo angle and $\Delta^R_{\text{inner}} = 0.024$ is the energy independent inner radiative correction factor.

5.4.2.2 $\nu_e + d$ Reactions

Discrete double differential cross section values, $d^2N/dE\,d\cos\theta$, for both the $\nu_e + d$ and $\overline{\nu}_e + d$ interactions are obtained from tables provided by Kubodera and Nozawa [97].

For the $\nu_e + d \rightarrow p + p + e^-$ reaction, only the electron is of interest. The electron kinetic energy, T_e, is constrained by

$$T_{e,max} = E_\nu - E_{thres}, \tag{5.31}$$

where E_{thres} is the energy threshold for the reaction. Electron kinetic energy and angular distribution quantities are chosen according to the differential cross section values.

In the case of the $\overline{\nu}_e + d \rightarrow n + n + e^+$ reaction, all three final state particles can be identified in the SNO detector. The positron energy is determined as above using the differential cross section, and properties of the two neutrons are determined by considering a di-neutron system [98]. In the lab frame, the momentum of the di-neutron system, $p_{2n,lab}$ is determined using conservation of momentum:

$$p_{2n,lab} = \sqrt{E_\nu^2 + p_e^2 - 2E_\nu p_e \cos\theta_e}, \tag{5.32}$$

where p_e is the momentum of the positron ($p_e = \sqrt{E_\nu^2 - m_e^2}$) and θ_e is the angle of the positron relative to the incoming neutrino direction. The mass of the di-neutron system is given by conservation of energy:

$$m_{2n} = \sqrt{E_{2n}^2 - p_{2n}^2}. \tag{5.33}$$

The di-neutron system then decays into two neutrons, n_1 and n_2. In the centre-of-mass (CM) frame, the momentum of n_1 is expressed as:

$$p_{n_1,cm} = 0.5\sqrt{m_{2n}^2 - 2m_n^2}, \tag{5.34}$$

where m_n is the mass of the neutron. The corresponding neutron energy in the CM frame is:

$$E_{n_1,cm} = \sqrt{p_{n_1,cm}^2 + m_n^2}. \tag{5.35}$$

Returning to the lab frame by using the Lorentz transformation along the z-direction, the energy for n_1 is given by:

$$E_{n_1,lab} = \gamma\left(E_{n_1,cm} + \beta p_{n_1,cm,z}\right) \tag{5.36}$$

and the z-component of the neutron momentum is expressed as:

$$p_{n_1,lab,z} = \gamma\left(p_{n_1,cm,z} + \beta E_{n_1,cm}\right), \tag{5.37}$$

where $p_{n_1,cm,z}$ is the z-component of the neutron CM momentum, β is the speed of the di-neutron system and $\gamma = 1/\sqrt{1-\beta^2}$. The angle θ_{n_1} of the neutron with respect to the incident neutrino direction is given as:

$$\cos\theta_{n_1} = \frac{p_{n_1,lab,z}}{E_{n_1}^2 - m_n^2}. \tag{5.38}$$

Having solved for the parameters describing the first neutron, the corresponding quantities for the second neutron are obtained in a straightforward manner using conservation of energy and momentum. The lab energy of the second neutron is given by:

$$E_{n_2} = E_\nu + m_d - E_e - E_{n_1}, \tag{5.39}$$

where m_d is the mass of the deuteron. Finally, the direction of the second neutron is determined by considering the components of $\vec{p}_{n_2}/p_{n_2}$ obtained using

$$\vec{p}_{n_2} = E_\nu \frac{\vec{p}_\nu}{p_\nu} - p_e \frac{\vec{p}_e}{p_e} - p_{n_1} \frac{\vec{p}_{n_1}}{p_{n_1}} \tag{5.40}$$

where $\vec{p}$ is the three-component momentum vector and p is the magnitude of the momentum vector.

5.4.2.3 ν_e + O Reactions

Theorists doing calculations for the charged current interactions involving oxygen combine the contributions from all naturally occurring isotopes of oxygen into one result. Henceforth, these reactions are referred to as ν_e + O reactions to indicate that all relevant isotopes are included in the treatment. For the SNO supernova generator, cross section values were obtained from two sources. For neutrino energies $E_\nu \leq 60$ MeV the values published by Haxton [99] were used, while for higher energy neutrinos, values published by Kuramoto *et al.* [72] were used, as recommended by Kuramoto *et al.*

5.4.3 Neutral Current

5.4.3.1 $\nu_x + d$ Reactions

Double differential cross section values for the $\nu_x + d \rightarrow \nu_x + p + n$ interactions are obtained from tables provided by Kubodera and Nozawa [97].

In all cases, only the neutron is detected in the final state. The maximum momentum of the neutron in the CM frame is given by [100]

$$p_{n,cm,max} = \frac{\sqrt{(s-(m_p+m_n)^2)(s-\Delta m_{np}^2)}}{2\sqrt{s}}, \tag{5.41}$$

where $s = m_d^2 + 2E_\nu m_d$, m_p is the mass of the proton, m_n is the mass of the neutron and Δm_{np} is the mass difference between the neutron and proton. The maximum total energy of the neutron in the CM frame is

$$E_{n,cm,max} = \sqrt{p_{n,cm,max}^2 + m_n^2}, \tag{5.42}$$

which corresponds to a maximum neutron lab energy of

$$E_{n,max} = \gamma \left(E_{n,cm,max} + \beta p_{n,cm,max} \right), \tag{5.43}$$

where $\beta = E_\nu/(E_\nu + m_d)$. A 5% correction factor is applied to the neutron kinetic energy to account for nucleon motion. The neutron energy and direction are then chosen according to the differential cross section values.

5.4.3.2 $\nu_{\mu,\tau}+ {}^{16}$O Reactions

In order to calculate the number of neutrinos that participate in these reaction, the cross section parameterization suggested by Beacom and Vogel [101] was used in conjunction with branching ratios calculated by Langanke *et al.* [73]. The gamma rays produced in the final state of Equations 4.17 and 4.18 have energies in the range $\approx$ 5–10 MeV [73], which is sufficiently high to register as an event in the SNO detector. However, final state energy and direction distributions for these reactions are not currently available[5].

[5] E. Kolbe has been contacted concerning these calculations.

Because of their high energy thresholds, these reactions also serve as a sensitive gauge of neutrino temperatures. Few events produced via these reactions would suggest relatively low "ν_μ" average energies, while on the other hand, a large number of events would would suggest relatively high "ν_μ" average energies.

5.4.4 Elastic Scattering

The differential cross section for producing a recoil electron with kinetic energy T_e by elastic scattering with a neutrino of initial energy, E_ν is given by [102]:

$$\frac{d\sigma}{dT_e} = \sigma_0^{\nu e}\left[g_L^2 + g_R^2\left(1 - \frac{T_e}{E_\nu}\right)^2 - g_L g_R m_e \frac{T_e}{E_\nu^2}\right], \tag{5.44}$$

where m_e is the electron mass and g_L and g_R are the electron chiral coupling constants to the weak neutral current [103]:

$$g_L = +0.5 + \sin^2\theta_W, \quad g_R = \sin^2\theta_W \qquad \text{for } \nu_e \tag{5.45}$$

$$g_L = \sin^2\theta_W, \qquad g_R = +0.5 + \sin^2\theta_W \quad \text{for } \overline{\nu}_e \tag{5.46}$$

$$g_L = -0.5 + \sin^2\theta_W, \quad g_R = \sin^2\theta_W \qquad \text{for } \nu_{\mu,\tau} \tag{5.47}$$

$$g_L = \sin^2\theta_W, \qquad g_R = -0.5 + \sin^2\theta_W \quad \text{for } \overline{\nu}_{\mu,\tau} \tag{5.48}$$

and $\sigma_0^{\nu e}$ is explicitly given as:

$$\begin{aligned} \sigma_0^{\nu e} &= \frac{2m_e^2}{\pi}\left[\frac{G_F}{(\hbar c)^3}\right]^2 (\hbar c)^2 \\ &= 8.806 \times 10^{-45}\,\mathrm{cm}^2, \end{aligned} \tag{5.49}$$

where G_F is the Fermi coupling constant. The values for all constants used in the elastic scattering formalism were obtained from the Particle Data Group [5]. Inspection of the differential cross section given in Equation 5.44 shows that the probability for elastic scattering is highest for events with low recoil electron kinetic energy.

The angle θ_e, between the direction of the recoil electron and the incoming neutrino is given by:

$$\cos\theta_e = \frac{E_\nu + m_e}{E_\nu}\sqrt{\frac{T_e}{(T_e + 2m_e)}}. \tag{5.50}$$

Expressed in terms of $\cos\theta_e$, the differential cross section becomes:

$$\frac{d\sigma}{d\cos\theta_e} = \frac{4(E_\nu + m_e)^2 E_\nu^2 \cos\theta_e}{\left[(E_\nu + m_e)^2 - E_\nu^2\cos^2\theta_e\right]^2}\left(\frac{d\sigma}{dT_e}\right)_{T_e(\cos\theta_e)}, \tag{5.51}$$

where $T_e(\cos\theta_e)$ is given by:

$$T_e(\cos\theta_e) = \frac{2m_e E_\nu^2\cos^2\theta_e}{(E_\nu + m_e)^2 - E_\nu^2\cos^2\theta_e}. \tag{5.52}$$

Using Equations 5.44, 5.51 and 5.52 the spectrum averaged angular distribution of the recoil electrons can be calculated by making use of:

$$P(\cos\theta_e) = \left\langle\frac{d\sigma}{d\cos\theta_e}\right\rangle = \int_0^{E_{\nu,max}} dE_\nu\, f(E_\nu, t_i)\left(\frac{d\sigma}{d\cos\theta_e}\right)_{T_e \geq T_{min}}, \tag{5.53}$$

where for supernova neutrinos $f(E_\nu, t_i)$ is taken as the normalized Fermi-Dirac spectrum. In order to simplify the integration over neutrino emission time, the time-independent energy spectra proposed by Beacom and Vogel (see Equation 5.6) is used for the calculations below. Figure 5.12 shows the fraction of cumulative probability for an electron to be scattered to any angle less than or equal to θ_e for a series of T_{min} values 0, 1.8, 3.8 and 7.7 MeV. As T_{min} approaches the maximum value allowed by energy conservation, more of the recoil electrons are scattered in the forward direction. Since the neutrinos emitted during a supernova explosion have higher average energies than their solar counterparts, the elastic scattering angular distribution for supernova neutrinos is expected to be even more forward peaked than for neutrinos originating from the Sun. Figure 5.12 also shows that at the SNO detector hardware threshold of NHIT = 16 PMTs (T_e = 1.8 MeV), there is very little difference between the total width of the distribution (fraction = 1) for ν_e, $\overline{\nu}_e$, $\nu_{\mu,\tau}$ and $\overline{\nu}_{\mu,\tau}$ neutrinos. In fact, at this energy threshold, the recoil electrons from all elastic

scattering reactions are expected to fall within 35°. Considering only 0.8 of the cumulative probability at the hardware energy threshold, "ν_μ" neutrinos have the most forward peaked distribution of the four neutrino classes distinguished in the cross section formalism. At the same energy, $\overline{\nu}_e$ neutrinos have the broadest angular distribution. As the energy threshold increases, ν_e neutrinos become the most forward peaked, whereas "ν_μ" neutrinos have the broadest peak.

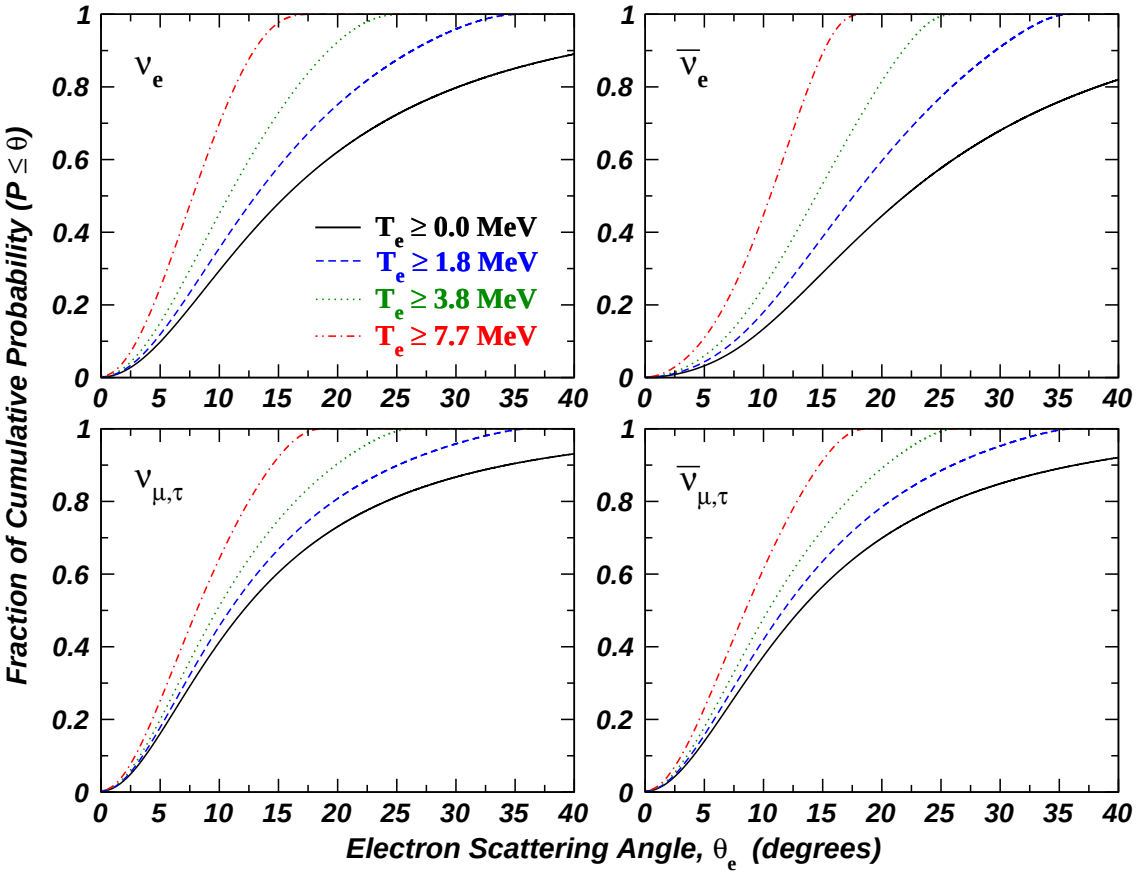

Figure 5.12: Elastic scattering recoil electron angular distribution for ν_e, $\overline{\nu}_e$, $\nu_{\mu,\tau}$ and $\overline{\nu}_{\mu,\tau}$ supernova neutrinos using energy spectrum of Beacom and Vogel. Shown is the fraction of cumulative probability for a recoil electron to be scattered to any angle less than or equal to θ_e. Distributions from four different electron energy thresholds are presented for each neutrino species showing that higher cuts on electron energy produce a more forward peaked distribution.

The expression for the total cross section is obtained by integrating Equation 5.44 from the detector energy threshold T_{min} to the maximum electron kinetic energy T_{max} allowed by energy and momentum conservation:

$$\begin{aligned}\sigma(E_\nu) &= \frac{\sigma_0^{\nu e}}{m_e}\left[(g_L^2+g_R^2)(T_{max}-T_{min}) - \left(\frac{g_R^2}{E_\nu}+\frac{g_L g_R m_e}{2E_\nu^2}\right)(T_{max}^2-T_{min}^2)\right. \\ &\quad \left. + \frac{g_R^2}{3E_\nu^2}(T_{max}^3-T_{min}^3)\right], \end{aligned} \tag{5.54}$$

where T_{max} is expressed as:

$$T_{max}(E_\nu) = \frac{2E_\nu^2}{2E_\nu + m_e}. \tag{5.55}$$

5.4.5 Interaction Summary

According to the supernova models considered in Section 5.3, most of the neutrinos interacting in the detector volume will have energies below 50 MeV. Since the charged current reactions have the highest cross section in this energy domain, they will contribute the highest number of interactions to the overall neutrino count total. Having the highest charged-current cross section, the $\overline{\nu}_e + p \rightarrow n + e^+$ reaction will play a dominant role. The main neutrino interaction cross sections are summarized in Figure 5.13.

Depending on the neutrino energy distributions, reactions involving oxygen may also play an important role. For the most part, these reactions have high energy thresholds (see Sections 5.4.2.3 and 5.4.3.2), which means that only high energy neutrinos are able to participate in these channels. Since different supernova models predict different neutrino energy distributions, these reactions will be more important in models that have higher neutrino energies. Figure 5.14 shows the interaction cross sections for the main reactions involving oxygen. As with the previous set of cross sections, the charged current reactions have the highest cross sections.

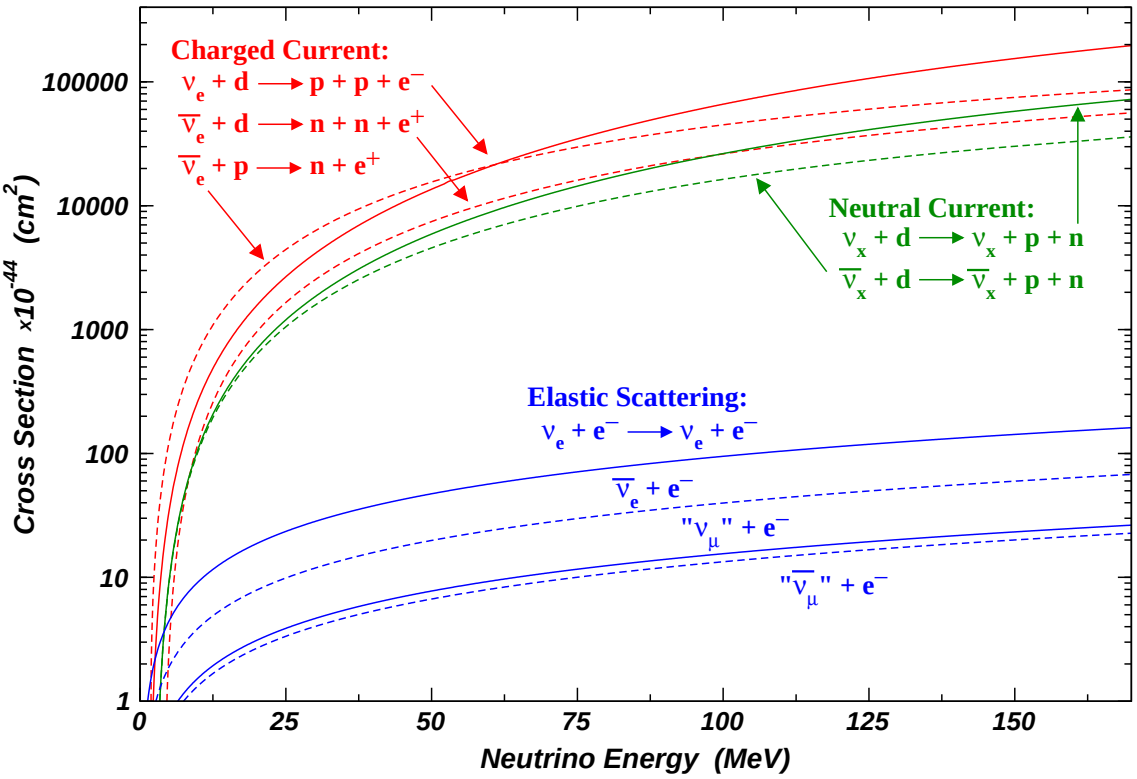

Figure 5.13: Cross sections for the main supernova neutrino interactions in the SNO detector. For the neutral current reactions, ν_x stands for all active neutrino flavours. Since the $\overline{\nu}_e + p \rightarrow n + e^+$ reaction has the highest cross section at energies below 50 MeV, and because there are a high relative number of targets available for this reaction, it will contribute the highest number of interactions.

5.5 SNO Targets

One final ingredient to consider is the number of target particles available to the interactions discussed above. Doe *et al.* [104] have made a careful study of the mass of the D_2O target in the SNO detector, and their values are used for the studies that follow. The number of targets related to the number of H_2O molecules is calculated assuming 1700 tonnes of light water between the face of the PMTs and the outer radius of the acrylic vessel. Table 5.3 summarizes the number of targets for each reaction being considered. Even

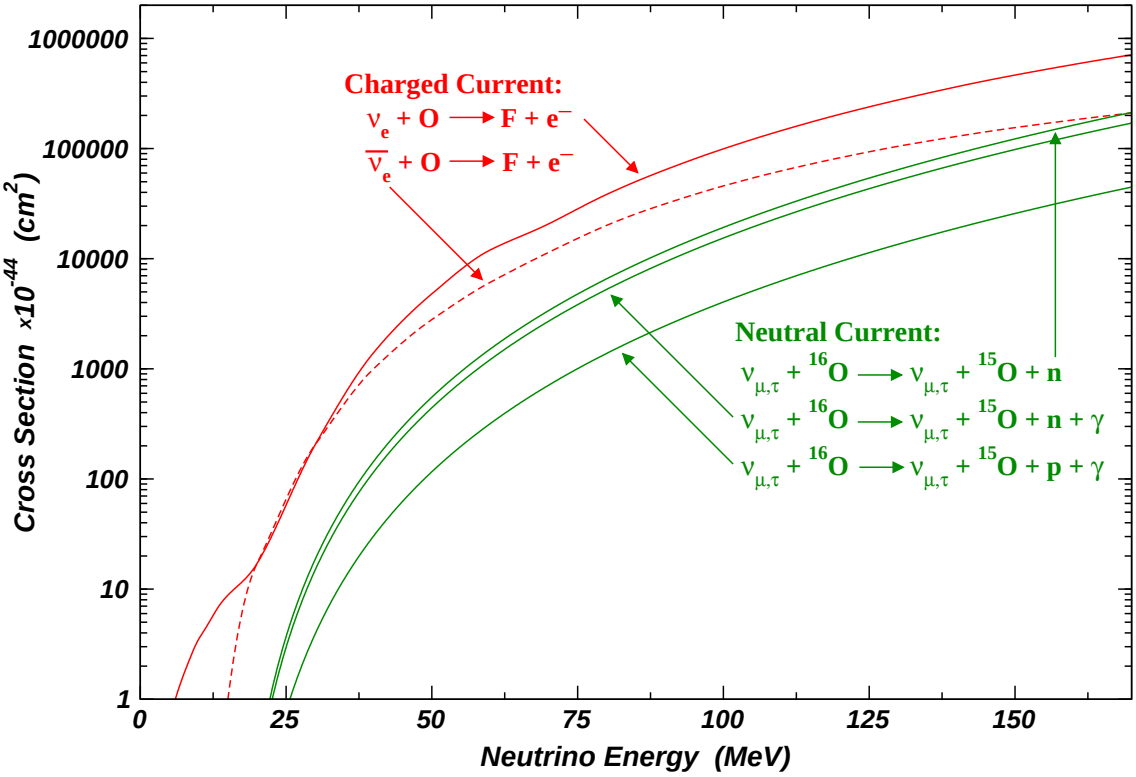

Figure 5.14: Cross sections for supernova neutrino interactions involving oxygen in the SNO detector. At low energies, the $\nu_e + \mathrm{O} \rightarrow \mathrm{F} + e^-$ cross section is enhanced by contributions from isotopes ^{17}O and ^{18}O. The slight depression in the $\nu_e + \mathrm{O} \rightarrow \mathrm{F} + e^-$ cross section at 70 MeV is the result of joining together cross section data from two different authors. The neutral current cross sections for $\overline{\nu}_{\mu,\tau}$ neutrinos are essentially identical to the ones shown for $\nu_{\mu,\tau}$ neutrinos and are not shown.

though the elastic scattering reactions have the highest number of target particles, the low cross section means that the total number of events from these channels will still be comparatively low.

Reaction	**Region**	**Number of Targets ($\times 10^{31}$)**	**Relative Number of Targets**
Charged Current:			
$\overline{\nu}_e + p \rightarrow n + e^+$	H_2O	11.3655	3.783
$\nu_e + d \rightarrow p + p + e^-$	D_2O	6.0086	2.000
$\overline{\nu}_e + d \rightarrow n + n + e^+$	D_2O	6.0086	2.000
$\nu_e + O \rightarrow F + e^-$	D_2O	3.0043	1.000
$\overline{\nu}_e + O \rightarrow N + e^+$	D_2O	3.0043	1.000
$\nu_e + O \rightarrow F + e^-$	H_2O	5.6827	1.892
$\overline{\nu}_e + O \rightarrow N + e^+$	H_2O	5.6827	1.892
Neutral Current:			
$\nu_e + d \rightarrow \nu_e + p + n$	D_2O	6.0086	2.000
$\overline{\nu}_e + d \rightarrow \overline{\nu}_e + p + n$	D_2O	6.0086	2.000
$\nu_{\mu,\tau} + d \rightarrow \nu_{\mu,\tau} + p + n$	D_2O	6.0086	2.000
$\overline{\nu}_{\mu,\tau} + d \rightarrow \overline{\nu}_{\mu,\tau} + p + n$	D_2O	6.0086	2.000
$\nu_{\mu,\tau} + {}^{16}O \rightarrow \nu_{\mu,\tau} + {}^{15}O + n + \gamma$	D_2O	3.0043	1.000
$\overline{\nu}_{\mu,\tau} + {}^{16}O \rightarrow \overline{\nu}_{\mu,\tau} + {}^{15}O + n + \gamma$	D_2O	3.0043	1.000
$\nu_{\mu,\tau} + {}^{16}O \rightarrow \nu_{\mu,\tau} + {}^{15}N + p + \gamma$	D_2O	3.0043	1.000
$\overline{\nu}_{\mu,\tau} + {}^{16}O \rightarrow \overline{\nu}_{\mu,\tau} + {}^{15}N + p + \gamma$	D_2O	3.0043	1.000
$\nu_{\mu,\tau} + {}^{16}O \rightarrow \nu_{\mu,\tau} + {}^{15}O + n$	D_2O	3.0043	1.000
$\overline{\nu}_{\mu,\tau} + {}^{16}O \rightarrow \overline{\nu}_{\mu,\tau} + {}^{15}O + n$	D_2O	3.0043	1.000
$\nu_{\mu,\tau} + {}^{16}O \rightarrow \nu_{\mu,\tau} + {}^{15}O + n + \gamma$	H_2O	5.6827	1.892
$\overline{\nu}_{\mu,\tau} + {}^{16}O \rightarrow \overline{\nu}_{\mu,\tau} + {}^{15}O + n + \gamma$	H_2O	5.6827	1.892
$\nu_{\mu,\tau} + {}^{16}O \rightarrow \nu_{\mu,\tau} + {}^{15}N + p + \gamma$	H_2O	5.6827	1.892
$\overline{\nu}_{\mu,\tau} + {}^{16}O \rightarrow \overline{\nu}_{\mu,\tau} + {}^{15}N + p + \gamma$	H_2O	5.6827	1.892
Elastic Scattering:			
$\nu_e + e^- \rightarrow \nu_e + e^-$	D_2O	30.1730	10.043
$\overline{\nu}_e + e^- \rightarrow \overline{\nu}_e + e^-$	D_2O	30.1730	10.043
$\nu_{\mu,\tau} + e^- \rightarrow \nu_{\mu,\tau} + e^-$	D_2O	30.1730	10.043
$\overline{\nu}_{\mu,\tau} + e^- \rightarrow \overline{\nu}_{\mu,\tau} + e^-$	D_2O	30.1730	10.043
$\nu_e + e^- \rightarrow \nu_e + e^-$	H_2O	56.8275	18.915
$\overline{\nu}_e + e^- \rightarrow \overline{\nu}_e + e^-$	H_2O	56.8275	18.915
$\nu_{\mu,\tau} + e^- \rightarrow \nu_{\mu,\tau} + e^-$	H_2O	56.8275	18.915
$\overline{\nu}_{\mu,\tau} + e^- \rightarrow \overline{\nu}_{\mu,\tau} + e^-$	H_2O	56.8275	18.915

Table 5.3: Number of interaction targets in the SNO detector for the various supernova neutrino reactions.

5.6 Event Sampling

Once the supernova neutrino events are determined for each reaction, specific neutrino events are produced by sampling the neutrino flux distribution at the detector according to Equation 5.11. The "acceptance-rejection method" [5] for sampling requires that independent random detection time, t_{ran}, and neutrino energy, $E_{\nu,ran}$, values are used to pick a corresponding neutrino flux at the detector, $P(t_{ran}, E_{\nu,ran}) = d^2N/dtdE_\nu(t_{ran}, E_{\nu,ran})$. The event is chosen if the neutrino flux, $P(t_{ran}, E_{\nu,ran})$, calculated using the random time and energy is less than a detector flux value, P_{ran}, chosen from a comparison distribution function. For these studies, the comparison function was taken to be a flat probability distribution function defined by the maximum and minimum $d^2N/dtdE_\nu(t, E_\nu)$ values. In this way, the boundary of the distribution is preserved by using $d^2N/dtdE_\nu(t_{ran}, E_{\nu,ran})$, and the probability of choosing a particular (t, E_ν) pair depends on the area under the curve. Therefore, every neutrino event consists of independently chosen detection time and neutrino energy values that are consistent with the $d^2N/dtdE_\nu$ distribution. With this neutrino information, detectable final state particles are sampled according to their differential cross sections. Each final state particle event consists of an interaction time, the total energy of the particle and a set of direction cosines that describe the direction of the particle in the detector coordinate system. The particles are then propagated in the detector volume using the SNO Monte Carlo and Analysis software package.

5.7 SNO Monte Carlo Settings

The previous sections describe in detail the parameters and calculations performed by the SNO supernova generator. In the last stage of the simulation, results from the generator are provided to the SNO Monte Carlo and Analysis software package (SNOMAN) that fully describes the detector geometry and response. For each final state particle, the interaction

Detector Characteristic	**SNOMAN Setting**	**Comment**
Čerenkov Light Generation:		
low wavelength cutoff	200 nm	
high wavelength cutoff	720 nm	
Čerenkov factor	0.35	individual PMT efficiency
PMT:		
PMT Model	3d PMT	full 3d model of PMT
PMT efficiency	0.561	PMT array efficiency
PMT noise rate	568 Hz	
Water Specs:		
H_2O fraction in D_2O	0.000824	
^{17}O fraction in D_2O	0.000487	neutron capture without γ cascade

Table 5.4: Detector characteristics specified in the supernova neutrino Monte Carlo simulations.

time, the total energy of the particle (kinetic energy for neutrons) and a set of direction cosines that describe the direction of the particle in the detector coordinate system are provided. The event position are distributed randomly in the relevant detector volumes. SNOMAN version 4.0186 is used for all Monte Carlo analysis. Characteristics of the SNO detector that are specified in the simulation are summarized in Table 5.4.

Chapter 6

SNO Supernova Neutrino Signal

6.1 Introduction

In order to study signals in the SNO detector from the possible supernova models suggested in the literature, a set of FORTRAN routines has been written to implement the supernova signal formalism discussed in Chapter 5. Collectively these routines are called the SNO supernova generator. The supernova generator is used to calculate properties of neutrinos that interact in the SNO detector and the resulting final state particles. Once the final state particles are created, the main SNO Monte Carlo package called SNOMAN is used to correctly describe subsequent scattering and assign the correct detector geometry and collection efficiencies. Results from the SNO supernova generator and the SNOMAN Monte Carlo are presented and discussed in the sections below.

6.2 SNO Supernova Neutrino Interactions

The first stage of the supernova signal analysis involves considering the number of neutrino interactions calculated using the SNO supernova generator for the possible reactions in the SNO detector. Since this analysis concerns the number of interactions and not the final detection signal, only the energy threshold associated with a given interaction is imposed at this point. Application of the SNO detection and analysis energy threshold is treated at a later stage. A detailed account of the number of neutrino interactions resulting from each of the five supernova models discussed in Chapter 5 is presented in this section. Where

possible, comparisons between the SNO supernova generator and results published by the authors of the various models are made. Results for the most generic models are presented first, followed by the more detailed models.

6.2.1 Beacom and Vogel Model

To compute the total number of counts for each reaction in the SNO detector using the Beacom and Vogel model, Equation 5.12 is used in conjunction with the model parameters outlined in Section 5.3.3. The limits of integration are chosen such that the total energy radiated as neutrinos is in agreement with the total model input energy. In the case of the Beacom and Vogel model, time is integrated from 0 s to 20 s in steps of 5 ms, and energy is integrated from 0.1 MeV to 170 MeV in steps of 0.1 MeV.

Before a detector energy threshold is applied, ~1200 neutrinos are expected to interact in the SNO detector for a supernova at 10 kpc according to the Beacom and Vogel model. The largest contribution for a single reaction channel is from the $\overline{\nu}_e + p \rightarrow n + e^+$ reaction due to the high cross section and large number of target molecules. Of the total supernova signal, 49.3% of the neutrinos interact via charged current interactions, 47.1% via neutral current interactions and 3.6% through elastic scattering interactions. The majority of neutrinos interact in the D_2O volume, namely 58.6%, while 41.4% of neutrinos are present in the H_2O volume. Of the neutrinos interacting in the light water region, the $\overline{\nu}_e + p \rightarrow n + e^+$ reaction constitutes almost the entire signal at 84.8%. 11.5% of the supernova neutrinos interacting in the SNO detector are ν_e neutrinos, 47.5% are $\overline{\nu}_e$ neutrinos and 41.0% are "ν_μ" neutrinos. Recall that there is no provision made in the Beacom and Vogel model for electron neutrinos being produced during the neutronization stage of collapse. However, the prompt ν_e neutrino signal is only expected to contribute 1–2% to the total number of supernova neutrinos that interact in the detector. Table 6.1 summarizes in detail the number of supernova neutrinos expected in the SNO detector using the Beacom and Vogel

Reaction	**Reaction Region**	**ν Counts (all time)**	**ν Counts ($t \leq$ 0.5 s)**
Charged Current:	*D_2O/ H_2O*	*161.83/428.57*	*22.03/58.34*
$\overline{\nu}_e + p \rightarrow n + e^+$	H_2O	419.96	57.17
$\nu_e + d \rightarrow p + p + e^-$	D_2O	79.26	10.79
$\overline{\nu}_e + d \rightarrow n + n + e^+$	D_2O	78.01	10.62
$\nu_e + O \rightarrow F + e^-$	D_2O	1.01	0.14
$\overline{\nu}_e + O \rightarrow N + e^+$	D_2O	3.55	0.48
$\nu_e + O \rightarrow F + e^-$	H_2O	1.90	0.26
$\overline{\nu}_e + O \rightarrow N + e^+$	H_2O	6.71	0.91
Neutral Current:	*D_2O/ H_2O*	*524.88/38.44*	*71.47/5.24*
$\nu_e + d \rightarrow \nu_e + p + n$	D_2O	34.42	4.69
$\overline{\nu}_e + d \rightarrow \overline{\nu}_e + p + n$	D_2O	50.94	6.94
$\nu_{\mu,\tau} + d \rightarrow \nu_{\mu,\tau} + p + n$	D_2O	221.21	30.12
$\overline{\nu}_{\mu,\tau} + d \rightarrow \overline{\nu}_{\mu,\tau} + p + n$	D_2O	178.38	24.28
$\nu_{\mu,\tau} + {}^{16}O \rightarrow \nu_{\mu,\tau} + {}^{15}O + n + \gamma$	D_2O	2.10	0.29
$\overline{\nu}_{\mu,\tau} + {}^{16}O \rightarrow \overline{\nu}_{\mu,\tau} + {}^{15}O + n + \gamma$	D_2O	2.09	0.28
$\nu_{\mu,\tau} + {}^{16}O \rightarrow \nu_{\mu,\tau} + {}^{15}N + p + \gamma$	D_2O	7.99	1.09
$\overline{\nu}_{\mu,\tau} + {}^{16}O \rightarrow \overline{\nu}_{\mu,\tau} + {}^{15}N + p + \gamma$	D_2O	8.14	1.11
$\nu_{\mu,\tau} + {}^{16}O \rightarrow \nu_{\mu,\tau} + {}^{15}O + n$	D_2O	9.98	1.36
$\overline{\nu}_{\mu,\tau} + {}^{16}O \rightarrow \overline{\nu}_{\mu,\tau} + {}^{15}O + n$	D_2O	9.63	1.31
$\nu_{\mu,\tau} + {}^{16}O \rightarrow \nu_{\mu,\tau} + {}^{15}O + n + \gamma$	H_2O	3.97	0.54
$\overline{\nu}_{\mu,\tau} + {}^{16}O \rightarrow \overline{\nu}_{\mu,\tau} + {}^{15}O + n + \gamma$	H_2O	3.95	0.54
$\nu_{\mu,\tau} + {}^{16}O \rightarrow \nu_{\mu,\tau} + {}^{15}N + p + \gamma$	H_2O	15.12	2.06
$\overline{\nu}_{\mu,\tau} + {}^{16}O \rightarrow \overline{\nu}_{\mu,\tau} + {}^{15}N + p + \gamma$	H_2O	15.40	2.10
Elastic Scattering:	*D_2O/ H_2O*	*14.90/28.06*	*2.03/3.81*
$\nu_e + e^- \rightarrow \nu_e + e^-$	D_2O	7.27	0.99
$\overline{\nu}_e + e^- \rightarrow \overline{\nu}_e + e^-$	D_2O	3.09	0.42
$\nu_{\mu,\tau} + e^- \rightarrow \nu_{\mu,\tau} + e^-$	D_2O	2.44	0.33
$\overline{\nu}_{\mu,\tau} + e^- \rightarrow \overline{\nu}_{\mu,\tau} + e^-$	D_2O	2.10	0.29
$\nu_e + e^- \rightarrow \nu_e + e^-$	H_2O	13.69	1.86
$\overline{\nu}_e + e^- \rightarrow \overline{\nu}_e + e^-$	H_2O	5.82	0.79
$\nu_{\mu,\tau} + e^- \rightarrow \nu_{\mu,\tau} + e^-$	H_2O	4.59	0.62
$\overline{\nu}_{\mu,\tau} + e^- \rightarrow \overline{\nu}_{\mu,\tau} + e^-$	H_2O	3.96	0.54
Total SNO ν_e Neutrinos		137.55	18.73
Total SNO $\overline{\nu}_e$ Neutrinos		568.08	77.33
Total SNO "ν_μ" Neutrinos		491.05	66.86
Total SNO D_2O Neutrinos		701.61	95.53
Total SNO H_2O Neutrinos		495.07	67.39
Total SNO Neutrinos		**1196.68**	**162.92**

Table 6.1: Neutrino counts for a supernova at 10 kpc calculated for the Beacom and Vogel model using the SNO supernova generator with no detector energy threshold.

model for a supernova at 10 kpc.

Notice the relatively large contribution from reactions involving oxygen. A combined total of 92 neutrino interactions (7.6% of the total signal) is expected from charged-current and neutral-current reactions involving oxygen in the SNO detector for a supernova at 10 kpc. Since Beacom and Vogel adopt relatively high neutrino temperatures (especially for "ν_μ" neutrinos), these reaction channels play a prominent role. Other models with lower neutrino temperatures will predict fewer counts from these interactions.

Due to the high cross section for the $\overline{\nu}_e + p \rightarrow n + e^+$ reaction, there exists the potential for a significant contribution to the SNO neutrino signal from neutrinos interacting with H_2O molecules in the D_2O volume. Careful assays of the water inside the acrylic vessel measure this fraction to be 0.0824%. The consequence in the Beacom and Vogel model is that 0.18 neutrino interactions of the is type (or 0.015% of the total set of neutrino counts in Table 6.1) would arise for a supernova at 10 kpc. This contribution is considered to be insignificant and is therefore ignored in further studies.

Once the total number of neutrino interactions is determined for each reaction, neutrino events are sampled from energy and time distributions consistent with the model parameters. Final state particle events are then obtained by using appropriate kinematic relations and sampling according to the prescription outlined in Section 5.6. Table 6.2 summarizes the average energies of the sampled neutrino events for each reaction as well as some of the properties of the final state particle events. 50000 neutrino events are produced for each reaction without any energy threshold so that the entire underlying neutrino spectrum can be studied. Notice that average neutrino energy values for the different neutrino types are higher than the emission average energies quoted in Table 5.2. For example, the neutral current reactions involving ^{16}O, which have the highest energy thresholds, also have the highest average energies of neutrinos that interact in the detector. The reason is that interactions within the detector do not select neutrinos evenly from the energy distribution.

Reaction	**Reaction Region**	$\langle E_\nu \rangle$ **(MeV)**	$\langle E_e \rangle$ **(MeV)**	$\langle \cos\theta_e \rangle$
Charged Current:		*24.92*	*21.99*	*−0.0022*
$\overline{\nu}_e + p \rightarrow n + e^+$	H_2O	25.06	23.08	0.0311
$\nu_e + d \rightarrow p + p + e^-$	D_2O	19.42	16.49	−0.1204
$\overline{\nu}_e + d \rightarrow n + n + e^+$	D_2O	27.45	21.69	−0.0614
$\nu_e + O \rightarrow F + e^-$	D_2O	28.68		
$\overline{\nu}_e + O \rightarrow N + e^+$	D_2O	40.82		
$\nu_e + O \rightarrow F + e^-$	H_2O	28.61		
$\overline{\nu}_e + O \rightarrow N + e^+$	H_2O	40.94		
Neutral Current:		*42.87*	*N/A*	*N/A*
$\nu_e + d \rightarrow \nu_e + p + n$	D_2O	19.68		
$\overline{\nu}_e + d \rightarrow \overline{\nu}_e + p + n$	D_2O	26.42		
$\nu_{\mu,\tau} + d \rightarrow \nu_{\mu,\tau} + p + n$	D_2O	42.87		
$\overline{\nu}_{\mu,\tau} + d \rightarrow \overline{\nu}_{\mu,\tau} + p + n$	D_2O	41.30		
$\nu_{\mu,\tau} + {}^{16}O \rightarrow \nu_{\mu,\tau} + {}^{15}O + n + \gamma$	D_2O	67.09		
$\overline{\nu}_{\mu,\tau} + {}^{16}O \rightarrow \overline{\nu}_{\mu,\tau} + {}^{15}O + n + \gamma$	D_2O	66.98		
$\nu_{\mu,\tau} + {}^{16}O \rightarrow \nu_{\mu,\tau} + {}^{15}N + p + \gamma$	D_2O	67.07		
$\overline{\nu}_{\mu,\tau} + {}^{16}O \rightarrow \overline{\nu}_{\mu,\tau} + {}^{15}N + p + \gamma$	D_2O	67.10		
$\nu_{\mu,\tau} + {}^{16}O \rightarrow \nu_{\mu,\tau} + {}^{15}O + n$	D_2O	67.10		
$\overline{\nu}_{\mu,\tau} + {}^{16}O \rightarrow \overline{\nu}_{\mu,\tau} + {}^{15}O + n$	D_2O	67.04		
$\nu_{\mu,\tau} + {}^{16}O \rightarrow \nu_{\mu,\tau} + {}^{15}O + n + \gamma$	H_2O	67.10		
$\overline{\nu}_{\mu,\tau} + {}^{16}O \rightarrow \overline{\nu}_{\mu,\tau} + {}^{15}O + n + \gamma$	H_2O	67.07		
$\nu_{\mu,\tau} + {}^{16}O \rightarrow \nu_{\mu,\tau} + {}^{15}N + p + \gamma$	H_2O	67.07		
$\overline{\nu}_{\mu,\tau} + {}^{16}O \rightarrow \overline{\nu}_{\mu,\tau} + {}^{15}N + p + \gamma$	H_2O	67.11		
Elastic Scattering:		*21.35*	*9.59*	*0.9066*
$\nu_e + e^- \rightarrow \nu_e + e^-$	D_2O	14.51	7.53	0.9095
$\overline{\nu}_e + e^- \rightarrow \overline{\nu}_e + e^-$	D_2O	20.62	6.76	0.8650
$\nu_{\mu,\tau} + e^- \rightarrow \nu_{\mu,\tau} + e^-$	D_2O	32.84	15.27	0.9349
$\overline{\nu}_{\mu,\tau} + e^- \rightarrow \overline{\nu}_{\mu,\tau} + e^-$	D_2O	32.80	14.35	0.9281
$\nu_e + e^- \rightarrow \nu_e + e^-$	H_2O	14.49	7.50	0.9078
$\overline{\nu}_e + e^- \rightarrow \overline{\nu}_e + e^-$	H_2O	20.61	6.74	0.8655
$\nu_{\mu,\tau} + e^- \rightarrow \nu_{\mu,\tau} + e^-$	H_2O	32.84	15.24	0.9351
$\overline{\nu}_{\mu,\tau} + e^- \rightarrow \overline{\nu}_{\mu,\tau} + e^-$	H_2O	32.79	14.38	0.9284
Total SNO ν_e Neutrinos		18.94	14.61	0.0948
Total SNO $\overline{\nu}_e$ Neutrinos		25.75	22.58	0.0316
Total SNO "ν_μ" Neutrinos		45.90	14.84	0.9319
Total SNO D_2O Neutrinos		36.69	18.25	−0.0048
Total SNO H_2O Neutrinos		28.34	22.24	0.0860
Total SNO Neutrinos		**33.21**	**21.13**	**0.0608**

Table 6.2: Average energy and angular distribution values for 50000 sampled neutrinos and their associated final state detectable particles in the Beacom and Vogel model with no detector energy threshold.

However, the energy hierarchy remains present. The "ν_μ" neutrinos that interact in the detector have significantly higher average energies than $\overline{\nu}_e$ neutrinos, which in turn have higher average energies than ν_e neutrinos. As well, the ratio of the average energy values for ν_e, $\overline{\nu}_e$ and "ν_μ" neutrinos stays practically the same at 1:1.4:2.4. The relative changes to the ratio of average neutrino energy values are modest: a 6% decrease in the $\overline{\nu}_e$ energy and a 6% increase in the average energy for the "ν_μ" neutrinos.

Because neutrons thermalize in the detector volume and are only detected through indirect capture reactions, much of the energy information carried by the "ν_μ" neutrinos is lost in the final state. In principle, however, the high threshold energy of the ^{16}O neutral current reactions can be used to gauge the energies of these neutrinos. A high number of counts from these channels would indicate that a significant fraction of "ν_μ" neutrinos have energies $E_\nu > 15$ MeV. According to the Beacom and Vogel model, almost 80 neutrino interactions (or 6.5% of the total number of neutrino events) from these neutral-current channels involving oxygen are expected.

Also listed in Table 6.2 are the $\langle \cos\theta_e \rangle$ values for the different reactions, where θ_e is the angle between the neutrino and lepton directions in the laboratory. A value of $\langle \cos\theta_e \rangle = +1$ means that the direction of the outgoing particle is perfectly correlated with the incoming neutrino direction, while $\langle \cos\theta_e \rangle = -1$ means that the direction of the outgoing particle is perfectly anticorrelated with the neutrino direction. Reactions in which the final state lepton is emitted isotropically with respect to the neutrino direction have $\langle \cos\theta_e \rangle = 0$. There is no asymmetry in the angular distribution to exploit in that case. Neutrons thermalize in the detector thereby losing any information about the initial supernova direction; therefore only $\langle \cos\theta_e \rangle$ values for electrons and positrons are considered. The three charged current reactions, which use either proton or deuteron targets, have only slight asymmetries in the angular distribution. Vogel and Beacom [71] discuss the individual angular distributions for the these reactions, and the $\langle \cos\theta_e \rangle$ values presented in Table 6.2

agree with what they present. Together, the results indicate that the asymmetries in the charged current reactions combine to become essentially 0. However, the slight asymmetries can be distinguished by considering the heavy- and light-water signals separately. Elastic scattering reactions, on the other hand, have angular distributions which are very forward peaked (see Section 5.4.4). In those cases, $\langle \cos\theta_e \rangle$ values are very close to being completely aligned with the incoming neutrino direction. While the elastic scattering interactions convey the most useful directional information about the location of the supernova, there are relatively few interactions in those channels. Pointing back to a supernova will involve identifying the forward elastic scattering peak on top of the flat background provided by the other reactions.

6.2.2 Comparison to Beacom and Vogel Published Results

To ensure that the supernova signal formalism and models have been implemented correctly and that the SNO supernova generator is yielding valid results, a number of quantities are used as a check. Among these checks are the total supernova energy and the average neutrino energy. However, the most comprehensive comparison is done by comparing integrated neutrino counts and neutrino count rates where possible.

Using Equation 5.3, the total neutrino energy calculated by the supernova generator is 3.0×10^{53} ergs, which is identical to the expected result quoted by Beacom and Vogel [15]. The energy fractions are also the same. A comparison of these quantities is listed in Table 6.3.

Table 6.4 shows neutrino counts comparing values for reactions published by Beacom and Vogel [15] and count values calculated using the SNO supernova generator. Some important differences need to be taken into account. Beacom and Vogel use 1 ktonne D_2O and 1.4 ktonne H_2O as the SNO detector volumes and impose a 5 MeV detector threshold on all of the charged-current and elastic scattering reactions. In the case of the

Parameter	Beacom Value	This Work Value
$E_{\nu_e,total}$	0.5×10^{53}	0.499×10^{53}
$E_{\overline{\nu}_e,total}$	0.5×10^{53}	0.499×10^{53}
$E_{\text{“}\nu_\mu\text{”},total}$	2.0×10^{53}	1.996×10^{53}
$E_{\nu,total}$	3.0×10^{53}	2.995×10^{53}
$\langle E_{\nu_e} \rangle$	11.0 MeV	11.025 MeV
$\left\langle E_{\overline{\nu}_e} \right\rangle$	15.8 MeV	15.750 MeV
$\left\langle E_{\text{“}\nu_\mu\text{”}} \right\rangle$	25.2 MeV	25.200 MeV

Table 6.3: Comparison of supernova source parameters determined using the SNO supernova generator and Beacom and Vogel published values [15].

$\overline{\nu}_e + p \rightarrow n + e^+$ reaction, an older cross section formula is used by the authors [105] and this is also taken into account. For the sake of comparison, these parameters are employed in the generator to produce the results listed in the last column of Table 6.4. There is excellent agreement between the Beacom and Vogel published values and the generator results, which indicates that the model has been implemented correctly in the generator.

6.2.3 Burrows *et al.* Model

To compute the total number of counts for each reaction in the SNO detector using the Burrows *et al.* model, Equation 5.12 is used in conjunction with the model parameters outlined in Section 5.3.4. The limits of integration are chosen such that the total energy radiated as neutrinos is in agreement with the total model input energy. For the Burrows model, two time regimes are used for the integration in order to preserve the signal structure at early times and yet cover the long duration of the total signal. Integration over the early burst region is performed from -0.100 s to 1 s in steps of 1 ms, while integration over the cooling region is performed from 1 s to 50 s in 10 ms steps. Neutrino energy is integrated from 0.1 MeV to 100 MeV in steps of 0.1 MeV.

Before a detector energy threshold is applied, $\sim$800 neutrino events are expected in the

Reaction	**Reaction Region**	**Beacom Counts**	**This Work Counts**
Charged Current:	*D_2O/ H_2O*	*160/365*	*155.73/363.67*
$\overline{\nu}_e + p \rightarrow n + e^+$	H_2O	365	363.67
$\nu_e + d \rightarrow p + p + e^-$	D_2O	80	78.28
$\overline{\nu}_e + d \rightarrow n + n + e^+$	D_2O	80	77.45
Neutral Current:	*D_2O/ H_2O*	*520/30*	*525.38/31.68*
$\nu_e + d \rightarrow \nu_e + p + n$	D_2O	35	34.46
$\overline{\nu}_e + d \rightarrow \overline{\nu}_e + p + n$	D_2O	50	50.99
$\nu_{\mu,\tau} + d \rightarrow \nu_{\mu,\tau} + p + n$	D_2O	220	221.42
$\overline{\nu}_{\mu,\tau} + d \rightarrow \overline{\nu}_{\mu,\tau} + p + n$	D_2O	180	178.54
$\nu_{\mu,\tau} + {}^{16}\mathrm{O} \rightarrow \nu_{\mu,\tau} + {}^{15}\mathrm{O} + n + \gamma$	D_2O	20	2.10
$\overline{\nu}_{\mu,\tau} + {}^{16}\mathrm{O} \rightarrow \overline{\nu}_{\mu,\tau} + {}^{15}\mathrm{O} + n + \gamma$	D_2O		2.09
$\nu_{\mu,\tau} + {}^{16}\mathrm{O} \rightarrow \nu_{\mu,\tau} + {}^{15}\mathrm{N} + p + \gamma$	D_2O		8.00
$\overline{\nu}_{\mu,\tau} + {}^{16}\mathrm{O} \rightarrow \overline{\nu}_{\mu,\tau} + {}^{15}\mathrm{N} + p + \gamma$	D_2O		8.15
$\nu_{\mu,\tau} + {}^{16}\mathrm{O} \rightarrow \nu_{\mu,\tau} + {}^{15}\mathrm{O} + n$	D_2O	15	9.99
$\overline{\nu}_{\mu,\tau} + {}^{16}\mathrm{O} \rightarrow \overline{\nu}_{\mu,\tau} + {}^{15}\mathrm{O} + n$	D_2O		9.64
$\nu_{\mu,\tau} + {}^{16}\mathrm{O} \rightarrow \nu_{\mu,\tau} + {}^{15}\mathrm{O} + n + \gamma$	H_2O	30	3.29
$\overline{\nu}_{\mu,\tau} + {}^{16}\mathrm{O} \rightarrow \overline{\nu}_{\mu,\tau} + {}^{15}\mathrm{O} + n + \gamma$	H_2O		3.26
$\nu_{\mu,\tau} + {}^{16}\mathrm{O} \rightarrow \nu_{\mu,\tau} + {}^{15}\mathrm{N} + p + \gamma$	H_2O		12.45
$\overline{\nu}_{\mu,\tau} + {}^{16}\mathrm{O} \rightarrow \overline{\nu}_{\mu,\tau} + {}^{15}\mathrm{N} + p + \gamma$	H_2O		12.68
Elastic Scattering:	*D_2O/ H_2O*	*10/15*	*8.72/13.52*
$\nu_e + e^- \rightarrow \nu_e + e^-$	D_2O	10	3.97
$\overline{\nu}_e + e^- \rightarrow \overline{\nu}_e + e^-$	D_2O		1.42
$\nu_{\mu,\tau} + e^- \rightarrow \nu_{\mu,\tau} + e^-$	D_2O		1.82
$\overline{\nu}_{\mu,\tau} + e^- \rightarrow \overline{\nu}_{\mu,\tau} + e^-$	D_2O		1.51
$\nu_e + e^- \rightarrow \nu_e + e^-$	H_2O	15	6.18
$\overline{\nu}_e + e^- \rightarrow \overline{\nu}_e + e^-$	H_2O		2.14
$\nu_{\mu,\tau} + e^- \rightarrow \nu_{\mu,\tau} + e^-$	H_2O		2.84
$\overline{\nu}_{\mu,\tau} + e^- \rightarrow \overline{\nu}_{\mu,\tau} + e^-$	H_2O		2.36
Total SNO ν_e Neutrinos		N/A	122.89
Total SNO $\overline{\nu}_e$ Neutrinos		N/A	495.67
Total SNO "ν_μ" Neutrinos		N/A	480.14
Total SNO D_2O Neutrinos		690	689.83
Total SNO H_2O Neutrinos		410	408.87
Total SNO Neutrinos		**1100**	**1098.70**

Table 6.4: Comparison of neutrino counts for a supernova at 10 kpc calculated using the SNO supernova generator and values published by Beacom and Vogel [15]. The parameters used by the authors to simulate neutrino interactions in the SNO detector are used to calculate the values in the last column. Instead of specifying the number of neutrino counts for each individual reaction, Beacom and Vogel provide only the count sum for a certain type of interaction in some cases.

SNO detector for a supernova at 10 kpc according to the Burrows model. Of this total, 49.2% of the neutrinos in the supernova signal interact via charged current interactions, 47.2% via neutral current interactions and 3.6% through elastic scattering interactions. The majority of neutrinos interact in the D_2O volume, namely 58.8%, while 41.2% are present in the H_2O volume. 11.5% of the supernova neutrinos interacting in the SNO detector are ν_e neutrinos, 47.3% are $\overline{\nu}_e$ neutrinos and 41.1% are "ν_μ" neutrinos. Table 6.5 summarizes the number of supernova neutrinos expected in the SNO detector using the Burrows model for a supernova at 10 kpc. As with the Beacom and Vogel model, the number of counts expected due to H_2O molecules in the D_2O volume is considered to be negligible (0.14 counts for a supernova at 10 kpc or 0.018% of the total signal).

In contrast to the Beacom and Vogel model, the Burrows model only predicts a total of 13 neutrino interactions (or 1.7% of the entire signal) from charged current and neutral current reactions involving oxygen. This is due mainly to the much lower neutrino temperatures used in the Burrows model for the "ν_μ" neutrinos.

Table 6.6 summarizes the average energies of the sampled neutrino events for each reaction as well as some of the properties of the final state particles. 50000 neutrino events are produced for each reaction without any energy threshold so that the entire underlying neutrino spectrum can be studied. In all cases, the neutrino and corresponding final state particle energies are lower than for the Beacom and Vogel model; however, the energy hierarchy remains. The lower energies also affect the angular distributions. For instance, the $\langle \cos\theta_e \rangle$ values for the elastic scattering reaction do not correlate with the initial neutrino direction as well as in the Beacom and Vogel model. This is due to the fact that when higher energy neutrinos undergo elastic scattering, the recoil electron maintains the initial direction better than lower energy neutrinos.

Reaction	**Reaction Region**	**ν Counts (all time)**	**ν Counts ($t \leq$ 0.5 s)**
Charged Current:	*D_2O/ H_2O*	*138.51/333.74*	*76.14/165.43*
$\overline{\nu}_e + p \rightarrow n + e^+$	H_2O	329.11	162.64
$\nu_e + d \rightarrow p + p + e^-$	D_2O	82.99	46.23
$\overline{\nu}_e + d \rightarrow n + n + e^+$	D_2O	53.08	28.44
$\nu_e + O \rightarrow F + e^-$	D_2O	1.08	0.61
$\overline{\nu}_e + O \rightarrow N + e^+$	D_2O	1.36	0.86
$\nu_e + O \rightarrow F + e^-$	H_2O	2.05	1.16
$\overline{\nu}_e + O \rightarrow N + e^+$	H_2O	2.58	1.63
Neutral Current:	*D_2O/ H_2O*	*261.24/3.11*	*120.09/1.69*
$\nu_e + d \rightarrow \nu_e + p + n$	D_2O	35.77	20.11
$\overline{\nu}_e + d \rightarrow \overline{\nu}_e + p + n$	D_2O	36.27	18.90
$\nu_{\mu,\tau} + d \rightarrow \nu_{\mu,\tau} + p + n$	D_2O	99.22	42.60
$\overline{\nu}_{\mu,\tau} + d \rightarrow \overline{\nu}_{\mu,\tau} + p + n$	D_2O	86.74	36.73
$\nu_{\mu,\tau} + {}^{16}O \rightarrow \nu_{\mu,\tau} + {}^{15}O + n + \gamma$	D_2O	0.17	0.09
$\overline{\nu}_{\mu,\tau} + {}^{16}O \rightarrow \overline{\nu}_{\mu,\tau} + {}^{15}O + n + \gamma$	D_2O	0.17	0.09
$\nu_{\mu,\tau} + {}^{16}O \rightarrow \nu_{\mu,\tau} + {}^{15}N + p + \gamma$	D_2O	0.65	0.35
$\overline{\nu}_{\mu,\tau} + {}^{16}O \rightarrow \overline{\nu}_{\mu,\tau} + {}^{15}N + p + \gamma$	D_2O	0.66	0.36
$\nu_{\mu,\tau} + {}^{16}O \rightarrow \nu_{\mu,\tau} + {}^{15}O + n$	D_2O	0.81	0.44
$\overline{\nu}_{\mu,\tau} + {}^{16}O \rightarrow \overline{\nu}_{\mu,\tau} + {}^{15}O + n$	D_2O	0.78	0.42
$\nu_{\mu,\tau} + {}^{16}O \rightarrow \nu_{\mu,\tau} + {}^{15}O + n + \gamma$	H_2O	0.32	0.17
$\overline{\nu}_{\mu,\tau} + {}^{16}O \rightarrow \overline{\nu}_{\mu,\tau} + {}^{15}O + n + \gamma$	H_2O	0.32	0.17
$\nu_{\mu,\tau} + {}^{16}O \rightarrow \nu_{\mu,\tau} + {}^{15}N + p + \gamma$	H_2O	1.22	0.67
$\overline{\nu}_{\mu,\tau} + {}^{16}O \rightarrow \overline{\nu}_{\mu,\tau} + {}^{15}N + p + \gamma$	H_2O	1.25	0.68
Elastic Scattering:	*D_2O/ H_2O*	*15.79/29.74*	*6.84/12.88*
$\nu_e + e^- \rightarrow \nu_e + e^-$	D_2O	8.52	4.13
$\overline{\nu}_e + e^- \rightarrow \overline{\nu}_e + e^-$	D_2O	3.19	1.32
$\nu_{\mu,\tau} + e^- \rightarrow \nu_{\mu,\tau} + e^-$	D_2O	2.19	0.75
$\overline{\nu}_{\mu,\tau} + e^- \rightarrow \overline{\nu}_{\mu,\tau} + e^-$	D_2O	1.89	0.64
$\nu_e + e^- \rightarrow \nu_e + e^-$	H_2O	16.05	7.77
$\overline{\nu}_e + e^- \rightarrow \overline{\nu}_e + e^-$	H_2O	6.01	2.49
$\nu_{\mu,\tau} + e^- \rightarrow \nu_{\mu,\tau} + e^-$	H_2O	4.12	1.41
$\overline{\nu}_{\mu,\tau} + e^- \rightarrow \overline{\nu}_{\mu,\tau} + e^-$	H_2O	3.56	1.21
Total SNO ν_e Neutrinos		146.46	80.01
Total SNO $\overline{\nu}_e$ Neutrinos		431.60	216.28
Total SNO "ν_μ" Neutrinos		204.07	86.78
Total SNO D_2O Neutrinos		415.54	203.07
Total SNO H_2O Neutrinos		366.59	180.00
Total SNO Neutrinos		**782.13**	**383.07**

Table 6.5: Neutrino counts for a supernova at 10 kpc calculated for the Burrows *et al.* model using the SNO supernova generator with no detector energy threshold.

Reaction	**Reaction Region**	$\langle E_\nu \rangle$ **(MeV)**	$\langle E_e \rangle$ **(MeV)**	$\langle \cos\theta_e \rangle$
Charged Current:		*20.22*	*17.65*	*−0.0196*
$\overline{\nu}_e + p \rightarrow n + e^+$	H_2O	19.93	18.19	0.0145
$\nu_e + d \rightarrow p + p + e^-$	D_2O	18.70	15.80	−0.1185
$\overline{\nu}_e + d \rightarrow n + n + e^+$	D_2O	22.56	17.21	−0.0760
$\nu_e + \mathrm{O} \rightarrow \mathrm{F} + e^-$	D_2O	30.00		
$\overline{\nu}_e + \mathrm{O} \rightarrow \mathrm{N} + e^+$	D_2O	36.68		
$\nu_e + \mathrm{O} \rightarrow \mathrm{F} + e^-$	H_2O	29.90		
$\overline{\nu}_e + \mathrm{O} \rightarrow \mathrm{N} + e^+$	H_2O	36.67		
Neutral Current:		*25.04*	*N/A*	*N/A*
$\nu_e + d \rightarrow \nu_e + p + n$	D_2O	18.96		
$\overline{\nu}_e + d \rightarrow \overline{\nu}_e + p + n$	D_2O	21.65		
$\nu_{\mu,\tau} + d \rightarrow \nu_{\mu,\tau} + p + n$	D_2O	26.40		
$\overline{\nu}_{\mu,\tau} + d \rightarrow \overline{\nu}_{\mu,\tau} + p + n$	D_2O	25.79		
$\nu_{\mu,\tau} + {}^{16}\mathrm{O} \rightarrow \nu_{\mu,\tau} + {}^{15}\mathrm{O} + n + \gamma$	D_2O	46.83		
$\overline{\nu}_{\mu,\tau} + {}^{16}\mathrm{O} \rightarrow \overline{\nu}_{\mu,\tau} + {}^{15}\mathrm{O} + n + \gamma$	D_2O	46.87		
$\nu_{\mu,\tau} + {}^{16}\mathrm{O} \rightarrow \nu_{\mu,\tau} + {}^{15}\mathrm{N} + p + \gamma$	D_2O	46.80		
$\overline{\nu}_{\mu,\tau} + {}^{16}\mathrm{O} \rightarrow \overline{\nu}_{\mu,\tau} + {}^{15}\mathrm{N} + p + \gamma$	D_2O	46.83		
$\nu_{\mu,\tau} + {}^{16}\mathrm{O} \rightarrow \nu_{\mu,\tau} + {}^{15}\mathrm{O} + n$	D_2O	46.81		
$\overline{\nu}_{\mu,\tau} + {}^{16}\mathrm{O} \rightarrow \overline{\nu}_{\mu,\tau} + {}^{15}\mathrm{O} + n$	D_2O	46.87		
$\nu_{\mu,\tau} + {}^{16}\mathrm{O} \rightarrow \nu_{\mu,\tau} + {}^{15}\mathrm{O} + n + \gamma$	H_2O	46.88		
$\overline{\nu}_{\mu,\tau} + {}^{16}\mathrm{O} \rightarrow \overline{\nu}_{\mu,\tau} + {}^{15}\mathrm{O} + n + \gamma$	H_2O	46.86		
$\nu_{\mu,\tau} + {}^{16}\mathrm{O} \rightarrow \nu_{\mu,\tau} + {}^{15}\mathrm{N} + p + \gamma$	H_2O	46.89		
$\overline{\nu}_{\mu,\tau} + {}^{16}\mathrm{O} \rightarrow \overline{\nu}_{\mu,\tau} + {}^{15}\mathrm{N} + p + \gamma$	H_2O	46.85		
Elastic Scattering:		*15.45*	*7.16*	*0.8924*
$\nu_e + e^- \rightarrow \nu_e + e^-$	D_2O	13.36	6.92	0.9022
$\overline{\nu}_e + e^- \rightarrow \overline{\nu}_e + e^-$	D_2O	15.55	5.18	0.8420
$\nu_{\mu,\tau} + e^- \rightarrow \nu_{\mu,\tau} + e^-$	D_2O	19.76	9.35	0.9119
$\overline{\nu}_{\mu,\tau} + e^- \rightarrow \overline{\nu}_{\mu,\tau} + e^-$	D_2O	19.70	8.82	0.9035
$\nu_e + e^- \rightarrow \nu_e + e^-$	H_2O	13.37	6.97	0.9047
$\overline{\nu}_e + e^- \rightarrow \overline{\nu}_e + e^-$	H_2O	15.61	5.25	0.8420
$\nu_{\mu,\tau} + e^- \rightarrow \nu_{\mu,\tau} + e^-$	H_2O	19.67	9.32	0.9126
$\overline{\nu}_{\mu,\tau} + e^- \rightarrow \overline{\nu}_{\mu,\tau} + e^-$	H_2O	19.74	8.82	0.9022
Total SNO ν_e Neutrinos		18.12	13.78	0.1151
Total SNO $\overline{\nu}_e$ Neutrinos		20.46	17.75	0.0217
Total SNO "ν_μ" Neutrinos		26.40	9.09	0.9078
Total SNO D_2O Neutrinos		22.97	15.39	0.0014
Total SNO H_2O Neutrinos		19.99	17.27	0.0873
Total SNO Neutrinos		**21.56**	**16.71**	**0.0617**

Table 6.6: Average energy and angular distribution values for 50000 sampled neutrinos and their associated final state detectable particles in the Burrows *et al.* model with no energy threshold.

6.2.4 Comparison to Burrows *et al.* Published Results

The the total neutrino energy as calculated by the SNO Supernova Monte Carlo is 2.90 $\times$ 10^{53} ergs, which is identical to the expected result quoted by Burrows *et al.* [60]. The average neutrino energies are also in excellent agreement with the published values. Table 6.7 summarizes the comparison of these values.

Parameter	**Burrows Value**	**This Work Value**
$E_{\nu_e,total}$	0.587×10^{53}	0.587×10^{53}
$E_{\overline{\nu}_e,total}$	0.518×10^{53}	0.518×10^{53}
$E_{\text{“}\nu_\mu\text{”},total}$	1.79×10^{53}	1.795×10^{53}
$E_{\nu,total}$	2.90×10^{53}	2.900×10^{53}
$\langle E_{\nu_e} \rangle$	9.9 MeV	9.894 MeV
$\langle E_{\overline{\nu}_e} \rangle$	11.6 MeV	11.620 MeV
$\langle E_{\text{“}\nu_\mu\text{”}} \rangle$	15.4 MeV	15.334 MeV

Table 6.7: Comparison of supernova source parameters determined using the SNO supernova generator and Burrows *et al.* published values [60].

To characterize the SNO detector, Burrows *et al.* use 1 ktonne D_2O and 1.6 ktonne H_2O as the target volumes and also impose a 5 MeV detector threshold on all charged current and elastic scattering reactions. In order to compare to the published values, these parameters as well as the cross sections presented in [60] are used in the supernova generator. Table 6.8 shows neutrino counts comparing count values for reactions published by Burrows *et al.* [60] and count values calculated using the supernova generator with their parameters. There is very good agreement between the two, which indicates that the model has been implemented correctly in the generator.

Reaction	**Reaction Region**	**Burrows Counts**	**This Work Counts**
Charged Current:	*D_2O/ H_2O*	*151.21/335.70*	*151.27/335.12*
$\overline{\nu}_e + p \rightarrow n + e^+$	H_2O	331	330.46
$\nu_e + d \rightarrow p + p + e^-$	D_2O	81.9	82.19
$\overline{\nu}_e + d \rightarrow n + n + e^+$	D_2O	66.7	66.46
$\nu_e + O \rightarrow F + e^-$	D_2O	1.17	1.18
$\overline{\nu}_e + O \rightarrow N + e^+$	D_2O	1.44	1.44
$\nu_e + O \rightarrow F + e^-$	H_2O	2.11	2.10
$\overline{\nu}_e + O \rightarrow N + e^+$	H_2O	2.59	2.56
Neutral Current:	*D_2O/ H_2O*	*272.40/0.00*	*272.43/0.00*
$\nu_e + d \rightarrow \nu_e + p + n$	D_2O	35.2	35.04
$\overline{\nu}_e + d \rightarrow \overline{\nu}_e + p + n$	D_2O	37.2	37.24
$\nu_{\mu,\tau} + d \rightarrow \nu_{\mu,\tau} + p + n$	D_2O	200	105.69
$\overline{\nu}_{\mu,\tau} + d \rightarrow \overline{\nu}_{\mu,\tau} + p + n$	D_2O		94.46
Elastic Scattering:	*D_2O/ H_2O*	*7.78/14.01*	*7.79/13.85*
$\nu_e + e^- \rightarrow \nu_e + e^-$	D_2O	4.35	4.35
$\overline{\nu}_e + e^- \rightarrow \overline{\nu}_e + e^-$	D_2O	1.07	1.08
$\nu_{\mu,\tau} + e^- \rightarrow \nu_{\mu,\tau} + e^-$	D_2O	2.36	1.18
$\overline{\nu}_{\mu,\tau} + e^- \rightarrow \overline{\nu}_{\mu,\tau} + e^-$	D_2O		1.18
$\nu_e + e^- \rightarrow \nu_e + e^-$	H_2O	7.83	7.73
$\overline{\nu}_e + e^- \rightarrow \overline{\nu}_e + e^-$	H_2O	1.93	1.92
$\nu_{\mu,\tau} + e^- \rightarrow \nu_{\mu,\tau} + e^-$	H_2O	4.25	2.10
$\overline{\nu}_{\mu,\tau} + e^- \rightarrow \overline{\nu}_{\mu,\tau} + e^-$	H_2O		2.10
Total SNO ν_e Neutrinos		132.56	132.59
Total SNO $\overline{\nu}_e$ Neutrinos		441.93	441.15
Total SNO "ν_μ" Neutrinos		206.61	206.71
Total SNO D_2O Neutrinos		431.39	431.49
Total SNO H_2O Neutrinos		349.71	348.97
Total SNO Neutrinos		**781.10**	**780.46**

Table 6.8: Comparison of neutrino counts for a supernova at 10 kpc calculated using the SNO supernova generator and values published by Burrows *et al.* [60]. The parameters used by the authors to simulate neutrino interactions in the SNO detector were used to calculate the values in the last column. Instead of specifying the number of neutrino counts for each individual reaction, Burrows *et al.* provide only the count sum for a certain type of interaction in some cases.

6.2.5 Bruenn Models

As the model input data to the SNO supernova generator, supernova source flux values, equivalent to the flux defined by Equation 5.1, are provided for a discrete set of time and energy values [106].

6.2.5.1 Bruenn 15 $M_\odot$ Model

Before a detector energy threshold is applied, ~340 neutrino events are expected in the SNO detector in the first 3.5 s after core collapse begins for a supernova at 10 kpc according to the Bruenn 15 $M_\odot$ model. Of this total, 67.8% of the neutrinos in the supernova signal interact via charged current interactions, 26.4% via neutral current interactions and 5.8% through elastic scattering interactions. Almost half of the neutrinos interact in the D_2O volume, namely 46.8%, while 53.2% are present in the H_2O volume. 19.4% of the supernova neutrinos interacting in the SNO detector are ν_e neutrinos, 63.2% are $\overline{\nu}_e$ neutrinos and 17.4% are "ν_μ" neutrinos. Table 6.9 summarizes the number of supernova neutrinos expected in the SNO detector using the Bruenn 15 $M_\odot$ model for a supernova at 10 kpc. As with the two generic models considered so far, the number of counts expected due to H_2O molecules in the D_2O volume is considered to be negligible (0.07 counts for a supernova at 10 kpc or 0.021% of the total signal). Since this signal does not extend for the full expected duration, the fractions quoted above do not necessarily hold for the total burst signal. In particular, the "ν_μ" signal is expected to accumulate more counts over time than the corresponding ν_e and $\overline{\nu}_e$ signals.

As with the Burrows model, the relative contribution of the reactions involving oxygen is small in the Bruenn 15 $M_\odot$ model. In the first 3.5 s after the initiation of core collapse, 4 neutrino interactions are expected, which comprise 1.3% of the calculated signal.

Reaction	**Reaction Region**	**ν Counts (all time)**	**ν Counts ($t \leq$ 0.5 s)**
Charged Current:	*D_2O/ H_2O*	*63.59/166.40*	*33.30/79.02*
$\overline{\nu}_e + p \rightarrow n + e^+$	H_2O	164.95	78.23
$\nu_e + d \rightarrow p + p + e^-$	D_2O	36.95	21.76
$\overline{\nu}_e + d \rightarrow n + n + e^+$	D_2O	25.88	11.12
$\nu_e + \mathrm{O} \rightarrow \mathrm{F} + e^-$	D_2O	0.36	0.24
$\overline{\nu}_e + \mathrm{O} \rightarrow \mathrm{N} + e^+$	D_2O	0.40	0.18
$\nu_e + \mathrm{O} \rightarrow \mathrm{F} + e^-$	H_2O	0.69	0.45
$\overline{\nu}_e + \mathrm{O} \rightarrow \mathrm{N} + e^+$	H_2O	0.76	0.34
Neutral Current:	*D_2O/ H_2O*	*88.41/1.04*	*39.56/0.40*
$\nu_e + d \rightarrow \nu_e + p + n$	D_2O	15.80	9.31
$\overline{\nu}_e + d \rightarrow \overline{\nu}_e + p + n$	D_2O	17.84	7.72
$\nu_{\mu,\tau} + d \rightarrow \nu_{\mu,\tau} + p + n$	D_2O	28.74	11.80
$\overline{\nu}_{\mu,\tau} + d \rightarrow \overline{\nu}_{\mu,\tau} + p + n$	D_2O	24.94	10.32
$\nu_{\mu,\tau} + {}^{16}\mathrm{O} \rightarrow \nu_{\mu,\tau} + {}^{15}\mathrm{O} + n + \gamma$	D_2O	0.06	0.02
$\overline{\nu}_{\mu,\tau} + {}^{16}\mathrm{O} \rightarrow \overline{\nu}_{\mu,\tau} + {}^{15}\mathrm{O} + n + \gamma$	D_2O	0.06	0.02
$\nu_{\mu,\tau} + {}^{16}\mathrm{O} \rightarrow \nu_{\mu,\tau} + {}^{15}\mathrm{N} + p + \gamma$	D_2O	0.22	0.08
$\overline{\nu}_{\mu,\tau} + {}^{16}\mathrm{O} \rightarrow \overline{\nu}_{\mu,\tau} + {}^{15}\mathrm{N} + p + \gamma$	D_2O	0.22	0.09
$\nu_{\mu,\tau} + {}^{16}\mathrm{O} \rightarrow \nu_{\mu,\tau} + {}^{15}\mathrm{O} + n$	D_2O	0.27	0.10
$\overline{\nu}_{\mu,\tau} + {}^{16}\mathrm{O} \rightarrow \overline{\nu}_{\mu,\tau} + {}^{15}\mathrm{O} + n$	D_2O	0.26	0.10
$\nu_{\mu,\tau} + {}^{16}\mathrm{O} \rightarrow \nu_{\mu,\tau} + {}^{15}\mathrm{O} + n + \gamma$	H_2O	0.11	0.04
$\overline{\nu}_{\mu,\tau} + {}^{16}\mathrm{O} \rightarrow \overline{\nu}_{\mu,\tau} + {}^{15}\mathrm{O} + n + \gamma$	H_2O	0.11	0.04
$\nu_{\mu,\tau} + {}^{16}\mathrm{O} \rightarrow \nu_{\mu,\tau} + {}^{15}\mathrm{N} + p + \gamma$	H_2O	0.41	0.16
$\overline{\nu}_{\mu,\tau} + {}^{16}\mathrm{O} \rightarrow \overline{\nu}_{\mu,\tau} + {}^{15}\mathrm{N} + p + \gamma$	H_2O	0.41	0.16
Elastic Scattering:	*D_2O/ H_2O*	*6.87/12.92*	*3.68/6.94*
$\nu_e + e^- \rightarrow \nu_e + e^-$	D_2O	4.19	2.45
$\overline{\nu}_e + e^- \rightarrow \overline{\nu}_e + e^-$	D_2O	1.60	0.73
$\nu_{\mu,\tau} + e^- \rightarrow \nu_{\mu,\tau} + e^-$	D_2O	0.58	0.27
$\overline{\nu}_{\mu,\tau} + e^- \rightarrow \overline{\nu}_{\mu,\tau} + e^-$	D_2O	0.50	0.23
$\nu_e + e^- \rightarrow \nu_e + e^-$	H_2O	7.88	4.62
$\overline{\nu}_e + e^- \rightarrow \overline{\nu}_e + e^-$	H_2O	3.01	1.37
$\nu_{\mu,\tau} + e^- \rightarrow \nu_{\mu,\tau} + e^-$	H_2O	1.09	0.51
$\overline{\nu}_{\mu,\tau} + e^- \rightarrow \overline{\nu}_{\mu,\tau} + e^-$	H_2O	0.94	0.44
Total SNO ν_e Neutrinos		65.87	38.83
Total SNO $\overline{\nu}_e$ Neutrinos		214.44	99.69
Total SNO "ν_μ" Neutrinos		58.92	24.38
Total SNO D_2O Neutrinos		158.87	76.54
Total SNO H_2O Neutrinos		180.36	86.36
Total SNO Neutrinos		**339.23**	**162.90**

Table 6.9: Neutrino counts for a supernova at 10 kpc calculated for the Bruenn 15 $M_\odot$ model using the SNO supernova generator with no detector energy threshold.

Reaction	**Reaction Region**	**ν Counts (all time)**	**ν Counts ($t \leq$ 0.5 s)**
Charged Current:	*D_2O/ H_2O*	*146.43/318.22*	*95.94/212.84*
$\overline{\nu}_e + p \rightarrow n + e^+$	H_2O	311.06	209.09
$\nu_e + d \rightarrow p + p + e^-$	D_2O	88.65	59.07
$\overline{\nu}_e + d \rightarrow n + n + e^+$	D_2O	53.99	34.89
$\nu_e + O \rightarrow F + e^-$	D_2O	2.01	1.05
$\overline{\nu}_e + O \rightarrow N + e^+$	D_2O	1.78	0.93
$\nu_e + O \rightarrow F + e^-$	H_2O	3.80	1.99
$\overline{\nu}_e + O \rightarrow N + e^+$	H_2O	3.36	1.76
Neutral Current:	*D_2O/ H_2O*	*148.12/2.97*	*104.75/1.77*
$\nu_e + d \rightarrow \nu_e + p + n$	D_2O	36.68	25.62
$\overline{\nu}_e + d \rightarrow \overline{\nu}_e + p + n$	D_2O	36.00	23.56
$\nu_{\mu,\tau} + d \rightarrow \nu_{\mu,\tau} + p + n$	D_2O	39.02	28.88
$\overline{\nu}_{\mu,\tau} + d \rightarrow \overline{\nu}_{\mu,\tau} + p + n$	D_2O	33.26	24.83
$\nu_{\mu,\tau} + {}^{16}O \rightarrow \nu_{\mu,\tau} + {}^{15}O + n + \gamma$	D_2O	0.17	0.10
$\overline{\nu}_{\mu,\tau} + {}^{16}O \rightarrow \overline{\nu}_{\mu,\tau} + {}^{15}O + n + \gamma$	D_2O	0.17	0.10
$\nu_{\mu,\tau} + {}^{16}O \rightarrow \nu_{\mu,\tau} + {}^{15}N + p + \gamma$	D_2O	0.63	0.37
$\overline{\nu}_{\mu,\tau} + {}^{16}O \rightarrow \overline{\nu}_{\mu,\tau} + {}^{15}N + p + \gamma$	D_2O	0.64	0.38
$\nu_{\mu,\tau} + {}^{16}O \rightarrow \nu_{\mu,\tau} + {}^{15}O + n$	D_2O	0.79	0.46
$\overline{\nu}_{\mu,\tau} + {}^{16}O \rightarrow \overline{\nu}_{\mu,\tau} + {}^{15}O + n$	D_2O	0.76	0.45
$\nu_{\mu,\tau} + {}^{16}O \rightarrow \nu_{\mu,\tau} + {}^{15}O + n + \gamma$	H_2O	0.31	0.18
$\overline{\nu}_{\mu,\tau} + {}^{16}O \rightarrow \overline{\nu}_{\mu,\tau} + {}^{15}O + n + \gamma$	H_2O	0.31	0.18
$\nu_{\mu,\tau} + {}^{16}O \rightarrow \nu_{\mu,\tau} + {}^{15}N + p + \gamma$	H_2O	1.19	0.70
$\overline{\nu}_{\mu,\tau} + {}^{16}O \rightarrow \overline{\nu}_{\mu,\tau} + {}^{15}N + p + \gamma$	H_2O	1.22	0.71
Elastic Scattering:	*D_2O/ H_2O*	*10.97/20.67*	*8.24/15.53*
$\nu_e + e^- \rightarrow \nu_e + e^-$	D_2O	7.05	5.32
$\overline{\nu}_e + e^- \rightarrow \overline{\nu}_e + e^-$	D_2O	2.58	1.85
$\nu_{\mu,\tau} + e^- \rightarrow \nu_{\mu,\tau} + e^-$	D_2O	0.72	0.57
$\overline{\nu}_{\mu,\tau} + e^- \rightarrow \overline{\nu}_{\mu,\tau} + e^-$	D_2O	0.62	0.50
$\nu_e + e^- \rightarrow \nu_e + e^-$	H_2O	13.28	10.03
$\overline{\nu}_e + e^- \rightarrow \overline{\nu}_e + e^-$	H_2O	4.86	3.49
$\nu_{\mu,\tau} + e^- \rightarrow \nu_{\mu,\tau} + e^-$	H_2O	1.36	1.08
$\overline{\nu}_{\mu,\tau} + e^- \rightarrow \overline{\nu}_{\mu,\tau} + e^-$	H_2O	1.17	0.93
Total SNO ν_e Neutrinos		151.47	103.08
Total SNO $\overline{\nu}_e$ Neutrinos		413.63	275.57
Total SNO "ν_μ" Neutrinos		82.28	60.42
Total SNO D_2O Neutrinos		305.52	208.93
Total SNO H_2O Neutrinos		341.86	230.14
Total SNO Neutrinos		**647.38**	**439.07**

Table 6.10: Neutrino counts for a supernova at 10 kpc calculated for the Bruenn 25 $M_\odot$ model using the SNO supernova generator with no detector energy threshold.

6.2.5.2 Bruenn 25 $M_\odot$ Model

Before a detector energy threshold is applied, ~650 neutrino events are expected in the SNO detector in the first 1 s after the start of core collapse for a supernova at 10 kpc according to the Bruenn 25 $M_\odot$ model. Of this total, 71.8% of the neutrinos in the supernova signal interact via charged current interactions, 23.3% via neutral current interactions and 4.9% through elastic scattering interactions. Almost half of the neutrinos interact in the D_2O volume, namely 47.2%, while 52.8% are present in the H_2O volume. 23.4% of the supernova neutrinos interacting in the SNO detector are ν_e neutrinos, 63.9% are $\overline{\nu}_e$ neutrinos and 12.7% are "ν_μ" neutrinos. Table 6.10 summarizes the number of supernova neutrinos expected in the SNO detector using the Bruenn 25 $M_\odot$ model for a supernova at 10 kpc. As with the Beacom and Vogel model, the number of counts expected due to H_2O molecules in the D_2O volume is considered to be negligible (0.14 counts for a supernova at 10 kpc or 0.022% of the total signal).

The higher energies in the Bruenn 25 $M_\odot$ model mean that reactions involving oxygen will contribute more neutrino interactions to the overall total. Before the onset of black hole formation at 1 s after core collapse, a total of 17 interactions is expected, which constitutes 2.6% of the entire signal. This is still a much smaller contribution than is predicted in the Beacom and Vogel model.

6.2.6 Liebendörfer Model

As the model input data to the SNO supernova generator, supernova source flux values, equivalent to the flux defined by Equation 5.1, are provided for a discrete set of time and energy values [107].

Before a detector energy threshold is applied, ~320 neutrino events are expected in the SNO detector in the first 590 ms from the start of core collapse for a supernova at 10 kpc according to the Liebendörfer 13 $M_\odot$ model. Of this total, 61.3% of the neutrinos

Reaction	**Reaction Region**	**ν Counts (all time)**
Charged Current:	*D_2O/ H_2O*	*67.34/129.21*
$\overline{\nu}_e + p \rightarrow n + e^+$	H_2O	120.84
$\nu_e + d \rightarrow p + p + e^-$	D_2O	40.49
$\overline{\nu}_e + d \rightarrow n + n + e^+$	D_2O	22.42
$\nu_e + O \rightarrow F + e^-$	D_2O	2.65
$\overline{\nu}_e + O \rightarrow N + e^+$	D_2O	1.78
$\nu_e + O \rightarrow F + e^-$	H_2O	5.01
$\overline{\nu}_e + O \rightarrow N + e^+$	H_2O	3.36
Neutral Current:	*D_2O/ H_2O*	*96.39/14.38*
$\nu_e + d \rightarrow \nu_e + p + n$	D_2O	17.59
$\overline{\nu}_e + d \rightarrow \overline{\nu}_e + p + n$	D_2O	14.74
$\nu_{\mu,\tau} + d \rightarrow \nu_{\mu,\tau} + p + n$	D_2O	26.42
$\overline{\nu}_{\mu,\tau} + d \rightarrow \overline{\nu}_{\mu,\tau} + p + n$	D_2O	22.72
$\nu_{\mu,\tau} + {}^{16}O \rightarrow \nu_{\mu,\tau} + {}^{15}O + n + \gamma$	D_2O	0.78
$\overline{\nu}_{\mu,\tau} + {}^{16}O \rightarrow \overline{\nu}_{\mu,\tau} + {}^{15}O + n + \gamma$	D_2O	0.78
$\nu_{\mu,\tau} + {}^{16}O \rightarrow \nu_{\mu,\tau} + {}^{15}N + p + \gamma$	D_2O	2.99
$\overline{\nu}_{\mu,\tau} + {}^{16}O \rightarrow \overline{\nu}_{\mu,\tau} + {}^{15}N + p + \gamma$	D_2O	3.04
$\nu_{\mu,\tau} + {}^{16}O \rightarrow \nu_{\mu,\tau} + {}^{15}O + n$	D_2O	3.73
$\overline{\nu}_{\mu,\tau} + {}^{16}O \rightarrow \overline{\nu}_{\mu,\tau} + {}^{15}O + n$	D_2O	3.60
$\nu_{\mu,\tau} + {}^{16}O \rightarrow \nu_{\mu,\tau} + {}^{15}O + n + \gamma$	H_2O	1.48
$\overline{\nu}_{\mu,\tau} + {}^{16}O \rightarrow \overline{\nu}_{\mu,\tau} + {}^{15}O + n + \gamma$	H_2O	1.48
$\nu_{\mu,\tau} + {}^{16}O \rightarrow \nu_{\mu,\tau} + {}^{15}N + p + \gamma$	H_2O	5.66
$\overline{\nu}_{\mu,\tau} + {}^{16}O \rightarrow \overline{\nu}_{\mu,\tau} + {}^{15}N + p + \gamma$	H_2O	5.76
Elastic Scattering:	*D_2O/ H_2O*	*4.57/8.61*
$\nu_e + e^- \rightarrow \nu_e + e^-$	D_2O	2.91
$\overline{\nu}_e + e^- \rightarrow \overline{\nu}_e + e^-$	D_2O	0.92
$\nu_{\mu,\tau} + e^- \rightarrow \nu_{\mu,\tau} + e^-$	D_2O	0.40
$\overline{\nu}_{\mu,\tau} + e^- \rightarrow \overline{\nu}_{\mu,\tau} + e^-$	D_2O	0.34
$\nu_e + e^- \rightarrow \nu_e + e^-$	H_2O	5.49
$\overline{\nu}_e + e^- \rightarrow \overline{\nu}_e + e^-$	H_2O	1.73
$\nu_{\mu,\tau} + e^- \rightarrow \nu_{\mu,\tau} + e^-$	H_2O	0.75
$\overline{\nu}_{\mu,\tau} + e^- \rightarrow \overline{\nu}_{\mu,\tau} + e^-$	H_2O	0.64
Total SNO ν_e Neutrinos		74.14
Total SNO $\overline{\nu}_e$ Neutrinos		165.79
Total SNO "ν_μ" Neutrinos		80.57
Total SNO D_2O Neutrinos		168.30
Total SNO H_2O Neutrinos		152.20
Total SNO Neutrinos		**320.50**

Table 6.11: Neutrino counts for a supernova at 10 kpc calculated for the Liebendörfer 13 $M_\odot$ model using the SNO supernova generator with no detector energy threshold.

in the supernova signal interact via charged current interactions, 34.6% via neutral current interactions and 4.1% through elastic scattering interactions. The majority of neutrinos interact in the D_2O volume, namely 52.5%, while 47.5% are present in the H_2O volume. 23.1% of the supernova neutrinos interacting in the SNO detector are ν_e neutrinos, 51.7% are $\overline{\nu}_e$ neutrinos and 25.1% are "ν_μ" neutrinos. Table 6.11 summarizes the number of supernova neutrinos expected in the SNO detector using the Liebendörfer 13 $M_\odot$ model for a supernova at 10 kpc. As with the other models, the number of counts expected due to H_2O molecules in the D_2O volume is considered to be negligible (0.05 counts for a supernova at 10 kpc or 0.016% of the total signal).

In their model calculation, Liebendörfer *et al.* predict relatively high neutrino temperatures, which results in a high number of interactions involving oxygen. In the first 590 ms from collapse, results using the Liebendörfer model show 42.1 neutrino interactions or 13.1% of the total signal. Over the same time, results from the Beacom and Vogel model indicate 12 neutrino interactions or 7.7% of the total signal at 500 ms after core bounce.

6.2.7 Neutrino Interaction Summary

It is useful to compare the neutrino interaction results discussed in the previous section for the various models. The neutrino interactions that constitute the prompt signal allow for a study of the neutronization peak. Table 6.12 presents the number of neutrino interactions in the first 10 ms after core bounce for a supernova at 10 kpc. In all models except the Beacom and Vogel model, there is a clear indication of ν_e neutrinos resulting from electron capture reactions in the core of the proto-neutron star. In those models that do contain signal structure information, over 90% of the prompt signal is due to ν_e neutrinos, with the model resulting in a black hole having the highest fraction at almost 97%. The actual number of prompt electron neutrino interactions varies from 15 in the Burrows model to between 5 and 7 for the detailed model calculations. Results from all models indicate

SN Signal Component ($t \leq$ 10 ms)	**Beacom Model**	**Burrows Model**	**Bruenn Models**		**Liebendörfer Model**
			15 $M_\odot$	**25 $M_\odot$**	**13 $M_\odot$**
Neutrino:					
ν_e	0.03	14.77	6.27	5.28	7.41
$\overline{\nu}_e$	0.11	0.93	0.03	0.03	0.06
"ν_μ"	0.10	0.70	0.22	0.15	0.50
Region:					
D_2O region	0.14	14.00	5.60	4.62	6.94
H_2O region	0.10	2.40	0.92	0.84	1.03
Interaction:					
charged current	0.12	9.57	3.57	2.94	4.45
neutral current	0.11	4.45	1.67	1.33	2.29
elastic scattering	0.01	2.38	1.28	1.19	1.23
Total Signal:	**0.24**	**16.40**	**6.52**	**5.46**	**7.97**
$\rightarrow \nu_e$ fraction	**12.5%**	**90.1%**	**92.8%**	**96.7%**	**93.0%**

Table 6.12: Comparison of the prompt signal between supernova models at 10 kpc for time $t \leq 10$ ms from core bounce. In all models where the neutronization peak is included, over 90% of the prompt signal is due to ν_e neutrinos.

that the majority of the prompt signal will be due to the ν_e charged current reaction $\nu_e + d \rightarrow p + p + e^-$ in the heavy water region.

It is difficult to compare the total signals from all models because some models only provide results for limited times. However, since all models extend in time to 500 ms, results to that point are compared in Table 6.13. Results show that the Bruenn 25 $M_\odot$ model produces the highest number of interactions. Similar values are calculated using the Liebendörfer *et al.* and Burrows *et al.* models. The Bruenn 15 $M_\odot$ model yields about half the number of interactions compared to the Liebendörfer model. Finally, the simple model of Beacom and Vogel predicts the lowest number of interactions at 500 ms after core bounce.

It is also useful to compare the contribution to the supernova signal from reactions

SN Signal Component ($t \leq$ 500 ms)	**Beacom Model**	**Burrows Model**	**Bruenn Models**		**Liebendörfer Model**
			15 $M_\odot$	**25 $M_\odot$**	**13 $M_\odot$**
Neutrino:					
ν_e	18.73	80.01	38.83	103.08	74.14
$\overline{\nu}_e$	77.33	216.28	99.69	275.57	165.79
"ν_μ"	66.86	86.78	24.38	60.42	80.57
Region:					
D_2O region	95.53	203.07	76.54	208.93	168.30
H_2O region	67.39	180.00	86.36	230.14	152.20
Interaction:					
charged current	80.37	241.57	112.32	308.78	196.55
neutral current	76.71	121.78	39.96	106.52	110.77
elastic scattering	5.84	19.72	10.62	23.77	13.18
Total Signal:	**67.39**	**383.07**	**162.90**	**439.07**	**320.50**

Table 6.13: Comparison of the total signal between supernova models at 10 kpc for time $t \leq 500$ ms from core bounce.

with oxygen. The high energy threshold for these interactions means that they are very sensitive to the incoming neutrino energy. Fewer events due to reactions with oxygen are expected using models that employ relatively low neutrino temperatures. The numbers of neutrino interactions using oxygen as the target are compared in Table 6.14 for the five models discussed in the previous sections. As expected, the models of Liebendörfer and Beacom and Vogel, which have the highest neutrino temperatures, also have the largest contribution from oxygen reactions. Results from the models of Bruenn and Burrows show that for neutrinos with lower temperatures oxygen reactions contribute only a few percent to the total signal.

For many of the studies that follow, only the two generic models are considered, therefore a comparison of the full duration signals is in order. Both models have signals which

SN Signal Component ($t \leq$ 500 ms)	**Beacom Model**	**Burrows Model**	**Bruenn Models**		**Liebendörfer Model**
			15 $M_\odot$	**25 $M_\odot$**	**13 $M_\odot$**
Neutrino:					
ν_e	0.40	1.77	0.69	3.04	7.66
$\overline{\nu}_e$	1.39	2.49	0.52	2.69	5.14
"ν_μ"	10.68	3.44	0.81	3.63	29.30
Region:					
D_2O region	6.06	3.22	0.83	3.84	19.35
H_2O region	6.41	4.48	1.19	5.52	22.75
Interaction:					
charged current	1.79	4.26	1.21	5.73	12.80
neutral current	10.68	3.44	0.81	3.63	29.30
elastic scattering	0.00	0.00	0.00	0.00	0.00
Total Signal:	**12.47**	**7.70**	**2.02**	**9.36**	**42.10**
$\rightarrow$ O fraction	**7.7%**	**2.0%**	**1.2%**	**2.1%**	**13.1%**

Table 6.14: Comparison of the signal due to reactions involving oxygen between supernova models at 10 kpc for time $t \leq 500$ ms from core bounce.

last for tens of seconds, but the Beacom and Vogel model predicts many more neutral current events due to the higher neutrino temperatures used. On the other hand, the Burrows model produces a larger fraction of ν_e neutrinos, due in part to the neutronization signal.

6.3 Supernova Neutrino Interaction Rate

In Section 6.2, the total number of neutrino interactions is determined by integrating Equation 5.11 over both time and energy. If instead only the energy integration is performed, the resulting value is the number of neutrino interactions within the detector per unit time, or the interaction rate. This is not a "count" rate as such because SNO does not directly detect neutrinos but rather the detectable final state particles resulting from neutrino interactions. In some cases, more than one detectable particle is created for a given neutrino

SN Signal Component	Beacom Model	Burrows Model
Burst Duration:	0–20 s	−0.01–50 s
Neutrino:		
ν_e	137.55	146.46
$\overline{\nu}_e$	568.08	431.60
"ν_μ"	491.05	204.07
Region:		
D_2O region	701.61	415.54
H_2O region	495.07	366.59
Interaction:		
charged current	590.40	472.25
neutral current	563.32	264.35
elastic scattering	42.96	45.53
Total Signal:	**1196.69**	**782.13**
→ O events	**91.54**	**13.42**

Table 6.15: Comparison of the full duration signals for the two generic supernova models at 10 kpc.

interaction.

6.3.1 Beacom and Vogel Model

There is very little structure to be seen in the interaction rates for the Beacom and Vogel model. The neutrino signal rises quickly to 400 Hz and then slowly falls off to 0 Hz 20 s later. Neutrino interaction rates highlighting various contributions to the signal for the Beacom and Vogel model are shown in Figure 6.1.

6.3.2 Burrows *et al.* Model

Adding contributions from all of the reactions listed in Table 6.5, many of the characteristics of the generic supernova signal described in Section 5.3.4 are preserved in the neutrino interaction rate for a supernova at 10 kpc. The neutronization peak continues to be the

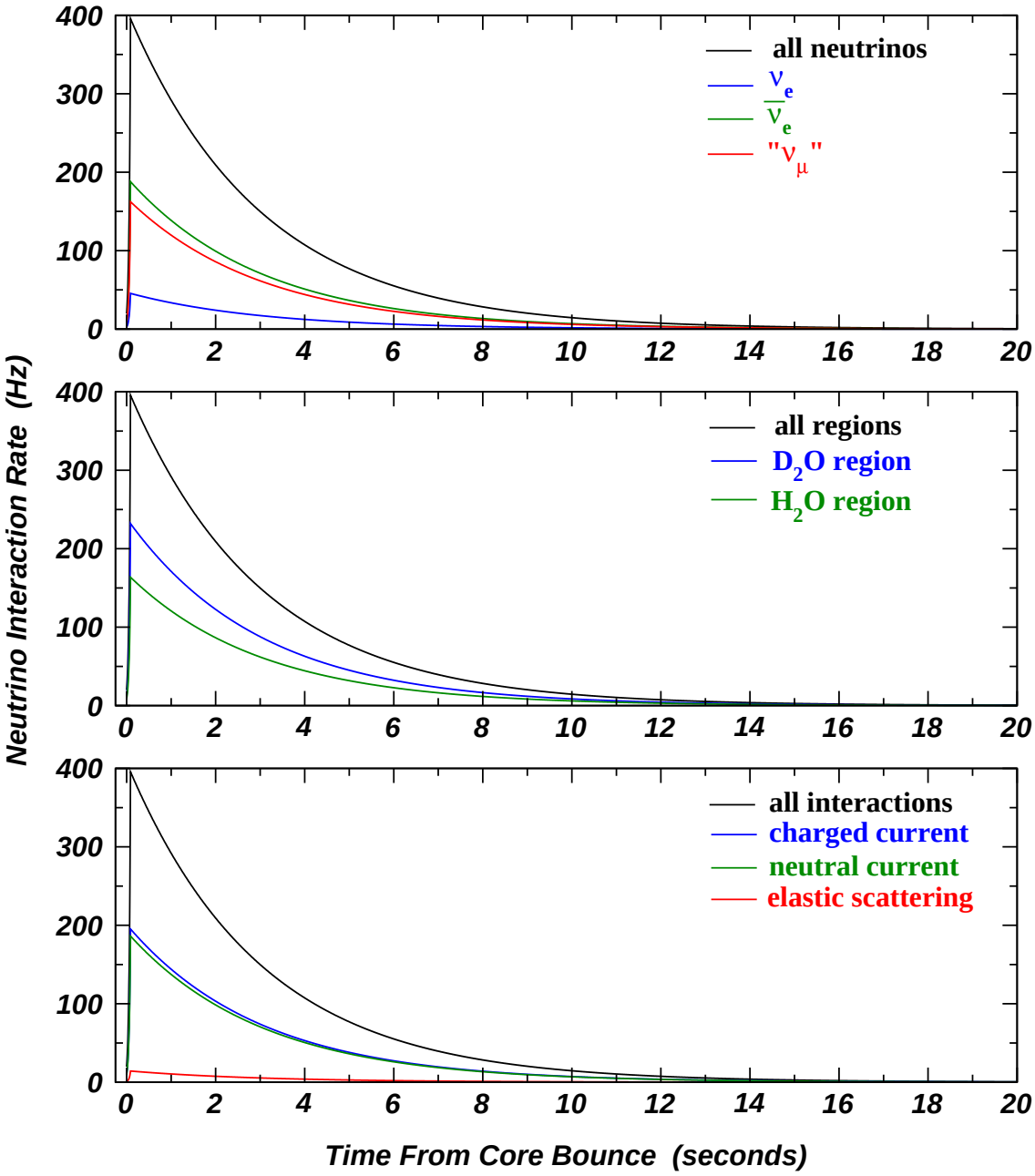

Figure 6.1: Neutrino interaction rate for a supernova at 10 kpc according to neutrino type in the SNO detector as a function of time using the model of Beacom and Vogel. Various components of the signal are shown including the contributions from different neutrinos, regions and interactions.

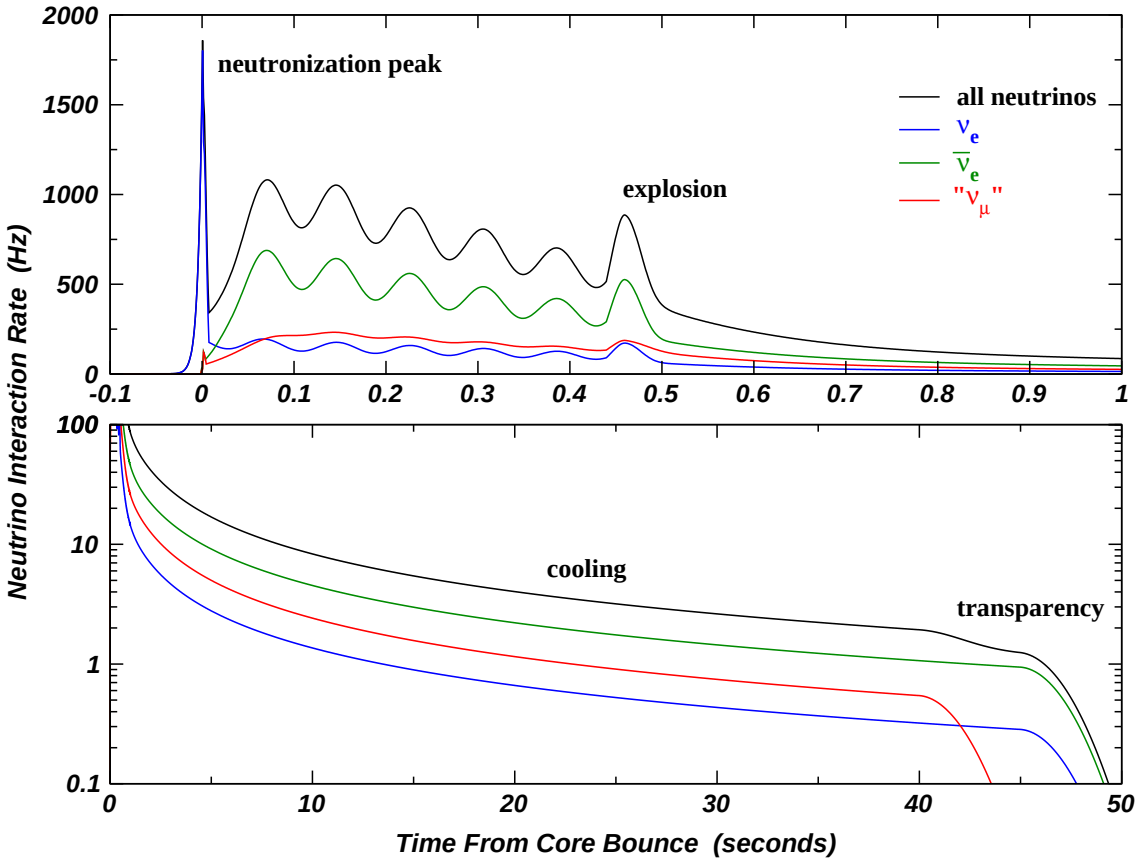

Figure 6.2: Neutrino interaction rate for a supernova at 10 kpc according to neutrino type in the SNO detector as a function of time using the model of Burrows *et al.*

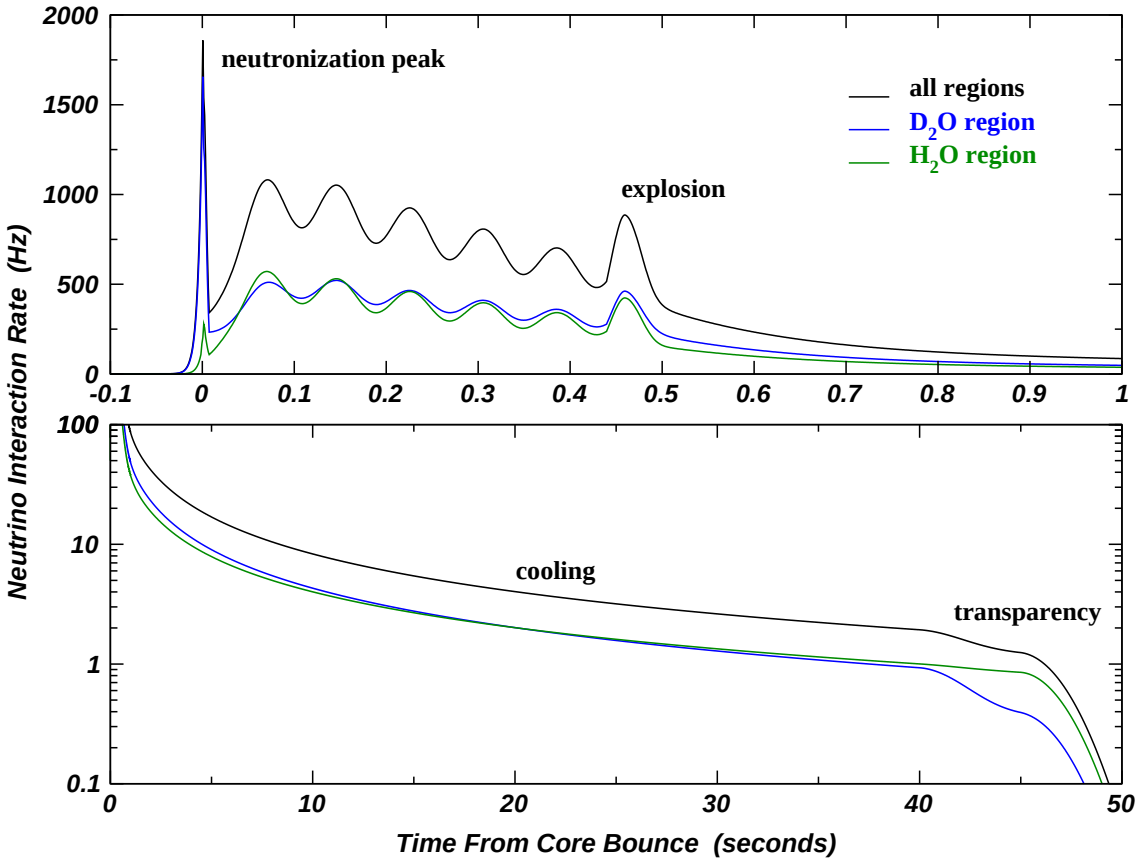

Figure 6.3: Neutrino interaction rate for a supernova at 10 kpc according to region type in the SNO detector as a function of time using the model of Burrows *et al.*

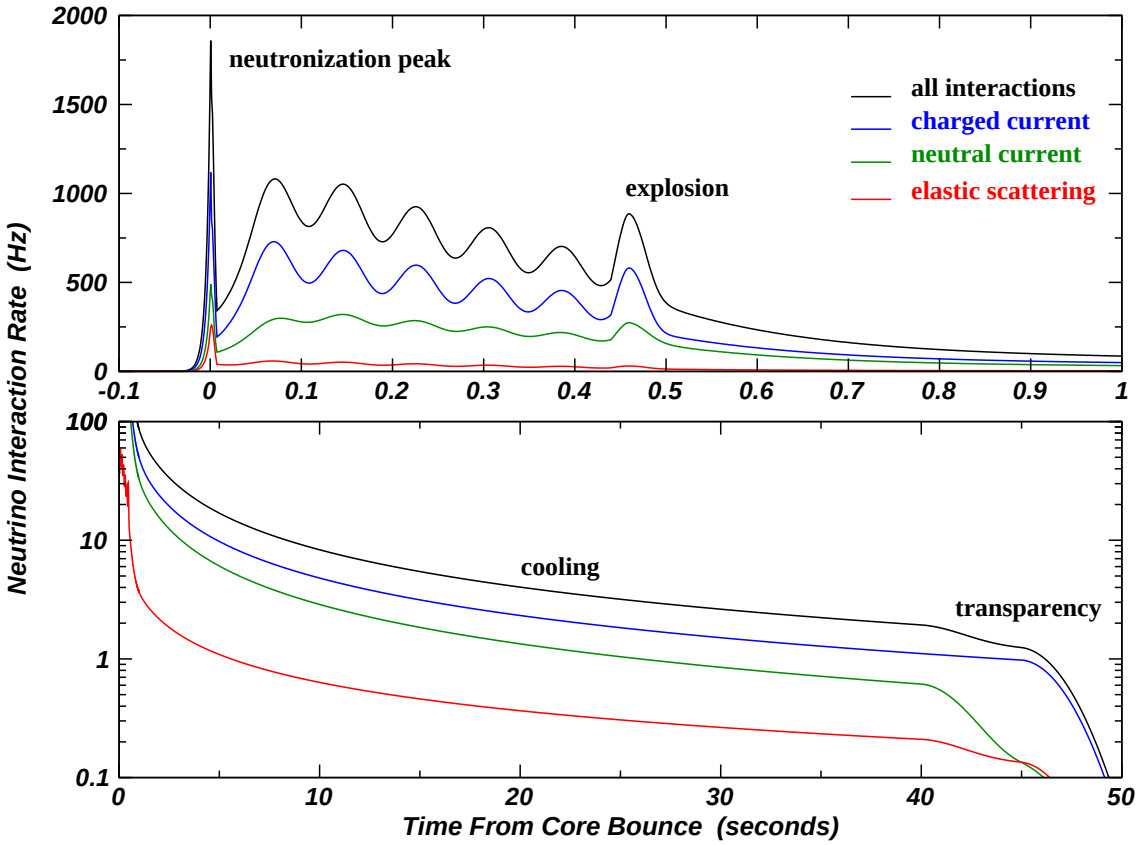

Figure 6.4: Neutrino interaction rate for a supernova at 10 kpc according to interaction type in the SNO detector as a function of time using the model of Burrows *et al.*

most dominant feature, and modulations due to ringing of the proto-neutron star mantle as well as the explosion are also clearly distinguishable. When considering the constituents of the neutrino interaction rate, further observations can be made. Figure 6.2 confirms that the neutronization peak is due to the large number of electron neutrinos interacting at the onset of the supernova signal, a sensitivity which is unique to the SNO detector. During the neutronization peak, the total count rate is expected to exceed 1 kHz on a millisecond time scale. Following the prompt peak, the ν_e signal falls off considerably, yet still remains significant, just below the level of the "ν_μ" contribution. Due to the large number of neutrinos that interact via the $\overline{\nu}_e + p \rightarrow n + e^+$ charged current reaction, electron antineutrinos are the most numerous. On the strength of that contribution, neutrino interaction rates in the light water are comparable to the signal resulting from reactions on deuterium in the heavy water region, as shown in Figure 6.3. Figure 6.4 demonstrates that charged current interactions make up the majority of the neutrino interaction signal, with a substantial contribution also coming from the neutral current reactions. There are relatively few neutrinos produced through elastic scattering reactions, which are important in determining the location of the supernova.

6.3.3 SNO Supernova Neutrino Energy Distribution

Integrating Equation 5.11 over time yields the number of neutrino interactions in the detector per unit energy. Since the predictions regarding the neutrino energy for the different neutrino species varies from one supernova model to the other, it is useful to compare the neutrino energy distributions for two generic models.

6.3.3.1 Beacom and Vogel Model

As indicated in Table 5.2, the Beacom and Vogel model predicts high average energies for the $\overline{\nu}_e$ and "ν_μ" neutrinos compared to other models. Since the cross section values increase with neutrino energy, relatively high numbers of interactions are expected for

these neutrino types. Furthermore, since the tails of the Fermi-Dirac supernova neutrino energy distributions extend to high energies (that is, they are not pinched as with the Burrows model), larger contributions to the observed signal from high energy neutrinos are expected. The energy distributions for neutrinos that interact in the SNO detector are shown in Figure 6.5.

6.3.3.2 Burrows *et al.* Model

The neutrino energies in the Burrows model differ from the high neutrino energies predicted by the Beacom and Vogel model. In particular, average energy values for the $\overline{\nu}_e$ and "ν_μ" neutrinos are lower in the Burrows model, therefore the majority of the signal is shifted to lower energy values. Also, because the Burrows model uses Fermi-Dirac neutrino energies that are pinched, fewer neutrino interactions take place at higher energies. Figure 6.6 shows the distribution for neutrinos that interact in the SNO detector according to the Burrows model[1].

6.4 Modifications to the Neutrino Signal

While this work does not consider the effects of neutrino mass on the supernova signal, there is mounting evidence [3],[4] that the neutrino mass is non-zero. Two important consequences of non-zero neutrino mass for the supernova neutrino signal include smearing effects due to time delay and flavour mixing through neutrino oscillations. A few qualitative comments regarding these aspects are included below.

6.4.1 Time Delay

As discussed in Section 3.4.2.1, massive neutrinos experience an energy-dependent time delay that affects the observed neutrino signal. Neutrinos with greater masses experience

[1]Note that coarser integration steps compared to those mentioned in Section 6.2.3 are used for this analysis to limit the computation time.

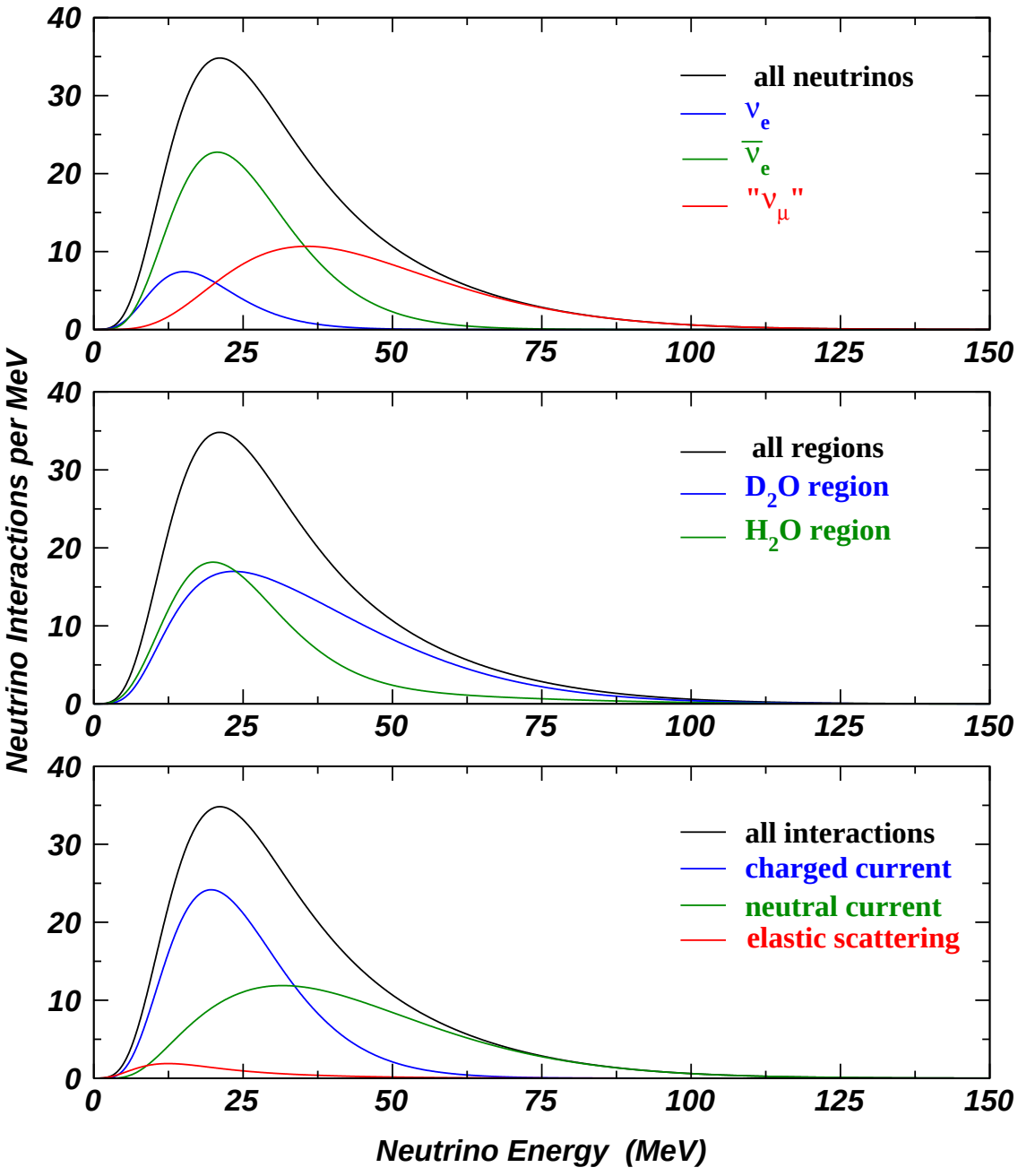

Figure 6.5: Neutrino counts per unit energy as a function of time for a supernova at 10 kpc in the SNO detector using the model of Beacom and Vogel. Various contributions are highlighted including neutrino type, region type and interaction type.

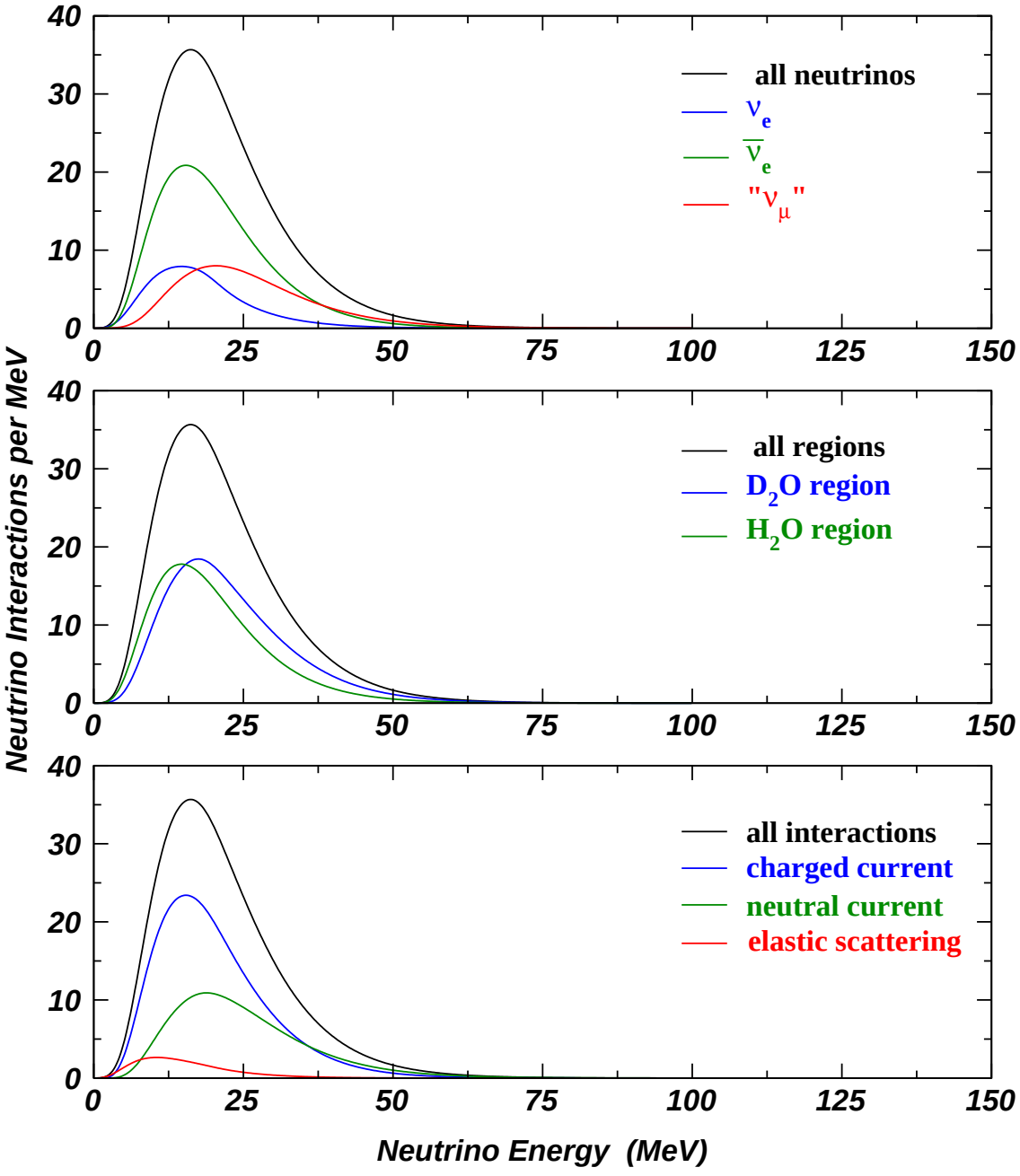

Figure 6.6: Neutrino counts per unit energy as a function of time for a supernova at 10 kpc in the SNO detector using the model of Burrows. Various contributions are highlighted including neutrino type, region type and interaction type.

longer time delays, while the time delay is decreased for neutrinos with higher energy. For example, Figure 6.7 shows the expected time delay for neutrinos that interact in the SNO detector according to the Burrows *et al.* supernova model. Neutrino masses of order 1 eV/c^2 give rise to average time delays of milliseconds for a supernova at 10 kpc.

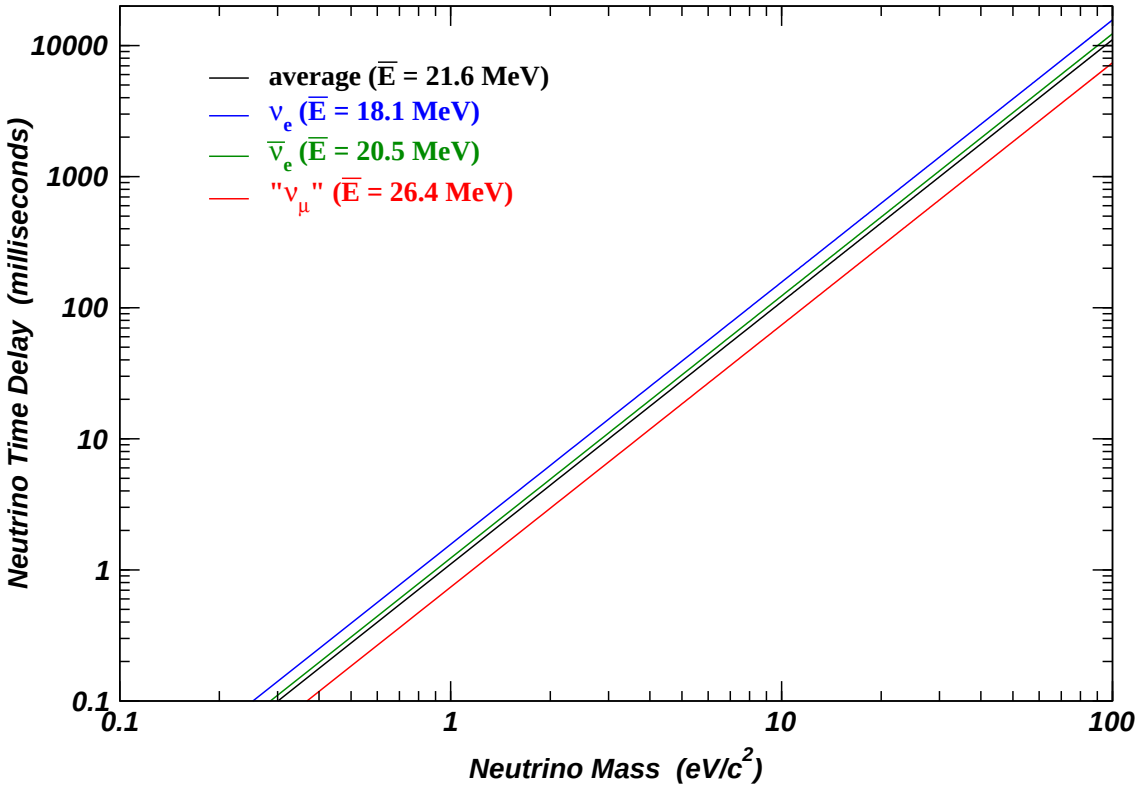

Figure 6.7: Energy-dependent time delay as a function of neutrino mass for a supernova at 10 kpc according to the Burrows *et al.* model. In each of the cases specified, the average energy of neutrinos that interact in the SNO detector is used. For a given neutrino mass, the "ν_μ" neutrinos have the shortest time delay due to their higher average energy.

In terms of the observed neutrino signal, the time delay serves to broaden the time distribution of events, as indicated in the study by Burrows *et al.* [60]. Even though the current upper limit on the mass of the electron neutrino is relatively small ($m_{\nu_e} <$ 3 eV/c^2), a neutrino mass of that order of magnitude may still significantly affect the

prompt neutronization signal.

6.4.2 Neutrino Oscillations

Neutrinos of all flavours are produced during the collapse of a massive star, and some of these neutrinos may transform into other neutrino flavours through either vacuum oscillation or matter-enhanced (MSW) neutrino oscillation. In either case, the partial or total mixing of neutrino flavours is expected to alter the observed neutrino signal.

6.4.2.1 Vacuum Oscillations

Neutrinos of all types are able to participate in vacuum oscillations through $\nu_e \leftrightarrow \nu_{\mu,\tau}$, $\overline{\nu}_e \leftrightarrow \overline{\nu}_{\mu,\tau}$ transitions. Vacuum oscillations do not take place in the high density regions within the supernova and within the Earth, but in the low density region of space while en route to the Earth.

Even though both neutrinos and antineutrinos participate in vacuum oscillations, a study performed by Burrows *et al.* [108] indicates that the observed neutrino signal is only slightly enhanced by these oscillations even at maximal mixing.

6.4.2.2 MSW Oscillations

Unlike vacuum oscillations, only certain transitions are available in matter-enhanced MSW neutrino oscillations. Assuming that the vacuum neutrino masses obey the standard mass hierarchy ($m_{\nu_\tau} > m_{\nu_\mu} > m_{\nu_e}$), MSW oscillations are not expected to affect antiparticles such as $\overline{\nu}_e$ neutrinos [109], which constitute the bulk of the detected supernova neutrino signal. Therefore, only the matter-enhanced $\nu_e \leftrightarrow \nu_{\mu,\tau}$ transformations are possible. Neutrinos produced in the dense core of a collapsing star traverse two resonance layers where flavour conversions are possible. The density of these resonance layers corresponds to the range of allowed atmospheric and solar neutrino MSW Δm^2 values. According to Dighe and Smirnov [110], the layer at higher densities (H resonance) corresponds to the larger

mass difference ($\Delta m^2 \approx 10^{-3}$ eV^2/c^4) associated with the atmospheric neutrino mixing parameters and is approximately $\rho_H \sim 10^3$–10^4 g/cm^3. The layer at lower densities (L resonance) is characterized by the smaller mass difference ($\Delta m^2 \approx 10^{-5}$–$10^{-6}$ eV^2/c^4) indicated by solar neutrino MSW investigations, and Dighe and Smirnov estimate that the density of that layer is on the order of $\rho_L \sim 5$–30 g/cm^3. Flavour mixing between $\nu_e \leftrightarrow \nu_\tau$ is expected to be possible in the high density resonance layer, while $\nu_e \leftrightarrow \nu_\mu$ transitions are expected to be possible in the low density resonance layer, as illustrated in Figure 6.8. Since these densities are too low to be found in the central core, flavour transitions are not expected to influence the dynamics of the supernova collapse or the cooling of the core. Matter enhanced oscillations do not occur in the intervening space between the outer envelope of the supernova and the Earth. Earth matter mixing effects are also considered by Dighe and Smirnov [110].

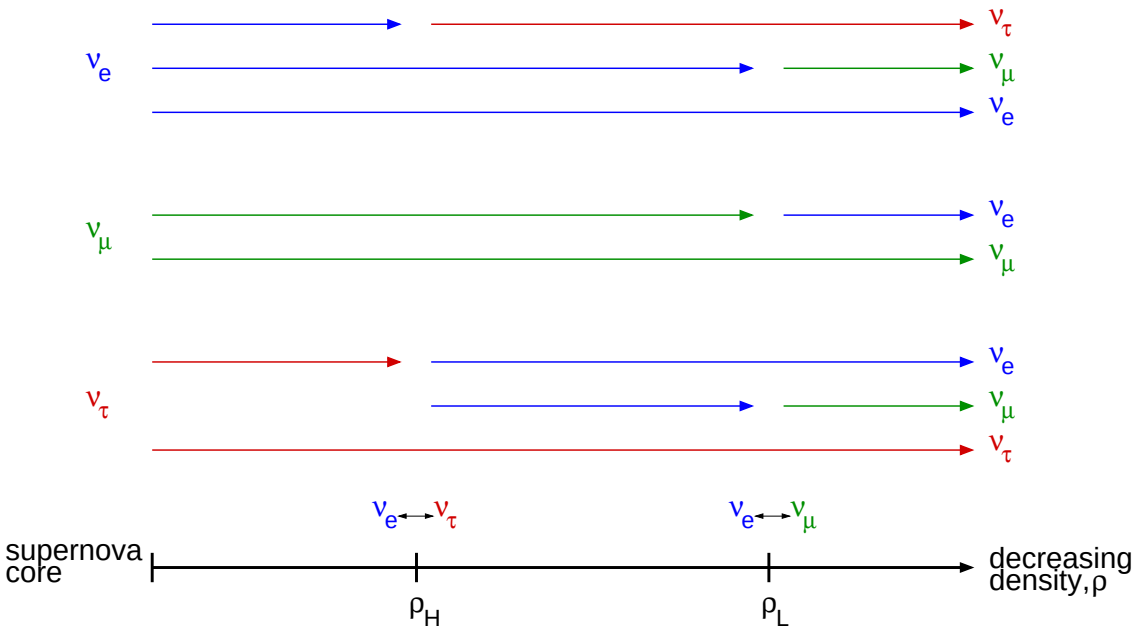

Figure 6.8: MSW matter neutrino oscillations in the high- and low-density resonance layers of a supernova. The density layers correspond to the allowed atmospheric and solar neutrino MSW Δm^2 regimes.

The most significant effect on the supernova neutrinos that arrive at the Earth concerns the ν_e neutrino signal[2]. Electron neutrinos are expected to acquire higher energies as a result of mixing with muon and tau neutrinos in the outer layers of the supernova. Therefore, a significant enhancement is predicted [108] for ν_e signal because the reaction cross sections increase with neutrino energy. In particular, a substantial increase in the number of events produced via interactions involving oxygen targets is expected due to the high energy thresholds for those reactions. At the same time however, the prompt ν_e neutronization peak becomes less prominent as supernova neutrinos undergo $\nu_e \leftrightarrow \nu_{\mu,\tau}$ flavour mixing. As well, the "ν_μ" signal decreases as low-energy ν_e neutrinos are converted to muon and tau neutrinos.

Finally, flavour mixing tends to dilute the effects due to the increased transit time of massive neutrinos. The ν_e signal is energized at the expense of the "ν_μ" neutrinos, and as a result more electron neutrinos are observed compared with muon and tau neutrinos due to the energy scaling of the cross section. While the time delay increases for lower energy "ν_μ" neutrinos, fewer of these interactions are detected relative to the more energetic (and less time delayed) electron neutrinos.

[2]Muon and tau neutrinos are expected to have identical time and energy spectra because they participate in the same interactions. Therefore evidence of $\nu_\mu \leftrightarrow \nu_\tau$ flavour mixing is not observable.

Chapter 7

SNO Supernova Observed Event Signal

In the previous section, neutrino interactions in the SNO detector were studied. The detected signal from SNOMAN simulations is discussed in the sections that follow, in which a detector hardware threshold of NHIT = 16 PMTs is used in all cases. Quantities used to characterize the observed signal include detected counts, time, energy, event position and event direction. While particles from reactions involving oxygen are not simulated in the detector, estimates of the signal contribution from those channels are provided. A detailed discussion of the analysis concerning this estimation can be found in Appendix C.

7.1 SNO Observed Supernova Counts

The number of observed counts depends on the particular running phase of the detector. Over its lifetime, the SNO detector will have three separate configurations: pure D_2O, salt and the neutral current detectors (NCDs). During each of these running phases, the SNO detector will have different sensitivities to supernova neutrinos, which are discussed in the sections below in terms of two generic supernova models. It should be noted that count values for the NCD phase are not simulated but are calculated using the detection efficiency, $\epsilon = 0.369$ NCD + 0.177 D_2O [69]. The reduction in Čerenkov light collection efficiency that is expected while the neutral current detectors are in place is not taken into account. This absorption is estimated to be 15% [69].

7.1.1 Beacom and Vogel Model

In order to investigate the SNO detection efficiencies, neutrinos from two independent sets of 100 supernovae are simulated. Therefore each data set using the Beacom and Vogel model involves simulating 126116 final state detectable particles from supernova neutrinos in the SNO detector. During the pure D_2O phase, 66.5% of the total number of possible final state particles are detected. The detection efficiency is much higher for the salt phase, where 90.6% of the particles are detected, and using the neutral current detectors in the heavy-water region, 75.0% of the particles are detected. According to the Monte Carlo results, the neutron detection efficiency is 37.9% in pure D_2O for supernova events above the hardware threshold and 85.6% in salt.

An additional 75–85 events are expected above the detector hardware energy threshold from reactions involving oxygen using the Beacom and Vogel model. The majority of these events are due to electrons/positrons and gamma rays. During all modes of operation, it is estimated that 13 electron/positron events and 52 γ-ray events would be detected above the hardware threshold. In the initial running mode with pure D_2O, a further 9 neutron events are expected. While operating with salt in the detector, 20 neutron events are expected and with NCDs in place 13 neutron events are expected. The contribution of events detected above the hardware threshold from oxygen events is between 7–8% of the total signal. Further details of this analysis are available in Appendix C.

Besides the 410 positrons produced via the $\overline{\nu}_e + p \rightarrow n + e^+$ reaction and the 20 electrons produced through elastic scattering, 8 $e^{\pm}$ events and 33 γ-ray events are expected from reactions involving oxygen. Including all of these contributions, electron antineutrinos are expected to constitute 88% of the H_2O signal above the detector hardware threshold of 16 PMTs according to the Beacom and Vogel model. Using this information, a large number of the electron antineutrino events can be isolated in the SNO detector volume.

Requiring at least 16 PMTs in coincidence imposes an energy threshold on the observed

Reaction	**Reaction Region**	**SNO Counts (all time)**		
		D_2O	**Salt**	**NCDs**
Charged Current:	*total*	*623.33*	*696.96*	*649.42*
$\overline{\nu}_e + p \rightarrow n + e^+$	H_2O	409.71	409.71	409.71
$\nu_e + d \rightarrow p + p + e^-$	D_2O	77.74	77.74	77.74
$\overline{\nu}_e + d \rightarrow n + n + e^+$	D_2O	135.88	209.51	161.97
Neutral Current:	*total*	*182.74*	*413.80*	*264.78*
$\nu_e + d \rightarrow \nu_e + p + n$	D_2O	12.83	29.41	18.79
$\overline{\nu}_e + d \rightarrow \overline{\nu}_e + p + n$	D_2O	19.43	43.59	27.81
$\nu_{\mu,\tau} + d \rightarrow \nu_{\mu,\tau} + p + n$	D_2O	83.14	188.54	120.78
$\overline{\nu}_{\mu,\tau} + d \rightarrow \overline{\nu}_{\mu,\tau} + p + n$	D_2O	67.34	152.26	97.40
Elastic Scattering:	*total*	*32.21*	*32.21*	*32.21*
$\nu_e + e^- \rightarrow \nu_e + e^-$	D_2O	5.66	5.66	5.66
$\overline{\nu}_e + e^- \rightarrow \overline{\nu}_e + e^-$	D_2O	2.18	2.18	2.18
$\nu_{\mu,\tau} + e^- \rightarrow \nu_{\mu,\tau} + e^-$	D_2O	2.13	2.13	2.13
$\overline{\nu}_{\mu,\tau} + e^- \rightarrow \overline{\nu}_{\mu,\tau} + e^-$	D_2O	1.84	1.84	1.84
$\nu_e + e^- \rightarrow \nu_e + e^-$	H_2O	9.64	9.64	9.64
$\overline{\nu}_e + e^- \rightarrow \overline{\nu}_e + e^-$	H_2O	3.68	3.68	3.68
$\nu_{\mu,\tau} + e^- \rightarrow \nu_{\mu,\tau} + e^-$	H_2O	3.78	3.78	3.78
$\overline{\nu}_{\mu,\tau} + e^- \rightarrow \overline{\nu}_{\mu,\tau} + e^-$	H_2O	3.30	3.30	3.30
Total SNO ν_e Events		105.87	122.45	111.83
Total SNO $\overline{\nu}_e$ Events		570.88	668.67	605.35
Total SNO "ν_μ" Events		161.53	351.85	229.23
Total SNO D_2O Events		408.17	712.86	516.30
Total SNO H_2O Events		430.11	430.11	430.11
Total SNO $e^{\pm}$ Events		596.44	596.44	596.44
Total SNO n Events		242.91	548.48	349.97
Total SNO Events		**838.28**	**1142.97**	**946.41**
Total SNO Events (with O)		**912.24**	**1228.37**	**1024.67**

Table 7.1: SNO supernova detected particle counts above NHIT = 16 PMTs using the Beacom and Vogel model for a supernova at 10 kpc. Two independent data sets with 100 supernovae at 10 kpc are used to calculate these count values. An additional ~75–85 events above the hardware threshold are expected from reactions involving oxygen.

signal. In the case of the elastic scattering events, this means that the angular distribution is more forward peaked than the signal presented in Section 6.2 before the hardware energy

threshold is applied. The energy and angular distribution properties of the final state electron and positron signals are summarized in Table 7.2. Since the detection of electrons and positrons is not affected by the addition of salt, only one set of values is necessary to describe the detector response.

Reaction	**Reaction Region**	$\langle$**NHIT**$_e\rangle$ **(PMTs)**	$\langle\cos\theta_e\rangle$
Charged Current:			
$\overline{\nu}_e + p \rightarrow n + e^+$	H_2O	127	0.0295
$\nu_e + d \rightarrow p + p + e^-$	D_2O	136	-0.1210
$\overline{\nu}_e + d \rightarrow n + n + e^+$	D_2O	177	-0.0624
Elastic Scattering:			
$\nu_e + e^- \rightarrow \nu_e + e^-$	D_2O	74	0.9615
$\overline{\nu}_e + e^- \rightarrow \overline{\nu}_e + e^-$	D_2O	72	0.9442
$\nu_{\mu,\tau} + e^- \rightarrow \nu_{\mu,\tau} + e^-$	D_2O	135	0.9668
$\overline{\nu}_{\mu,\tau} + e^- \rightarrow \overline{\nu}_{\mu,\tau} + e^-$	D_2O	130	0.9642
$\nu_e + e^- \rightarrow \nu_e + e^-$	H_2O	58	0.9651
$\overline{\nu}_e + e^- \rightarrow \overline{\nu}_e + e^-$	H_2O	57	0.9493
$\nu_{\mu,\tau} + e^- \rightarrow \nu_{\mu,\tau} + e^-$	H_2O	97	0.9697
$\overline{\nu}_{\mu,\tau} + e^- \rightarrow \overline{\nu}_{\mu,\tau} + e^-$	H_2O	93	0.9676

Table 7.2: Average NHIT and angular distribution values for final state electrons/positrons simulated in the SNO detector above the detector hardware threshold of 16 PMTs according to the model of Beacom and Vogel.

7.1.2 Burrows *et al.* Model

As with the Beacom and Vogel model, two independent data sets using neutrinos from 100 supernovae are used to simulate the detection signal. The final state count values for the reactions used in the simulation are presented in Table 7.3, where the count values have been scaled down by a factor of 100 to reflect the counts of a single supernova a 10 kpc. Of the total 87487 final state detectable particles from supernova neutrinos simulated in the SNO detector, 70.9% are detected during the pure D_2O phase, 90.9% during the salt phase and 78.1% during the NCD phase. According to the Monte Carlo results, the neutron

detection efficiency during the pure D_2O phase is 37.6% for supernova events above the hardware threshold and 85.6% for the salt phase. Both the Beacom and Vogel and the Burrows models predict that 32 elastic scattering events are observed above the detector hardware threshold for a supernova at 10 kpc.

An additional 12–13 events are expected above the detector hardware threshold using the Burrows model from reactions involving oxygen. The majority of these events are due to electrons/positrons and gamma rays. During all modes of operation, it is estimated that 7 electron/positron events and 4 γ-ray events would be detected above the hardware threshold. In the initial running mode with pure D_2O, a further 0.7 neutron events are expected. While operating with salt in the detector, 2 neutron events are expected and with NCDs in place 1 neutron event is expected. The contribution of events detected above the hardware threshold from oxygen events is of order 2% of the total signal. Further details of this analysis are available in Appendix C.

In addition to the 320 positrons produced via the $\overline{\nu}_e + p \rightarrow n + e^+$ reaction and the 20 electrons produced through elastic scattering, 4 $e^{\pm}$ events and 3 γ-ray events are expected from reactions involving oxygen. Including all of these contributions, electron antineutrinos are expected to constitute 93% of the H_2O signal above the detector hardware threshold of 16 PMTs according to the Burrows model. With this knowledge, a large number of the electron antineutrino events can be isolated in the SNO detector volume.

As with the Beacom and Vogel model, requiring 16 PMTs means that the angular distribution for the elastic scattering events is more forward peaked than with no detector threshold applied. The energy and angular distribution properties of the final state electron and positron signals are summarized in Table 7.4. Since the detection of electron and positrons is not affected by the addition of salt or NCDs, only one set of values is necessary to describe the detector response.

Reaction	**Reaction Region**	**SNO Counts (all time)**		
		D_2O	**Salt**	**NCDs**
Charged Current:	*total*	*492.31*	*543.07*	*510.89*
$\overline{\nu}_e + p \rightarrow n + e^+$	H_2O	319.81	319.81	319.81
$\nu_e + d \rightarrow p + p + e^-$	D_2O	81.03	81.03	81.03
$\overline{\nu}_e + d \rightarrow n + n + e^+$	D_2O	91.47	142.23	110.05
Neutral Current:	*total*	*96.59*	*220.30*	*140.88*
$\nu_e + d \rightarrow \nu_e + p + n$	D_2O	13.34	30.35	19.66
$\overline{\nu}_e + d \rightarrow \overline{\nu}_e + p + n$	D_2O	13.66	30.84	19.66
$\nu_{\mu,\tau} + d \rightarrow \nu_{\mu,\tau} + p + n$	D_2O	37.16	84.22	54.60
$\overline{\nu}_{\mu,\tau} + d \rightarrow \overline{\nu}_{\mu,\tau} + p + n$	D_2O	32.43	74.89	46.96
Elastic Scattering:	*total*	*31.76*	*31.76*	*31.76*
$\nu_e + e^- \rightarrow \nu_e + e^-$	D_2O	6.50	6.50	6.50
$\overline{\nu}_e + e^- \rightarrow \overline{\nu}_e + e^-$	D_2O	2.01	2.01	2.01
$\nu_{\mu,\tau} + e^- \rightarrow \nu_{\mu,\tau} + e^-$	D_2O	1.69	1.69	1.69
$\overline{\nu}_{\mu,\tau} + e^- \rightarrow \overline{\nu}_{\mu,\tau} + e^-$	D_2O	1.54	1.54	1.54
$\nu_e + e^- \rightarrow \nu_e + e^-$	H_2O	11.09	11.09	11.09
$\overline{\nu}_e + e^- \rightarrow \overline{\nu}_e + e^-$	H_2O	3.25	3.25	3.25
$\nu_{\mu,\tau} + e^- \rightarrow \nu_{\mu,\tau} + e^-$	H_2O	3.16	3.16	3.16
$\overline{\nu}_{\mu,\tau} + e^- \rightarrow \overline{\nu}_{\mu,\tau} + e^-$	H_2O	2.52	2.52	2.52
Total SNO ν_e Events		111.96	128.97	118.28
Total SNO $\overline{\nu}_e$ Events		430.20	498.14	454.78
Total SNO "ν_μ" Events		78.50	168.02	110.47
Total SNO D_2O Events		280.83	455.30	343.70
Total SNO H_2O Events		339.83	339.83	339.83
Total SNO $e^\pm$ Events		484.69	484.69	484.69
Total SNO n Events		136.78	311.82	198.84
Total SNO Events		**620.66**	**795.13**	**683.53**
Total SNO Events (with O)		**632.48**	**807.87**	**695.70**

Table 7.3: SNO supernova detected particle counts above NHIT = 16 PMTs using Burrows' model for a supernova at 10 kpc. Two independent data sets with 100 supernovae at 10 kpc are used to calculate these count values. An additional ~12–13 events above the hardware threshold are expected from reactions involving oxygen.

Reaction	**Reaction Region**	$\langle$**NHIT**$_e\rangle$ **(PMTs)**	$\langle\cos\theta_e\rangle$
Charged Current:			
$\overline{\nu}_e + p \rightarrow n + e^+$	H_2O	104	0.0116
$\nu_e + d \rightarrow p + p + e^-$	D_2O	131	-0.1197
$\overline{\nu}_e + d \rightarrow n + n + e^+$	D_2O	142	-0.0759
Elastic Scattering:			
$\nu_e + e^- \rightarrow \nu_e + e^-$	D_2O	70	0.9611
$\overline{\nu}_e + e^- \rightarrow \overline{\nu}_e + e^-$	D_2O	60	0.9410
$\nu_{\mu,\tau} + e^- \rightarrow \nu_{\mu,\tau} + e^-$	D_2O	91	0.9608
$\overline{\nu}_{\mu,\tau} + e^- \rightarrow \overline{\nu}_{\mu,\tau} + e^-$	D_2O	87	0.9583
$\nu_e + e^- \rightarrow \nu_e + e^-$	H_2O	55	0.9649
$\overline{\nu}_e + e^- \rightarrow \overline{\nu}_e + e^-$	H_2O	49	0.9464
$\nu_{\mu,\tau} + e^- \rightarrow \nu_{\mu,\tau} + e^-$	H_2O	68	0.9645
$\overline{\nu}_{\mu,\tau} + e^- \rightarrow \overline{\nu}_{\mu,\tau} + e^-$	H_2O	66	0.9623

Table 7.4: Average NHIT and angular distribution values for final state electrons/positrons simulated in the SNO detector above the detector hardware threshold of NHIT = 16 PMTs according to the model of Burrows *et al.*.

7.2 SNO Observed Supernova Counts at Various Distances

The number of events observed in the SNO detector will depend very much on the distance to the collapsing star. Scaling the events from a nominal supernova at 10 kpc (see Table 7.3), SNO remains sensitive to bursts of neutrinos from as far away as ~100 kpc. Within our galaxy, SNO should expect to see on average at least 100 events from a supernova burst, regardless of the neutron detection method being used. For a supernova located at the distance of 1987A, the SNO signal falls to only an average of 26 events during the pure D_2O operation phase and 31 events with salt. The Andromeda galaxy is comparable in mass to the Milky Way, but at a distance of approximately 790 kpc, SNO would expect to observe only 0.1 events. However, should the star Betelgeuse end its life in a Type

II supernova explosion, between 8 and 9 million events are expected above the hardware threshold in the SNO detector. Figure 7.1 indicates the number of events expected as a function of distance from the Earth, and summarizes the features discussed above. Notice that for the recent historical galactic supernovae, SNO would have measured a substantial signal in the range of 10000–20000 events.

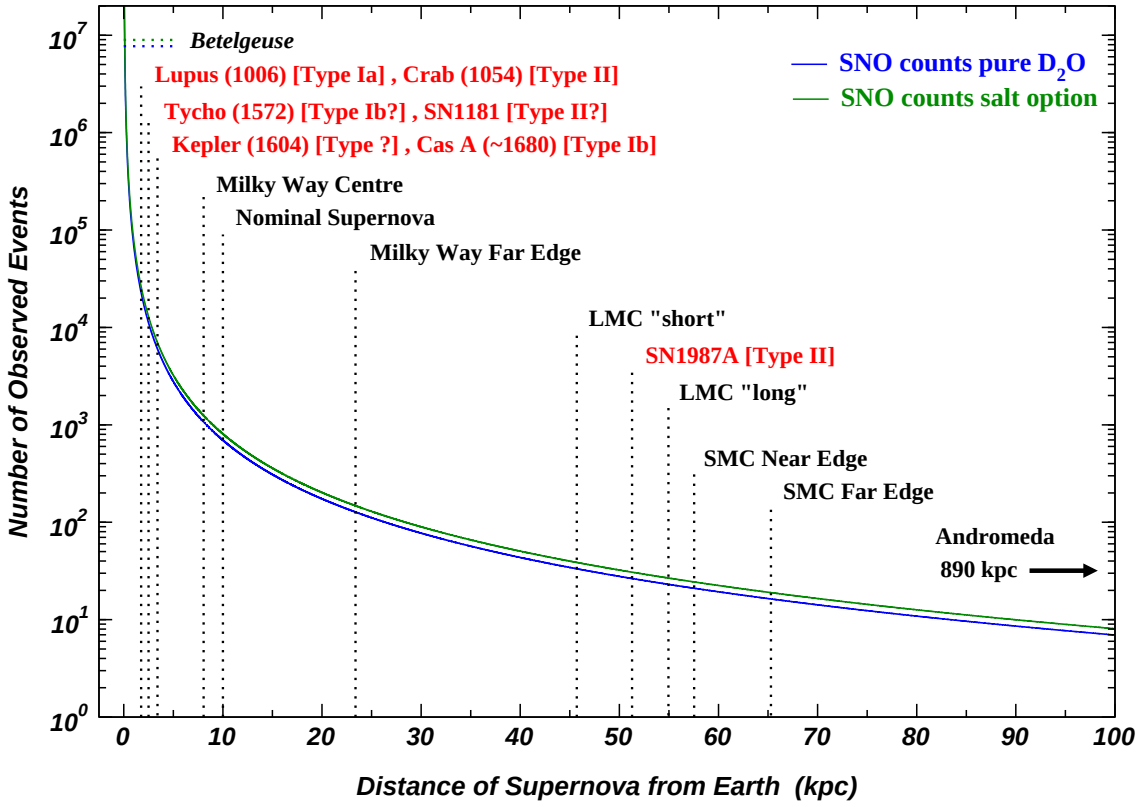

Figure 7.1: SNO supernova detected particle counts as a function of supernova distance from Earth. The dotted lines indicate the distance of a particular feature, and where they cross the plotted lines corresponds to the number of expected counts above the hardware threshold in the SNO detector expected.

Another important consideration in determining the number of events to expect for a supernova burst in our galaxy is the spatial distribution of stars. Bahcall and Soneira [111] have constructed a detailed model for the disk and spheroid components of our galaxy.

Fitting tabulated values from this model [112], yields the distribution shown in Figure 7.2. The steepest part of the curve corresponds to the bulge near the centre of the galaxy. The centre of the steep slope of the curve corresponds to 8.4 kpc, which agrees roughly with the measured distance to the centre of the galaxy. The large number of stars in this region means that a larger weighting is placed on those distances.

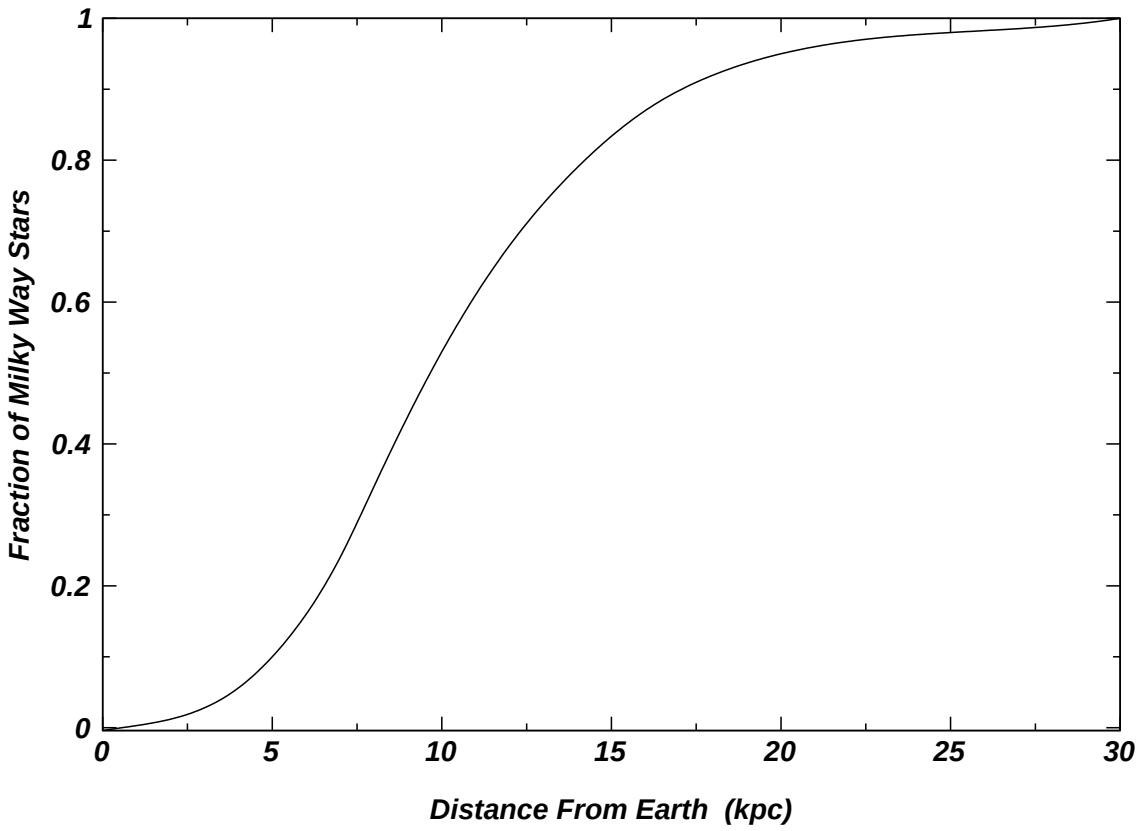

Figure 7.2: Fraction of Milky Way stars as a function of distance from the Sun according to the Bahcall and Soneira model of the galaxy [111].

Combining the $1/r^2$ flux information from Figure 7.1 and the weighting function from Figure 7.2, the number of detected events as a function of the fraction of galactic stars can be determined. Figure 7.3 shows that for a distance that includes 33.4% of the stars in the Milky Way, at least 1000 events would be expected during the pure D_2O phase. In the salt

running phase, the expectation of 1000 events would extend to a distance that included 43.5% of the stars. The median number of events expected for a supernova in the galaxy is 663 during the pure D_2O phase and 849 during the salt phase. The equivalent distance for the median number of events is 9.7 kpc (recall that the nominal distance is usually quoted as 10 kpc). Notice how practically all of the historical supernovae fall within the 5% of stars closest to us. The fraction of the galaxy visible to the naked-eye is severely limited by interstellar dust.

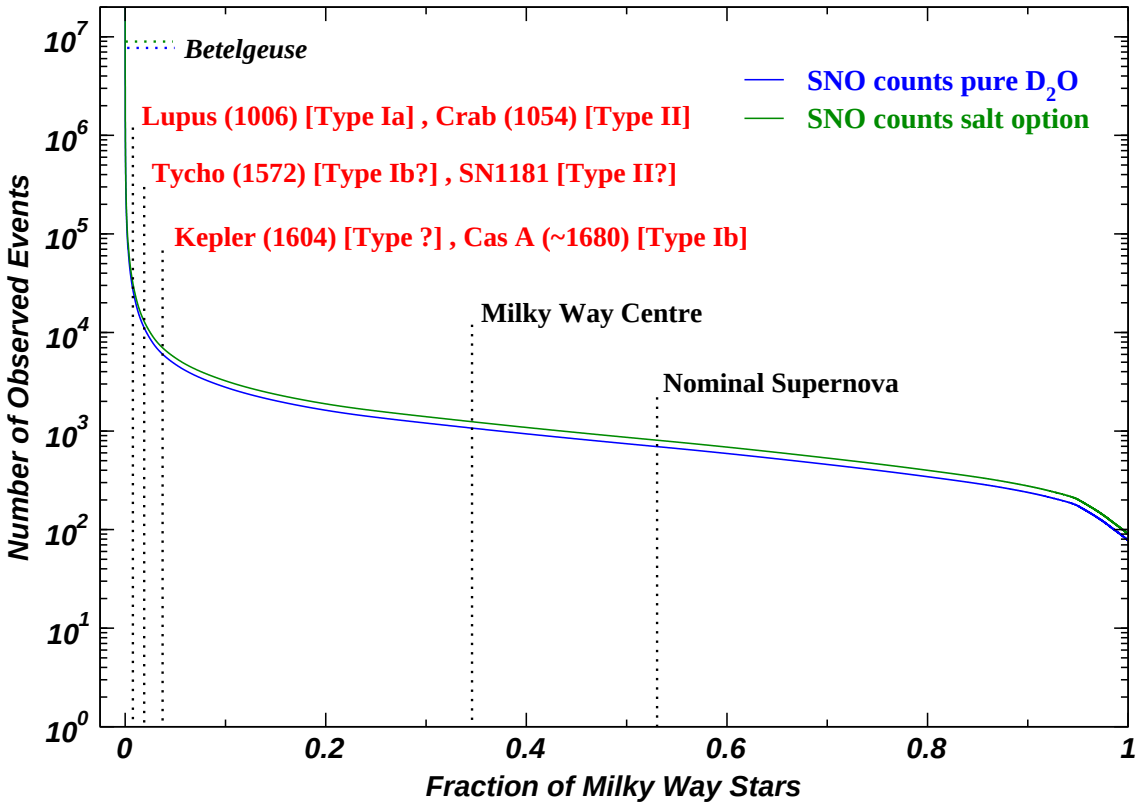

Figure 7.3: SNO supernova detected particle counts as a function of supernova distance from the Sun expressed as the fraction of Milky Way stars using the Bahcall and Soneira model of the galaxy [111] and the Burrows supernova model.

7.3 SNO Supernova Time Spectrum

One of the key features that distinguishes a burst of supernova neutrinos from other events in the SNO detector is the time spectrum of events. In the generic models under consideration, the observed event signal is expected to have a sharp initial rise followed by a decaying count rate that remains distinguishable above background for many seconds.

7.3.1 Beacom and Vogel Model

Almost 30% of the observed signal in the Beacom and Vogel model is expected in the first 1 s of the burst, which is rather low compared to other models. The observed signal count rate (without oxygen reactions) reaches a peak value of 300 Hz over millisecond time scales during the pure D_2O phase and then falls off to 10 Hz after 10 s. During salt running, the peak count rate reaches 400 Hz over millisecond time scales and falls off to 10 Hz in the same time as the pure D_2O signal. For instruments that integrate time over 1 s to compute the event rate, the peak count rate is 225 Hz for pure D_2O and 300 Hz for salt.

7.3.2 Burrows *et al.* Model

In contrast to the Beacom and Vogel model, the Burrows model predicts that 60% of the signal will arrive in the first 1 s of the burst. Therefore, the count rates are higher at 800 Hz over millisecond time scales during the pure D_2O phase and 1000 Hz during the salt phase. For instruments that integrate time over 1 s to compute the event rate, the peak count rate is 375 Hz for pure D_2O and 450 Hz for salt. As with the Beacom and Vogel model, the count rate in both cases falls to 10 Hz after 10 s. Figures 7.4, 7.5, 7.6 and 7.7 show the various contributions to the time spectrum during the pure D_2O and salt running phases. Plots of the cumulative counts as a function of time are shown for both running phases in Figures 7.8 and 7.9.

The detected particle count rate using only neutrinos from a single supernova at 10 kpc

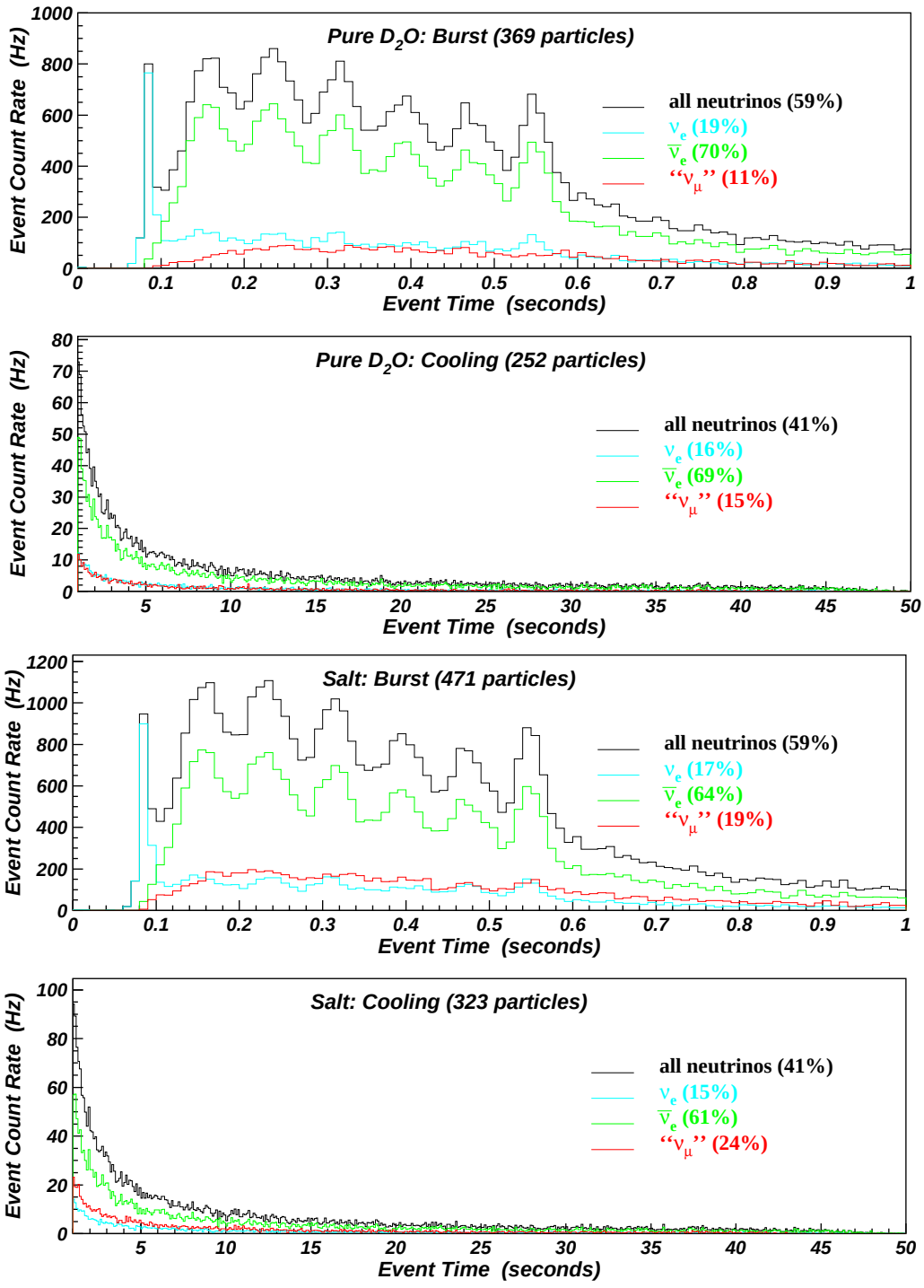

Figure 7.4: SNO supernova detected particle count rate above NHIT = 16 PMTs for the different neutrino types according to Burrows' model. The top two plots show the expected signal using only pure D_2O in the detector, while the bottom two plots show the signal with salt added to the D_2O volume. In both cases, 100 supernovae at 10 kpc are simulated, and the plots show the signal scaled down to 1 supernova at 10 kpc.

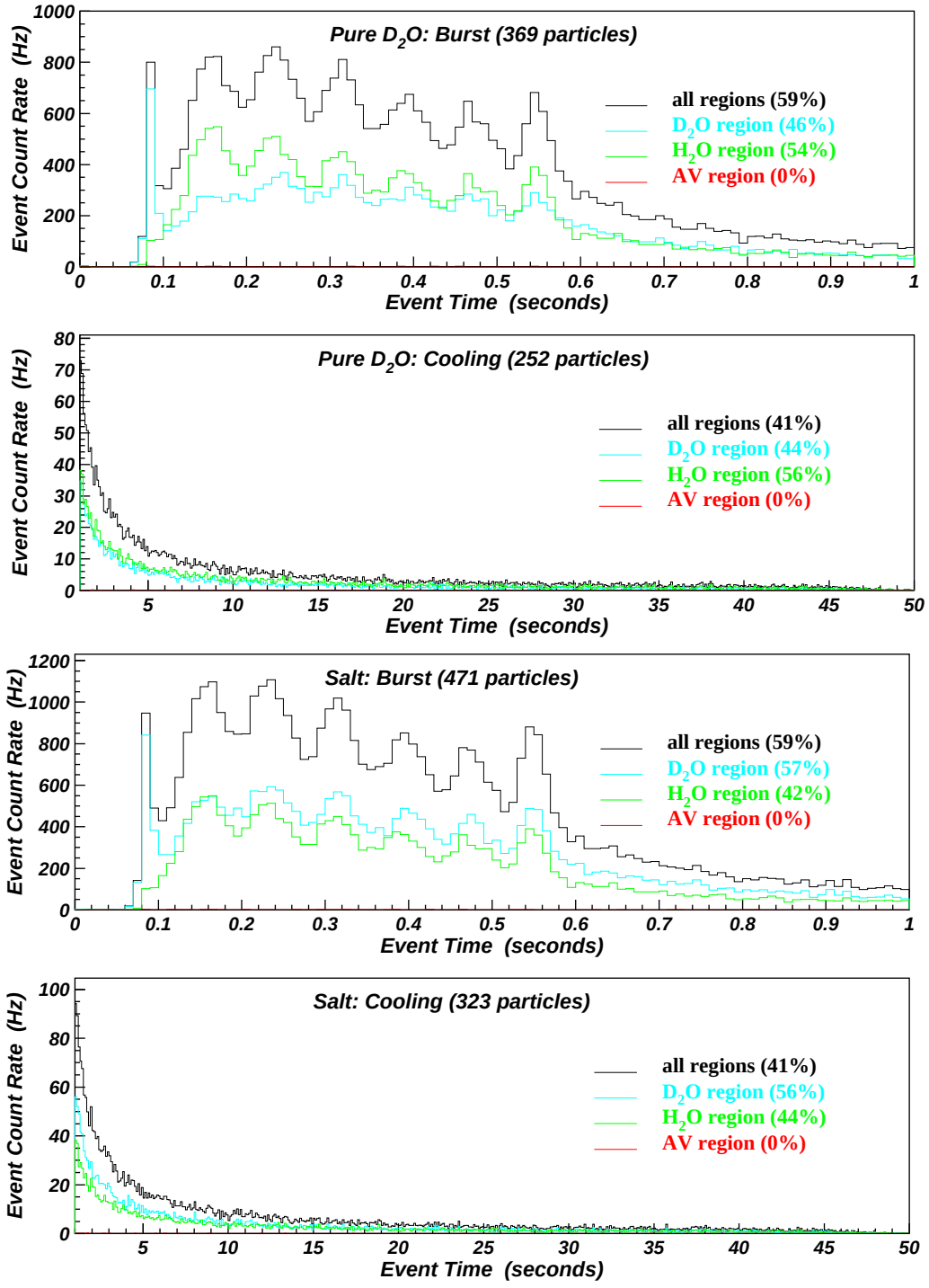

Figure 7.5: SNO supernova detected particle count rate above NHIT = 16 PMTs according to Burrows' model for the different region types. The top two plots show the expected signal using only pure D_2O in the detector, while the bottom two plots show the signal with salt added to the D_2O volume. In both cases, 100 supernovae at 10 kpc are simulated, and the plots show the signal scaled down to 1 supernova at 10 kpc.

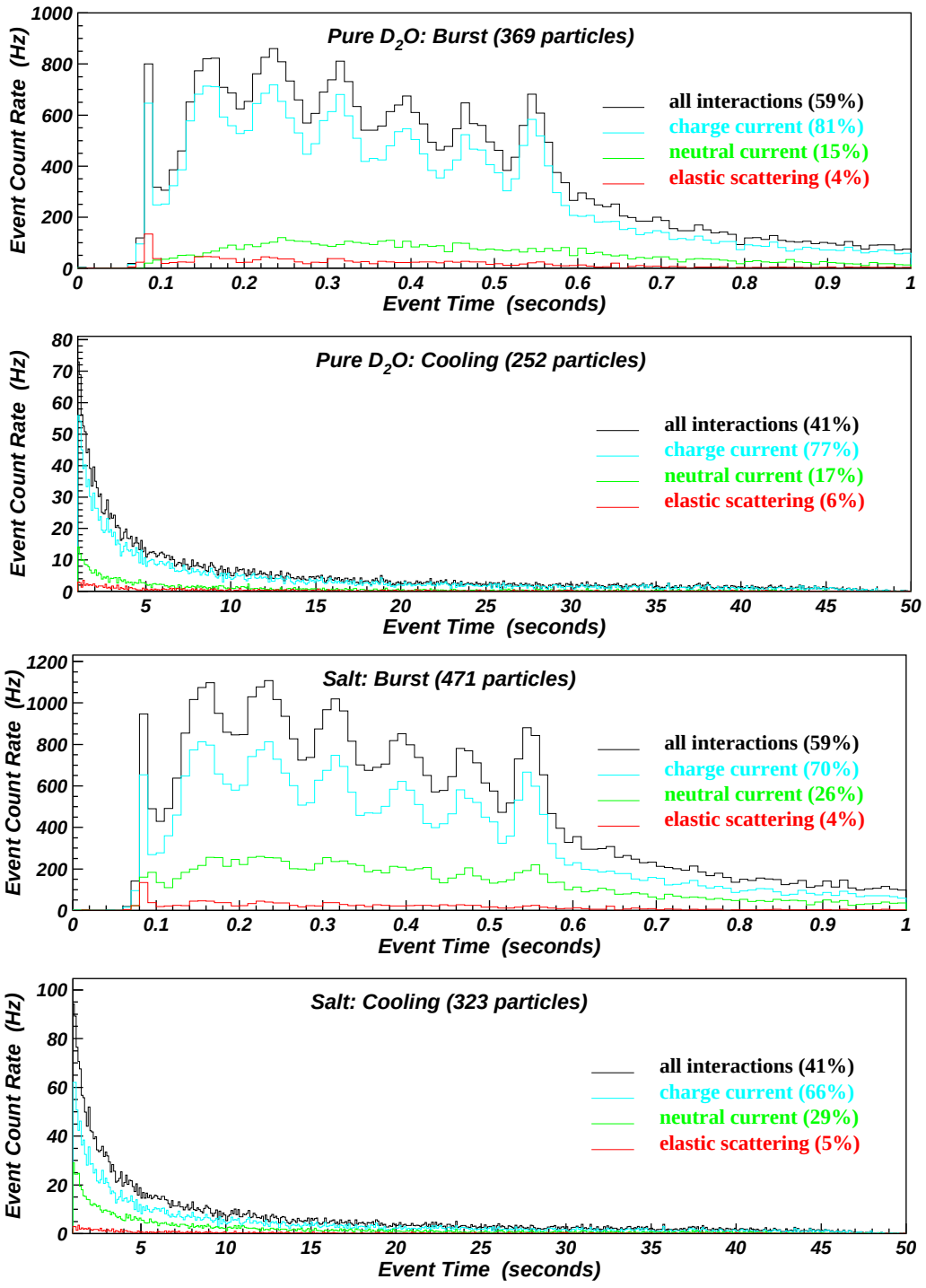

Figure 7.6: SNO supernova detected particle count rate above NHIT = 16 PMTs according to Burrows' model for the different interaction types. The top two plots show the expected signal using only pure D_2O in the detector, while the bottom two plots show the signal with salt added to the D_2O volume. In both cases, 100 supernovae at 10 kpc are simulated, and the plots show the signal scaled down to 1 supernova at 10 kpc.

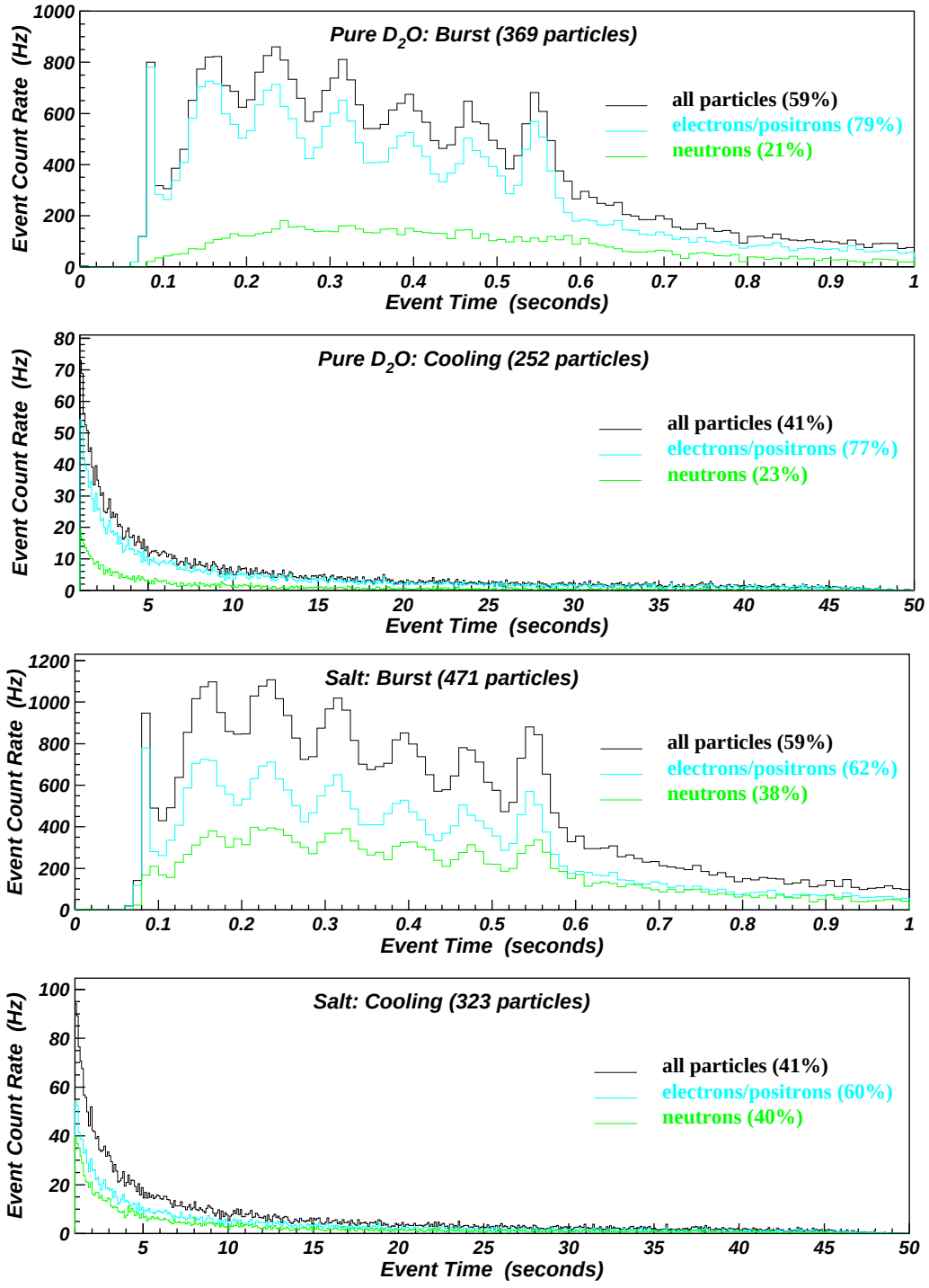

Figure 7.7: SNO supernova detected particle count rate above NHIT = 16 PMTs according to Burrows' model at 10 kpc for the different particle types. The top two plots show the expected signal using only pure D_2O in the detector, while the bottom two plots show the signal with salt added to the D_2O volume. In both cases, 100 supernovae at 10 kpc are simulated, and the plots show the signal scaled down to 1 supernova at 10 kpc.

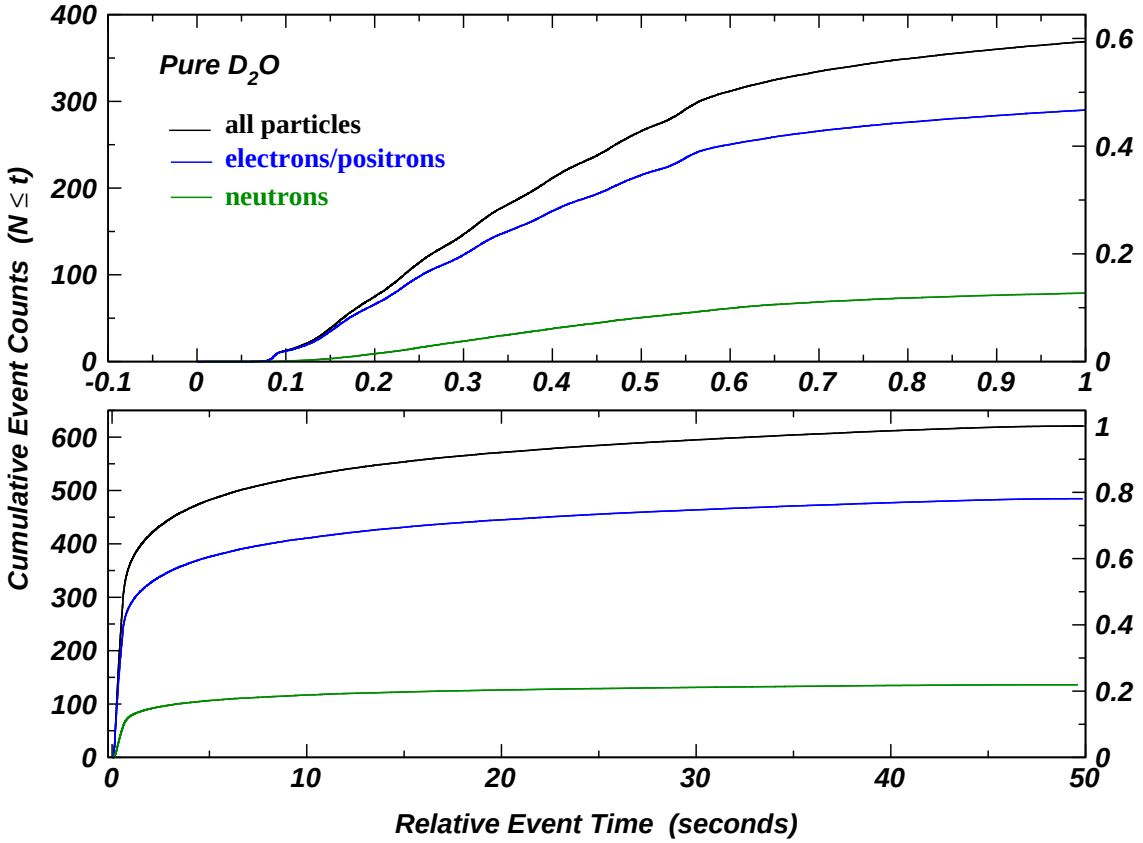

Figure 7.8: Cumulative SNO supernova detected particle count rate above the detector hardware threshold of 16 PMTs according to Burrows' model at 10 kpc for the different particle types during the pure D_2O phase. The top plot shows the accumulated counts in the first 1 second after core bounce, whereas the bottom plot shows the entire time range of the burst. On each graph, the total number of events is indicated on the left-hand y-axis, while the y-axis on the right-hand side denotes the count fraction of the total burst.

is shown in Figure 7.10. Compared to the high-statistics data set that uses neutrinos from 100 supernovae, the underlying distribution is not as clear. However, even with the lower statistics, it is still possible to discern a slight enhancement in the initial signal due to the ν_e signal from neutronization in the collapsing core of the supernova. As well, the signal is clearly higher before the explosion at 550 ms than after the explosion. Therefore, it should be straightforward for SNO to observe this feature of the delayed supernova

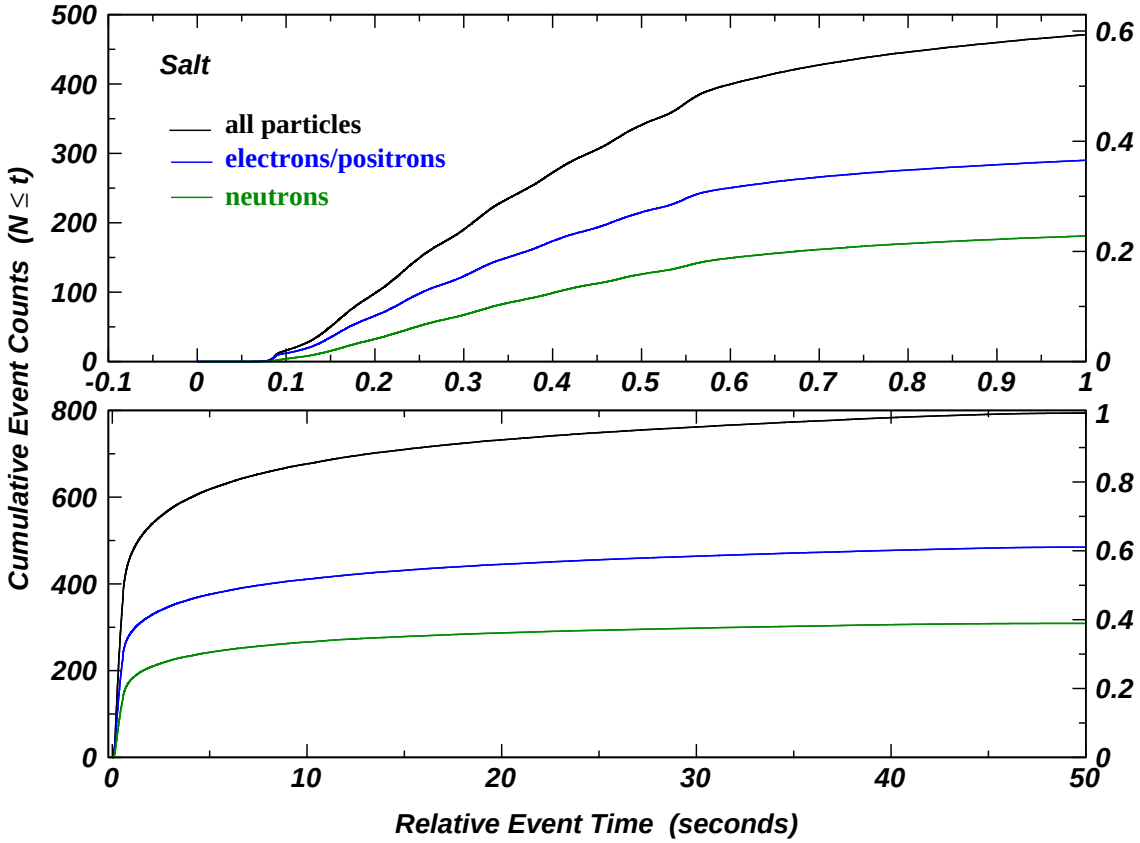

Figure 7.9: Cumulative SNO supernova detected particle count rate above the detector hardware threshold of 16 PMTs according to Burrows' model at 10 kpc for the different particle types during the salt phase. The top plot shows the accumulated counts in the first 1 second after core bounce, whereas the bottom plot shows the entire time range of the burst. On each graph, the total number of events is indicated on the left-hand y-axis, while the y-axis on the right-hand side denotes the count fraction of the total burst.

explosion mechanism. Structure in the signal that occurs on timescales of 100 ms, such as the pulsations that are included in the Burrows model, may be difficult to distinguish.

7.3.3 Prompt Signal

In addition to the time evolution of the supernova signal, it is also useful to consider the detailed composition of the prompt signal. Information about the neutronization process

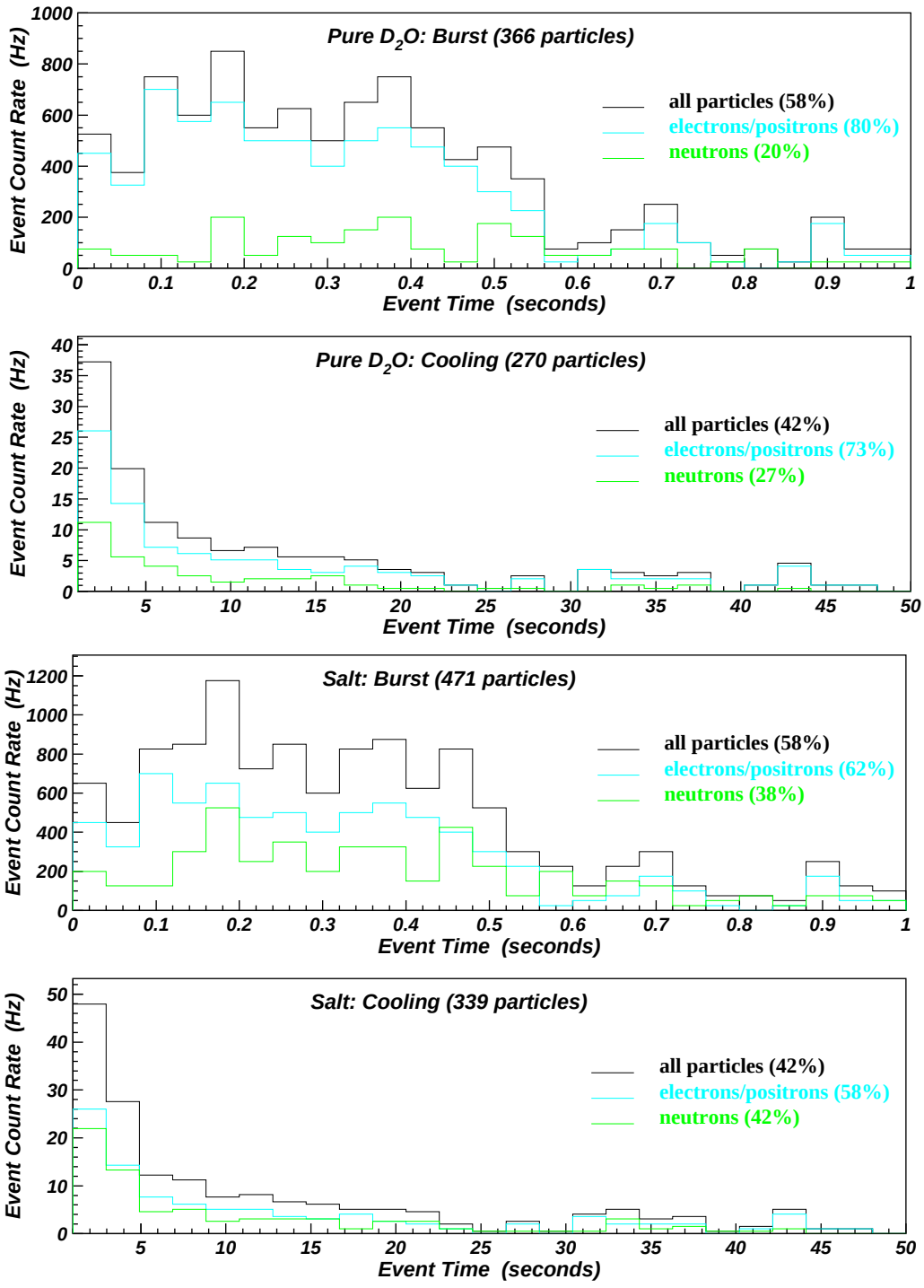

Figure 7.10: SNO supernova detected particle count rate above NHIT = 16 PMTs according to Burrows' model for the different particle types using only neutrinos from a single supernova at 10 kpc. The top two plots show the expected signal using only pure D_2O in the detector, while the bottom two plots show the signal with salt added to the D_2O volume.

during core collapse may be contained in the events recorded in the first 100 ms of the burst. According to the Burrows model, 10–12 events from ν_e neutrino interactions are expected within 100 ms of the onset of the signal for a supernova at 10 kpc. Of the entire signal over that period, 92% of the events above the detector hardware threshold are due to reactions with electron neutrinos in the pure D_2O phase, whereas 90% of the events are due to reactions with electron neutrinos in the salt phase. In contrast, the Beacom and Vogel signal does not include any contribution due to the neutronization process and so acts as a baseline prediction. In the scenario where the supernova signal is not enhanced by contributions from the neutronization process, roughly 16% of the signal is due to ν_e neutrinos during the pure D_2O phase and 13% of the signal is due to ν_e neutrinos during the salt phase. The results for both models are summarized in Table 7.5.

7.4 SNO Supernova NHIT Spectrum

The number of PMTs that receive light in a given event is referred to as the "NHIT" of the event, and is directly related to the energy of that event. Regardless of supernova model or whether the detector is being operated with pure D_2O or salt, there are two main features prominent in the NHIT spectrum: a peak at low NHIT values superimposed over a broad distribution. The peak at NHIT $<$ 100 PMTs is due mainly to the neutron signal in the D_2O volume. The neutron capture signal in SNO does not preserve information about the energy of the parent neutrino, therefore the shape of the neutron peak is not expected to vary significantly between models. In the case of the pure D_2O signal, there are actually two peaks at low NHIT. The lowest energy peak is due to neutron capture on the proton in the heavy water molecule, while a second higher energy peak is due to capture on the deuteron. For the salt phase, the first low energy peak is not expected because of the high neutron capture efficiency on chlorine.

SN Signal Component ($t \leq 100$ ms)	**Beacom Model**		**Burrows Model**	
	D_2O	**Salt**	**D_2O**	**Salt**
Neutrino:				
ν_e	1.48	1.71	9.55	11.55
$\overline{\nu}_e$	6.69	8.19	0.82	1.00
"ν_μ"	0.85	3.76	0.07	0.32
Region:				
D_2O region	3.42	8.06	8.84	11.27
H_2O region	5.59	5.59	1.58	1.58
AV region	0.01	0.01	0.02	0.02
Interaction:				
charged current	7.59	8.76	8.50	8.65
neutral current	0.92	4.39	0.38	2.67
elastic scattering	0.51	0.51	1.55	1.55
Particle:				
electron/positron	7.77	7.77	10.02	10.02
neutron	0.92	4.39	0.41	2.84
Total Signal:	**9.02**	**13.66**	**10.43**	**12.86**
$\rightarrow \nu_e$ fraction	**16.4%**	**12.5%**	**91.6%**	**89.8%**

Table 7.5: Comparison of the signal for relative time $t \leq 100$ ms above the detector hardware threshold between two generic supernova models at 10 kpc.

Čerenkov light from relativistic electrons and positrons comprise the broad distribution that extends to almost NHIT = 500. The peak of this distribution will vary between models depending on the neutrino temperatures used, and is mainly sensitive to the $\overline{\nu}_e$ neutrino temperature. Neutral current reactions involving oxygen, which are sensitive to the energy of "ν_μ" neutrinos, are not included in the SNO detection simulations. However, the most useful signatures of these reactions are the 5–10 MeV γ rays emitted in both the heavy- and light-water volumes. In terms of the NHIT spectrum, these γ rays would contribute to

the signal in the NHIT range of 35–70 PMTs[1], which is the same NHIT range spanned by the neutron peak during both the pure D_2O and salt running phases. The neutron NHIT spectrum is fairly well understood, so it is very likely that a significant γ-ray contribution from reactions involving oxygen would be measurable.

7.4.1 Beacom and Vogel Model

The expected NHIT distributions using the Beacom and Vogel model are shown in two sets of plots. Figure 7.11 illustrates the characteristics of the NHIT signal for running during the pure D_2O phase, while Figure 7.12 shows the same signal during the salt phase. As predicted, the neutron contribution is clearly situated at NHIT < 100 PMTs. Comparing the low NHIT peak in the two figures clearly shows the neutron detection enhancement during the salt phase. The peak of the broad electron/positron distribution is roughly NHIT $= 100$ in the Beacom and Vogel model, and remains the same in both detector running phases. The bottom graph on both figures indicates the strong $\overline{\nu}_e$ content of the high NHIT signal.

7.4.2 Burrows *et al.* Model

Compared to the Beacom and Vogel model, the shape of the neutron peaks for the Burrows model in the pure D_2O and salt signals is similar. However, since the neutrino temperatures used in this model are lower than those used by Beacom and Vogel, the electron/positron NHIT spectrum will tend to lower values. The peak of the Burrows electron/positron NHIT spectrum is roughly NHIT $\simeq 80$ PMTs, which is located lower than that of the Beacom and Vogel model. The SNO supernova detected particle NHIT distribution above NHIT $=$ 16 PMTs is shown in Figures 7.13 and 7.14. Figure 7.13 describes various components of the signal expected during the pure D_2O running phase, while the corresponding plots for

[1]The correlation between γ-ray energy and NHIT is 1 MeV $\simeq$ 7 PMTs. Fewer PMTs are hit for gamma-ray events than for electron/positron events because some energy is lost during Compton scattering.

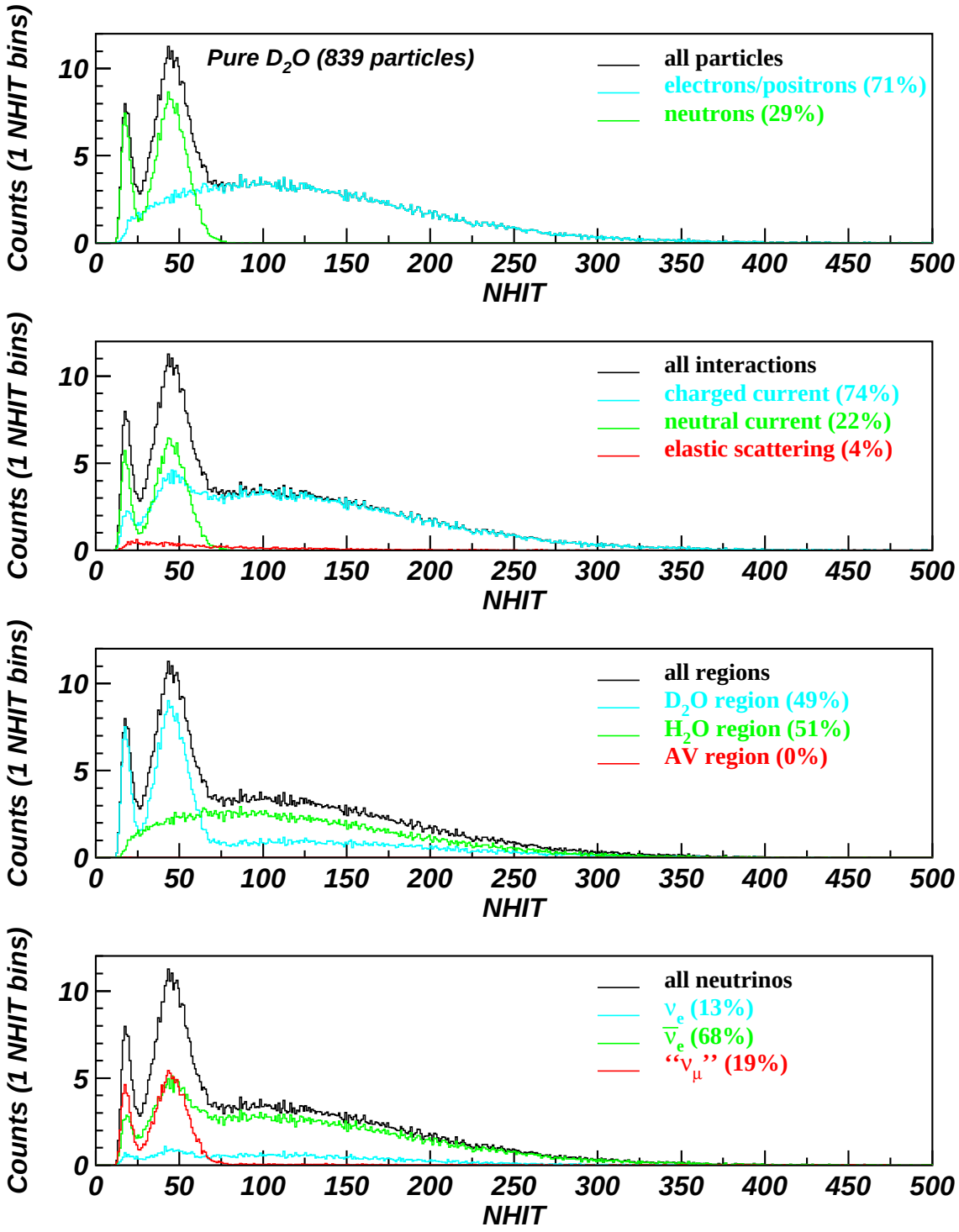

Figure 7.11: SNO supernova detected particle NHIT distribution above NHIT = 16 PMTs for the pure D_2O phase according to the Beacom and Vogel model. In all cases, 100 supernovae at 10 kpc are simulated, and the plots show the signal scaled down to 1 supernova at 10 kpc.

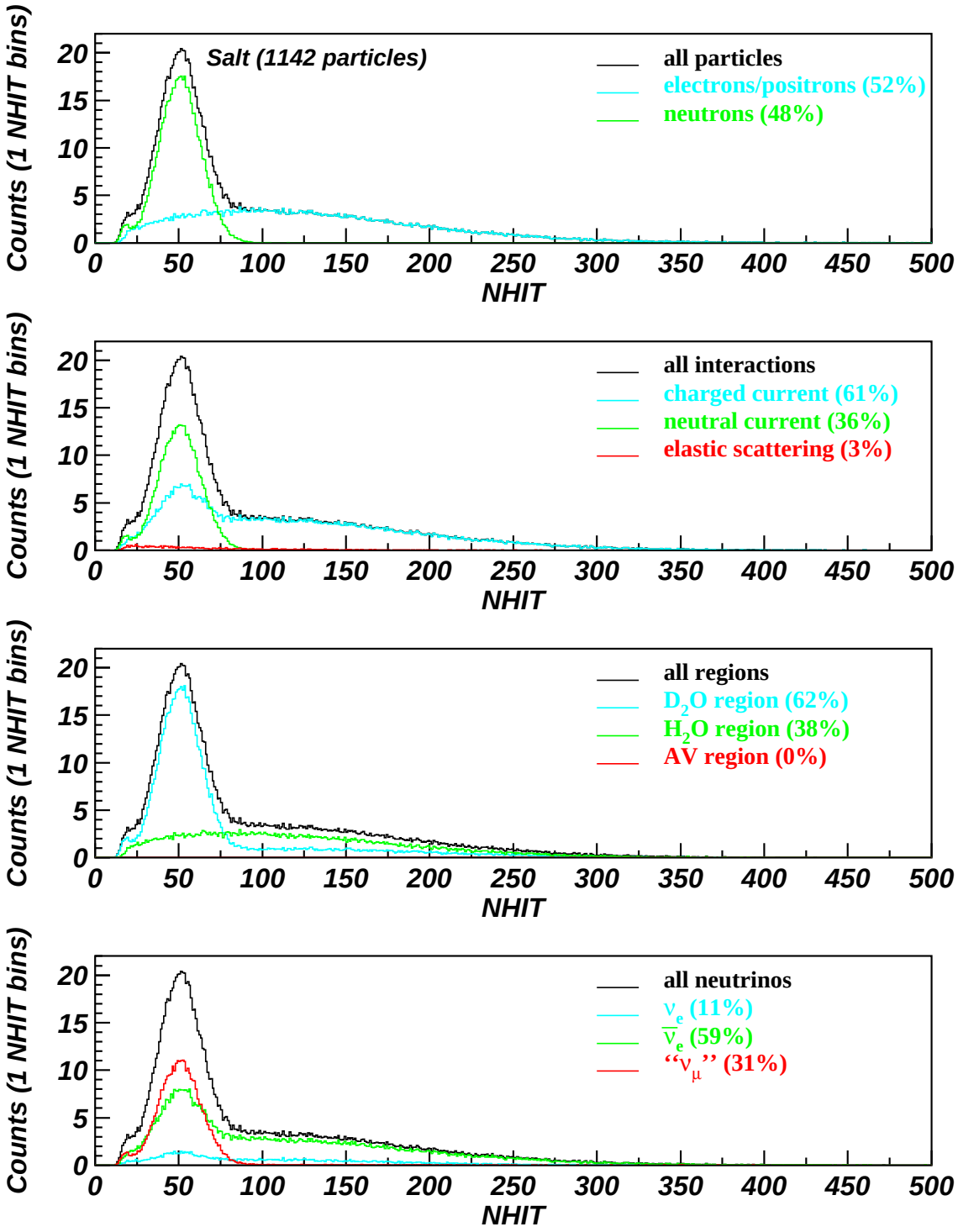

Figure 7.12: SNO supernova detected particle NHIT distribution above NHIT = 16 PMTs for the salt phase according to the Beacom and Vogel model. In all cases, 100 supernovae at 10 kpc are simulated, and the plots show the signal scaled down to 1 supernova at 10 kpc.

the salt phase are shown in Figure 7.14.

In pure D_2O, 46% of the observed signal above the hardware threshold is in the D_2O volume, while the remaining 54% of the signal is detected in the H_2O region. With the enhanced neutron detection provided by salt, most of the signal, 57%, can be found in the heavy water volume, whereas 43% will be observed in the light water volume.

7.5 SNO Supernova Vertex Position Distribution

The distribution of supernova event vertex positions for a supernova at 10 kpc detected during the pure D_2O phase is shown in Figure 7.15. In order to simplify the dimensions of the detector volume, the radius of the acrylic vessel, R_{AV}, is used to normalize the radial position, R/R_{AV}, where $R_{AV} = 600$ cm. This quantity is then cubed, $(R/R_{AV})^3$, so that shells of equal volume are plotted. In the pure D_2O phase, the vertex position distribution is relatively even across the two detector volumes, with a dip in the number of counts around $(R/R_{AV})^3 = 1$ due to the presence of the acrylic vessel. On average, there are 1.5 times as many counts per bin in the heavy-water region as compared to the light water region. The slight enhancement inside the AV becomes much more prominent when salt is added to the heavy-water region. Once again the distribution is roughly flat over the D_2O volume, but Figure 7.16 shows the number of counts per bin is approximately 2.5 times greater than the counts in the H_2O region. Compared to the Burrows model, the ratios of the counts in the two regions is approximately the same with the Beacom and Vogel model. For pure D_2O running, the count ratio is about 1.5, but for the salt phase, the ratio is even higher at around 2.7.

7.6 SNO Supernova Angular Distribution

The direction of a particle in the SNO detector is defined by a quantity called the direction cosine. Using the momentum vector, $\vec{p} = p_x\hat{\imath} + p_y\hat{\jmath} + p_z\hat{k}$, the components of the direction

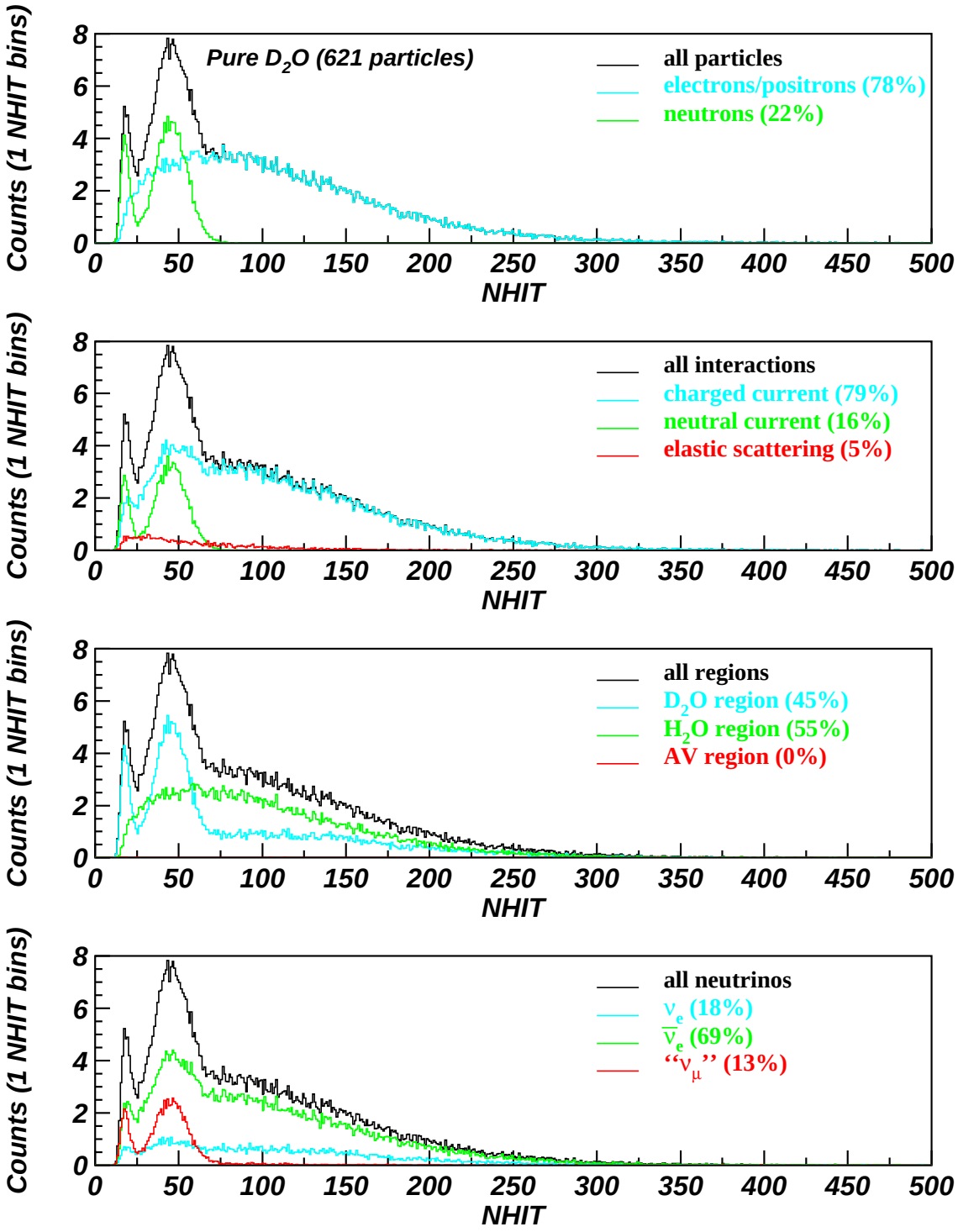

Figure 7.13: SNO supernova detected particle NHIT distribution above NHIT = 16 PMTs for the pure D_2O phase according to Burrows' model. In all cases, 100 supernovae at 10 kpc are simulated, and the plots show the signal scaled down to 1 supernova at 10 kpc.

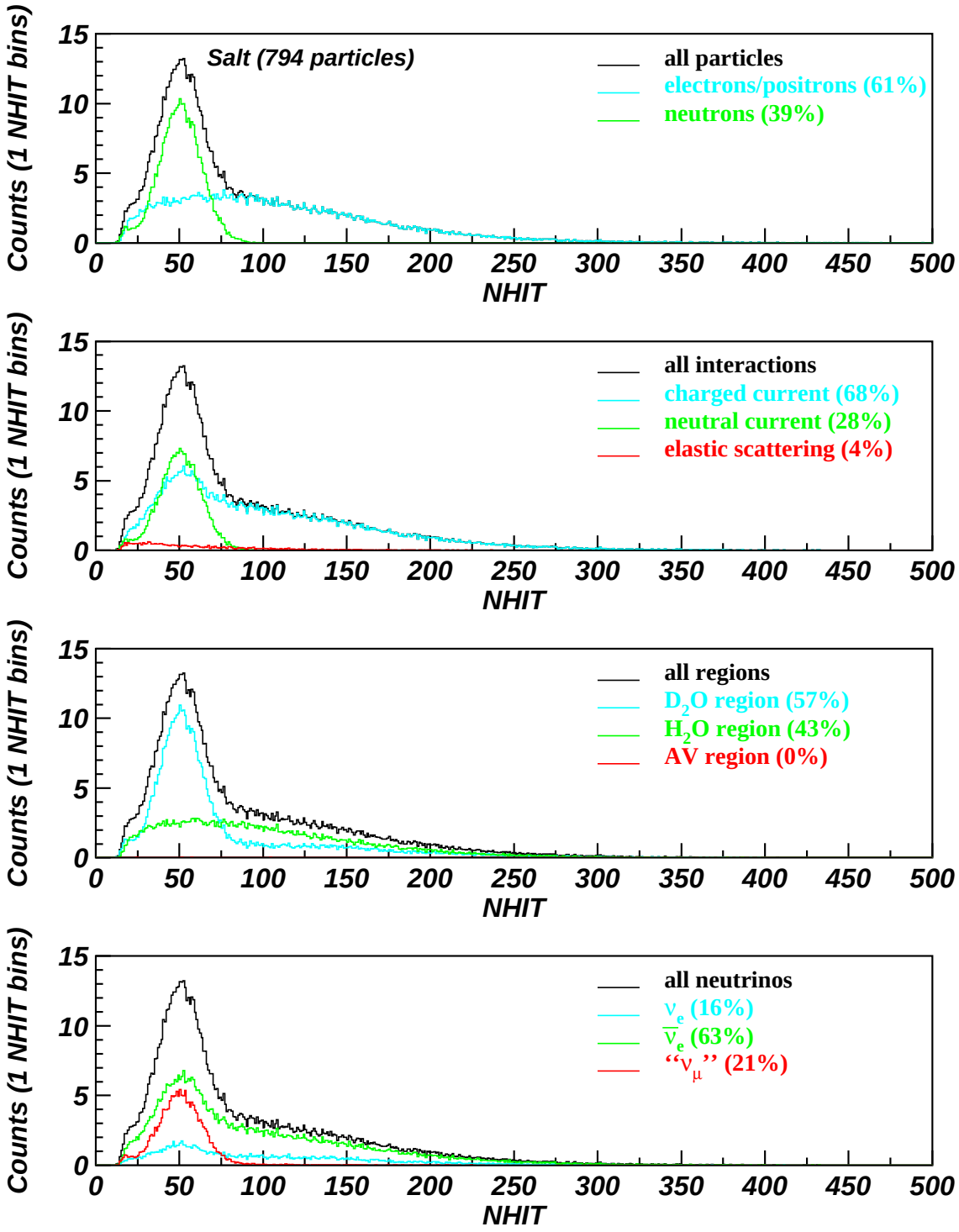

Figure 7.14: SNO supernova detected particle NHIT distribution above NHIT = 16 PMTs for the salt phase according to Burrows' model. In all cases, 100 supernovae at 10 kpc are simulated, and the plots show the signal scaled down to 1 supernova at 10 kpc.

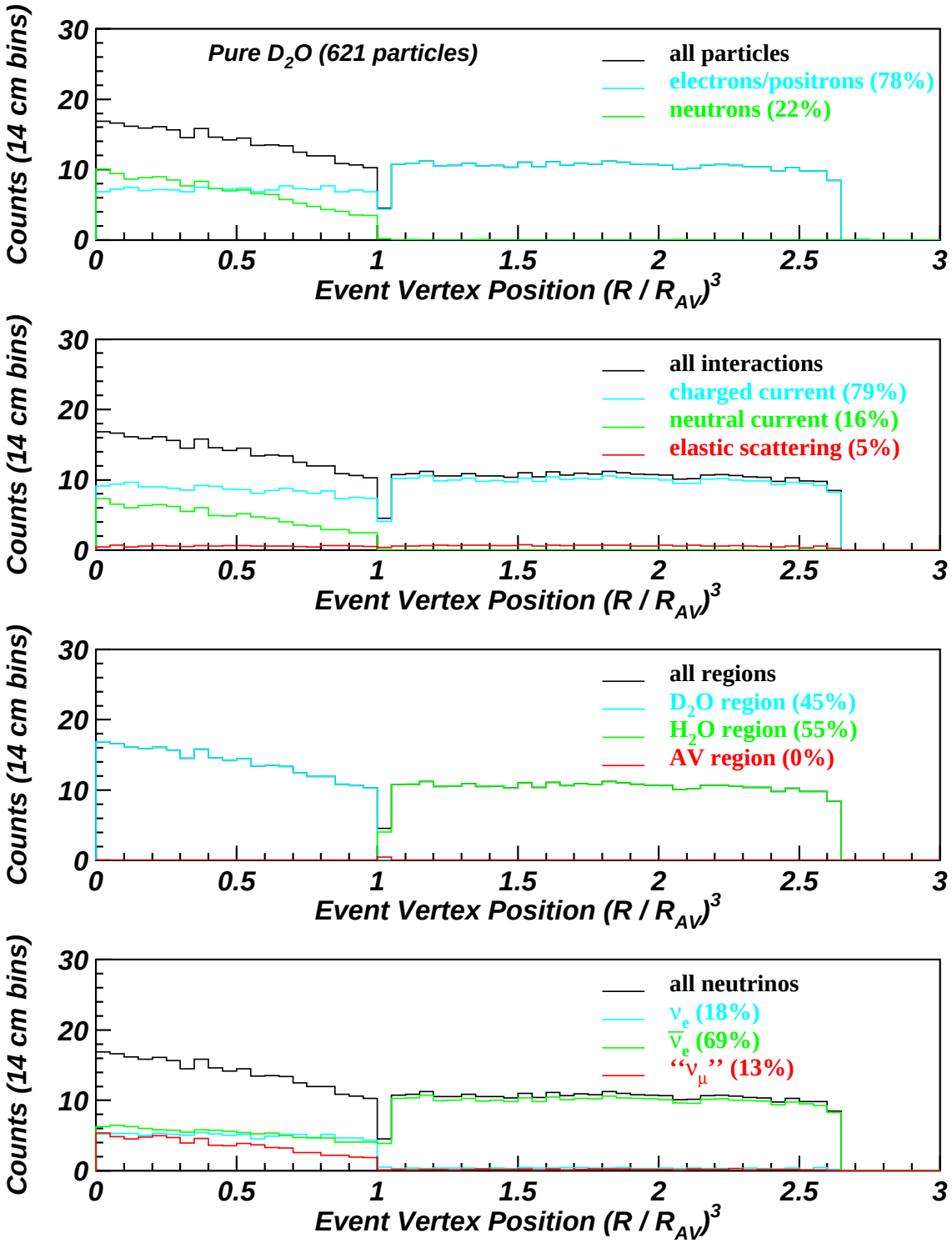

Figure 7.15: SNO supernova detected particle vertex position distribution above NHIT = 16 PMTs for the pure D_2O phase according to the model of Burrows *et al.* In all cases, 100 supernovae at 10 kpc are simulated, and the plots show the signal scaled down to 1 supernova at 10 kpc.

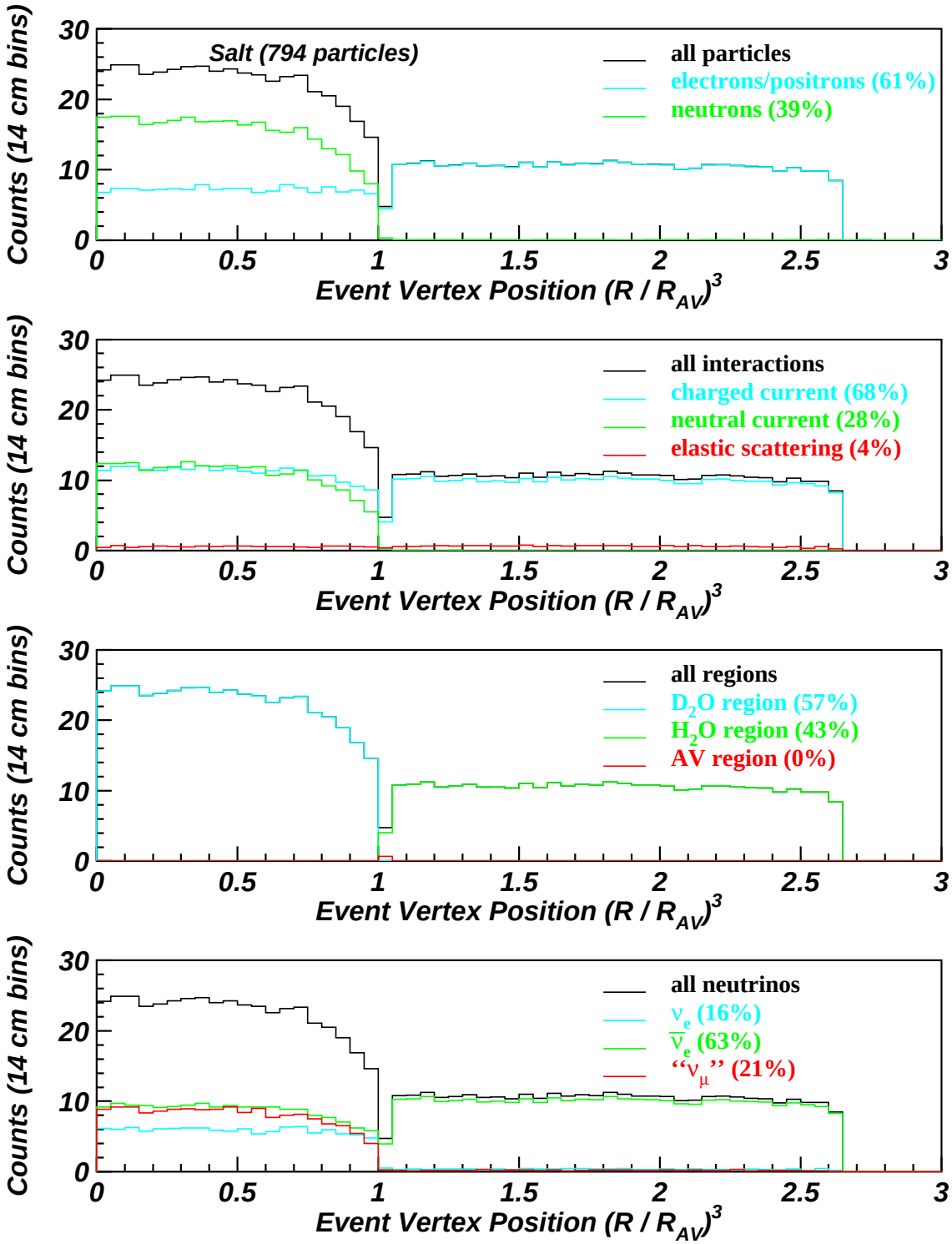

Figure 7.16: SNO supernova detected particle vertex position distribution above NHIT = 16 PMTs for the salt phase according to the model of Burrows *et al.* In all cases, 100 supernovae at 10 kpc are simulated, and the plots show the signal scaled down to 1 supernova at 10 kpc.

cosine vector are defined as:

$$\cos\alpha = \frac{p_x}{|\vec{p}|} \quad \cos\beta = \frac{p_y}{|\vec{p}|} \quad \cos\gamma = \frac{p_z}{|\vec{p}|}, \tag{7.1}$$

where $|\vec{p}| = \sqrt{p_x^2 + p_y^2 + p_z^2}$ is the magnitude of the momentum vector and the direction angles α, β and γ are the angles that the momentum vector makes with the positive x-, y-, and z-axes in detector coordinates. Similarly, the direction of the supernova can be defined in terms of a direction cosine vector with components $\cos\alpha_{SN}$, $\cos\beta_{SN}$ and $\cos\gamma_{SN}$. The angle θ_{SN} between the event direction and the direction of the supernova is determined by taking the dot product between the individual event direction cosine vector and the direction cosine vector of the supernova:

$$\cos\theta_{SN} = \cos\alpha\ \cos\alpha_{SN} + \cos\beta\ \cos\beta_{SN} + \cos\gamma\ \cos\gamma_{SN} \tag{7.2}$$

Events that are observed traveling in the forward direction away from supernova will have $\cos\theta_{SN} = +1$, while events traveling in the backward direction toward the supernova will have $\cos\theta_{SN} = -1$.

As outlined in Section 5.4, recoil electrons from elastic scattering interactions are expected to have an angular distribution that is very forward peaked. Figure 7.17 shows the detected particle $\cos\theta_{SN}$ distribution from reactions that are fully treated in the SNO supernova generator. As predicted, electrons from elastic scattering reactions above the NHIT = 16 detection energy threshold fall within 35°, or $\cos\theta_{SN} = 0.8$. The elastic scattering signal in the D_2O and H_2O regions contribute at roughly the same level.

Three charged current reactions have slight angular asymmetries, which cancel when summed together in the total signal. Photons resulting from neutron capture are emitted isotropically, therefore the angular distribution for the entire signal is a flat background over which the elastic scattering peak can be identified.

Introducing salt in the heavy-water volume serves only to enhance the flat background

without affecting the counts due to elastic scattering. Therefore, the ability to determine the direction of the supernova will be slightly worse during the salt phase due to the decreased signal-to-noise ratio.

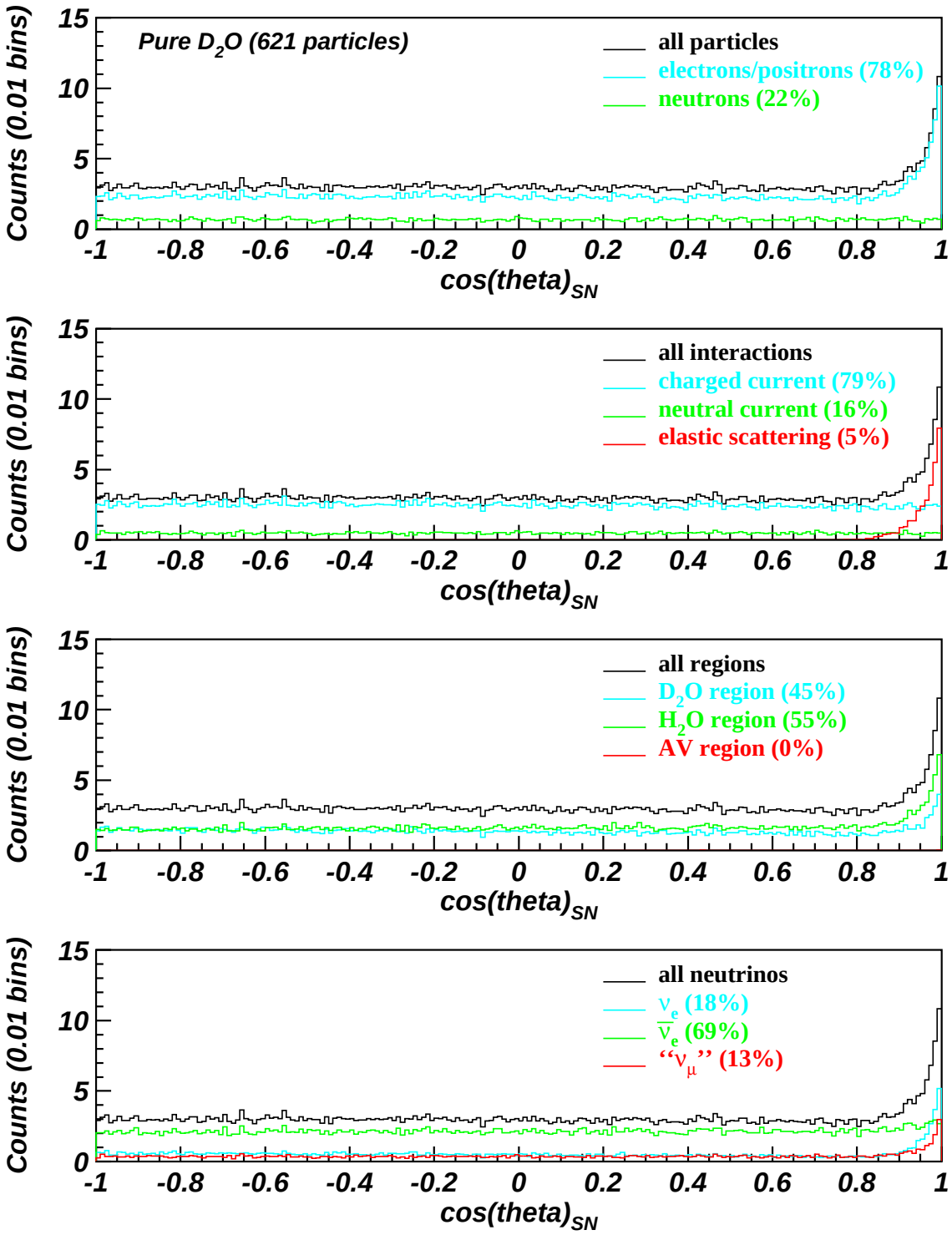

Figure 7.17: SNO supernova detected particle $\cos\theta_{SN}$ distribution above NHIT = 16 PMTs for the pure D_2O phase according to the model of Burrows *et al.* In all cases, 100 supernovae at 10 kpc are simulated, and the plots show the signal scaled down to 1 supernova at 10 kpc.

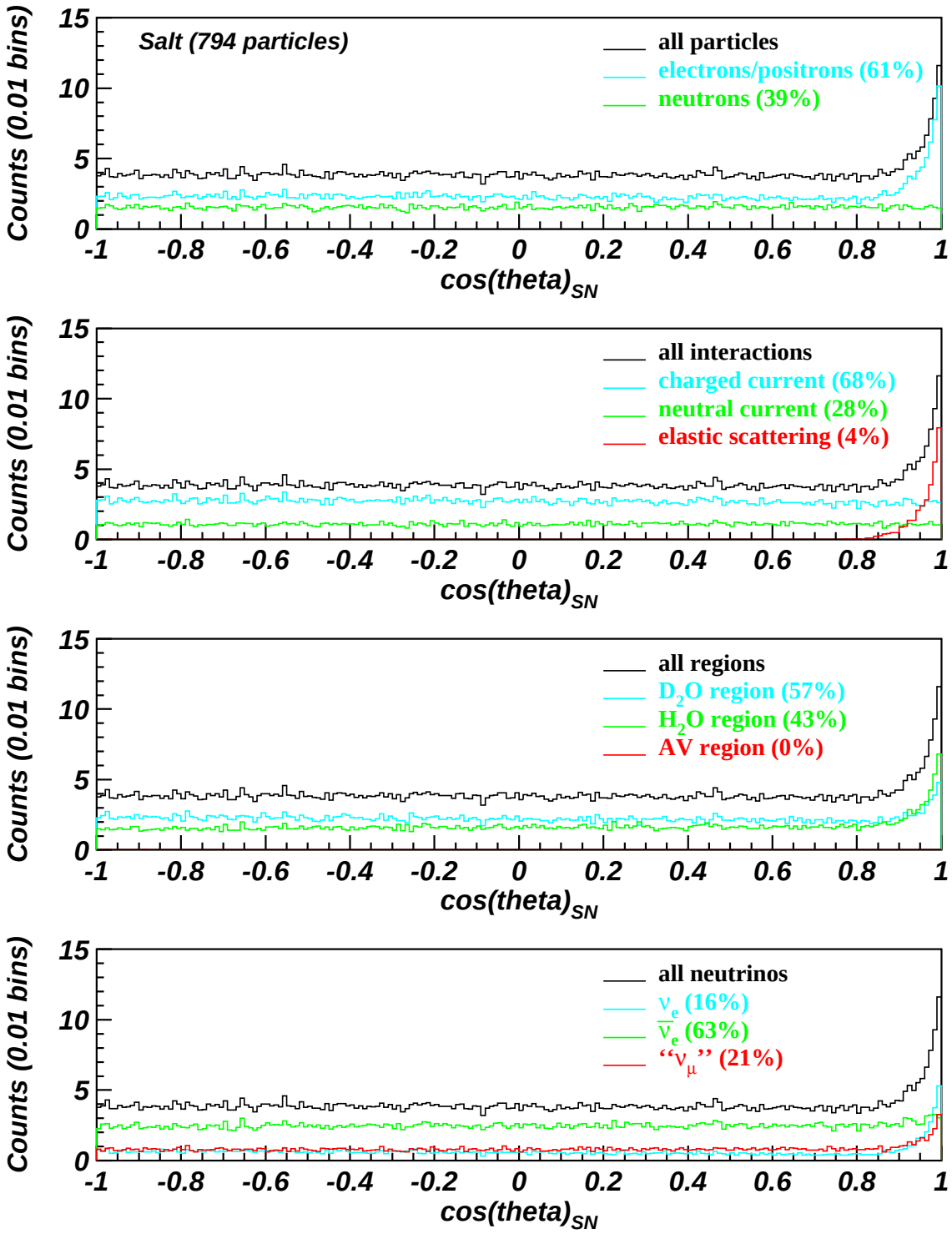

Figure 7.18: SNO supernova detected particle $\cos\theta_{SN}$ distribution above NHIT = 16 PMTs for the salt phase according to the model of Burrows *et al.* In all cases, 100 supernovae at 10 kpc are simulated, and the plots show the signal scaled down to 1 supernova at 10 kpc.

Chapter 8

SNO Supernova Analysis

8.1 Introduction

The Monte Carlo studies presented in Chapter 7 characterize the supernova neutrino signal in the absence of detector background events. Events from a number of sources of instrumental noise must be removed from the raw detector data before the physics signal can be extracted. A discussion of topics related to detector background events and the corresponding analysis energy threshold relevant to supernova neutrinos is presented in the sections that follow.

8.2 SNO Background Events

Two classes of background events exist in the SNO detector: instrumental backgrounds and physics backgrounds. Instrumental backgrounds are those events which are induced by the detector itself or the surrounding environment, and are not caused by any physics interaction. The category of physics backgrounds covers those events caused by physics processes that are not of interest for a particular analysis. For instance, physics backgrounds include the radioactive decay of contaminants in the detector, such as those discussed in Section 4.4. Another form of physics background is due to events that follow muons.

Studies of various background events in SNO have led to the development of a standardized set of data reduction cuts, which are made available to all collaboration members by means of the SNO database (see Section 4.10). Background events that fail these cuts

are not removed from the data but simply tagged. The SNO event rate is not so high that retaining these events is space prohibitive.

8.2.1 Instrumental Backgrounds

Several different sources of instrumental background events persist in the SNO detector. Actual light is produced by PMT flashers, PMT failures, some forms of high voltage breakdown and by static electric discharge across insulators in the detector. Other sources of instrumental background trigger the electronics discriminators due to electrical pickup.

8.2.1.1 PMT Flasher Events

The most consistent and potentially the most serious SNO background events are known as PMT "flashers". The exact mechanism of these events is not completely understood, but through some process a small amount of light is given off randomly by the PMT, originating possibly somewhere in its dynode structure. On average, each PMT emits light through this process approximately once per week, resulting in a detector-wide PMT flasher rate of one per minute [113]. Bursts of flasher PMT events have also been correlated with mine blasting activity. The number of PMTs that are hit in a flasher event is between 20–500 PMTs, which covers not only the solar neutrino spectrum but closely matches the expected supernova neutrino NHIT range.

Fortunately, most PMT flasher events have a distinctive topology. The signal has two identifiable components: a small cluster of PMTs is hit on one side of the detector and a second set of hit PMTs diametrically opposite have a characteristic diffuse elliptical pattern. The small cluster of PMTs often has one hit with very high charge (the flasher PMT) accompanied by a number of adjacent hits with zero charge consistent with electronic pickup. The separation in time between the early cluster of PMTs and the later hits is of order 70 ns, which corresponds to the transit time for light to travel across from one side of the PSUP to the other.

A number of cuts were developed by the collaboration to eliminate flasher events by exploiting the charge and PMT clustering information. The QCluster cut [114] identifies the cluster of pickup hits around the high charge flasher PMT. A second independent cut also examines the event geometry. The FGC cut [115] identifies flasher events by looking for hit clusters and comparing the cluster position to the rest of the PMTs in an event. Flasher events are also tagged by the QvT cut [116] using the fact that light from the flasher event is emitted over a longer period than is expected for a Čerenkov event. Further discrimination is provided by a HIB–9000 hydrophone, which is immersed in the light water to detect pressure waves caused by events such as mine blasting.

8.2.1.2 PMT Failure Events

Another class of instrumental background event is thought to be associated with the failure of PMTs. Sometimes when a PMT fails, light is produced in the detector for a relatively long period. These events are also known as "flat TAC" events (where TAC refers to uncalibrated PMT time), and are characterized by a roughly equal number of PMT hits at all times within an event. PMT failure events are relatively rare. The measured PMT failure rate in the SNO detector is 0.7% per year and increasing [117].

Events due to PMT failure are mainly removed by two cuts that examine the time structure of the PMT hits within an event. The two cuts are the ITC cut [118] and the FTS cut [119].

8.2.1.3 High Voltage Breakdown

The underwater (wet end) connection between the PMT base and the high voltage/signal cable does not hold high voltage reliably in the presence of ultra-pure, degassed water. Since the connectors were fastened before the PMTs were submerged in water, some air was trapped in the open volume of the connector. When these connectors were then surrounded by degassed water, the trapped air gradually leaked out, and the lower gas

pressure that resulted made the connector more susceptible to high voltage breakdown. The long-term solution to this problem was to regas the water with pure nitrogen gas. Originally, the water was degassed in order to reduce radioactivity and inhibit biological growth, and neither reason is compromised with the introduction of pure nitrogen gas from liquid nitrogen boil-off. While some wet-end breakdown events still occur, they are for the most part relatively rare.

High voltage breakdown can also occur where the high voltage/signal cables are connected to the electronics PMTIC high voltage cards (dry end). In this case, the breakdown can be due to a damaged high voltage cable or improper connection. When dry-end breakdown occurs, a particular channel can often be isolated as the cause and a repair can be made.

In the SNO solar neutrino analysis, background events due to both wet- and dry-end breakdown are removed using a series of burst cuts. However, supernova events by their nature are bursts, therefore cuts that remove events based on the relative timing of events cannot be used. Noise events due to dry-end breakdown typically occur within a few electronics cards within a single crate and can be identified using the The Crate Isotropy cut [120]. A large fraction of high voltage breakdown events can be tagged by the AMB cut [121], which examines the shape of the ESUM signal to determine if the number of PMTs hit in the event is consistent with a standard physics event. In fact, the AMB cut has proven to be efficient at tagging almost all instrumental background events.

8.2.1.4 Neck Events

Another background in the SNO detector is possibly due to static discharge in the vicinity of the chimney (or neck) region of the acrylic vessel. Since the acrylic used in the construction of the chimney does not transmit UV light, the light produced due to static discharge is directed downward to the PMTs located at the bottom of the detector. To identify events

due to this source, four PMTs were installed in the chimney to tag light originating in the neck region. The Neck cut [122] requires that either both neck PMTs register a hit or that one PMT signal has large charge and occurs early in time with respect to the other hits in the event.

8.2.1.5 Electronic Pickup

There are several sources of electronic pickup in the SNO detector, including high voltage breakdown, static discharge, and electrical equipment. These cause the channel discriminators to trigger in the absence of light in the detector. The charge of these signals integrates to zero, a feature that is used to tag pickup events. The QvNHIT cut [123] removes events which have anomalously low charge for the number of PMTs participating in the event. The Crate Isotropy cut [120] also makes use of that fact that electronic pickup often induce signal events in just one electronics crate. The ROF cut [124] is able to isolate events in which there is pickup up in the first and last electronic cards in an electronics crate.

8.2.2 Physics Backgrounds

Due to the relatively short duration of the expected supernova signal, there are few physics backgrounds to contend with. For instance, the detection rate of solar neutrinos in the SNO detector is on the order of 0.01 events/minute [125] at the proposed supernova analysis threshold. Therefore, solar neutrino events do not constitute a background to the analysis of a supernova burst. However, there is one class of physics events associated with muons that does provide a small background.

8.2.2.1 Muon Spallation

In SNO, spallation occurs when a high energy muon undergoes inelastic scattering with an oxygen, deuterium or hydrogen nucleus in the detector volume, producing free neutrons and radioactive nuclei. For instance, spallation of ^{16}O may produce ^{9}Li, which can decay

by emitting a neutron and has a relatively long half-life, $\tau_{1/2} = 0.178$ s. Examples of muon-induced spallation products that decay by β emission include ^{16}N and ^{11}Be, with half-lives of 7.13 s and 13.8 s, respectively [126].

In order to monitor the background due to the presence of muons, a number of pieces of information are used to tag muon events. The first indication of a muon event is provided in the light water region surrounding the PSUP. There, the outward-looking (OWL) PMTs receive Čerenkov light as the muon passes through the light water. At least 5 of the 91 OWL PMTs are required to have a signal by the muon identification algorithm. The muon event signal measured by the main array of PMTs is often quite spectacular, with nearly all of the PMTs registering a hit. However, in some events where the muon travels close to the PMT array through the inner H_2O volume, fewer PMTs are hit. A signal from 150 PMTs is sufficient to identify muons when used in conjunction with the OWL PMT information. This then allows the subsequent muon spallation events to be identified.

8.3 SNO Supernova Analysis Threshold

Using the set of data reduction cuts deemed appropriate for a burst analysis, the rate of background events is investigated over the period from November 2, 1999 to January 15, 2001.

The most meaningful measure of the background is obtained by considering the number of events that pass the data reduction cuts during a set of well-understood running conditions. To this end, 245.61 days of data used for the solar neutrino analysis[1] are used to determine the supernova analysis threshold. Figure 8.1 shows the average residual instrumental background event rate for various analysis threshold NHIT threshold settings. Since a supernova burst is expected to last for approximately 1 minute, the background

[1] The livetime quoted for the solar neutrino analysis using these same data set is 240.95 days. However, an additional set of burst cuts that are not used in this analysis are employed to further reduce the solar neutrino data set.

event data are presented as the number of background events per minute. For subsequent analysis, the NHIT threshold is chosen such that on average one background event or fewer is present in a supernova burst above the NHIT threshold and after the data reduction cuts have been applied. Since the supernova signal has a large contribution due to neutrons at NHIT $\approx$ 50 PMTs (see Section 7.4), it was felt that one background event was an acceptable compromise to ensure that a substantial portion of the neutron peak remained for analysis. Using an analysis threshold of 34 PMTs, a livetime weighted average background event rate of 0.96 $\pm$ 0.09 events/minute is obtained. Therefore, a value of NHIT=34 is adopted as the supernova analysis threshold setting, and is used in the SNO supernova online burst monitor that is discussed in Chapter 9. This NHIT=34 threshold corresponds roughly to an energy threshold of 3.8 MeV.

Having established the analysis NHIT threshold, Figure 8.2 shows the average background event rate above the NHIT=34 analysis threshold as a function of time during the period from November 2, 1999 to January 15, 2000. It appears that after experiencing relatively high event rates during the first 50–60 days of running, the detector event rate above NHIT=34 reached an average plateau of approximately 2–3 events/minute. However, a slight downward trend is observed in the event rate above both the NHIT=34 threshold and the data reduction cuts. Occasional periods of high event rates that decrease quickly are due to lab power interruptions, after which the detector is typically noisier. The abnormally high average event rate on November 26, 1999 (day number 25) is the result of unstable detector conditions in PMTs that are not used for the solar neutrino analysis. This data is not used for the supernova neutrino burst search in Chapter 10. The relatively low average event rate on February 14, 2000 (day number 105) is likely due to the fact that the run was less than 1 hour long.

It should also be noted that the analysis threshold for an actual supernova event will likely be determined based on the background event rate experienced at the time of the

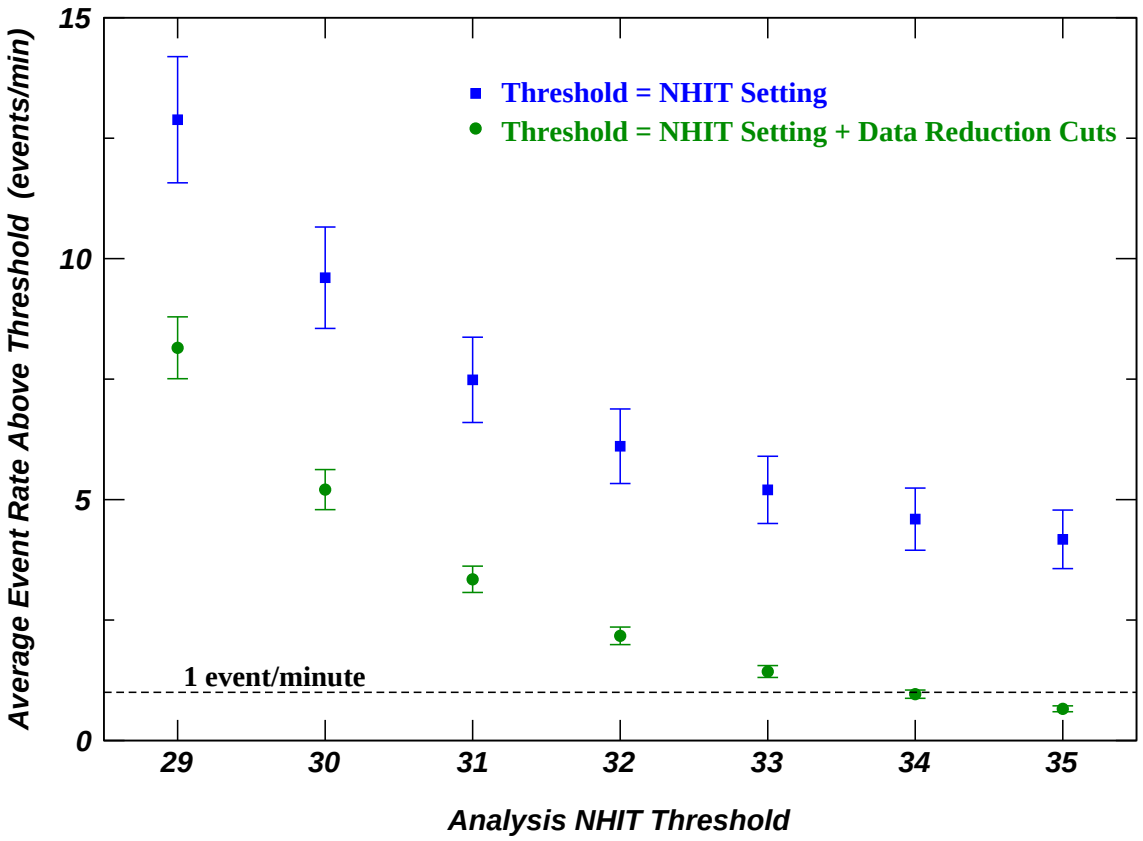

Figure 8.1: Average background event rate for various analysis NHIT threshold settings using data chosen for the solar neutrino analysis. The choice of NHIT=34 is adopted for the successive analyses.

burst. In many of the more recent data sets analyzed, a threshold of 30–31 PMTs is sufficient to restrict the background event rate to approximately 1 event/minute. Therefore, in many instances an analysis threshold of less than 34 PMTs would be possible.

The data used in this background study are taken exclusively during the pure D_2O mode of operation, and in the strictest sense may only be applied to studies of the supernova signal in that mode. However, initial studies of the salt data indicate that the analysis threshold determined for analyzing data gathered in the pure D_2O phase is also valid for analyzing salt data. Results from background studies performed on a small number of stable salt runs

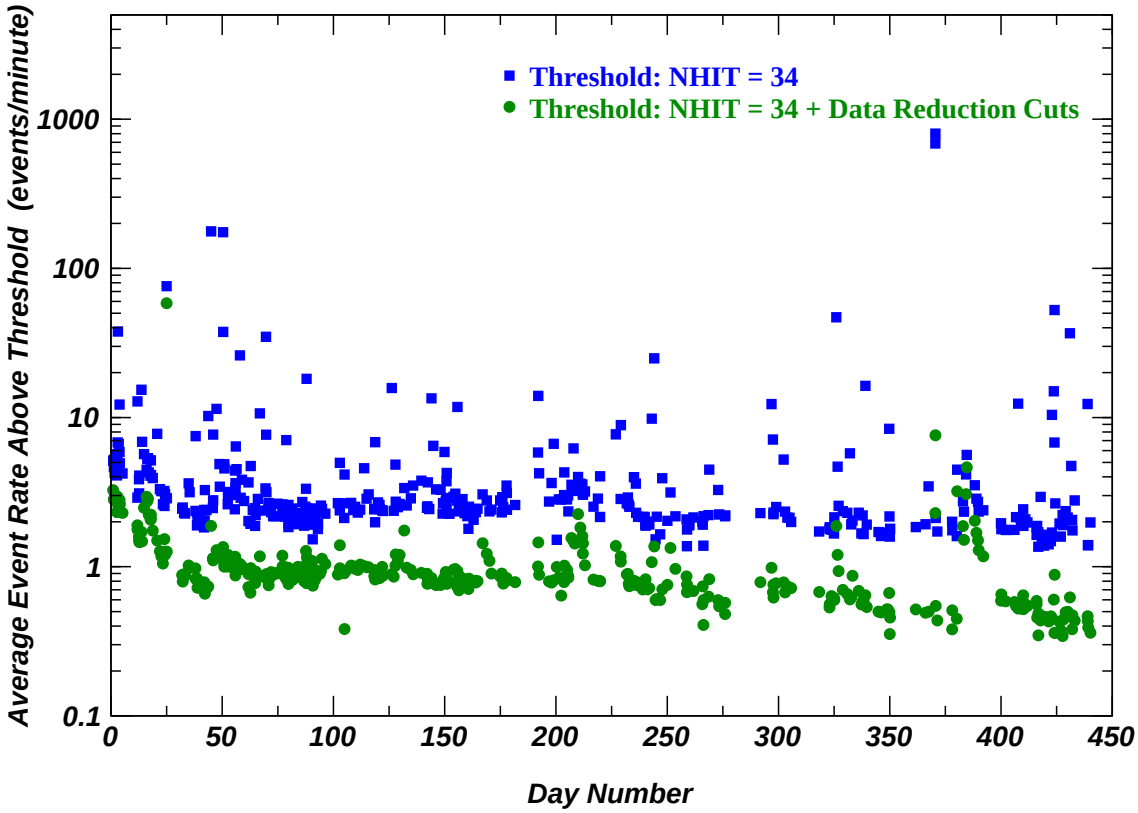

Figure 8.2: Average background event rate above the NHIT=34 analysis threshold as a function of time during the period from November 2, 1999 to January 15, 2001 using data chosen for the solar neutrino analysis. The abnormally high circle data point on day number 25 is due to detector instabilities.

show an average event rate of 1.3 events/minute above NHIT=34 and 0.35 events/minute above NHIT=34 and that pass the data reduction cuts. Events recorded using the neutral current detectors will not experience many of the instrumental backgrounds described above. Therefore, a separate investigation will be necessary in order to characterize the supernova neutrino analysis threshold for data taken using the NCDs.

8.4 Supernova Signal Above Analysis Threshold

The number of final state particle counts expected above the supernova neutrino analysis threshold of 34 PMTs for both the Beacom and Vogel model and the Burrows model is presented in the sections that follow. Since the analysis threshold to be used during NCD operation cannot be determined at this time, only predictions for the pure D_2O and salt running modes are discussed.

8.4.1 Beacom and Vogel Model

Above the supernova analysis threshold of 34 PMTs, Monte Carlo simulations of the supernova signal indicate that 740 counts are expected during the pure D_2O phase and 1060 counts are expected during the salt phase according to the Beacom and Vogel model for a supernova at 10 kpc. The observed counts above the analysis threshold are summarized in Table 8.1. According to the estimates of the observed signal due to reactions involving oxygen (see Appendix C), an average of 53 additional events are expected during the pure D_2O phase and 65 events are expected during the salt phase for a supernova at 10 kpc. Therefore, the best estimate for the total signal for a supernova at 10 kpc is 793 counts during pure D_2O operation and 1126 counts during salt operation according to the Beacom and Vogel model. These observed count values correspond to 58.5% and 83.0% of the total signal for pure D_2O and salt, respectively.

As discussed in Chapter 7, the electron antineutrino signal constitutes the majority of the signal in the light-water region. A total of 8 electron/positron events and 20 γ-ray events are expected in the H_2O region due to reactions with oxygen. Combining those events with the 392 positrons produced via the $\overline{\nu}_e + p \rightarrow n + e^+$ reaction and the 15 electrons produced through the $\nu + e^- \rightarrow \nu + e^-$ reaction yields a total of 398 events in the light water region due to interactions with $\overline{\nu}_e$ neutrinos for a supernova at 10 kpc. Therefore, according to the Beacom and Vogel model, approximately 91.5% of the signal in the H_2O region is due

Reaction	**Reaction Region**	**SNO Counts (all time)**	
		D_2O	**Salt**
Charged Current:	*total*	*586.28*	*664.26*
$\overline{\nu}_e + p \rightarrow n + e^+$	H_2O	392.09	392.09
$\nu_e + d \rightarrow p + p + e^-$	D_2O	76.26	76.26
$\overline{\nu}_e + d \rightarrow n + n + e^+$	D_2O	117.93	195.91
Neutral Current:	*total*	*129.44*	*372.23*
$\nu_e + d \rightarrow \nu_e + p + n$	D_2O	9.46	26.30
$\overline{\nu}_e + d \rightarrow \overline{\nu}_e + p + n$	D_2O	13.67	39.17
$\nu_{\mu,\tau} + d \rightarrow \nu_{\mu,\tau} + p + n$	D_2O	58.78	169.83
$\overline{\nu}_{\mu,\tau} + d \rightarrow \overline{\nu}_{\mu,\tau} + p + n$	D_2O	47.53	136.93
Elastic Scattering:	*total*	*24.68*	*24.68*
$\nu_e + e^- \rightarrow \nu_e + e^-$	D_2O	4.37	4.37
$\overline{\nu}_e + e^- \rightarrow \overline{\nu}_e + e^-$	D_2O	1.74	1.74
$\nu_{\mu,\tau} + e^- \rightarrow \nu_{\mu,\tau} + e^-$	D_2O	1.86	1.86
$\overline{\nu}_{\mu,\tau} + e^- \rightarrow \overline{\nu}_{\mu,\tau} + e^-$	D_2O	1.64	1.64
$\nu_e + e^- \rightarrow \nu_e + e^-$	H_2O	6.83	6.83
$\overline{\nu}_e + e^- \rightarrow \overline{\nu}_e + e^-$	H_2O	2.44	2.44
$\nu_{\mu,\tau} + e^- \rightarrow \nu_{\mu,\tau} + e^-$	H_2O	3.13	3.13
$\overline{\nu}_{\mu,\tau} + e^- \rightarrow \overline{\nu}_{\mu,\tau} + e^-$	H_2O	2.67	2.67
Total SNO ν_e Events		96.92	113.76
Total SNO $\overline{\nu}_e$ Events		527.87	631.35
Total SNO "ν_μ" Events		115.61	316.06
Total SNO D_2O Events		333.24	654.01
Total SNO H_2O Events		407.16	407.16
Total SNO $e^\pm$ Events		568.69	568.69
Total SNO n Events		171.72	492.36
Total SNO Events		**740.40**	**1061.17**
Total SNO Events (with O)		**793.49**	**1126.17**

Table 8.1: SNO supernova detected particle counts above NHIT = 34 PMTs using the Beacom and Vogel model for a supernova at 10 kpc. Two independent data sets with 100 supernovae at 10 kpc are used to calculate these count values.

to reactions with $\overline{\nu}_e$ neutrinos.

Setting the supernova analysis threshold at 34 PMTs affects both the observed average energy and the average angular distribution values for the observed signal due to elastic

Reaction	**Reaction Region**	$\langle$**NHIT**$_e\rangle$ **(PMTs)**	$\langle\cos\theta_e\rangle$
Charged Current:			
$\overline{\nu}_e + p \rightarrow n + e^+$	H_2O	132	0.0311
$\nu_e + d \rightarrow p + p + e^-$	D_2O	139	−0.1214
$\overline{\nu}_e + d \rightarrow n + n + e^+$	D_2O	178	−0.0620
Elastic Scattering:			
$\nu_e + e^- \rightarrow \nu_e + e^-$	D_2O	88	0.9758
$\overline{\nu}_e + e^- \rightarrow \overline{\nu}_e + e^-$	D_2O	90	0.9643
$\nu_{\mu,\tau} + e^- \rightarrow \nu_{\mu,\tau} + e^-$	D_2O	148	0.9766
$\overline{\nu}_{\mu,\tau} + e^- \rightarrow \overline{\nu}_{\mu,\tau} + e^-$	D_2O	144	0.9753
$\nu_e + e^- \rightarrow \nu_e + e^-$	H_2O	73	0.9791
$\overline{\nu}_e + e^- \rightarrow \overline{\nu}_e + e^-$	H_2O	76	0.9692
$\nu_{\mu,\tau} + e^- \rightarrow \nu_{\mu,\tau} + e^-$	H_2O	113	0.9801
$\overline{\nu}_{\mu,\tau} + e^- \rightarrow \overline{\nu}_{\mu,\tau} + e^-$	H_2O	109	0.9789

Table 8.2: Average NHIT and angular distribution values for final state electrons/positrons simulated in the SNO detector above the supernova analysis threshold of 34 PMTs according to the model of Beacom and Vogel.

scattering in particular. The energy and angular distribution properties of the final state electron and positron signals are summarized in Table 8.2. Since the detection of electrons and positrons is not affected by the addition of salt, only one set of values is necessary to describe the detector response. Results for events observed above the analysis threshold show that on average electrons from elastic scattering reactions are distributed within approximately $\theta = 15^\circ$ of the supernova direction ($\langle\cos\theta_e\rangle = 0.96$).

8.4.2 Burrows *et al.* Model

Above the supernova analysis threshold of 34 PMTs, Monte Carlo simulations of the supernova signal indicate that 545 counts are expected during the pure D_2O phase and 727 counts are expected during the salt phase according to the Burrows model for a supernova at 10 kpc. The observed counts above the analysis threshold are summarized in Table 8.3.

An estimated 10 additional events are also expected from reactions with oxygen during the pure D_2O phase for a supernova at 10 kpc (see Appendix C). The corresponding estimate with salt in the heavy water is that 11 events are expected from reactions with oxygen. Therefore, the total supernova signal for a burst at 10 kpc is 555 counts observed above the supernova analysis threshold during pure D_2O operation and 737 counts during salt operation. These observed count values correspond to 62.5% and 83.0% of the total detectable particle signal for pure D_2O and salt, respectively

Considering the electron antineutrino signal in the H_2O region, a total of 4 electron/positron events and 2 γ-ray events are expected from reactions with oxygen for a supernova at 10 kpc. Therefore a total of 298 $\overline{\nu}_e$ events are expected above the supernova analysis threshold for a supernova at 10 kpc. This corresponds to approximately 94.6% of the signal in the H_2O region.

The energy and angular distribution properties of the final state electron and positron signals using the Burrows model are summarized in Table 8.4. Results for events observed above the analysis threshold show that on average electrons from elastic scattering reactions are distributed within approximately $\theta = 15^\circ$ of the supernova direction ($\langle \cos\theta_e \rangle = 0.96$).

8.5 Signal Loss

Two analysis factors contribute to the loss of supernova signal. The first is the NHIT analysis threshold and the second is the effect of the data reduction cuts.

8.5.1 Analysis Threshold

The amount of supernova signal removed due to the analysis threshold of NHIT=34 PMTs is obtained by comparing the numbers of counts expected above the hardware threshold of NHIT=16 PMTs and the numbers of counts expected above the analysis threshold of NHIT=34 PMTs.

Reaction	**Reaction Region**	**SNO Counts (all time)**	
		D_2O	**Salt**
Charged Current:	*total*	*453.30*	*506.62*
$\overline{\nu}_e + p \rightarrow n + e^+$	H_2O	295.97	295.97
$\nu_e + d \rightarrow p + p + e^-$	D_2O	78.83	78.83
$\overline{\nu}_e + d \rightarrow n + n + e^+$	D_2O	78.50	131.82
Neutral Current:	*total*	*69.59*	*197.55*
$\nu_e + d \rightarrow \nu_e + p + n$	D_2O	9.62	27.40
$\overline{\nu}_e + d \rightarrow \overline{\nu}_e + p + n$	D_2O	9.83	27.70
$\nu_{\mu,\tau} + d \rightarrow \nu_{\mu,\tau} + p + n$	D_2O	26.80	75.77
$\overline{\nu}_{\mu,\tau} + d \rightarrow \overline{\nu}_{\mu,\tau} + p + n$	D_2O	23.34	66.68
Elastic Scattering:	*total*	*22.55*	*22.55*
$\nu_e + e^- \rightarrow \nu_e + e^-$	D_2O	5.05	5.05
$\overline{\nu}_e + e^- \rightarrow \overline{\nu}_e + e^-$	D_2O	1.39	1.39
$\nu_{\mu,\tau} + e^- \rightarrow \nu_{\mu,\tau} + e^-$	D_2O	1.34	1.34
$\overline{\nu}_{\mu,\tau} + e^- \rightarrow \overline{\nu}_{\mu,\tau} + e^-$	D_2O	1.28	1.28
$\nu_e + e^- \rightarrow \nu_e + e^-$	H_2O	7.30	7.30
$\overline{\nu}_e + e^- \rightarrow \overline{\nu}_e + e^-$	H_2O	1.95	1.95
$\nu_{\mu,\tau} + e^- \rightarrow \nu_{\mu,\tau} + e^-$	H_2O	2.38	2.38
$\overline{\nu}_{\mu,\tau} + e^- \rightarrow \overline{\nu}_{\mu,\tau} + e^-$	H_2O	1.86	1.86
Total SNO ν_e Events		100.80	118.08
Total SNO $\overline{\nu}_e$ Events		387.64	458.83
Total SNO "ν_μ" Events		57.00	149.31
Total SNO D_2O Events		235.98	417.26
Total SNO H_2O Events		309.46	309.46
Total SNO $e^{\pm}$ Events		447.81	447.81
Total SNO n Events		97.64	279.42
Total SNO Events		**545.44**	**726.72**
Total SNO Events (with O)		**555.14**	**737.37**

Table 8.3: SNO supernova detected particle counts above NHIT = 34 PMTs using the Burrows model for a supernova at 10 kpc. Two independent data sets with 100 supernovae at 10 kpc are used to calculate these count values.

For the Beacom and Vogel model, the loss during the pure D_2O phase corresponds to 11.7% of the observable supernova signal. In the operation mode with salt, 7.2% of the observable supernova signal is removed with an analysis threshold of 34 PMTs. Fewer

Reaction	**Reaction Region**	$\langle$**NHIT**$_e\rangle$ **(PMTs)**	$\langle\cos\theta_e\rangle$
Charged Current:			
$\overline{\nu}_e + p \rightarrow n + e^+$	H_2O	111	0.0141
$\nu_e + d \rightarrow p + p + e^-$	D_2O	134	-0.1195
$\overline{\nu}_e + d \rightarrow n + n + e^+$	D_2O	145	-0.0748
Elastic Scattering:			
$\nu_e + e^- \rightarrow \nu_e + e^-$	D_2O	84	0.9762
$\overline{\nu}_e + e^- \rightarrow \overline{\nu}_e + e^-$	D_2O	78	0.9643
$\nu_{\mu,\tau} + e^- \rightarrow \nu_{\mu,\tau} + e^-$	D_2O	105	0.9747
$\overline{\nu}_{\mu,\tau} + e^- \rightarrow \overline{\nu}_{\mu,\tau} + e^-$	D_2O	102	0.9732
$\nu_e + e^- \rightarrow \nu_e + e^-$	H_2O	71	0.9791
$\overline{\nu}_e + e^- \rightarrow \overline{\nu}_e + e^-$	H_2O	68	0.9688
$\nu_{\mu,\tau} + e^- \rightarrow \nu_{\mu,\tau} + e^-$	H_2O	84	0.9781
$\overline{\nu}_{\mu,\tau} + e^- \rightarrow \overline{\nu}_{\mu,\tau} + e^-$	H_2O	83	0.9769

Table 8.4: Average NHIT and angular distribution values for final state electrons/positrons simulated in the SNO detector above the supernova analysis threshold of 34 PMTs according to the Burrows model.

events are removed with the salt neutron detection option than for pure D_2O because the Compton scattered photons from neutron capture on salt have higher energies than those from neutron capture on deuterium.

Slightly higher values for the signal loss are obtained using the model of Burrows *et al.* since electron/positron events in that model tend to have lower energies that those in the Beacom and Vogel model. Using the Burrows model, the loss during the pure D_2O phase corresponds to 12.1% of the observable supernova signal; with salt, the signal loss is 8.6%.

8.5.2 Data Reduction Cuts

Relatively little signal loss is expected to be due to the data reduction cuts. Studies using ^{16}N calibration source data indicate that a volume-weighted signal loss of $0.44 \pm 0.01\%$ over the D_2O volume for the set of data reduction cuts listed in Section 8.2. In the H_2O region,

the signal loss is higher than in the central D_2O region, especially close to the PMTs, as is shown in Figure 8.3. The volume-weighted signal loss in the H_2O volume is estimated to be $3.86 \pm 0.03\%$. Combining the results from both regions, the total volume-weighted signal loss for the entire detector is $2.60 \pm 0.02\%$. In all cases, the errors quoted are statistical errors.

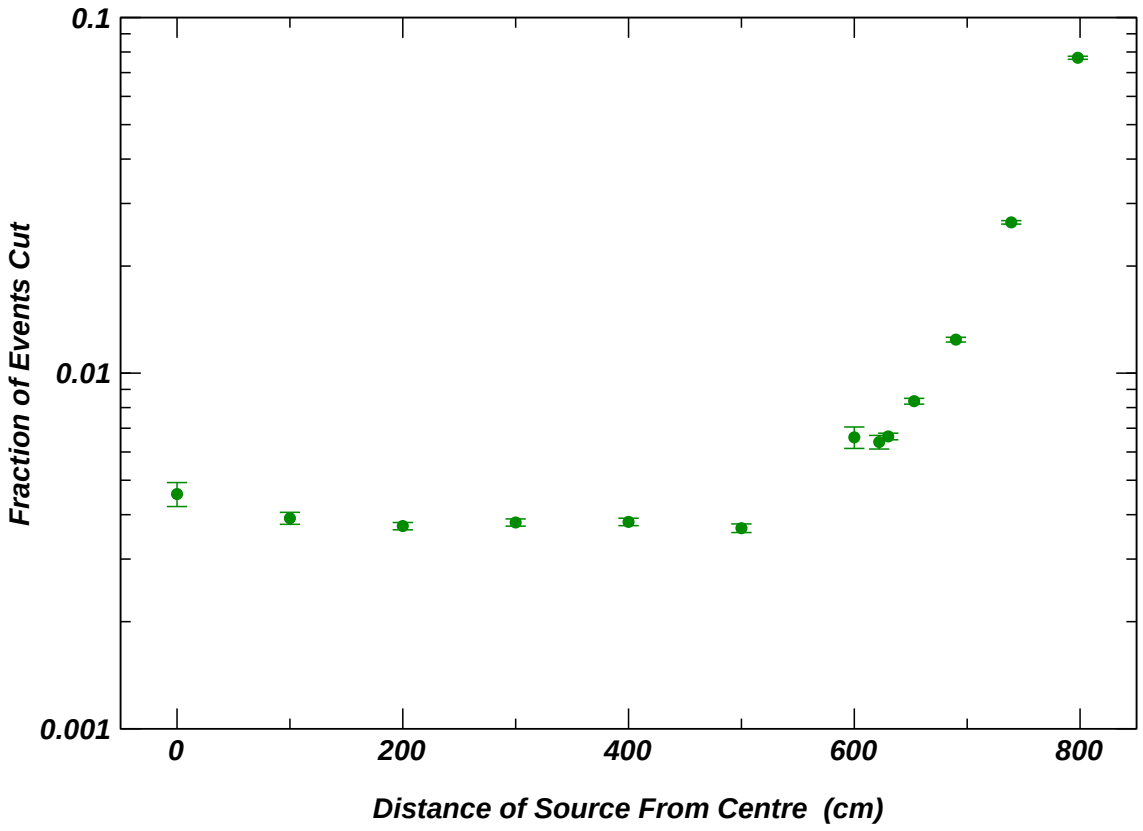

Figure 8.3: Signal loss measured using ^{16}N data as a function of source position in the detector, resulting from the use of the data reduction cuts chosen for the supernova analysis.

8.6 Summary

Instrumental background is removed from the SNO data by use of a set of data reduction cuts. The cuts adopted for the supernova neutrino analysis do not remove burst events. Naturally occurring physics events (non-calibration events) do not constitute a large background to the supernova analysis. The majority of physics backgrounds are usually associated with a high energy muon event, which is tagged during the supernova analysis. Table 8.5 summarizes the data reduction cuts and physics tags that are used for the SNO supernova neutrino analysis.

Cut/Tag	**Description**	**Background**
QCluster	charge cluster cut	PMT flasher
QvT	charge versus time cut	PMT flasher
FGC	flasher geometry cut	PMT flasher
ITC	in-time channel cut	PMT failure electrical pickup
FTS	fitterless time spread cut	PMT failure
NECK	uses PMTs installed in chimney	neck light
QvNHIT	charge/NHIT ratio cut	electrical pickup
ROF	pickup in cards 1, 15	electrical pickup
ISO	crate isotropy cut	electrical pickup
AMB	ESUM pulse shape analysis	high voltage breakdown
MUON	muon tag	muon spallation products

Table 8.5: Data reduction cuts used for the supernova analysis.

Based on the background event rate experienced during 244 days of stable detector running conditions, a threshold of 34 PMTs is assigned for analysis of the supernova signal.

Combining the predictions from both the Beacom and Vogel model and the Burrows model for a supernova at 10 kpc indicates that a total of 550–800 events would be observed above the supernova analysis threshold during the pure D_2O phase. During the salt phase, a total of approximately 750–1125 events would be observed for a supernova at 10 kpc. Furthermore, 92–95% of the signal in the light water region is expected to be due to

SN Signal Component ($t \leq 100$ ms)	**Beacom Model**		**Burrows Model**	
	D_2O	**Salt**	**D_2O**	**Salt**
Neutrino:				
ν_e	1.36	1.57	8.98	10.81
$\overline{\nu}_e$	6.32	7.78	0.72	0.88
"ν_μ"	0.67	3.36	0.05	0.24
Region:				
D_2O region	3.01	7.39	8.46	10.64
H_2O region	5.33	5.33	1.27	1.27
AV region	0.01	0.02	0.02	0.02
Interaction:				
charged current	7.25	8.76	8.27	8.40
neutral current	0.70	3.91	0.24	2.29
elastic scattering	0.40	0.40	1.24	1.24
Particle:				
electron/positron	7.77	7.77	9.49	9.49
neutron	0.92	4.39	0.26	2.44
Total Signal:	**9.02**	**13.66**	**9.75**	**11.93**
$\rightarrow \nu_e$ fraction	**16.4%**	**12.5%**	**92.1 %**	**90.6%**

Table 8.6: Comparison of the prompt signal above the detector hardware threshold between two generic supernova models at 10 kpc for relative time $t \leq 100$ ms.

$\overline{\nu}_e$ neutrino interactions, making it possible to essentially isolate that component of the supernova signal for study.

The prompt signal ($t \leq 100$ ms) above the analysis threshold contains between 9 and 11 events due to ν_e interactions according to the Burrows model for a supernova at 10 kpc. Therefore, the electron neutrino neutronization burst corresponds to approximately 92% of the total signal during that time period. In the case of the Beacom and Vogel model where no effects due to neutronization are included, 13–16% of the events are due to ν_e processes.

Approximately 12% of the supernova events in pure D_2O above the detector hardware

threshold are below the supernova analysis threshold of NHIT = 34. The corresponding fraction of the supernova signal that is removed during salt operation is roughly 8% of events. Due to the higher energy photons emitted during neutron capture on ^{35}Cl, fewer events are removed during the salt phase than during the pure D_2O phase.

A comparison of the results in Tables 8.1 and 8.3 with the corresponding results in Tables 7.1 and 7.3, indicates that the main component of the supernova signal that is removed by applying a threshold cut of 34 PMTs is the neutron signal. In the Beacom and Vogel model, the neutron signal decreases by 29% during pure D_2O operation and 10% during the salt phase. Results for the Burrows model show a similar decrease in the neutron signal. The decrease in the electron/positron signal when applying a threshold cut of 34 PMTs is 5% using the Beacom and Vogel model and 8% using the Burrows model. A larger number of electron/positron events are below the NHIT = 34 threshold in the Burrows model due to the lower neutrino temperatures used. The effect of the analysis threshold cut during pure D_2O and salt operation is illustrated in Figure 8.4 using the Burrows model.

The effect of setting an analysis threshold is shown in Figure 8.5, where NHIT as a function of time is shown for the supernova signal expected from Burrows model as well as for stable detector running.

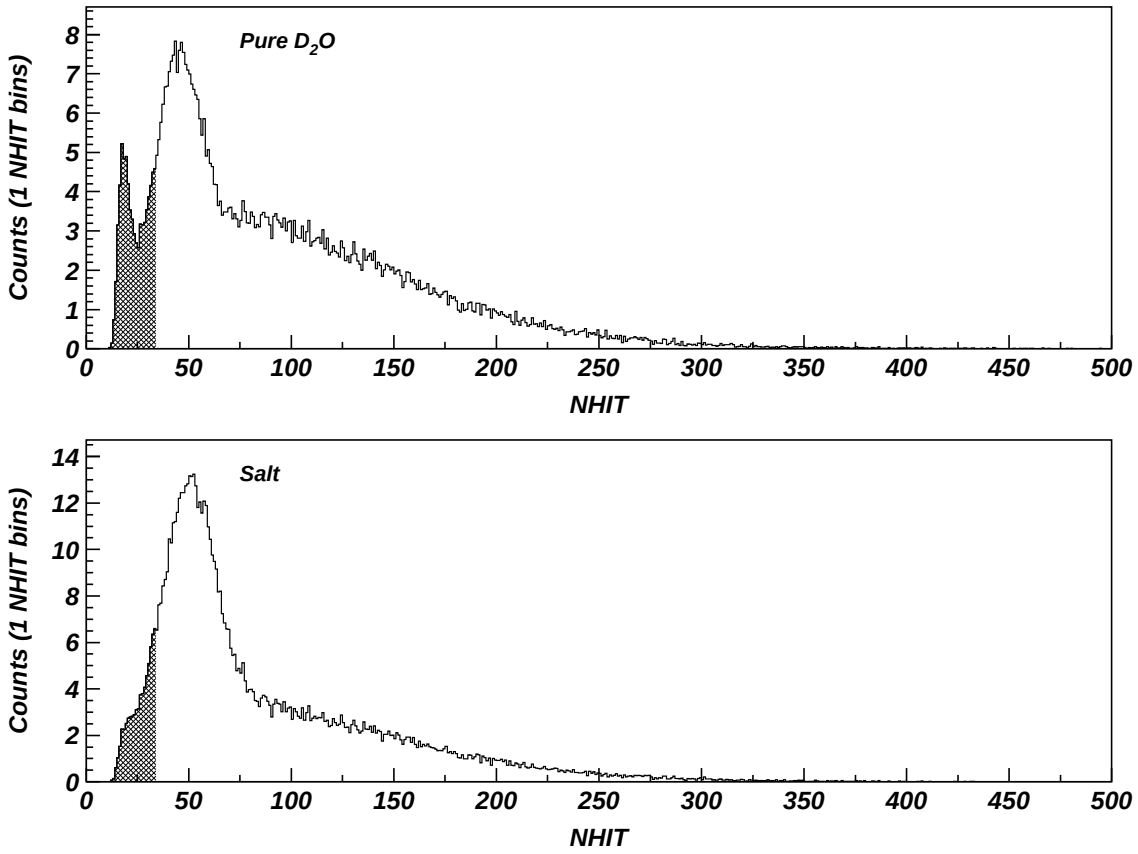

Figure 8.4: SNO supernova detected particle NHIT distribution where the shaded area indicates the supernova signal excluded by using an analysis threshold of NHIT = 34 PMTs.

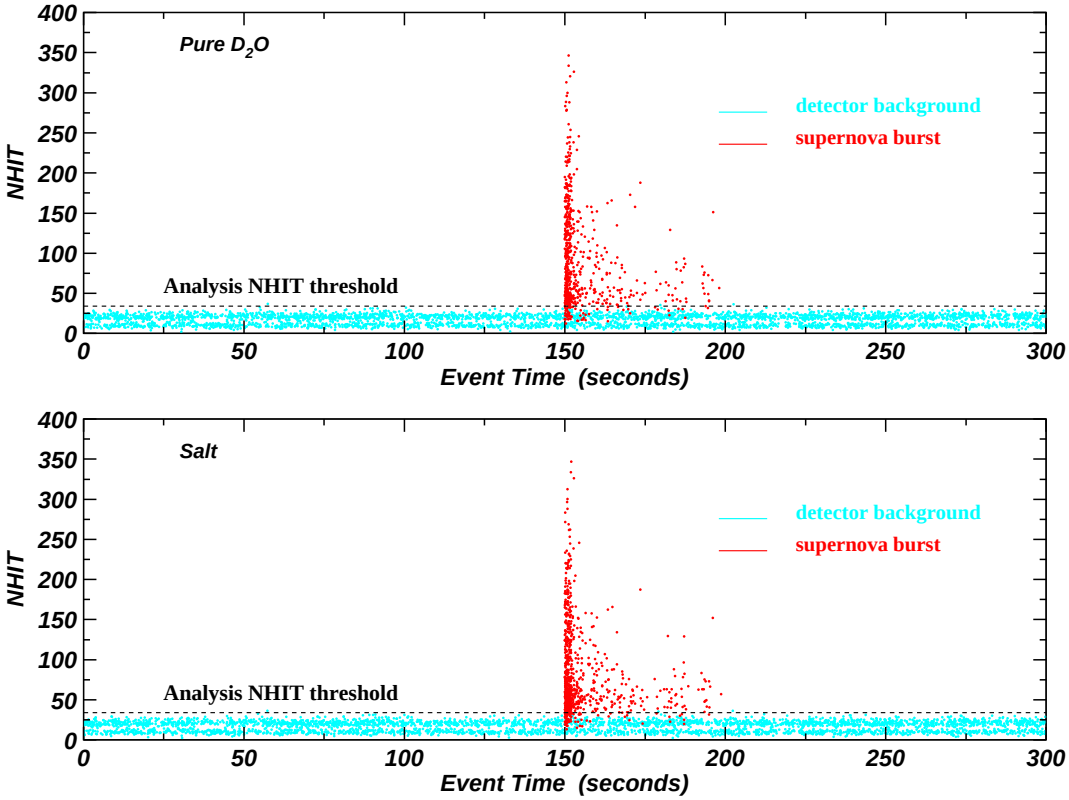

Figure 8.5: NHIT as a function of time showing the expected supernova signal, the detector background and the effect of the analysis NHIT threshold.

Chapter 9

SNO Supernova Monitoring Programme

9.1 Introduction

A data analysis program to identify neutrinos from a galactic supernova burst was installed on February 23, 2000[1] as part of the online system at the Sudbury Neutrino Observatory. The system was commissioned after several months of both offline and online testing and development. Some aspects of this development are summarized in Appendix E.

The goal of the Supernova Monitor at the Sudbury Neutrino Observatory is to be able to identify neutrinos from a Type II/Ib galactic supernova in time to provide an alert to the astronomical community. As mentioned in Section 3.4.3, the neutrino emission is expected to precede the optical signal, where the time delay depends on the mass envelope surrounding the collapsing star, and may vary from a few minutes to several hours. To be useful, the alert from the neutrino astronomy community must come as quickly as possible. The SNO supernova monitoring program aims to be able to provide a reliable alert within 20–30 minutes.

9.2 Online Supernova Monitor

In order to identify a significant burst of neutrino events in the SNO detector, a data analysis program has been installed in the online data stream that automatically analyzes burst

[1] The fact that this date is the 13th anniversary of SN1987A is purely coincidental.

data. Analysis results for all "interesting" bursts are made available to the SNO Supernova Working Group and to the detector operator on shift. The SNO online supernova monitor is located within the SNO data acquisition system (see Section 4.8). PMT data from the readout electronics is processed by a task called the "event builder", which resides on a Sun Ultra Sparc 1/170 workstation computer. The event builder assembles the individual PMT hits into events. Once built, the event data are written to tape and also transferred along a 2 km ethernet fibre to a Sun Ultra Sparc 1/170 computer on surface, where a second archive copy of the data is made and a process called the "event dispatcher" is responsible for managing all of the processes that subscribe to the online data stream. An overview of the SNO data flow system is shown in Figure 9.1.

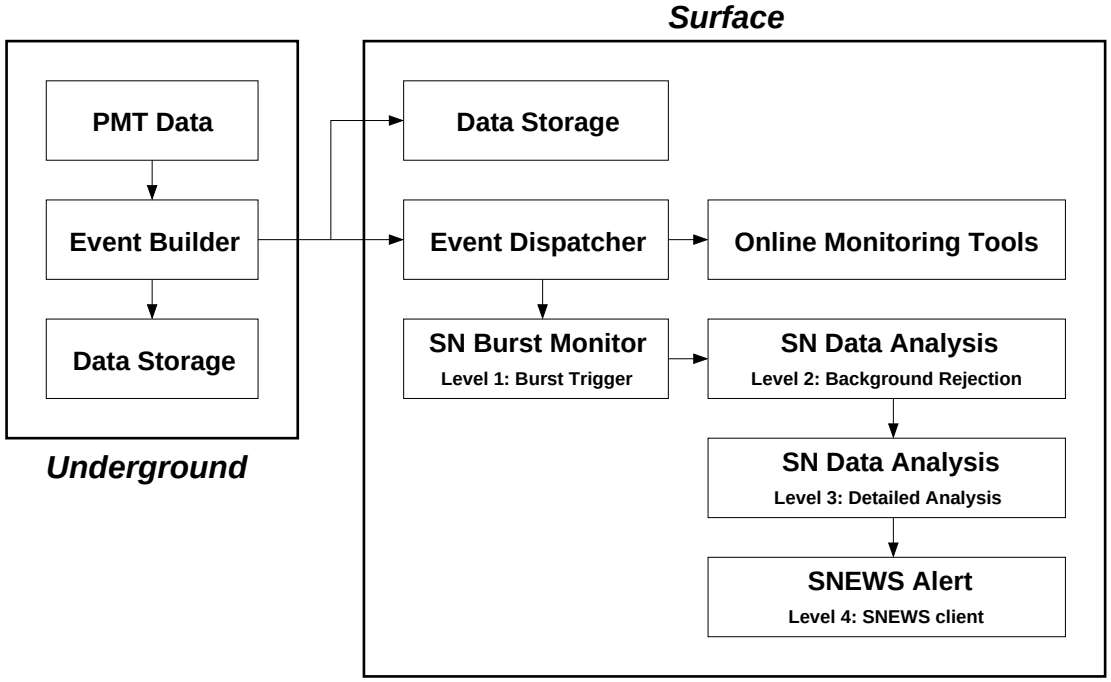

Figure 9.1: Schematic overview of the SNO data flow system. The connection between underground and surface is via a 2 km ethernet cable.

The online supernova monitoring system for SNO can be logically broken up into four

distinct levels, the first three of which are completely automated. The "Level 1" burst trigger monitors the data stream for significant increases in the event rate. In the case of such a burst, events passing the Level 1 trigger are copied out of the data stream and passed to the "Level 2" analysis routine, where events due to instrumental noise are removed. If 35% or more of the events pass the Level 2 stage, the detector operator is notified and the "Level 3" routine is then called to reconstruct a time, energy, location in the detector and direction for each event. Should the burst be identified as having significant physics content, the final stage of SNO's response, "Level 4", would be to manually communicate the details of the burst to the SuperNova Early Warning System (SNEWS) [127] and to issue an alert to the astronomical community. Each of the levels is described below.

9.2.1 Level 1

9.2.1.1 Burst Trigger

The Level 1 burst monitor involves looking for a certain number of events (NEVENT) over a certain energy threshold (NHIT) within a certain time window. To this end, one of the existing SNO online data monitoring tools has been modified to hold a circular FIFO buffer and apply the burst criteria to the incoming data on an event-by-event basis [128]. In the current default configuration, the FIFO buffer holds 30 events above the supernova NHIT analysis threshold of 34 PMTs. The burst criteria are met when the time difference between the first and last event in the buffer is less than 2 s. The expected count rate sustained over 2 seconds for events above the NHIT analysis threshold of 34 PMTs is approximately 185 Hz during the pure D_2O mode and 275 Hz during the salt mode for a supernova at 10 kpc, regardless of the supernova model. Figure 9.2 indicates the time structure of a supernova burst compared to the typical detector event rate of 15–20 Hz.

Once a burst has been identified, the burst events are copied from this circular buffer to a separate file until the events in the FIFO buffer no longer satisfy the burst criteria and

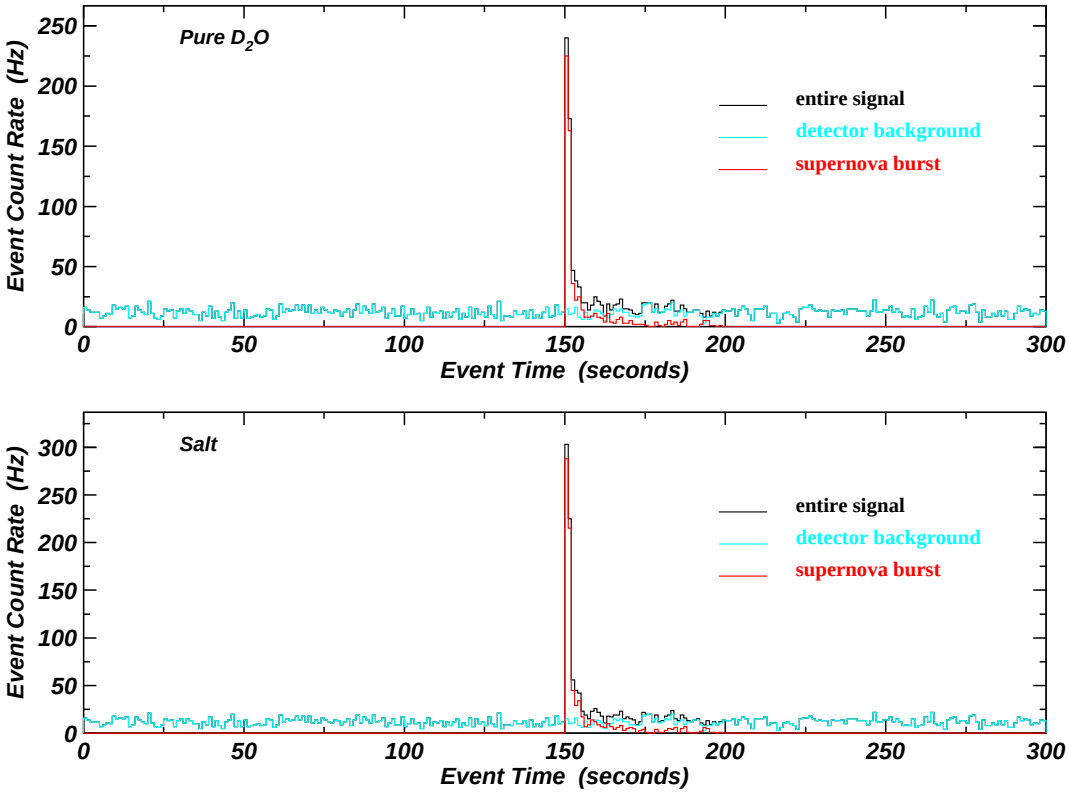

Figure 9.2: Expected detector count rate in the presence of a supernova burst. The typical detector event rate is 15–20 Hz.

the burst ends. In order to ensure a prompt analysis of the events, bursts that last longer than 60 seconds are forced to end prematurely and the remaining events are assigned to a successive burst. The burst monitor currently resides on a Sun Ultra Sparc 1/170 workstation computer; a parallel burst monitor process resides on an Intel Pentium III 600 MHz based computer. Once the parallel system on the faster Intel Pentium computer has been fully commissioned, it will become the official process and the Sun will be used only as a backup.

Run Condition	Level 1 Burst Monitor NHIT100 Threshold	
	(PMTs)	(MeV)
Default	34	3.8
Calibration:		
• ^{16}N, ^{8}Li	69	7.7
• ^{252}Cf (all strengths)	69	7.7
• U, Th	44	4.9
• all other sources	34	3.8

Table 9.1: Level 1 burst monitor NHIT100 trigger thresholds during different detector activities. In all cases, the Level 1 trigger requires 30 events above the appropriate NHIT100 trigger threshold in a 2 second time window.

9.2.1.2 Run-Specific Thresholds

In addition to the default settings, several calibration sources require higher thresholds, which are assigned depending on the run type. The ^{16}N and ^{8}Li calibration sources make use of a gas system to transport radioactive nuclei to the detector, as described in Section 4.9. Although both of these sources have an internal PMT to tag decay events, some of the nuclei decay en route to the decay chamber, causing the detector to register an event without the corresponding internal calibration source tag. The decay products of the ^{252}Cf, U and Th calibration sources are not tagged and would normally swamp the data stream burst monitor. In order to avoid having physics events from the ^{16}N, ^{8}Li, ^{252}Cf, U and Th calibration sources in the data set, the burst monitor sensitivity during these runs is decreased by raising the trigger threshold. Additional instrumental light is observed during the operation of the source manipulator system[2]. The Level 1 burst monitor parameter settings during various detector activities are presented in Table 9.1. All run conditions require 30 events above the appropriate NHIT threshold in a time window of 2 seconds.

[2]The current online burst monitor uses an NHIT threshold of 124 PMTs during running conditions in which the source manipulator system is in operation. That threshold setting is not used in this analysis.

9.2.1.3 Offline Performance

Once the online burst monitor was sufficiently mature, its performance was investigated offline for the period between November 2, 1999 and January 4, 2001, consisting of 391.6 days of live data. To perform the offline study, a set of FORTRAN routines that provide much of the same functionality as the online monitor was used. The supernova analysis event NHIT threshold of 34 PMTs in conjunction with a time window of 2 seconds were specified in the offline analysis routines. Several NEVENT settings were employed in order to thoroughly study the response of the monitoring system. In all cases, the run-specific thresholds listed in Table 9.1 were also employed. One slight difference between the online and offline burst monitor software is that a burst is not ended once a duration of 60 seconds is reached, as is the case in the online version.

The burst rate observed in the SNO detector depends on the number of events required to form the burst trigger. An average of 44.0 bursts/day are observed during the offline study using the default online burst monitor parameters. For comparison, the total burst rate using NEVENT=50 is approximately 26.5 bursts/day. Results of the offline study for different NEVENT parameters are shown in Figure 9.3. The increase in the burst rate as a function of the number of events required to form the trigger is mainly due to calibration activity.

Before the results of the offline study were available, a conservative trigger setting requiring 50 events was used in the official online monitor. This choice was based on early studies during the development of the trigger and a desire to not overwhelm the detector operators with too many bursts. The current NEVENT setting is 30 events, but for much of the online operation, NEVENT = 50 was used. Therefore the NEVENT = 50 setting is often used for comparison in the offline studies.

The bursts identified in the offline study can be classified to first order by considering the three general classes of detector operating conditions:

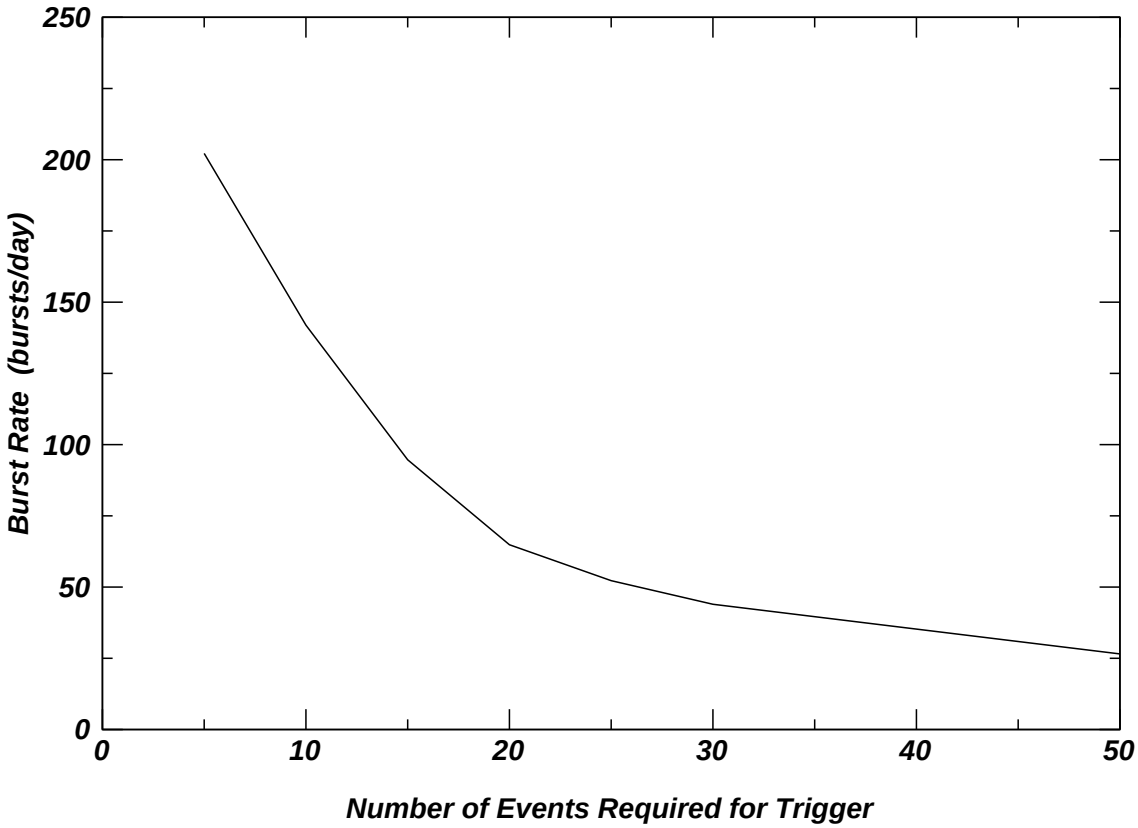

Figure 9.3: Level 1 burst rate as a function of the NEVENT burst trigger parameter studied offline during the period between November 2, 1999 and January 4, 2001. The online Level 1 burst monitor currently uses NEVENT = 30, which results in a burst rate of approximately 44 bursts/day. The vast majority of these bursts are due to calibration activity.

- neutrino: stable running mode; data used for most physics search analyses come from this class of data;

- calibration: running mode associated with detector calibration activities, which includes actual calibration source data as well as data during which the calibration sources are being prepared for use;

- maintenance: running mode during which the detector is either unstable or some

Burst Cause	NEVENT = 50		NEVENT = 30	
	Rate (day^{-1})	Fraction of Total Bursts	Rate (day^{-1})	Fraction of Total Bursts
Calibration	10.1	38.2%	21.8	49.4%
Maintenance	9.4	35.5%	11.7	26.6%
Neutrino	7.0	26.3%	10.5	23.9%
Total	**26.5**	**100%**	**44.0**	**100%**

Table 9.2: Total average Level 1 burst rate experienced during difference detector operating conditions. A number of bursts recorded during the neutrino and maintenance operating modes are also due to calibration activity.

maintenance or diagnostic procedure is being performed.

The burst rates experienced during different detector operating conditions are indicated in Table 9.2. As expected based on experience with the online system, the majority of burst events are due to calibration activities. One factor that significantly skews the burst rate associated with a particular running condition is that of operator error. On numerous occasions, detector activities are not properly reported in the data, in particular calibration activities. As a result, a larger number of bursts are recorded because the run-specific trigger thresholds are not implemented when they should be. This also means that burst rates quoted for the "neutrino" and "maintenance" conditions are higher than warranted for the activities intended for those running conditions.

Most of the bursts are grouped closely together in time as shown in Figure 9.4, which suggests that a single source is often responsible for causing more than one burst. Taking this factor into account reduces the Level 1 burst rate to an average of about 7.5 groups of bursts per day at the default NEVENT setting, most of which are due to calibration activity. During the period where 50 events were required by the online burst monitor, SNO experienced roughly 6 groups of bursts per day.

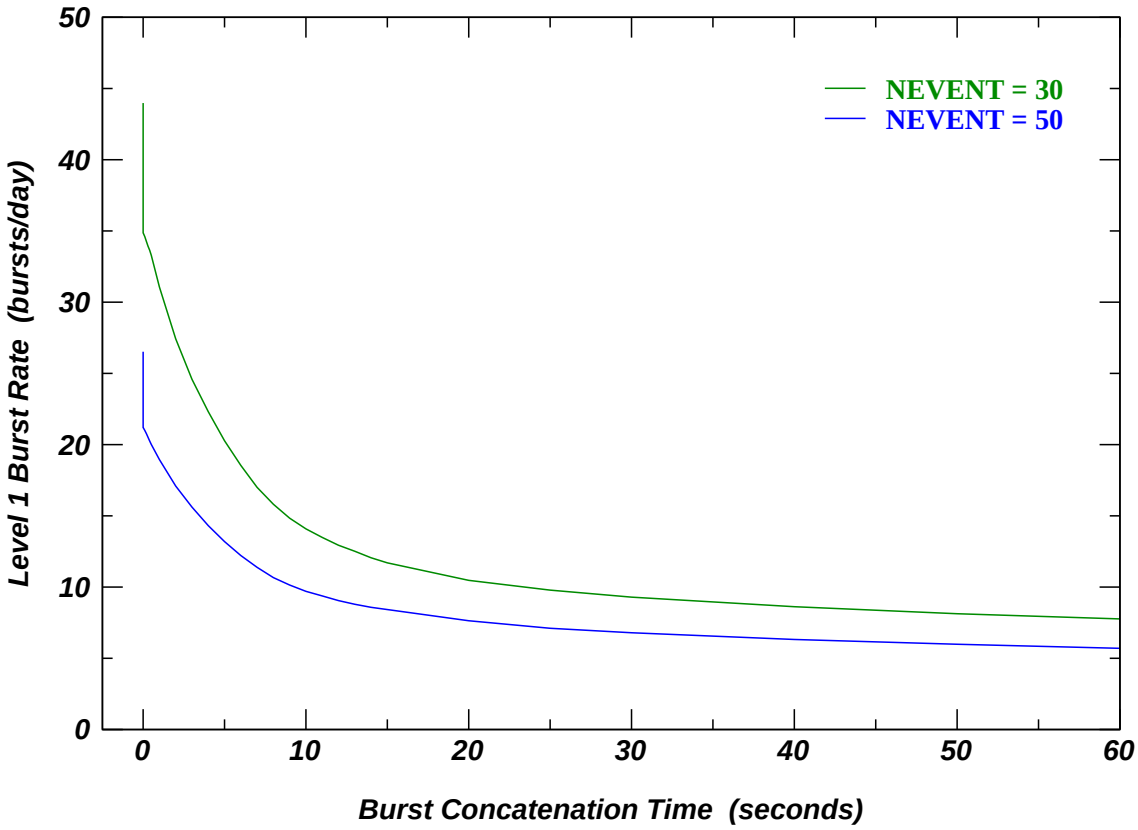

Figure 9.4: Level 1 burst rate as a function of the time between bursts, determined offline for the period between November 2, 1999 and January 4, 2001. Most burst events occur within 10 seconds of the preceding burst and are therefore likely due to the same source. The most significant contribution to this effect is from calibration activity.

9.2.2 Level 2

Once a burst has been identified by the Level 1 trigger, the events are analyzed event-by-event using computer software routines developed by the SNO Supernova Working Group, which are linked against the main SNO data analysis software package SNOMAN. This analysis is performed on a Sun Enterprise E450 computer and in parallel on an Intel Pentium III 600 MHz based computer, running the Solaris x86 operating system.

The main task of this second-level analysis is to remove instrumental background events

by applying the data reduction cuts outlined in Section 8.2. One drawback to analyzing data online is that the results of the data reduction cuts for the events are not readily available in the SNO database, so the data reduction filters must be applied manually in the SNOMAN routines. As well, it is necessary to provide the latest ECA electronics constants as input to the analysis routines since these values take some time to be included in the SNO database. All data in the SNO database has a validity time range, so additional provisions have been made within the database software to apply the latest detector constants in the event that a certain validity range has expired.

9.2.2.1 Burst Classification

The Level 2 analysis also attempts to characterize the nature of the burst based on the fraction of events that are tagged by the various data reduction cuts. There are currently 13 categories that exist in the burst classification algorithm, including the category of "Unknown". Six of these categories are associated with the SNO instrumental background sources discussed in Section 8.2:

- Flasher: QCluster ≥ 0.50, FGC ≥ 0.45
- Flat TAC: ITC tags higher fraction of events than any other cut
- Wet-End Breakdown: AMB ≥ 0.75, QCluster ≥ 0.35, QvT ≥ 0.35, ITC ≥ 0.35, QvNHIT ≤ 0.20, NECK ≤ 0.35, FTS ≤ 0.35, FGC < 0.45 (veto Flasher)
- Dry-End Breakdown: Isotropy ≥ 0.80
- Neck: NECK ≥ 0.90, AMB ≥ 0.65, FTS ≥ 0.50, QvNHIT ≤ 0.33
- Electrical Pickup: QvNHIT ≥ 0.33

An additional five burst categories are due to calibration activities and certain water activities. Light is occasionally produced in the detector during D_2O circulation either for

the purpose of purification or for monitoring. Pertinent running conditions are included in the data structure, and this information is used by the burst classification algorithm:

- Manipulator Light: Calibration source moving bit, AMB ≥ 0.75, ITC ≥ 0.65, NECK ≤ 0.20
- PCA Retrigger: Calibration PCA source bit, QvNHIT > 0.33
- D2O Circulation: D2O Circulation bit, either FTS tags higher fraction of events than any other cut or NECK ≥ 0.75, FTS ≥ 0.50
- D2O Assay: D2O Sample Line Assay bit, AMB ≥ 0.75, NECK ≥ 0.75.

Another burst classification is designed to alert to the detector operator to the possibility of a malfunction of the 10 MHz experiment clock. If the experiment clock is not updating as it should, PMT flasher events accumulate until they trigger the Level 1 burst monitor. This type of burst is identified by comparing the duration of the burst according to the 10 MHz clock and the 50 MHz clock:

- Problem Clock: duration (10 MHz) $= 0$, duration (50 MHz) ≥ 1 second.

All bursts are also required to have fewer than 35% of the events pass all of the data reduction cuts.

The final burst category is that of "Spallation", which is mentioned as a SNO physics background in Section 8.2. Spallation bursts are identified by using information provided by the muon tag and the fraction of events that pass the set of Level 2 data reduction cuts. Bursts in which 35% or more of the events survive the data reduction cuts undergo additional processing in the Level 3 stage (see Section 9.2.3). In order to reduce the contamination due to calibration events, the spallation classification also requires that 90% or fewer of all events pass the data reduction cuts:

Burst Cause	**NEVENT = 50**		**NEVENT = 30**	
	Rate (day^{-1})	**Fraction of Total Bursts**	**Rate (day^{-1})**	**Fraction of Total Bursts**
PMT Flasher	0.96	3.6%	1.55	3.5%
Flat TAC	1.48	5.6%	1.64	3.7%
Wet-End HV Breakdown	0.27	1.0%	0.28	0.6%
Dry-End HV Breakdown	0.51	1.9%	0.69	1.6%
Neck	0.58	2.2%	1.03	2.3%
Electrical Pickup	2.87	10.8%	5.62	12.8%
Manipulator Light	1.54	5.8%	1.67	3.9%
Retrigger	0.13	0.5%	0.18	0.4%
D_2O Activity	2.50	9.4%	3.12	7.1%
Broken Clock	0.19	0.7%	0.26	0.6%
Spallation	0.03	0.1%	0.06	0.1%
Unknown	15.46	58.3%	27.85	63.3%
Total	**26.52**	**100%**	**43.95**	**100%**

Table 9.3: Burst rate due to various causes as identified by the Level 2 burst classification algorithm. Results are included for two settings of the NEVENT burst trigger parameter. The majority of "Unknown" bursts are due to calibration activities.

- 1 muon tag
- $0.35 \leq$ fraction passing data reduction cuts ≤ 0.90.

To further restrict the number of events incorrectly identified as spallation events due to calibration activity, it is necessary to exclude data in which the source manipulator system is in use. The impact on the livetime is negligible at 1.4% of all NHIT100 live data.

The results of the burst classification algorithm for the bursts identified during the offline analysis are summarized in Table 9.3 for the NEVENT = 30 and NEVENT = 50 data sets. Analysis of the offline burst data set indicate that the rate of PMT flasher events is about 1/day. The source of these bursts is almost exclusively due to mine blasting activities, which occur on average once per day (usually at approximately 03:00 Sudbury local time). The PMT flasher rate using the NEVENT = 30 setting is slightly higher than

the rate with NEVENT = 50 because the trigger is more sensitive to seismic activity, which also causes bursts of PMT flasher events. Other significant differences in the burst rate are observed for bursts due to neck and electrical pickup events. Within a burst, these events tend to be clustered together at discrete times, and with a lower events required to form the trigger, these bursts are often identified as several smaller bursts. Also, more spallation events are identified with a more sensitive trigger. In this case, high energy muon events that have fewer associated follower events are able to satisfy the burst trigger. On average, 1 spallation event is identified by the burst trigger every 18 days for the NEVENT = 30 setting and 1/39 days for the NEVENT = 50 setting. Characteristics for a number of spallation bursts are presented in Table 9.4. Notice that almost all of the PMT channels register a hit due to the muon event. As many as 227 follower events have been observed in the few seconds after the muon event.

Run #	**Muon NHIT**	**Muon GTID**	**# Events (pass cuts)**	**Duration (seconds)**
10008	9338	1697058	47	0.23
10946	9578	299141	227	1.71
11038	9473	260531	33	3.27
11291	9491	1017045	129	1.96
11347	9572	92584	37	0.27
11531	9598	3506018	42	1.71
12257	9362	1088642	75	1.68
12568	9554	417782	177	1.96
13401	9427	2674171	54	1.47
14418	9306	7801105	58	0.41

Table 9.4: Characteristics of bursts classified as spallation events when 50 events are required to form the burst trigger.

While the current burst classification algorithm often provides useful information, it does not properly classify all bursts. Sometimes, this is due to the fact that bursts from two different sources of instrumental noise coincide. For example, a flasher PMT burst

is occasionally accompanied by wet-end breakdown as a result of mine blasting activities. However, the spallation event identification appears to be robust.

9.2.2.2 Analysis Summaries

A text summary of the relevant run conditions and burst characteristics is made available to the detector operator on shift. Included in the summary is information regarding the burst time, number of burst events, the fraction of events that satisfy various triggers (including the hydrophone) and results of the data reduction cuts. An example summary text message is shown in Figure 9.5 for a Monte Carlo supernova burst at 10 kpc according to the Burrows supernova model.

In addition to the Level 2 text summary, a set of histograms showing various relevant distributions are produced, including NHIT, time, trigger types and the number of PMT hits sorted according to electronics crate, card and channel. Two sets of histograms are provided to show the burst data before and after the data reduction cuts are applied. Distributions of event NHIT and relative time can be compared to the plots shown in Section 7.1 for the simulated supernova signal. Events from a genuine supernova are expected to have NHIT values in the range 34–500 PMTs spread over tens of seconds. Many bursts due to instrumental noise have events with NHIT $>$ 1000 PMTs and occur over times of less than 1 second. While the supernova signal is expected to have a significant contribution from the OWL PMTs, the majority of the detector triggers will be due to NHIT triggers and not ESUM triggers. The remaining plots in the analysis summary histograms characterize various levels of electronics channel groupings. In each case, the signal due to a supernova is expected to have a roughly equal number of PMT hits in each of the electronics crates, cards and channels. Figures 9.6 and 9.7 show an example of the Level 2 analysis summary histograms for a Monte Carlo supernova burst at 10 kpc according to

```
Ref. burst_10000_001

A supernova burst candidate has been found by the first level trigger
and has been analysed by the second level trigger.

Burst ZDAB file: burst_10000_001.zdab
                          (in /scratch/lt/sstream/snwatch/zdabs on SURF)
Analysis summary PDF file: burst_10000_001.pdf
                          (in /scratch/lt/sstream/snwatch/level2/pdf on SURF)
Analysis Info Summary:
----------------------
SNOMAN version ........... 4.0186
SNOMAN analysis time .....    0.58 minutes

Run Info Summary:
-----------------
Run type ................. Neutrino
Run flags ................ UC bit OFF
Run crate flags .......... 0-18, Tub ON
Run N100_med threshold ... 16 hits

Supernova Level 2 Analysis Summary:
-----------------------------------
RUN # ....................     3  (starting at GTID =        1 )
Date / Time .............. 20/01/2000 at 02h 16m 07s (Sudbury local time)
Time duration .............     47.4995483 s
Burst size ...............    572 events
NHIT100 triggers ......... 100.0%
ESUM triggers .............   0.0%
OWL triggers ..............   0.0%
HYDROPHONE triggers ......    0 events

Data cleaning tags:
                           #Passed
 MUON_TAG .................     0

Data cleaning cuts:
                           %Failed
 AMB_CUT ..................    0.0%
 NECK_CUT .................    0.0%
 RING_OF_FIRE_CUT .........    0.0%
 QvT_CUT ..................    0.2%
 FTS_CUT ..................    0.3%
 QvNHIT_CUT ...............    0.0%
 CRATE-ISOTROPY_CUT .......    0.0%
 QCLUSTER_CUT .............    0.0%
 ITC_CUT ..................    0.2%
 FGC_CUT ..................    0.0%

==> Events remaining after all cuts: 99.3% (   568 events)

==> Event type: UNKNOWN
```

Figure 9.5: Level 2 analysis summary text message.

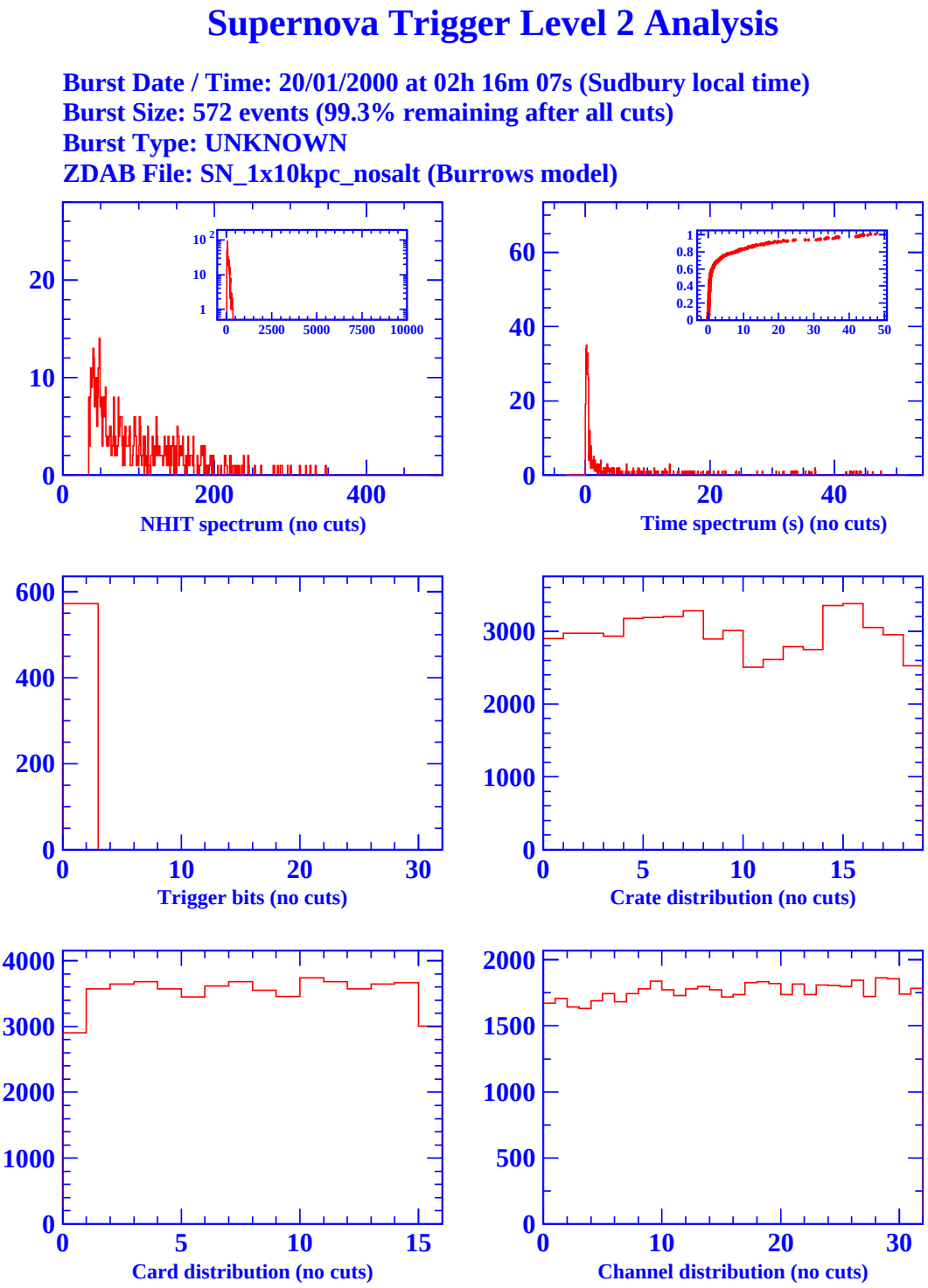

Figure 9.6: Level 2 analysis summary histograms showing the raw burst data before the data reduction cuts have been applied. The example shown is a simulated supernova burst at 10 kpc according to the Burrows model.

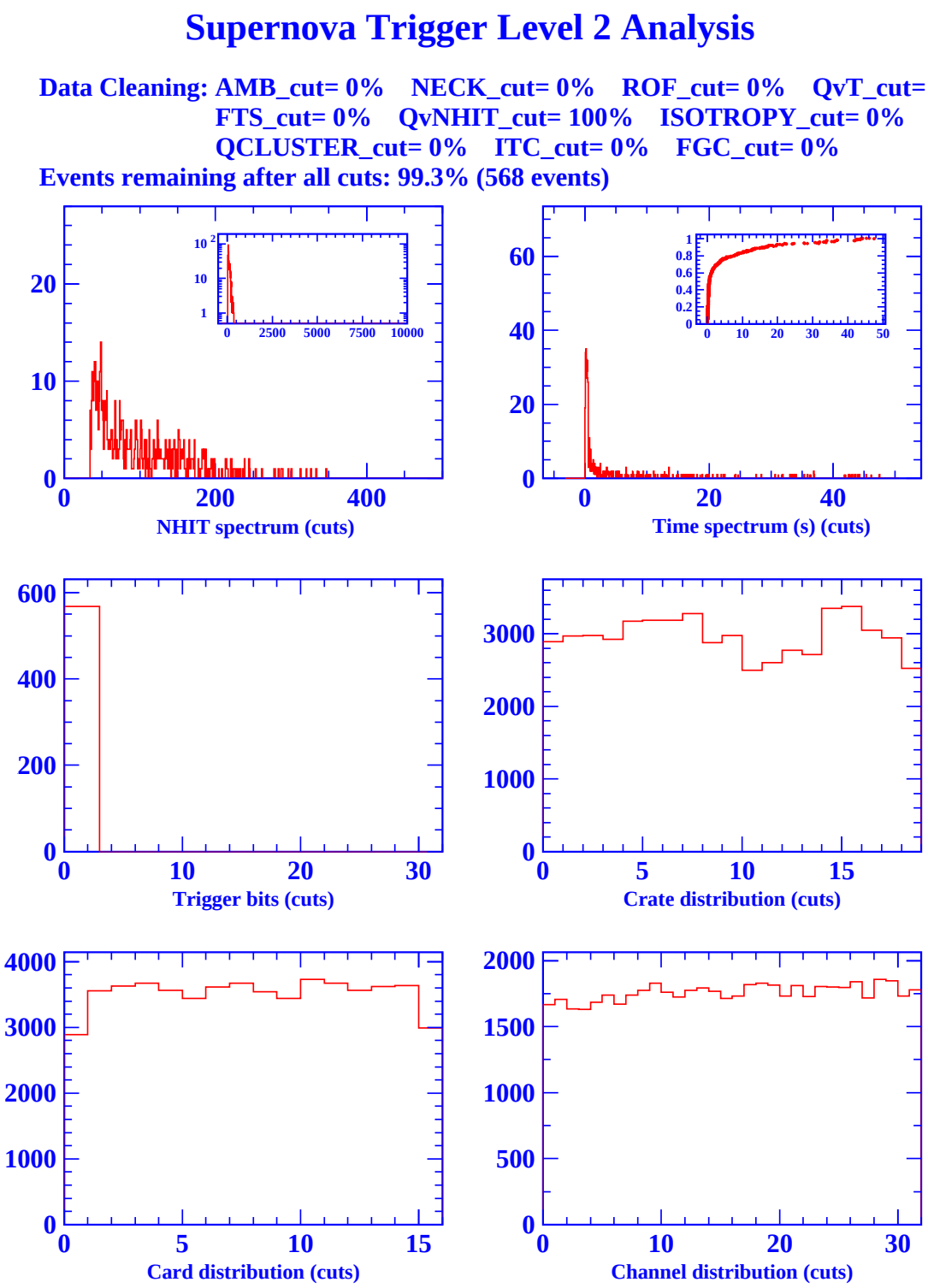

Figure 9.7: Level 2 analysis summary histograms showing the burst data after the data reduction cuts have been applied. The example shown is a simulated supernova burst at 10 kpc according to the Burrows model.

the Burrows model. The inset plot in the NHIT histogram shows the full NHIT range (0–10000 PMTs) in order to indicate the number of events with NHIT $>$ 1000. An inset plot showing the cumulative time distribution is also provided for the time histogram.

These burst characterizations are not only useful for recognizing an actual supernova, but they also allow the detector operator to diagnose bursts due to instrumental noise or detector instability online. The supernova analysis isolates the burst events in a timely manner so that the detector operator can diagnose the problem almost immediately.

9.2.2.3 Communication

Analysis results from the Level 2 analysis are saved to a log file and the summary text file and histograms are sent by email to members of the SNO Supernova Working Group, the detector operator email account as well as being posted to an internal website. Detailed procedures [129], [130] are also available at the website outlining how a detector operator on shift is expected to respond to a Level 2 burst alarm and how to interpret the results of the Level 2 analyses.

For bursts in which fewer than 35% of the events pass all of the Level 2 data reduction cuts, detector operators are instructed to investigate any burst that is identified by the burst classification algorithm as "Unknown". The popup alert window shown in Figure 9.8 is used to inform the detector operator of such an event. If a burst is identified as one of the known types, no alert is issued other than the log file entry.

A burst in which 35% or more of the events pass the all of the Level 2 data reduction cuts also automatically triggers a dial-out computer [131], which currently calls three cell phones carried by members of the SNO Supernova Working Group[3]. A pre-recorded voice message indicating that a significant burst has occurred is stored on the dial-out computer. Text-to-speech software is used to provide additional information in the phone message

[3]The author is one of the members of the SNO Supernova Working Group that carries a cell phone for supernova support.

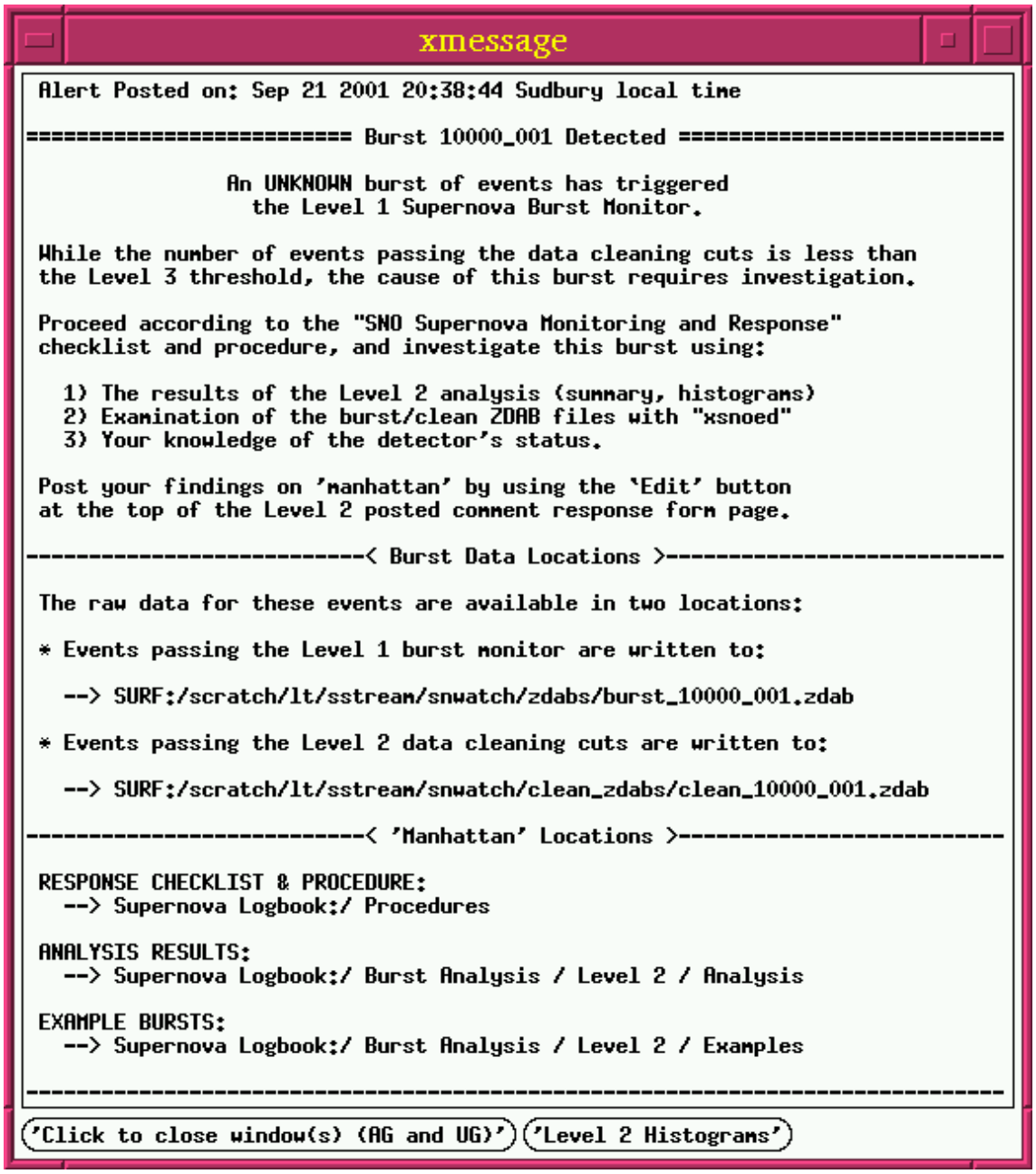

Figure 9.8: Level 2 popup window alerting the detector operator that a burst has been identified as "Unknown" by the burst classification algorithm.

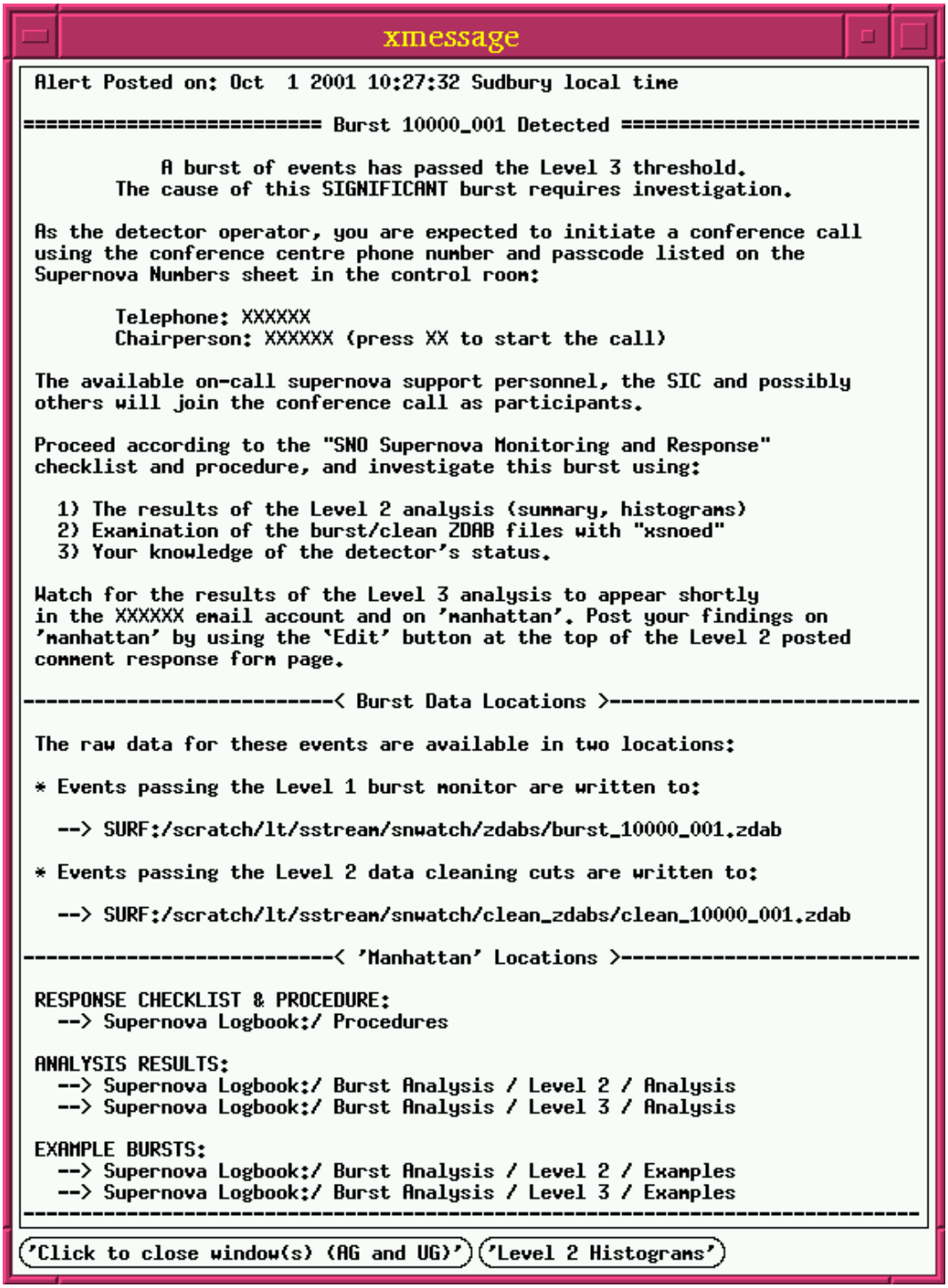

Figure 9.9: Level 2 popup window alerting the detector operator that a burst in which 35% or more of the events have passed the data reduction cuts. An appropriate sound also accompanies this alert window.

such as the run type, specific detector conditions and the fraction of events passing the data reduction cuts. The dial-out computer is a Pentium 133 MHz based computer with a Dialogic ProLine/2V dial-out card installed. Tests of the dial-out phone connection are performed once every hour and a test of the full dial-out system, where the cell phones are actually called, is performed once every week. The detector operator on shift is notified by a popup window as well as email that the dial-out has occurred and at that point the operator initiates a conference call to which the cell phone carriers call in and join as participants. The alert window for this scenario is shown in Figure 9.9.

9.2.3 Level 3

Bursts in which 35% or more of the events pass the all of the Level 2 data reduction cuts pass on to the Level 3 analysis where they are analyzed event-by-event using a set of SNOMAN software routines similar to the ones developed for the Level 2 analysis.

9.2.3.1 Threshold

The number of bursts removed due to various Level 3 threshold values is shown in Figure 9.10. A large number of bursts are removed for threshold settings less than 35%. However, for threshold values greater than 35%, the number of bursts removed stays roughly constant until calibration events are removed with threshold values greater than 90%. An examination of observed muon-induced spallation events indicates that essentially none of these events are removed with a 35% Level 3 threshold. Therefore, it is felt that 35% represents a conservative threshold for a burst of supernova neutrinos.

Note that in Figure 9.10 not all bursts are removed with a Level 3 threshold of 100% because only the bursts in which the fraction of burst events passing the data reduction cuts is strictly less than the threshold value are cut.

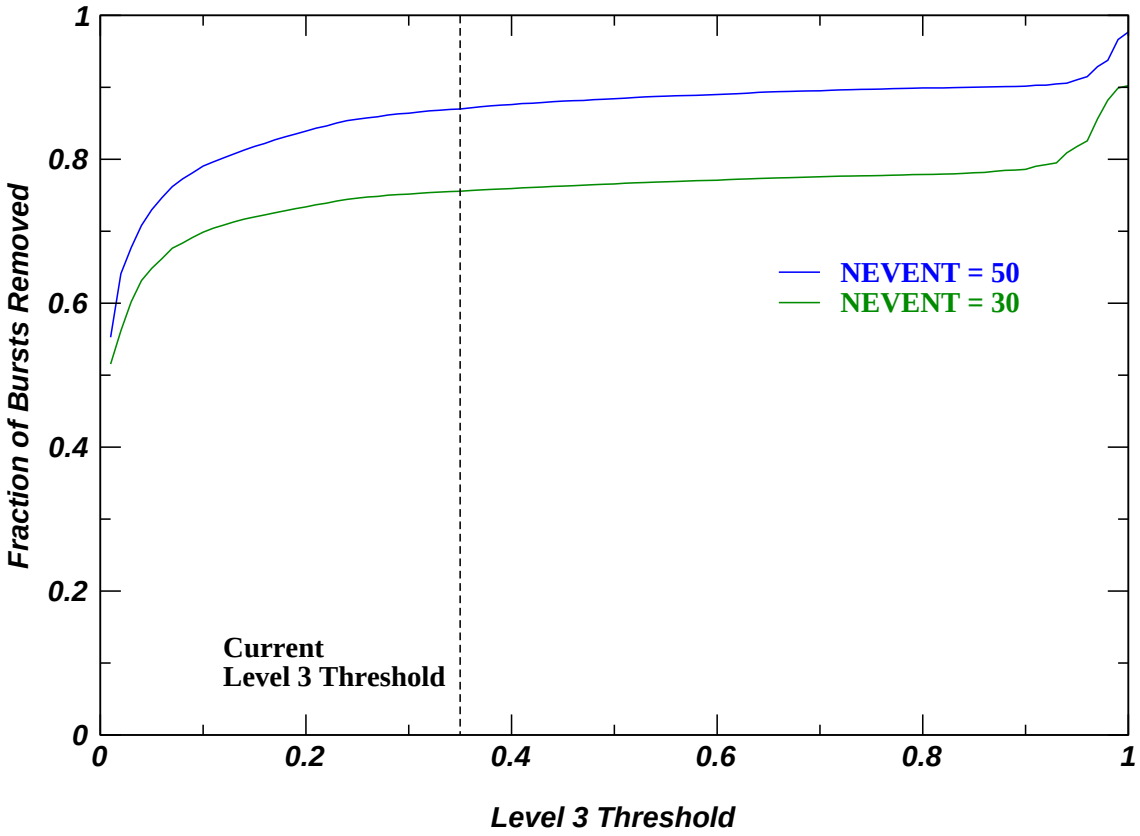

Figure 9.10: The number of bursts removed using various Level 3 threshold values. The current threshold value of 35% is indicated.

9.2.3.2 Event Reconstruction

Unlike in the Level 2 analysis, each event is reconstructed in the Level 3 analysis to determine the event time, position and direction cosines (the direction is only meaningful for electron/positron events and for γ-ray events). In water, low energy electrons (and positrons) travel only a few centimetres at relativistic speeds, therefore the Čerenkov light from these particles can be assumed to originate from a point source at one instant in time. The location of the event interaction vertex, $\vec{x}_{fit}$, and the time the interaction took place, t_{fit}, can be reconstructed using the time that each PMT is hit. The time, t_i that PMT i

receives light is given by:

$$t_i = t_{fit} + \frac{|\vec{x}_i - \vec{x}_{fit}|}{c/n}, \tag{9.1}$$

where $\vec{x}_i$ is the position of PMT i and c/n is the speed of light in a medium of refractive index n. The interaction vertex position and time are then determined by minimizing the time residual, R_i, for each PMT:

$$R_i = t_i - t_{fit} - \frac{|\vec{x}_i - \vec{x}_{fit}|}{c/n} \tag{9.2}$$

using the χ^2 quantity

$$\chi^2 = \sum_{i=1}^{N} \frac{R_i^2}{\sigma_i^2}. \tag{9.3}$$

The σ_i value is the 1-sigma width in the PMT timing resolution, which is determined for each PMT using the laserball calibration source. PMTs that have high residual values (PMT noise events or events due to reflection) are removed from the χ^2 and the remaining PMT hits are reconstructed. This minimization algorithm is called the "time fitter" in SNOMAN. The direction provided by the time fitter is determined by considering the mean value of the reconstructed vertex $\vec{x}_{fit}$ values.

A more sophisticated reconstruction method employs a simulated annealing algorithm to determine which orientation of a cone best fits the PMT hit data [132]. As mentioned in Section 4.2, Čerenkov light is emitted in a cone of half angle $\theta_{\check{C}} = 42^\circ$ with respect to the trajectory of the charged particle. The reconstruction is performed by minimizing the residual quantity $\sin^2\phi$, where ϕ is the angle between the axis of the cone and the vector from the event vertex position to the PMT. When performing the summation over PMT hits, weights based on the $\sin^2\phi$ values are assigned to each PMT. Those PMT hits with high residual values are given a lower weight in the fit. The simulated annealing method, which is used to identify the global minimum, essentially weights the weighting factors. Initially, all of the PMT hits are used to reconstruct the cone, and then gradually the selective power of the residuals is increased and PMT hits with high residual values

contribute less pull to the orientation of the cone. This algorithm is called the "elastic fitter" in SNOMAN and is the method used to assign to event reconstruction information for the online supernova analysis.

Other reconstruction methods exist, but the algorithms are considerably more computationally intensive than the elastic fitter. Therefore, in the interest of obtaining a reliable result within as short a time as possible, the elastic fitter is adopted as the reconstruction method to be used in the Level 3 analysis stage. Those events which have reconstructed positions within $r = 840$ cm (the fiducial volume enclosed by the PMTs) are designated as *valid* events and are the focus of the remaining analysis.

9.2.3.3 Locating the Supernova

The direction cosine components of each valid event are used to search for elastic scattering events, which are expected to best convey information about the direction of the possible supernova. Without any detector background, the angular resolution obtained by considering only the elastic scattering events is [85]

$$\delta\theta \simeq \frac{25^\circ}{\sqrt{N_{ES}}}, \tag{9.4}$$

where N_{ES} is the number of electron events due to elastic scattering interactions that are observed above the supernova analysis threshold in SNO. According to the results presented in Section 8.4, approximately 25 elastic scattering events are expected using the Beacom and Vogel model whereas 23 events are expected using the Burrows model. Using this naive prescription, SNO would be able to locate the position of the supernova to within an angle $\delta\theta \simeq 5^\circ$. However, events from other supernova neutrino interactions constitute a background that makes it more difficult to isolate the signal due to elastic scattering.

One crude method used to search for the elastic scattering peak is to simply to sum the individual components of the direction cosine values. The idea is that the isotropic background due to the other neutrino reactions cancel, while the forward-peaked contributions

due to elastic scattering reactions sum to a non-zero value. However, this method appears to have limited success.

A more sophisticated technique involves binning the direction cosine data. Using an angular bin window of $\theta = 24.1^\circ$ (corresponding to $\cos\theta = 0.91$), the burst data is examined for a peak in the angular distribution. The elastic scattering peak search algorithm initially considers 234 cardinal directions on a sphere as possible sources of the neutrino burst (corresponding to points on a spherical grid separated by 22.5°). The algorithm then concentrates on the most likely direction from the first stage and searches in a progressively finer 8-point grid around that point in order to identify the direction that yields the maximum number of events in the angular bin window [133], [134].

Investigations concerning how well SNO can locate the angular position of the supernova have been carried out with simulated burst data sets produced using the Burrows model. In order to generate the large number of independent data sets needed for this study, ten sets of 100 supernovae at 10 kpc are produced and then sampled randomly to create many smaller data sets. The elastic scattering peak search algorithm is then applied to each of the smaller data sets in order to determine the probability that the algorithm successfully located the supernova within a certain angle, $\delta\theta$. The data shown in Figure 9.11 demonstrate that the current peak search algorithm is able to determine the location of a supernova as far away as 7.4 kpc to within $\delta\theta = 20^\circ$ (probability $> 50\%$) during pure D_2O operation and 4.5 kpc during salt operation. With salt in the heavy water, the neutron detection efficiency increases and it becomes more difficult to identify the elastic scattering peak. For the same 20° angular deviation, the peak search algorithm is able to locate the position of a 10 kpc supernova approximately 35% of the time in the pure D_2O mode and only approximately 17% of the time in the salt mode. The distribution of angular deviations from the true supernova position are presented for several supernova distances in Figure 9.12. At greater distances, for which the supernova signal contains fewer elastic scattering events, the peak

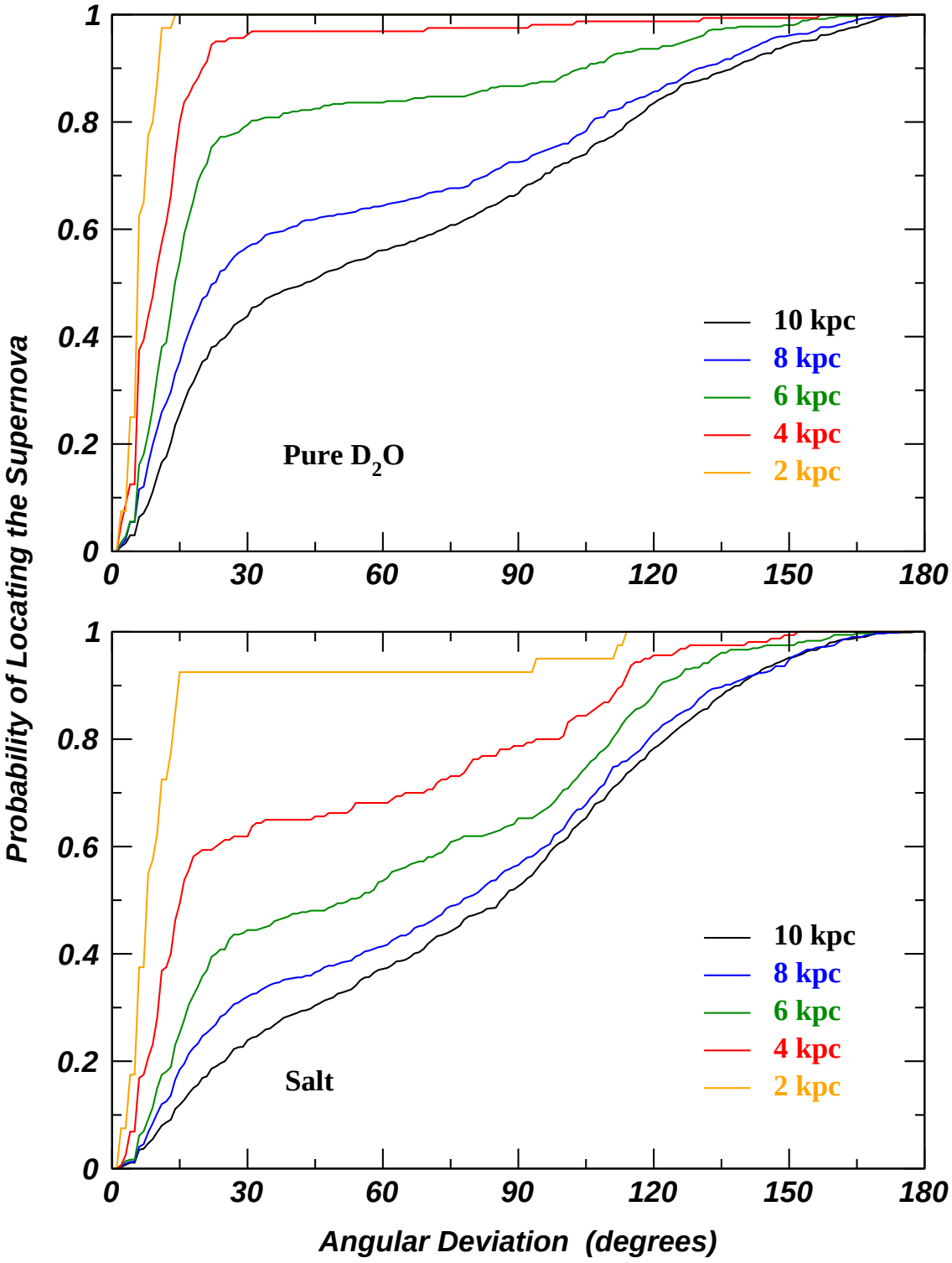

Figure 9.11: Probability of locating a supernova at various distances as a function of the angular deviation from the true supernova location for both the pure D_2O and salt detector modes.

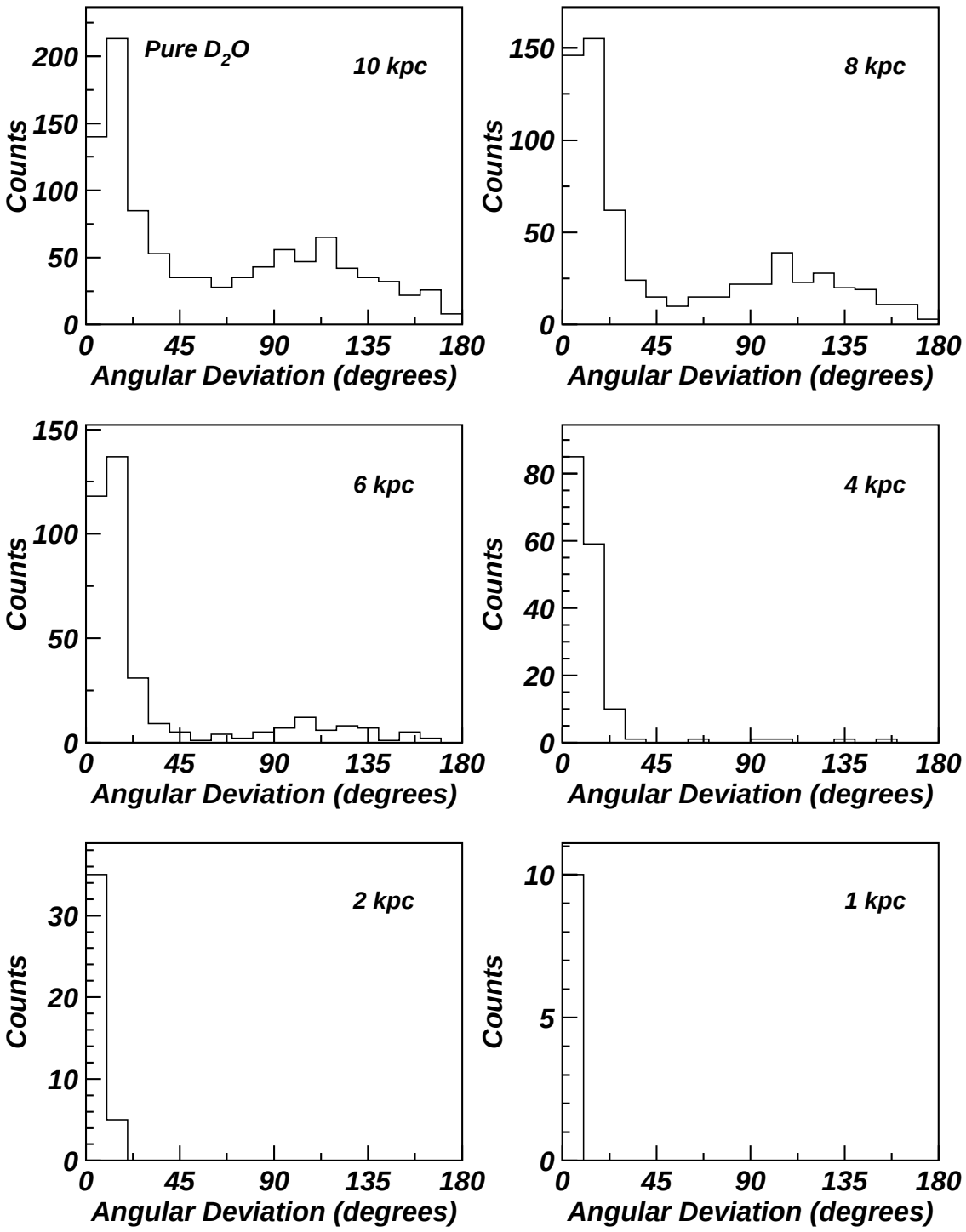

Figure 9.12: The angular difference between the actual supernova position and the position specified by the Level 3 analysis during pure D_2O operation. The angular deviation histograms for the salt mode are similar.

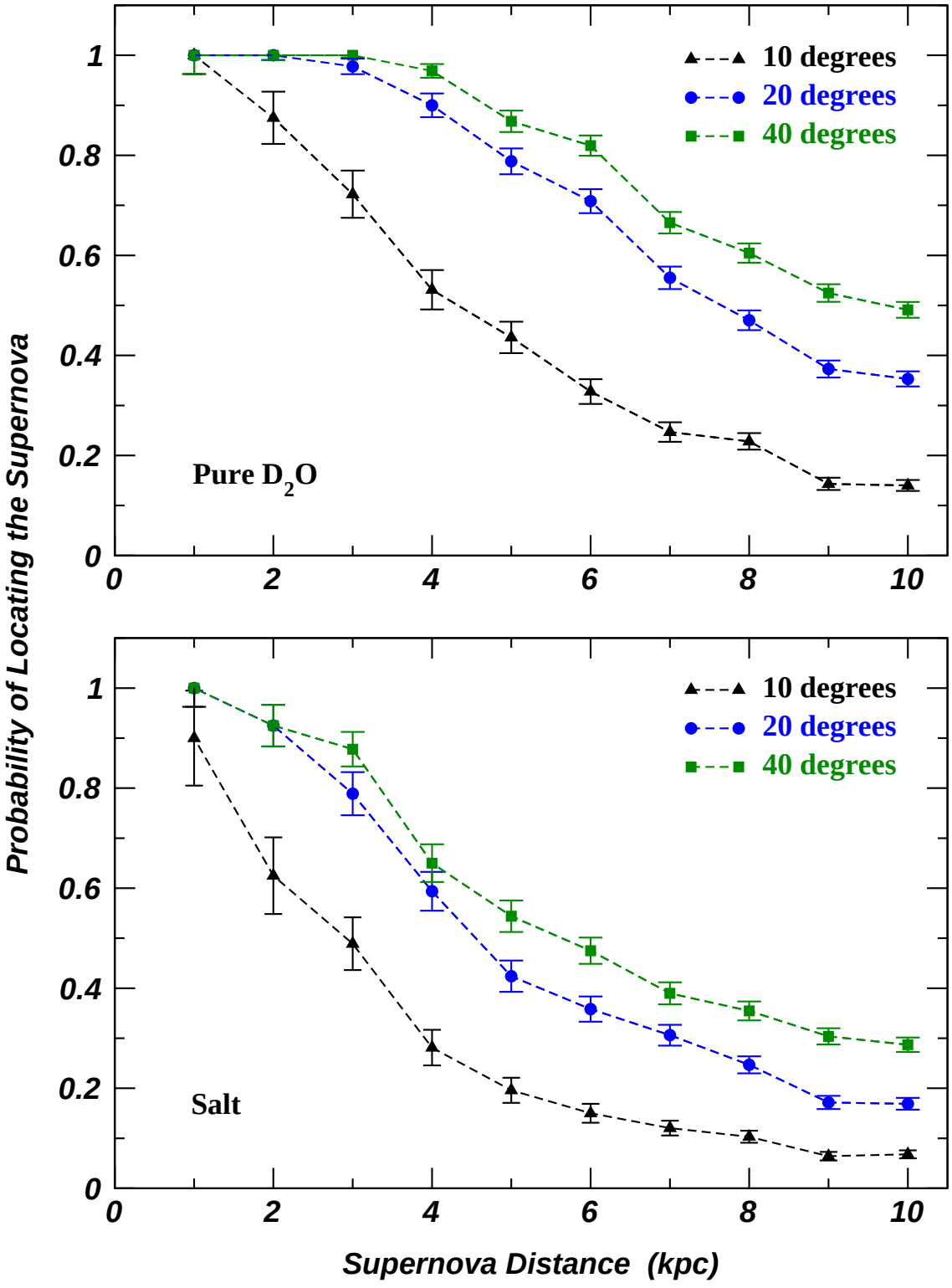

Figure 9.13: Probability of locating a supernova within various angular areas as a function of supernova distance for both the pure D_2O and salt detector modes.

finding algorithm often completely fails to locate the supernova. In some instances, this failure is due to the low number of elastic scattering events in that trial. The random sampling technique used in this analysis does not guarantee that all trials have the same number of elastic scattering events. Figure 9.13 illustrates the probability of locating a supernova as a function of distance for various angular resolution values. For a supernova at 10 kpc, it is possible to locate the supernova to within 42° during the pure D_2O mode and 86° during the salt mode.

Further studies are required in order to further optimize the peak search algorithm and to investigate means of decreasing the background to the elastic scattering peak. It should be possible to reduce the charged-current contribution by using a high energy cut. The tail of the elastic scattering event NHIT distribution does not extend as far as the charged-current event tail. Therefore, a high energy cut would serve to increase the ratio of elastic scattering events to the events remaining from other interactions. An energy cut is not an effective method to reduce the neutral-current contribution, however, because those events have the same energies as the majority of the elastic scattering events.

9.2.3.4 Analysis Summaries

As with the Level 2 analysis, a text summary of the burst characteristics resulting from the Level 3 analysis is made available to the detector operator on shift. The information provided in the summary includes the number of valid events in each of the D_2O and H_2O regions as well as the results of the elastic scattering peak finding algorithm. An example summary text message is shown in Figure 9.14 for a Monte Carlo supernova burst at 10 kpc according to the Burrows supernova model.

As well, a set of summary histograms is produced for each Level 3 burst. The plots show the NHIT and relative time distributions for the valid events in addition to the volume-weighted distribution of radial positions and the detector ϕ and θ angular distributions.

```
Ref. burst_10000_001

A supernova burst candidate has passed the level 2 analysis threshold
and is now being analysed by the third level trigger.

Cleaned ZDAB file: burst_10000_001.zdab
                        (in /scratch/lt/sstream/snwatch/clean_zdab on SURF)
Analysis Info Summary:
----------------------
SNOMAN version ........... 4.0186
SNOMAN analysis time .....    2.41 minutes

Supernova Level 3 Analysis Summary:
-----------------------------------
RUN # ..........................     3  (starting at GTID =        1 )
Date / Time ..................... 20/01/2000 at 02h 16m 08s (Sudbury time)
Time duration of clean events ...     47.4995483 s   (50 MHz)
Total number of clean events ....    551 events

Fitted Data Results (elastic fitter, vertex within PSUP)
--------------------
Date / Time ........ 20/01/2000 at 07h 16m  7.3245958 s (Universal time)
Time duration ......     47.499548341 s   (50 MHz + fit)
Number of events ...    420
NHIT100 triggers ... 100.0%
  NHIT  < 75 .......  37.9%
  NHIT >= 75 .......  62.1%
ESUM triggers ......   0.0%
OWL triggers .......   0.0%
Summed dircos ......  0.614904 −0.315363 −0.722799  (toward SN)

                                  D2O region          H2O region
                                  ----------          ----------
Fraction of events .............       50.7%               49.3%
Fraction of NHIT100 triggers ..       50.7%               49.3%
  Fraction of NHIT  < 75 ......       26.0%               11.9%
  Fraction of NHIT >= 75 ......       24.8%               37.4%
Fraction of ESUM triggers .....        0.0%                0.0%
Summed dircos (toward SN)......  0.91  0.00 −0.41   −0.95 −0.32 −0.04

Supernova Direction Analysis Results
------------------------------------
Direction cosines (toward SN) ...  0.16973 −0.68643 −0.70711
Zenith, azimuth ................. 135.00002 degrees  166.11109 degrees E of N
Declination, right ascension .... −45.39728 degrees   17.33792 hours
```

Figure 9.14: Level 3 analysis summary text message.

Results from the elastic scattering peak finding algorithm are also used to plot a histogram of the $\cos\theta_{SN}$ distribution, where θ_{SN} is the angle between the event direction and the direction of the supernova, as described in Section 7.6. Events in the D_2O and H_2O regions are also analyzed separately to ensure the consistency of the burst events. An example of the Level 3 analysis summary histograms are shown in Figure 9.15. The analysis histograms for

the heavy- and light-water regions which are also part of the set, are shown in Figures 9.16 and 9.17 (also see Appendix D).

9.2.3.5 Communication

The summary text file and analysis histograms are sent via email to members of the SNO Supernova Working Group, the detector operator email account, as well as being posted to an internal website. By the time that the Level 3 analysis results are available, members of the SNO Supernova Working Group should already have contacted the detector operator and assessed the significance of the burst. The SNO Supernova Working Group, in consultation with the detector operator, will determine whether or not to manually issue an external alert at the Level 4 stage.

9.2.3.6 Burst Causes

Despite the application of the data reduction cuts during the Level 2 analysis stage, a number of bursts in which 35% or more of the events remain pass on to be analyzed by the Level 3 stage. Based on the number of bursts experienced at the Level 2 stage, it is not surprising that the vast majority of the bursts that reach the Level 3 stage are due to calibration activities. In any case, the cause of each burst is investigated by reviewing the detector shift reports and by studying the the burst data files and is correctly assigned in Table 9.5. Instances in which the detector operator does not provide information that properly reflected the status of the detector in the case of some calibration activities has been accounted for in the results presented in Table 9.5.

Results comparing the Level 3 burst rate using the NEVENT=30 and 50 burst trigger parameter settings are also presented in Table 9.5. The main difference observed between the two settings is the significant increase in the burst rate due to calibration activity, while the burst rates due to the other sources change only slightly. Changing the NEVENT parameters can sometimes reduce the size of a burst and therefore the fraction of events

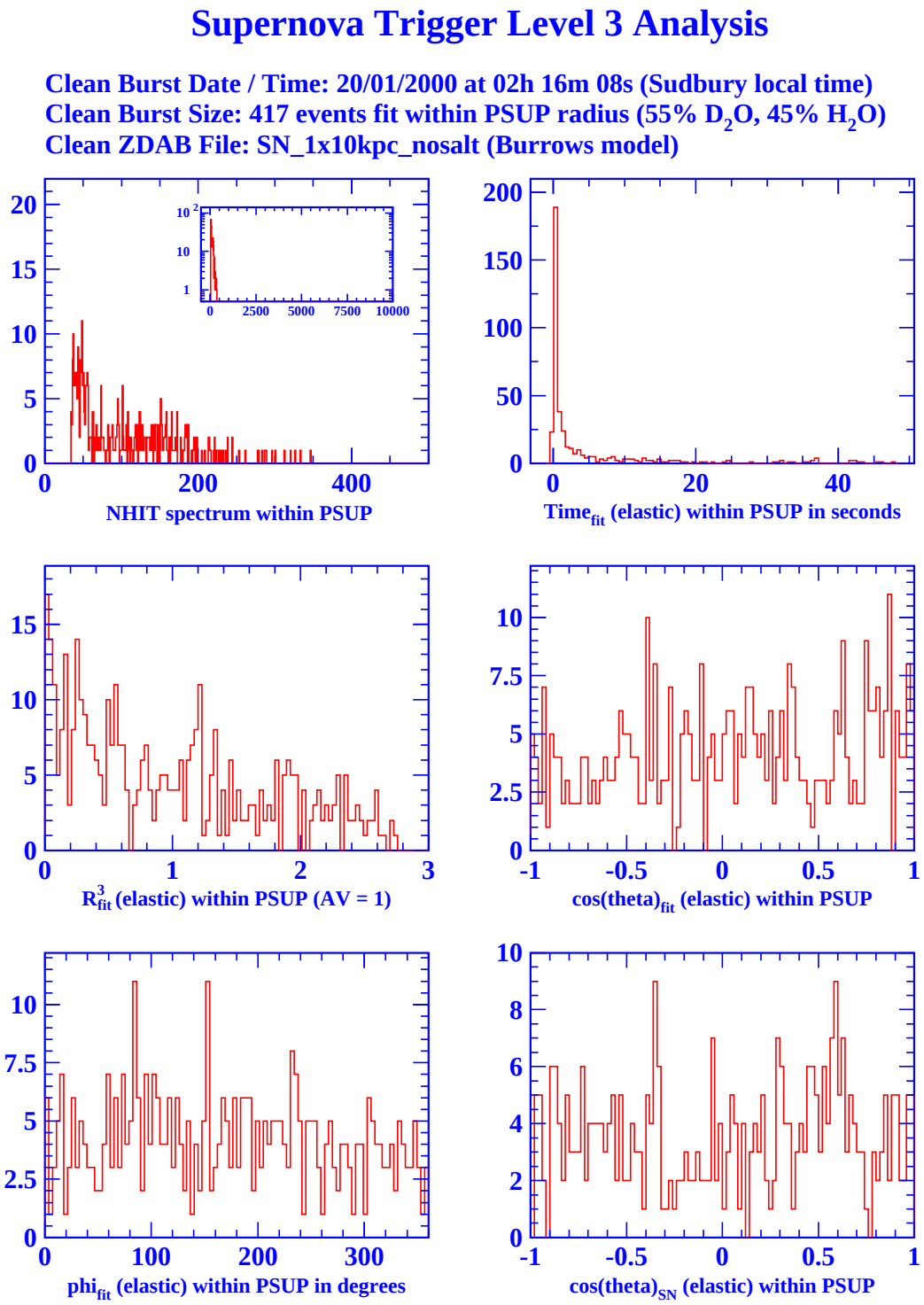

Figure 9.15: Level 3 analysis summary histograms showing various distributions for all burst events that are reconstructed within the detector volume. The example shown is a simulated supernova burst at 10 kpc according to the Burrows model.

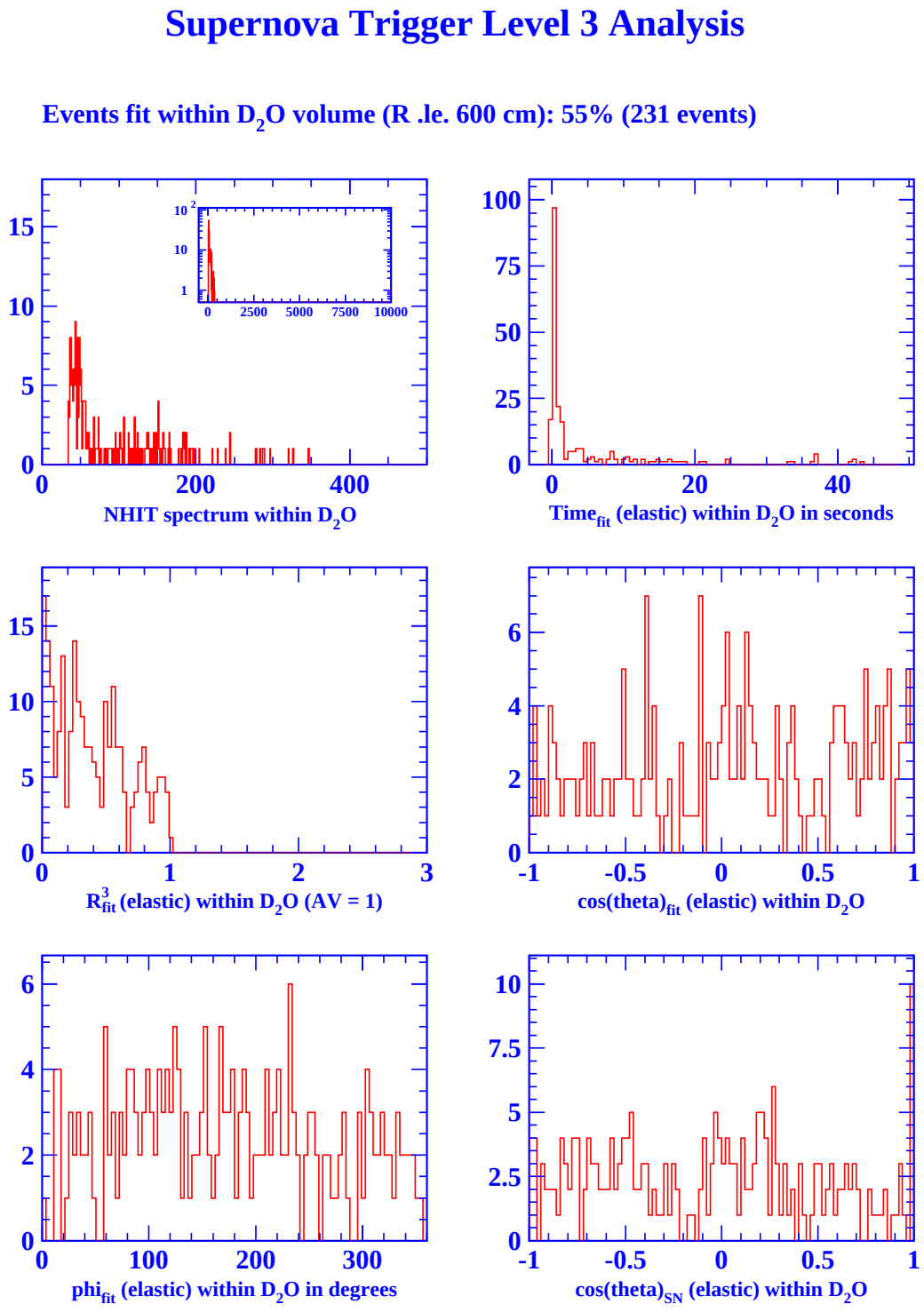

Figure 9.16: Level 3 analysis summary histograms showing various distributions for burst events that are reconstructed within the D_2O region. The example shown is a simulated supernova burst at 10 kpc according to the Burrows model.

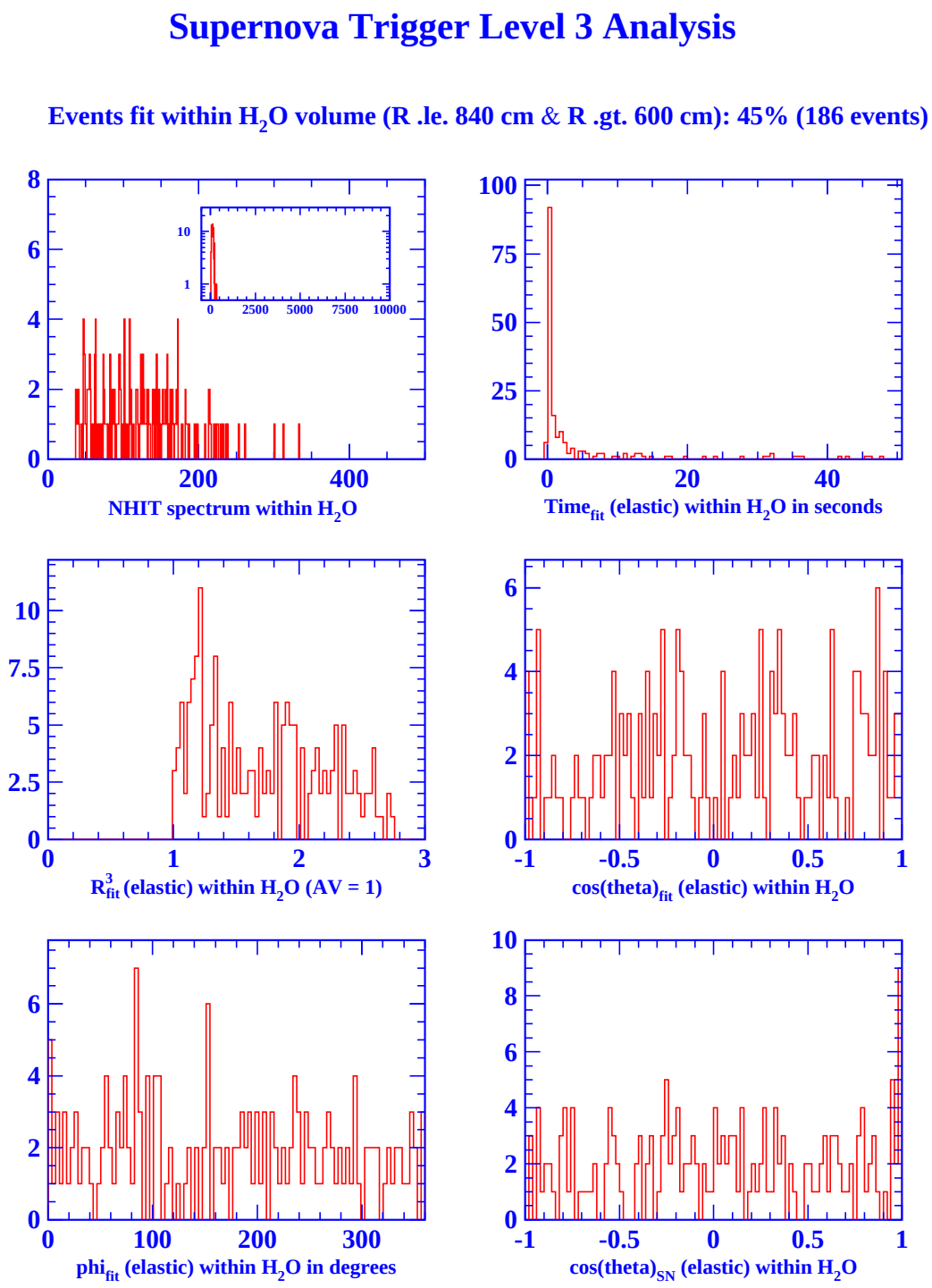

Figure 9.17: Level 3 analysis summary histograms showing various distributions for burst events that are reconstructed within the H_2O region. The example shown is a simulated supernova burst at 10 kpc according to the Burrows model.

Burst Cause	NEVENT = 50		NEVENT = 30	
	Rate (day^{-1})	Fraction of Total Bursts	Rate (day^{-1})	Fraction of Total Bursts
Calibration	2.98	86.5%	10.06	93.6%
Water Activities	0.41	11.9%	0.61	5.7%
Spallation	0.03	0.7%	0.06	0.5%
Electronics	0.03	0.9%	0.02	0.2%
Neck Static	0.00	0.0%	0.00	0.0%
Total	**3.45**	**100%**	**10.75**	**100%**

Table 9.5: Rate of bursts due to various causes in which 35% or more of the events remain after the Level 2 analysis stage. Results are included for two settings of the NEVENT burst trigger parameter.

that pass the Level 2 data reduction cuts. This difference accounts for the decrease in the burst rate due to electronics sources. As discussed in Section 9.2.2.1, the rate of spallation events increases as fewer events are required to form the trigger.

Since the majority of the events that reach the Level 3 stage are due to calibration activities, many of the bursts are due to a single cause, as observed with the Level 1 burst monitor. Figure 9.18 shows the rate of Level 3 bursts as a function of the time between bursts, indicating that there are approximately 0.6 bursts/day using the NEVENT = 30 setting.

9.2.4 Level 4

The final stage in the SNO response is to issue an alert to the astronomical community. Interested parties have already approached the SNO collaboration and asked to be placed on a contact list; however, at the time of this thesis, no formal contact list has been established. In the event of a real supernova, the first alert will likely be issued via the SNEWS network.

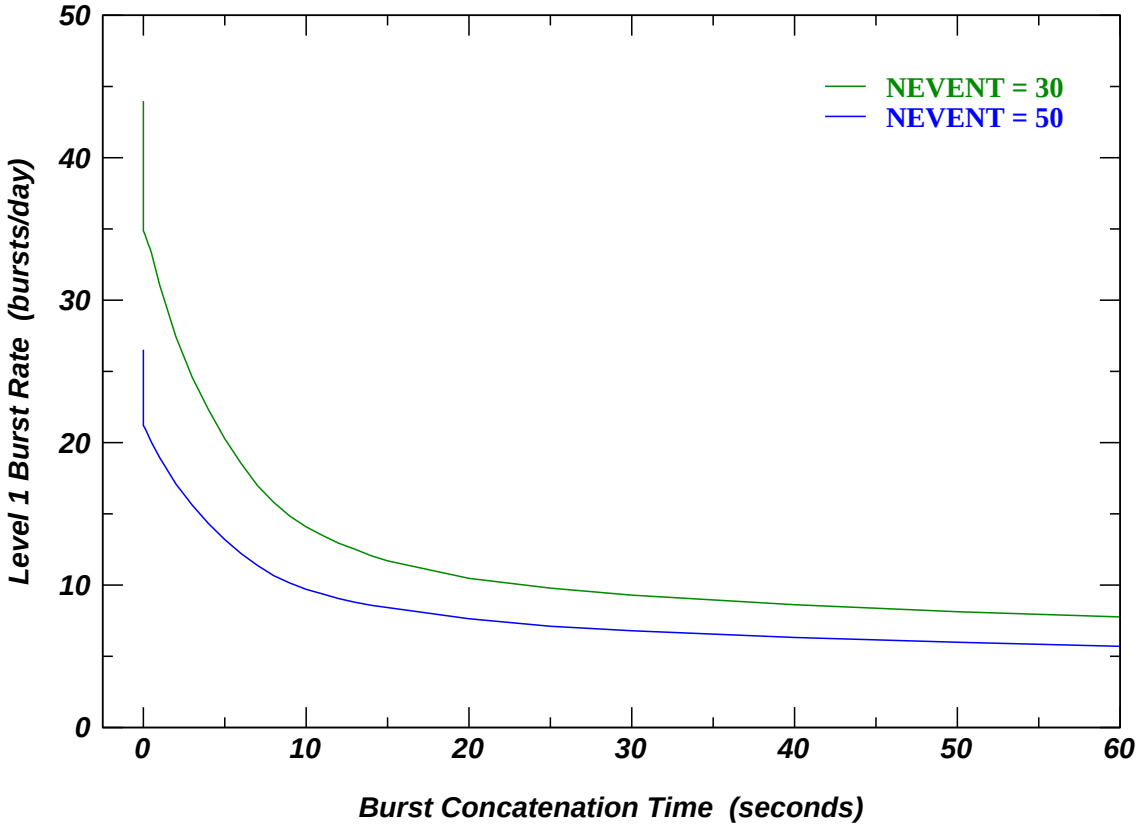

Figure 9.18: Level 3 burst rate as a function of the time between bursts, determined offline for the period between November 2, 1999 and January 4, 2001. The most significant contribution to this effect is from calibration activity.

9.2.4.1 SNEWS

The inter-experiment SuperNova Early Warning System (SNEWS) is designed to provide a fast and reliable alert to the astronomical community by requiring a coincidence of burst signals from several operating experiments. Alert signals issued by individual experiments are transmitted as secure encrypted text datagrams via the internet to redundant coincidence servers located in Japan and Italy. An alert to the astronomical community would be issued in the event that two or more experiments identified a burst within a coincidence time of 10 seconds. Assuming that the individual alerts are distributed according to

Poisson statistics, an alert based on a false coincidence would be issued only once per century [135]. Experiments that are currently participating in SNEWS include LVD [136] and Super-Kamiokande[4] [137]. The MACRO [138] was also an early SNEWS participant, but that experiment has now been decommissioned. While SNO is not yet officially connected to the SNEWS network, members of the SNO collaboration are part of the working group that constitutes the SNEWS collaboration.

9.2.4.2 Communication

In the event of a significant burst, SNO would manually connect to the two SNEWS coincidence servers using a client developed by the SNEWS working group. The client provides a secure means of transmitting the following burst information:

- experiment identification number
- universal time stamp of first valid event
- total number of valid events.

Information on the celestial location of the supernova can also be submitted to the coincidence server. It is expected that SNO will begin providing automatic alerts once the monitoring programme is determined to be sufficiently mature.

9.2.5 SNO Supernova Response Time

Once a burst is determined to have significant physics content, an alert must be sent as quickly as possible in order to be useful to the astronomical community. The expected time required to send an alert to SNEWS is discussed below.

[4] As of July 16, 2001, the Super-Kamiokande detector has been taken offline in order to proceed with PMT replacement work. They had expected to be back online in mid-December but an accident on November 12 destroyed over 50% of the detector PMTs. It is not currently known when the detector will be able to resume operation.

The first supernova neutrino interaction starts the response time stopwatch. A small amount of time is required to build the hit PMT information into events and send them to the Level 1 burst monitor computer on the surface. Once the events are in the burst trigger FIFO buffer, it is only a matter of milliseconds before the Level 1 trigger is satisfied. For the following discussions on the analysis stages, Monte Carlo bursts with ~ 500 events were analyzed on the supernova analysis computer. The Level 2 background rejection analysis is expected to take on the order of 2 minutes, which is relatively fast compared to the more detailed analysis at the Level 3 stage. The Level 3 analysis takes the longest time since this is where the events are fit to extract time, position and direction information. During the Level 3 analysis, the three members of the Supernova Working Group with cell phones join a conference call initiated by the detector operator and determine whether or not to send an alert to the SNEWS coincidence computer. An overview of the predicted response time is presented in Table 9.6. The goal of the Sudbury Neutrino Observatory is to be able to send an alert with an estimate of the supernova direction to SNEWS within approximately 20 minutes from the time of the first event in the detector with essentially zero possibility of false alarm.

SNO Supernova Response Stage	**Individual Stage Time (minutes)**	**Cumulative Stage Time (minutes)**
First SN neutrino interacts in detector	0	0
Data processing offset	0.5	0.5
Level 1 trigger satisfied	0.003	0.5
Level 2 analysis (based on Monte Carlo)	2	2.5
Level 3 analysis (based on Monte Carlo)	15	17.5
Conference call (during Level 3 analysis)	20	22.5
Alert SNEWS (manually)	1	23.5

Table 9.6: Expected time required to perform the SNO burst analysis and issue an alert to SNEWS. The times for the Level 2 and Level 3 analyses are estimated using Monte Carlo simulations running on the supernova burst analysis computer.

Chapter 10

SNO Supernova Sensitivity

10.1 Introduction

SNO is considered to be sensitive to neutrinos when the PMTs have nominal high voltage and when the appropriate detector triggers are in use. As mentioned in Section 4.7, the primary trigger used for physics analyses is the NHIT100 trigger, which requires a coincidence of a certain number of hit PMTs within 100 ns. Different running modes have different trigger requirements, however the time that the NHIT100 trigger is operative defines the detector livetime. A further consideration concerns the degree of sensitivity that SNO possesses during its livetime. Both of these aspects are discussed in the sections that follow.

10.2 SNO Detector Livetime

Since a supernova may occur at any time, an effort has been made to maintain supernova sensitivity throughout all types of detector activity. During times when the detector is being triggered externally, such as when the laser calibration light source is in use, the formation of NHIT100 trigger is delayed slightly relative to the calibration signal to allow the detector to remain sensitive to neutrino events. Table 10.1 summarizes the NHIT100 trigger thresholds and associated NHIT100 livetime fractions during different detector running conditions. The livetime statistics span the period beginning November 2, 1999 and ending January 4, 2001. For most of this time, the main "neutrino" NHIT100 trigger required 18 hit PMTs

Run Condition	**NHIT100 Threshold**				**Fraction of NHIT100 Livetime**
	Default		**Monitor**		
	(PMTs)	**(MeV)**	**(PMTs)**	**(MeV)**	
Neutrino	18	2.0	34	3.8	80.0%
	16	1.8	34	3.8	3.3%
Calibration:					
• *electronics*	*35*	*3.9*	*35*	*3.9*	*1.5%*
• *laser (external trigger)*	*50*	*5.6*	*50*	*5.6*	*3.0%*
→ *source setup*	*50*	*5.6*	*50*	*5.6*	*0.8%*
• ^{16}N, ^{8}Li, ^{252}Cf	*18*	*2.0*	*69*	*7.7*	*2.5%*
→ *source setup*	*50*	*5.6*	*69*	*7.7*	*0.5%*
• *U, Th*	$\leq$ *44*	$\leq$ *4.9*	*44*	*4.9*	*1.0%*
	45–60	*5.0–6.7*	*45–60*	*5.0–6.7*	*0.1%*
→ *source setup*	*50*	*5.6*	*50*	*5.6*	*0.1%*
• *other*	$\leq$ *25*	*2.8*	*34*	*3.8*	*0.2%*
	35–50	*3.9–5.6*	*35–50*	*3.9–5.6*	*0.1%*
Maintenance	40	5.0	40	5.0	4.9%
Diagnostic	35	3.9	35	3.9	0.1%
	55	6.1	55	6.1	0.1%
Unstable Conditions	35	3.9	35	3.9	1.6%
Other	18	2.0	34	3.8	0.2%
Average Threshold	**21.0**	**2.3**	**36.2**	**4.0**	**100%**

Table 10.1: The 100 ns coincidence trigger thresholds during various detector running conditions and their associated NHIT100 livetime fractions for the period from November 2, 1999 to January 4, 2001. The default threshold values are those implemented by the detector event trigger, whereas the monitor values denote the threshold used in the burst identification algorithm.

within 100 ns; however, in December 2000, the neutrino trigger threshold was lowered to 16 PMTs in coincidence. In total, 86.7% of the data collected with the NHIT100 trigger enabled was at a trigger threshold of 2 MeV or lower. Since November 1999, the SNO detector had high voltage enabled for 92.1% of the time, with the NHIT100 trigger enabled for 98.7% of that time. Therefore, the fraction of time that SNO has been sensitive to neutrinos is 90.9%, as shown in Figure 10.1. Detector downtime is mainly due to power outages during electrical storms and interruptions in the power arising from

mining operations. For instance, the significant downtime during the months of August and September 2000 is due to power interruptions resulting from a large number of electrical storms.

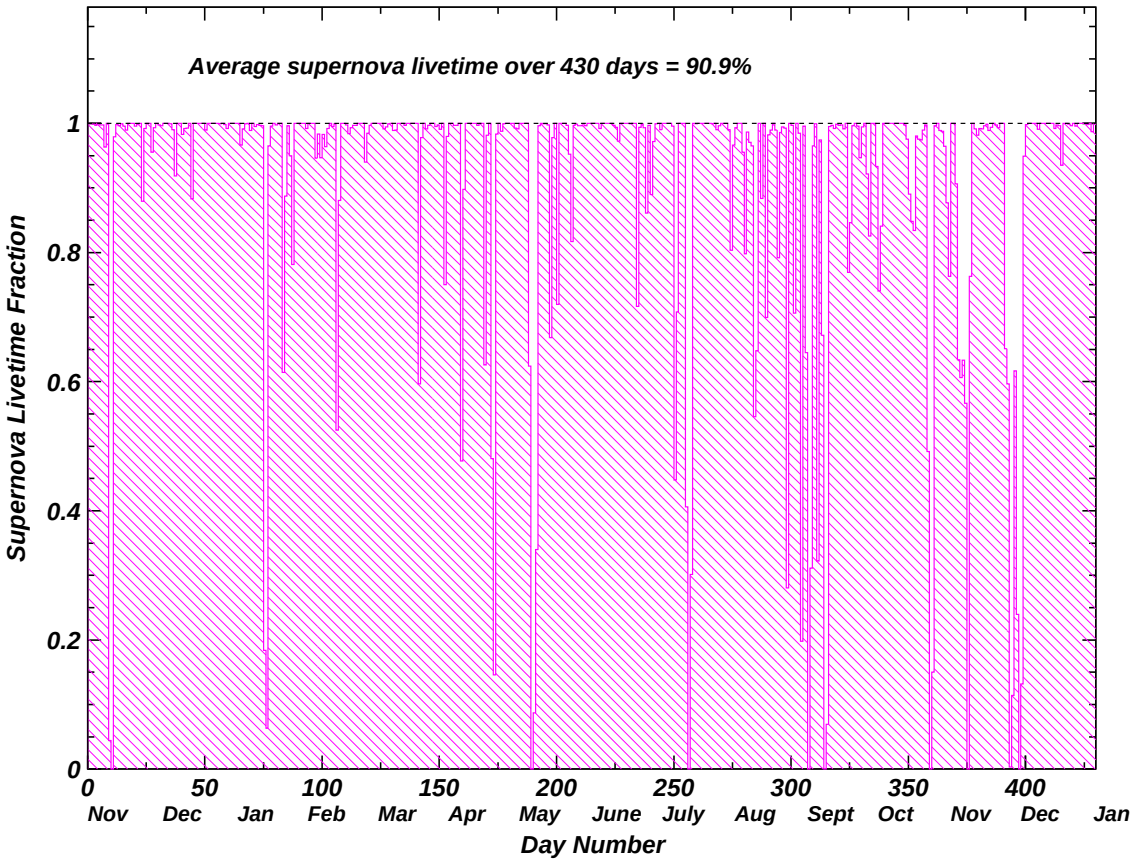

Figure 10.1: SNO supernova livetime as a function of time for the period from November 2, 1999 to January 4, 2001.

The average detector NHIT threshold during the time that SNO was sensitive to neutrinos was approximately 21.1 PMTs or 2.4 MeV. Taking into account the run-specific thresholds discussed in Section 9.2.1.2 for various operating conditions, the average monitoring NHIT threshold was 36.2 PMTs or 4.0 MeV. Before December 16, 1999, when the global trigger channel was not included in all events, the burst monitoring threshold was

1 PMT higher (∼0.1 MeV) in the cases where the threshold was applied by the burst monitor and not the detector trigger.

10.3 SNO Distance Sensitivity

The maximum distance to which SNO is sensitive to a burst of neutrinos from a supernova is determined by considering the minimum supernova signal that satisfies the Level 1 burst trigger. In order to characterize the SNO distance sensitivity, data from two independent simulations of 100 supernovae at 10 kpc using the Burrows model[1] are used to determine the fraction of events that satisfy the NHIT and time window trigger criteria. A time window of 2 seconds is used in all cases. This fraction is then used to scale the minimum number of events required for the trigger to the number of events expected over the course of the full duration of the burst. The scaled number of events corresponds to the total number of events in the burst, which is associated with a standard supernova at a certain distance. For example, of the 545 events that register in the detector above the analysis threshold during the pure D_2O phase, approximately 69% of the events in the first 2 seconds have NHIT $\geq$ 34 PMTs, and are considered by the burst trigger. In the case where 30 such events are required to form the trigger (NEVENT), the corresponding number of events in the full burst becomes 30/0.69=43 events with NHIT $\geq$ 34 PMTs. A total burst of 43 events translates into a supernova at a distance of 35 kpc. Hence, the NHIT trigger parameter determines the fraction of the total signal that meets the trigger criteria, while the NEVENT parameter determines the minimum size of the supernova burst signal. When the number of events in the first 2 seconds with NHIT $\geq$ 34 PMTs is less than the NEVENT setting, the burst monitor will not trigger and SNO is no longer sensitive to a supernova using this algorithm.

[1]The simulated data sets do not contain the contribution due to reactions involving oxygen. For the Burrows model, this contribution is estimated to be less than 2% of the total number of events.

10.3.1 NHIT Trigger Parameter

Fewer events are available to form a burst trigger during periods in which high NHIT thresholds are used, and therefore the detector is less sensitive to neutrinos from a supernova during those times. Figure 10.2 shows how the SNO distance sensitivity is affected as a function of the burst trigger NHIT threshold. The increase in the number of events due to the neutron signal is clearly pronounced in the NHIT region below 100 PMTs. In the unlikely event that the detector trigger threshold (or a future implementation of the burst monitor) is set to NHIT = 215 PMTs, SNO would no longer possess sensitivity to a generic Burrows-like supernova[2] using the burst search method that has been described. However, the small fraction of events that are present above this threshold (approximately 5.4% during the pure D_2O mode and 4.2% in the salt mode) would still exist in the data and could be identified using other search algorithms.

According to the Burrows supernova model, the average distance sensitivity during pure D_2O operation is approximately 35 kpc using the supernova analysis threshold of 34 PMTs and requiring 30 events to form the trigger in conjunction with the standard run-specific thresholds. The corresponding distance sensitivity during the salt running mode is approximately 40 kpc. When 50 events are required to form the trigger instead of 30, the average distance sensitivity decreases to 27 kpc and 31 kpc for pure D_2O and salt, respectively. Similar results are obtained using the Beacom and Vogel supernova model. Using the default burst monitor parameters and simulated data with the Beacom and Vogel model, the distance sensitivity is 34 kpc during the pure D_2O running mode and 41 kpc during the salt running mode.

Figure 10.2 also shows that the distance sensitivity does not increase significantly for

[2]The corresponding upper NHIT threshold limit according to the Beacom and Vogel model is slightly higher because of the higher neutrino temperatures used in that model.

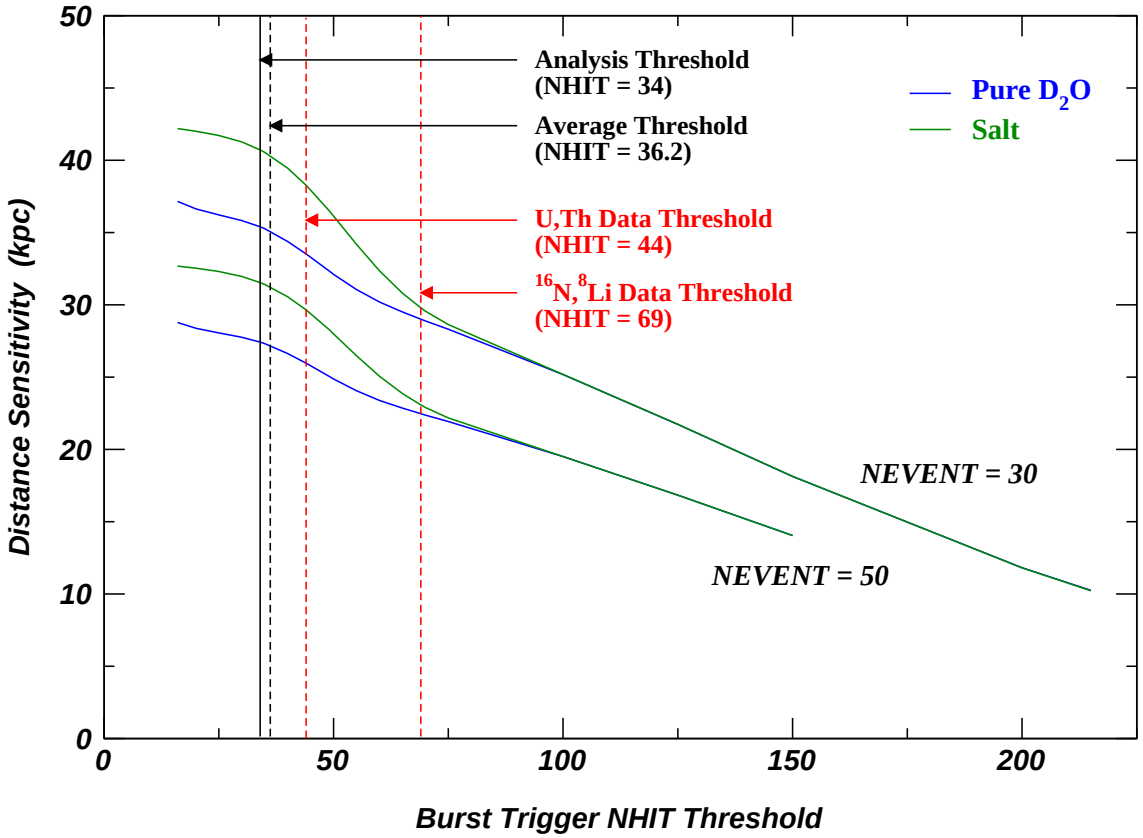

Figure 10.2: SNO supernova distance sensitivity as a function of the online burst trigger NHIT threshold determined using simulated data sets that employ the Burrows supernova model. Various threshold settings are labelled to indicate the corresponding distance sensitivity values during the pure D_2O and salt detector operation phases for two NEVENT trigger parameter settings.

an NHIT setting below the current analysis threshold of 34 PMTs. Therefore, any considerable increase in the sensitivity to distant supernovae will result from adjustments to the NEVENT parameter rather than the NHIT parameter.

10.3.2 NEVENT Trigger Parameter

Lowering the number of events required for the burst trigger allows the trigger to be more sensitive to smaller bursts, thereby increasing the sensitivity to supernovae located at

greater distances. Figure 10.3 illustrates the increase in distance sensitivity as fewer events are required to form the trigger. The two NHIT threshold values that are shown indicate the range of threshold settings used during different detector running conditions. Using the default settings, the SNO detector maintains sensitivity to the entire Milky Way galaxy during all running conditions.

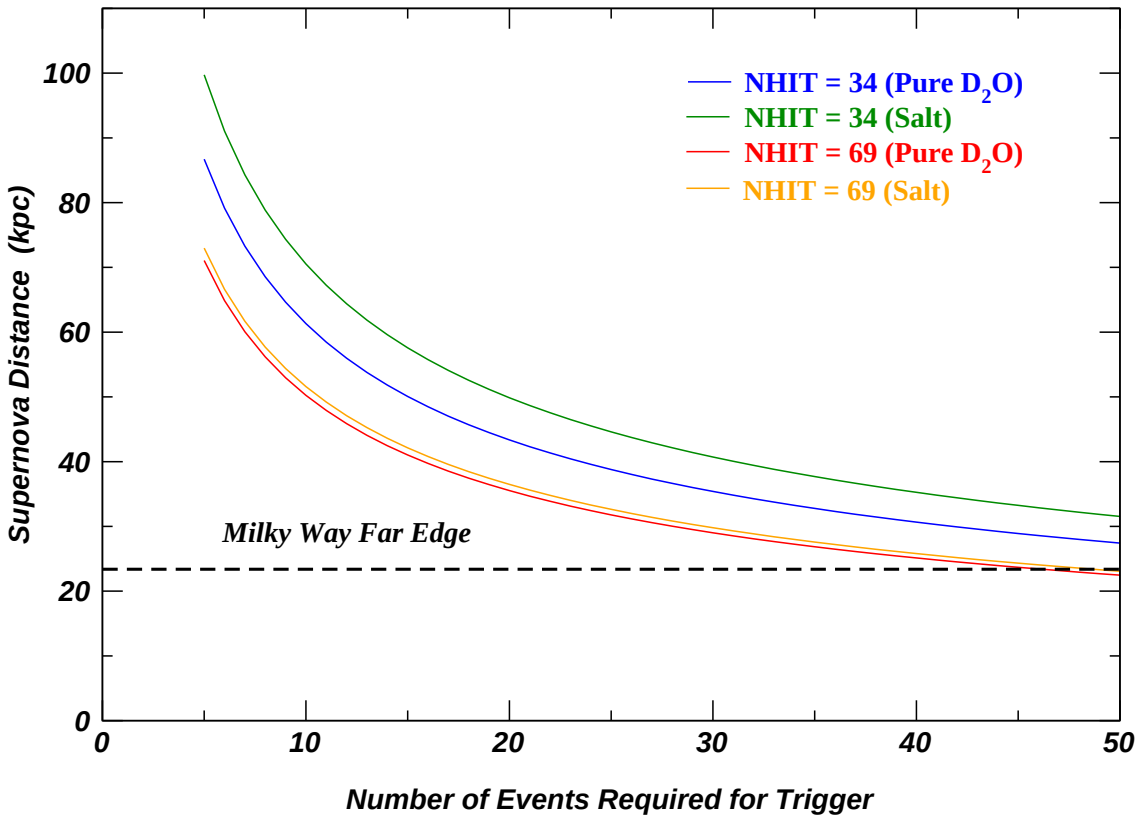

Figure 10.3: SNO supernova distance sensitivity as a function of the number of events required to form the burst trigger. Two NHIT values are shown to indicate the range of threshold settings used during different detector running conditions. The default parameters are NHIT = 34 and NEVENT = 30.

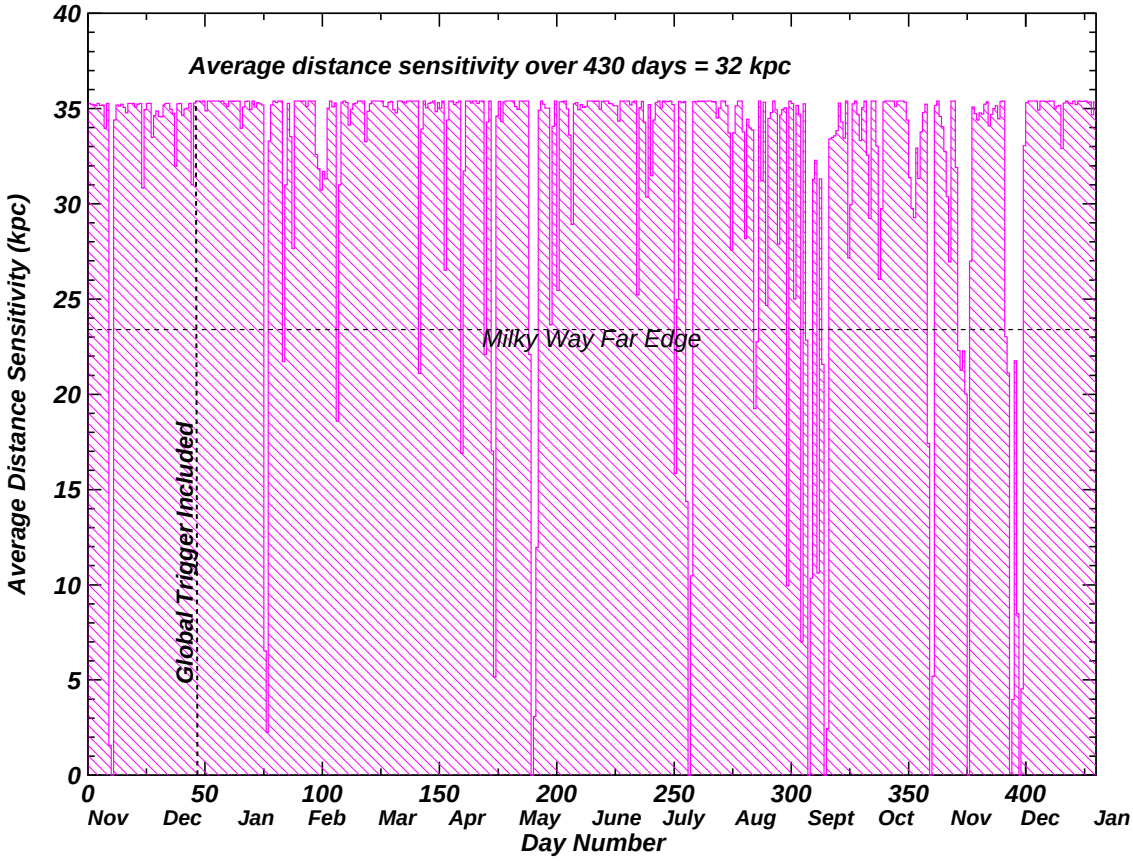

Figure 10.4: SNO supernova distance sensitivity as a function of time using the default parameters for the period from November 2, 1999 to January 4, 2001.

10.3.3 Detector Livetime

As described in Section 10.2, the SNO detector is completely insensitive to neutrinos approximately 8.7% of the time because the detector is not operating. The average distance sensitivity values mentioned above for the Burrows supernova model decrease slightly when the detector livetime is taken into account. During pure D_2O operation, the average livetime corrected distance sensitivity is approximately 32 kpc and for salt operation the average livetime corrected distance sensitivity is 37 kpc. From Earth, the distance to the far edge of the Milky Way galaxy is roughly 23 kpc, which means that during both operation

modes, the SNO distance sensitivity extends beyond the far edge of the Milky Way galaxy. However, the current online mode of operation is not sensitive to bursts originating in the Large or Small Magellanic Clouds (∼55 kpc and ∼65 kpc, respectively). Figure 10.4 shows the distance sensitivity as a function of time for the offline study in which 30 events are required to form the trigger. The various NHIT conditions outlined in Table 10.1 are also included, as is the small effect of not including due to the global trigger channel in each event as was the case during the initial running conditions (see Section 10.2).

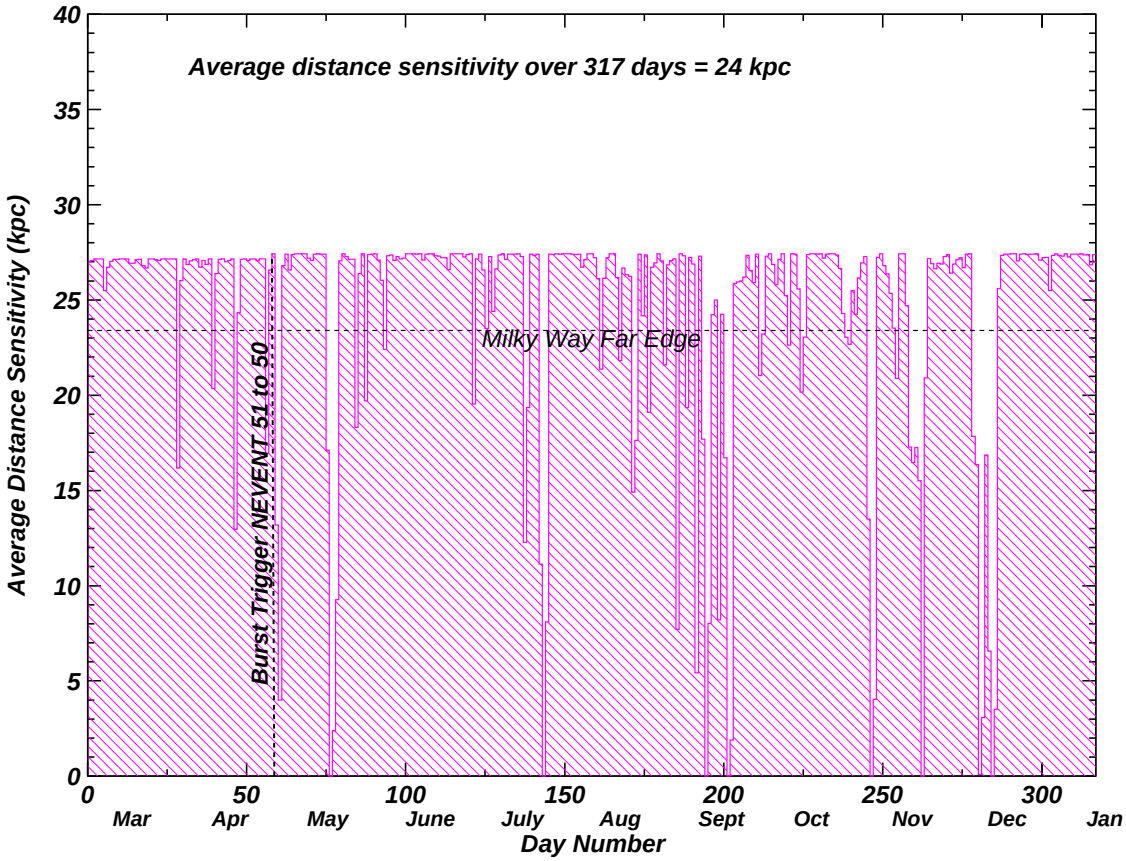

Figure 10.5: SNO supernova distance sensitivity as a function of time using the online burst monitor parameters for the period from February 23, 2000 to January 4, 2001.

The corresponding plot showing the distance sensitivity as a function of time using the

actual online parameters over the period from February 23, 2000 to January 4, 2001 is provided in Figure 10.5. The average distance sensitivity achieved with the online burst monitor is approximately 24 kpc (during the pure D_2O operating mode), which extends beyond the far edge of the galaxy.

10.4 Burst Identification Efficiency

The efficiency of the burst identification algorithm is determined using Monte Carlo data that was generated using the Burrows supernova model. Two independent data sets each containing detected SNO events for 100 supernovae at 10 kpc are separated into many smaller data sets by randomly choosing a certain number of events corresponding to a particular supernova distance. The events in each of the smaller data sets are then subjected to the burst trigger conditions, where n events are required above an NHIT threshold in a certain time window. The burst identification efficiency, $\epsilon(d)$, is defined as

$$\epsilon(d) = \frac{N_{trig}(d)}{N_{total}(d)}, \tag{10.1}$$

where d is the distance to the supernova, N_{trig} is the number of successful triggers and N_{total} is the total number of trials. As the supernova distance increases, the number of events in each trial decreases and therefore so does the number of successful triggers.

Figure 10.6 shows the burst identification efficiency as a function of supernova distance during both the pure D_2O and salt operating modes. In all cases, the analysis threshold NHIT = 34 and the time window of 2 seconds are used. As the number of events required to form the trigger is lowered, the burst identification algorithm becomes sensitive to a Burrows-like supernova at greater distances away from Earth. For the default setting in which $n = 30$ events is used, SNO maintains 100% detection efficiency throughout our galaxy in both the pure D_2O and salt operating phases. The SNO burst identification algorithm decreases to 50% efficiency at approximately 36 kpc during the pure D_2O mode

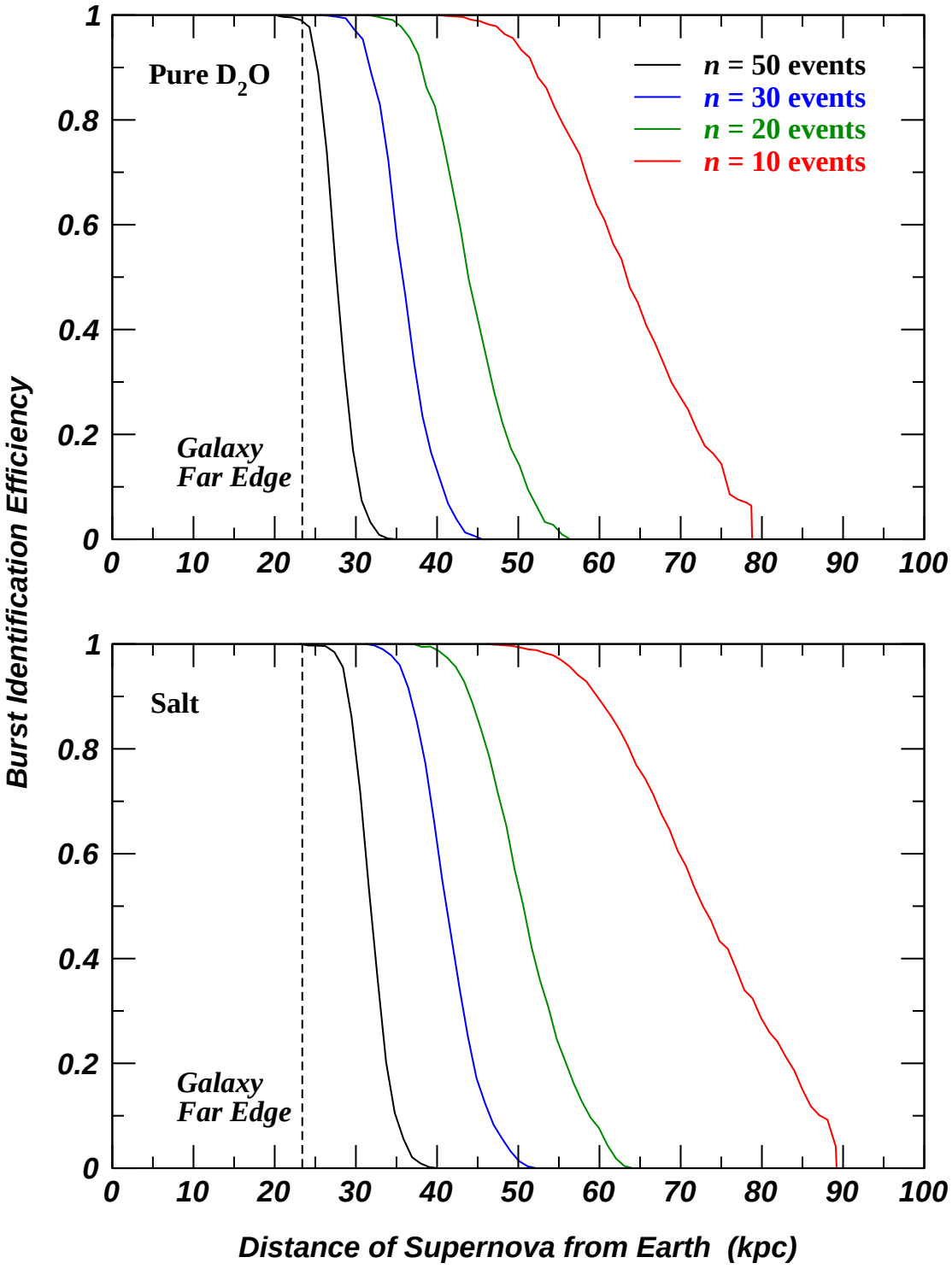

Figure 10.6: SNO burst identification efficiency as a function of supernova distance for both the pure D_2O and salt operating phases. In all cases, the burst trigger requires n events above the NHIT = 34 threshold in 2 seconds.

and 41 kpc during the salt mode using the default settings for the burst trigger. The abrupt decrease at the large distance tail of both of the $n = 10$ event curves occurs when the number of events in the burst falls below the number of events required to form the trigger.

The maximum distance sensitivity values discussed in Section 10.3 correspond to burst identification efficiency values of $\epsilon = 50\%$. This detection efficiency is taken to be the burst detection threshold.

Chapter 11

Analysis of 241 Days' Data

11.1 Introduction

The data collected with the offline burst identification algorithm outlined in Chapter 9 are used in the supernova burst search analysis.

11.2 Data Selection

For the first supernova search performed using SNO data, only events recorded during a well-understood set of detector conditions are studied. Therefore, the analysis concentrates on burst events observed in data used for the solar neutrino analysis during the period from November 2, 1999 to January 4, 2001. These data were selected by the SNO Data Selection Committee [139], which uses many criteria including the following:

- runs with livetime greater than 30 minutes;
- no more than 25% livetime correction resulting from data reduction cuts;
- magnetic compensation coils all on and working properly;
- limited number of channels offline;
- screened for an excessive number of events which were not properly assigned to an event;
- screened for detector maintenance or calibration activity.

In addition, Run #10236 is excluded from the supernova burst search data set due to prolonged excessive count rates in the diagnostic PMTs in the outer light water region, the outward-looking PMTs and the neck PMTs[1]. Most analyses do not use detector triggers caused by the outward-looking PMTs, so this run was deemed to be otherwise acceptable. Accounting for these factors, the subset of data used for the search analysis constitutes 241.0 days (or 56.2% of the total period), as indicated in Figure 11.1.

Since this data set was collected exclusively during "neutrino" running conditions, no run-specific thresholds were applied. Therefore, the NHIT threshold used for the burst identification algorithm was 34 PMTs for the entire period.

11.3 Search Criteria

There is uncertainty associated with the time and energy distributions of a supernova neutrino burst, so care must be taken when choosing the burst search criteria. From the discussion in Chapter 9, muon-induced spallation is expected to constitute a significant background to a burst search analysis. The characteristic durations of these spallation events is on the order of a few seconds. According to some supernova model predictions (see, for example, Section 5.3.5.2), black hole formation may occur on the same time scale. As with the supernova rate itself, the relative frequency of black hole formation compared to neutron star formation varies considerably. It has recently been suggested [140] that a large fraction of supernovae leading to black hole formation may account for the abundance of heavy elements produced through r-process nucleosynthesis[2]. Therefore, assigning constraints for the burst search based on the burst timing is ruled out.

One other possibility for removing bursts due to muon events involves identifying the

[1]Information from the detector shift report of November 29, 1999 indicates that this period of high rates lasted approximately 90 minutes and was possibly due to a light leak of some sort.

[2]The r-process is a form of stellar nucleosynthesis that is responsible for producing the majority of stable isotopes of nuclei with atomic mass $A > 60$ via rapid neutron capture.

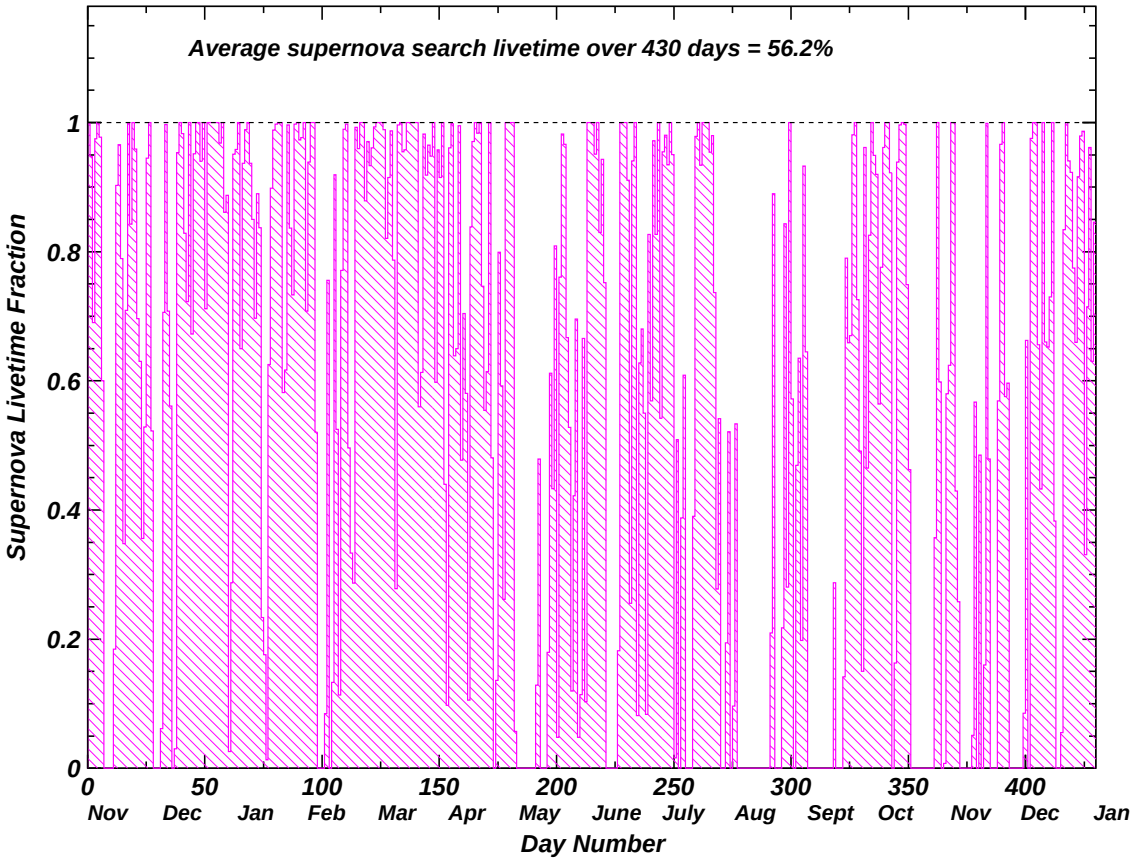

Figure 11.1: Supernova burst search livetime as a function of time for the period from November 2, 1999 to January 4, 2001.

muon. In Section 9.2.2.1, the muon tag is used to identify spallation events. However, the muon tag algorithm relies on the outward-looking PMTs to classify events involving as few as 125 PMTs as possible muons. Not only will a burst of supernova neutrinos have many events with NHIT > 125, but a large number of neutrino interactions will take place in the outer light-water volume. It is not currently possible to simulate events in the outer H_2O volume of the detector, therefore the signal obtained from the outward-looking PMTs in the event of a burst of supernova neutrinos is not well understood. As a consequence, it is necessary to use an NHIT cut to remove spallation bursts. The principal

uncertainty associated with the supernova burst NHIT distribution is the peak of the broad electron/positron energy spectrum. According to the studies performed in Section 7.4, the maximum observed NHIT value determined from simulated data corresponds to NHIT $\sim$ 500. The NHIT distribution between NHIT = 90 and NHIT = 700 is well fit by a Gaussian function of standard deviation $\sigma \approx 110$ (the NHIT spectrum from the Burrows model provides the greatest width). An NHIT cut set at 5000 PMTs is 45 standard deviations away from the predicted supernova neutrino maximum.

Considering the arguments listed above, bursts meeting the requirements of the burst identification criteria are then subjected to the following set of tests defining the search algorithm:

- 35% or more of the events in the burst pass the data reduction cuts;
- all burst events have NHIT < 5000.

11.4 Search Background

In order to characterize the background for the supernova burst search, a pre-defined search region is identified corresponding to the number of events required to form the burst trigger. For this investigation, the search is performed using the NEVENT = 30 data set.

The number of background bursts identified by the burst search algorithm can be described by an exponential distribution:

$$P(n) = N\, e^{-n/\overline{n}}, \tag{11.1}$$

where N is a normalization factor, n is the number of events used to form the trigger and $\overline{n}$ is the mean of the distribution. Figure 11.2 shows the distribution of the number of background bursts identified by the search algorithm as well as the exponential curve fit using the MINUIT function minimization and error analysis software package [141]. Using

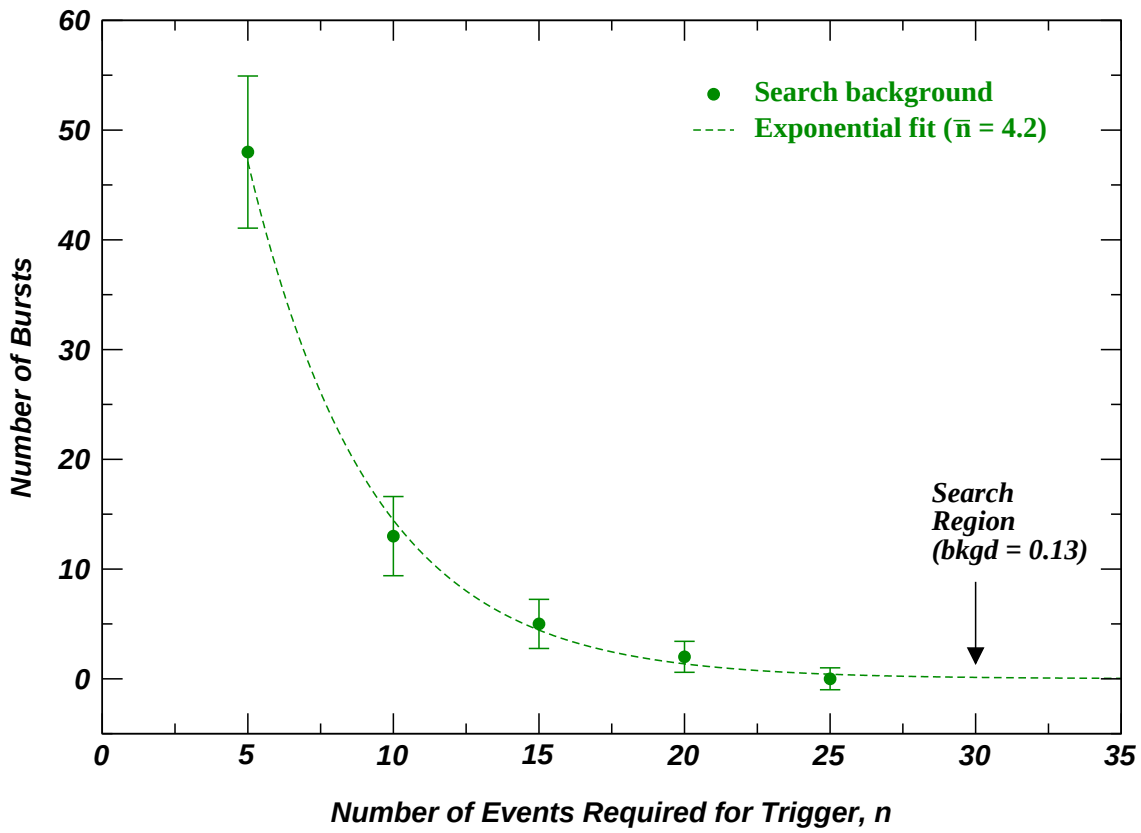

Figure 11.2: The number of background bursts identified by the burst search parameters as a function of the number of events required to form the trigger. An exponential function is fit to the background events below the search region of $n = 30$.

the fitted parameters for the background distribution below the search region of $n = 30$, the expected number of events in the search region is 0.13 bursts.

11.5 Search Results

The number of bursts at the various steps in the search algorithm are shown in Figure 11.3. Bursts due to instrumental noise are removed with the requirement that 35% or more of the events in the burst pass the data reductions cuts, and muon induced bursts are removed when the NHIT < 5000 constraint is applied. No supernova candidate bursts are observed

in the search region of $n = 30$.

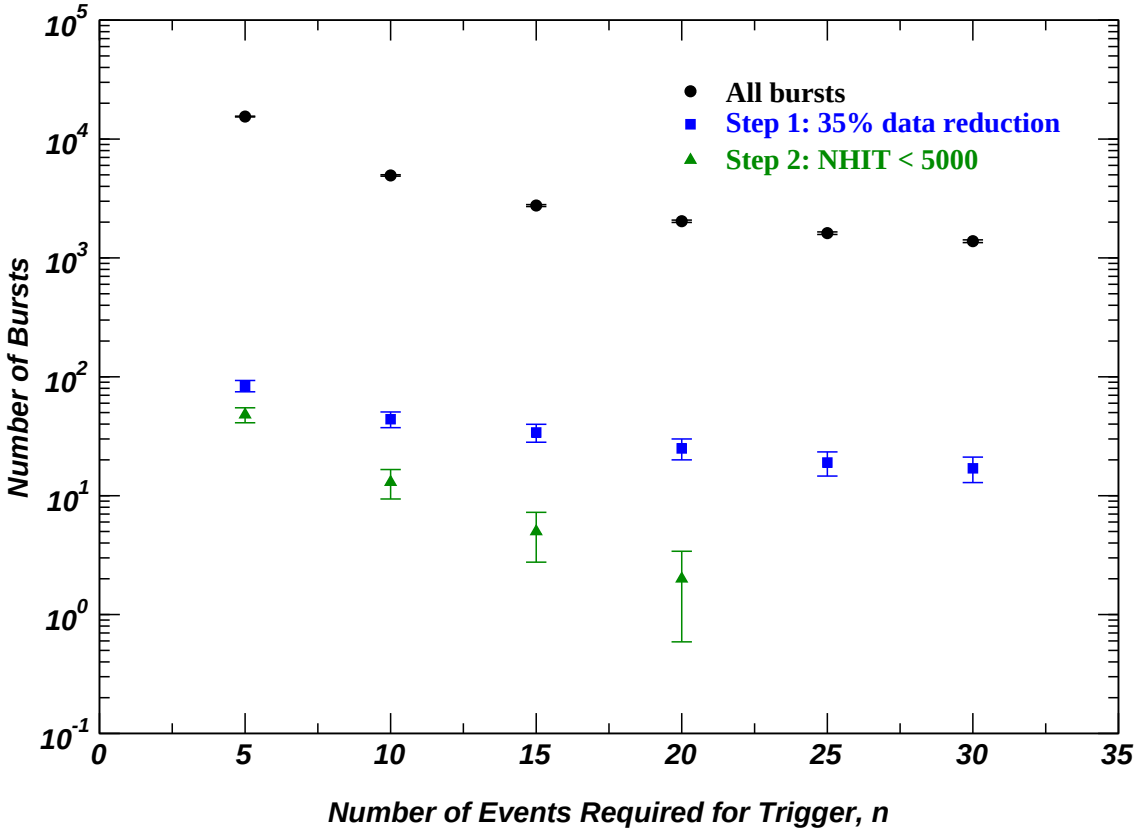

Figure 11.3: The number of bursts for various burst trigger requirements as the different search criteria are applied. The search region is $n = 30$.

The upper limit on the supernova rate, R, as a function of distance, d, and confidence interval, α, is given by

$$R(\alpha, d) = \frac{N_{Pois}(\alpha, d)}{\epsilon(d)\, t_{live}}, \tag{11.2}$$

where $\epsilon(d)$ is the burst identification efficiency as a function of distance and t_{live} is the detector livetime over the search period. According to the prescription for the statistical analysis of small signals governed by a Poisson distribution [142], the upper limit of the signal is $N_{Pois} = 2.29$ events or less with 90% confidence when zero events are observed with an expected background of 0.13 events. The corresponding upper limit on the galactic

supernova rate at the 90% confidence level according to Equation 11.2 is

$$R_{galaxy} < 3.5 \text{ per year.} \tag{11.3}$$

Previous studies that placed upper limits on the galactic supernova rate at the 90% confidence level include $R < 4.5$ per year during a 187 day search at MACRO [143], $R < 4.3$ per year during a 215 day search using the AMANDA detector array at the South Pole [144], $R < 0.71$ per year during the 3.25 year search at the IMB detector [145], $R < 0.39$ for the combined Kamiokande (4.26 years) and Super-Kamiokande (1.66 years) search [146] and $R < 0.21$ per year during the 12 year study at Baksan [147]. Tammann *et al.* also provide a 10 year combined limit of $R < 0.08$ supernovae per year using results from the Kamiokande, Baksan, Mont Blanc and IMB detectors [28].

The upper limit on the supernova rate quoted in Equation 11.3 extends beyond the far edge of the galaxy to approximately 30 kpc. However, there are very few stars in the region between 23 kpc and the Large Magellanic Cloud at 45–50 kpc. The upper limit of the supernova rate as a function of distance for various confidence levels is shown in Figure 11.4. As the burst identification efficiency decreases toward zero, the confidence level increases dramatically.

Future searches for supernova neutrinos will involve data collected over a longer period time. The upper limit of the supernova rate as a function of livetime is shown in Figure 11.5 for various confidence levels assuming no supernova observation and the current background rate.

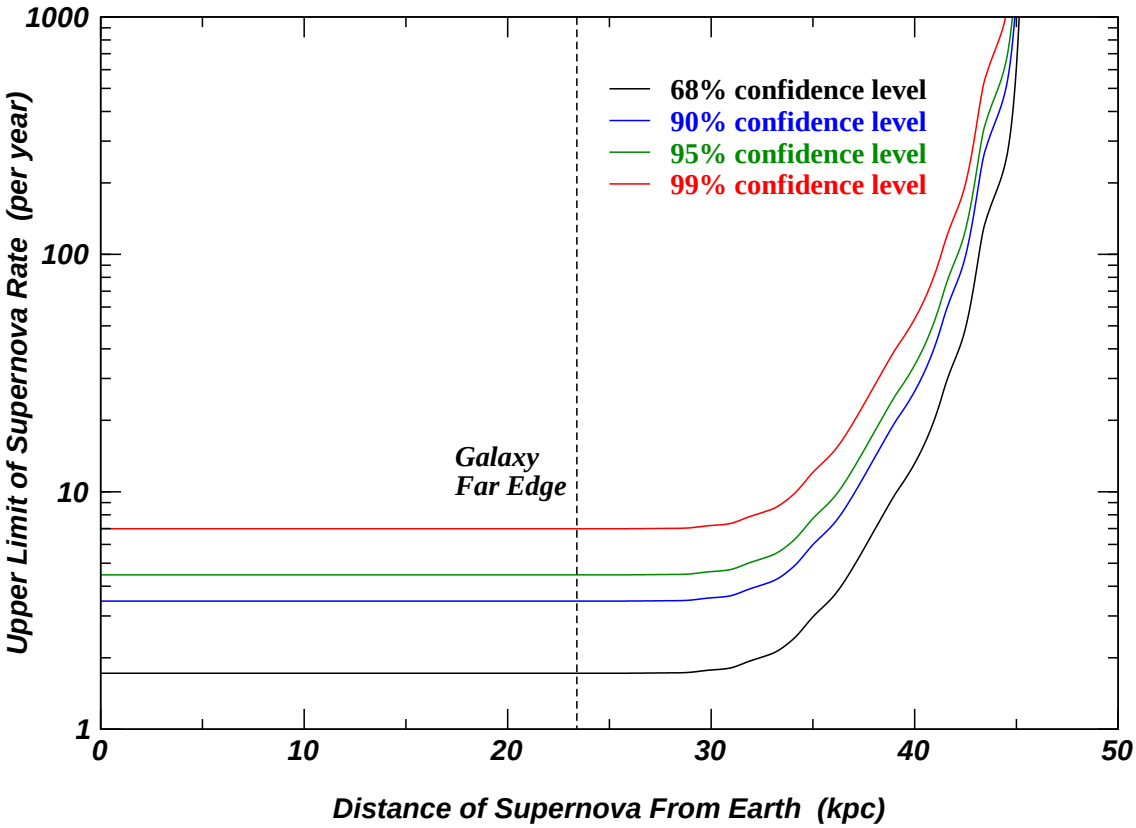

Figure 11.4: The upper limit of the supernova rate as a function of distance for various confidence levels.

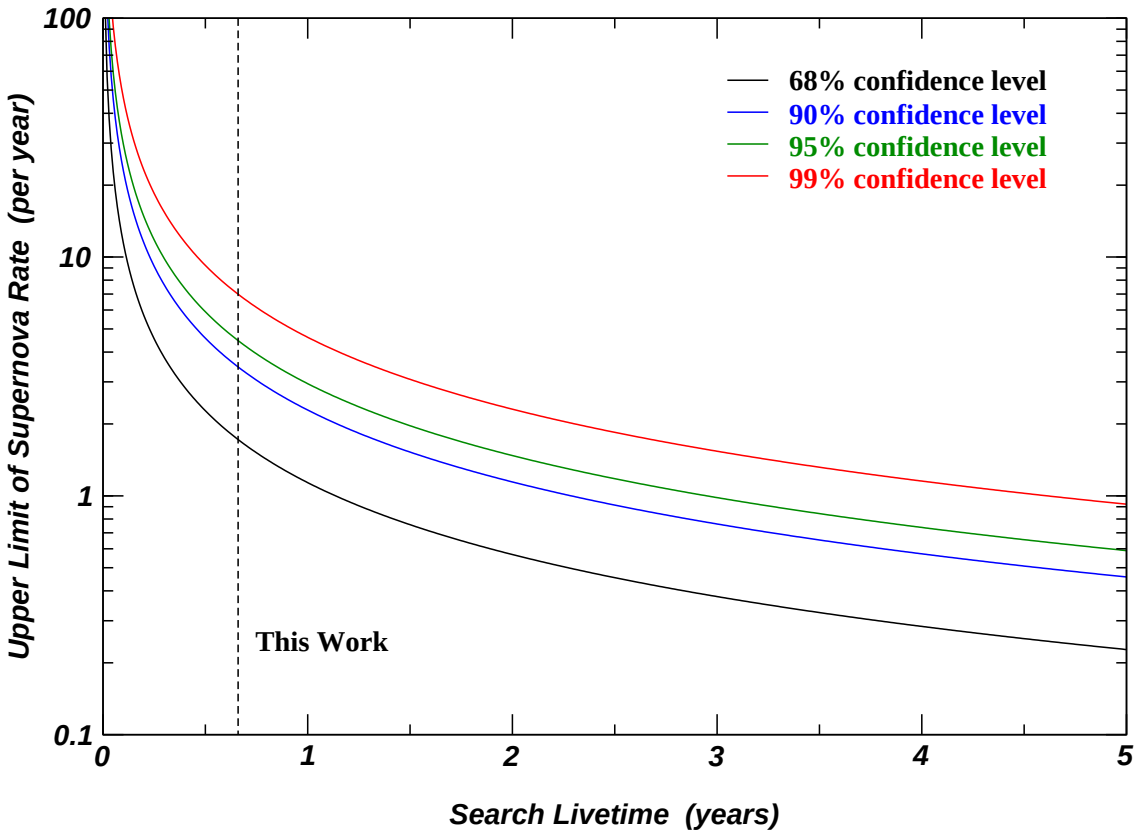

Figure 11.5: The upper limit of the supernova rate as a function of livetime for various confidence levels assuming no supernova observation.

Chapter 12

Conclusion

Neutrinos are produced in many physical processes, and are known to play a vital role in certain types of supernova explosion mechanisms, where essentially all of the gravitational energy of the collapse is carried away by neutrinos.

The SNO detector has unique capabilities that make it very useful as a supernova neutrino detector. The fiducial mass of the detector consists of 1000 tonnes of D_2O, which provides sensitivity to all neutrino flavours via reactions where a free neutron is produced from the dissociation of the deuterium nucleus. Over the lifetime of the experiment, three methods for detecting neutrons will be employed: a pure D_2O stage, a stage where salt is introduced into the heavy water and finally a stage where ^{3}He proportional counters are deployed in the D_2O region. Neutrino interactions can also be observed in the 1700 tonnes of H_2O that surrounds the heavy-water volume.

Software has been developed to simulate supernova signals in the SNO detector according to different supernova models. In this study, the simulated supernova signals from two generic models are used to characterize the detector response. For a core collapse supernova at 10 kpc, 630–910 neutrino events are expected to be observed in the SNO detector over tens of seconds during the pure D_2O operation period. Once salt is added to the heavy water, the expected signal observed from supernova neutrinos rises to 810–1230 neutrino events due to the increased neutron detection efficiency.

A study of detector performance during the pure D_2O operating mode indicates that approximately 1 event/minute or less would be present as background to a supernova

signal above an analysis threshold requiring 34 PMTs in coincidence. For a supernova at 10 kpc, the expected signal above this supernova analysis threshold is 555–795 neutrino events during the pure D_2O mode and 735–1125 neutrino events during the salt mode. It is possible to isolate various components of the supernova signal by considering events in certain regions of the detector and over certain time intervals. Electron antineutrinos are expected to comprise 92–95% of the signal in the light-water region. Furthermore, approximately 92% of the events in the first 100 ms of the supernova signal are expected to be due to electron neutrinos that are produced in the neutronization process during the early stages of stellar collapse. For a supernova at 10 kpc, simulations using the Burrows model indicate that on the order of 10 events due to ν_e interactions would be detected during that time.

A data analysis program to identify neutrinos from a galactic supernova burst has been installed in the online system at SNO. The program automatically analyzes burst data and it is anticipated that a manual alert to the Supernova Early Warning System could be issued within 20–30 minutes with essentially no possibility of a false alarm. The SNO detector was sensitive to a burst of supernova neutrinos from beyond the far edge of the Milky Way during 91.3% of the period between November 2, 1999 and January 4, 2001. In that time, the average distance sensitivity achieved with the online burst monitor was approximately 24 kpc.

A search for supernova neutrinos was performed using 241.0 days of data collected between November 2, 1999 and January 4, 2001. The distance sensitivity during that time was 36 kpc with greater than 50% detection efficiency. There was no evidence of a gravitational collapse supernovae within 30 kpc of the Earth during the live period of this search. Therefore, this result corresponds to an upper limit on the rate of Type II/Ib supernovae in our galaxy of < 3.5 per year at the 90% confidence level.

Bibliography

[1] W. Pauli "Collected scientific papers", volume 2, edited by R. Kronig and V.F. Weisskopf, Interscience Publishers, New York, 1964.

[2] F. Reines and C.L. Cowan, Jr., "Detection of the free neutrino", *Physical Review* **92**, 830–831 (1953).

[3] Y. Fukuda *et al.*, "Evidence for oscillation of atmospheric neutrinos", *Physical Review Letters* **81**, 1562–1567 (1998).

[4] Q.R. Ahmad *et al.*, "Measurement of the rate of $\nu_e + d \rightarrow p + p + e^-$ interactions produced by solar neutrinos at the Sudbury Neutrino Observatory", *Physical Review Letters* **87**, 071301 (2001).

[5] D.E. Groom *et al.*, *The European Physical Journal* **C15**, 1 (2000).

[6] M.S. Turner, "Dark energy", in the Proceedings of the XIX International Conference on Neutrino Physics and Astrophysics, *Nuclear Physics* **B91**, 405–409 (2001).

[7] T. Padmanabhan, "Structure Formation in the Universe", Cambridge University Press, Cambridge, 1995.

[8] G.J. Fishman and C.A. Meegan, "Gamma-ray bursts", *Annual Reviews of Astronomy and Astrophysics* **33**, 415–458 (1995).

[9] D. Guetta, M. Spada and E. Waxman, "On the neutrino flux from gamma-ray bursts", *Submitted to Astrophysical Journal, astro-ph/0102487* (2001).

[10] P. Meszaros and M.J. Rees, "Multi-GeV neutrinos from internal dissipation in gamma-ray burst fireballs", *Astrophysical Journal* **541**, L5–L8 (2000).

[11] Y.C. Pei and S.M. Fall, "Cosmic chemical evolution", *Astrophysical Journal* **454**, 69–76 (1995).

[12] M. Kaplinghat, G. Steigman and T.P. Walker, "Supernova relic neutrino background", *Physical Review* **D62**, 043001 (2000).

[13] T.G. Gaisser, "Cosmic Rays and Particle Physics", Cambridge University Press, Cambridge, 1990.

[14] R.S. Raghavan *et al.*, "Measuring the global radioactivity in the earth by multidetector antineutrino spectroscopy", *Physical Review Letters* **80**, 635–638 (1998).

[15] J.F. Beacom and P. Vogel, "Mass signature of supernova ν_μ and ν_τ neutrinos in the Sudbury Neutrino Observatory", *Physical Review* **D58**, 093012 (1998).

[16] E. Cappellaro and M. Turatto, "Supernova types and rates", *astro-ph:/0012455* (2000).

[17] S. Perlmutter *et al.*, "Measurements of Ω and Λ from 42 high redshift supernovae", *Astrophysical Journal* **517**, 565–586 (1999).

[18] A.V. Filippenko and A.G. Riess, "Type Ia supernovae and their cosmological implications", in *Type Ia Supernovae: Theory and Cosmology* edited by J.C. Niemeyer and J.W. Truran, Cambridge University Press, Cambridge, 2000.

[19] W.J. Kaufmann, "Universe", 3rd edition, W.H. Freeman and Company, New York, 1990.

[20] W.D. Arnett, J.N. Bahcall, R.P. Kirshner and S.E. Woosley, "Supernova 1987A", *Annual Review of Astronomy and Astrophysics* **27**, 629–700 (1989).

[21] H.A. Bethe, "Supernova mechanisms", *Reviews of Modern Physics* **62**, 801–866 (1990).

[22] A. Burrows, "Neutrinos from supernova explosions", *Annual Review of Nuclear and Particle Science* **40**, 181–212 (1990).

[23] S.E. Woosley and T.A. Weaver, "The physics of supernova explosions", *Annual Review of Astronomy and Astrophysics* **24**, 205–253 (1986).

[24] R. Bowers and T. Deeming, "Astrophysics I: Stars", Jones and Bartlett Publishers, Inc., Boston, 1984.

[25] D.A. Dicus, "Stellar energy-loss rates in a convergent theory of weak and electromagnetic interactions", *Physical Review* **D6**, 941–949 (1972).

[26] N. Itoh *et al.*, "Neutrino energy loss in stellar interiors. III. pair, photo-, plasma, and bremsstrahlung processes", *Astrophysical Journal* **339**, 354–364 (1989).

[27] J.R. Wilson in *Numerical Astrophysics*, edited by J.M. Centrella, J.M. LeBlanc and R.L. Bowers, Jones and Bartlett Publishers, Inc., Boston, 1985.

[28] G.A. Tammann, W. Löffler and A. Schröder, "The galactic supernova rate", *Astrophysical Journal Supplement Series* **92**, 487–493 (1994).

[29] S. van den Bergh and G.A. Tammann, "Galactic and extragalactic supernova rates", *Annual Reviews of Astronomy and Astrophysics* **29**, 363–407 (1991).

[30] D.H. Clark and F.R. Stephenson, "Do all galactic supernovae produce long-lived remnants?", *Monthly Notices of the Royal Astronomical Society* **179**, 87–92 (1977).

[31] R.G. Strom, "'Guest' stars, sample completeness and the local supernova rate', *Astronomy and Astrophysics* **288**, L1–L4 (1994).

[32] B.E. Schaeffer, "Peak brightness of historical supernovae and the Hubble constant", *Astrophysical Journal* **459**, 438–454 (1996).

[33] A. Burrows, "Supernova explosions in the universe", *Nature* **403**, 727–733 (2000).

[34] J.E. Reed, J.F. Hester, A.C. Fabian and P.F. Winkler, "The three-dimensional structure of the cassiopeia A supernova remnant. I. The spherical shell", *Astronomical Journal* **440**, 706–721 (1995).

[35] W.B. Ashworth, "A probably Flamsteed observation of the cassiopeia-A supernova", *Journal of Historical Astronomy* **11**, 1 (1980).

[36] D.A. Leahy and X. Wu, "The galactic distribution of shell-type supernova remnants", *Publications of the Astronomical Society of the Pacific* **101**, 607–613 (1989).

[37] D. Hartmann *et al.*, "Gamma-ray constraints on the galactic supernova rate", *Astronomy and Astrophysics Supplement Series* **97**, 219-220 (1993).

[38] C. Dupraz *et al.*, "COMPTEL three-year search for galactic sources of ^{44}Ti gamma-ray line emission at 1.157 MeV", *Astronomy and Astrophysics* **324**, 683–689 (1997).

[39] B. Aschenbach, A.F. Iyudin, V. Schönfelder, "Constraints of age, distance and progenitor of the supernova remnant RX J0852.0-4622 / GRO J0852-4642", *astro-ph/9909415* (1999).

[40] A.F. Iyudin *et al.*, "Emission from ^{44}Ti associated with a previously unknown galactic supernova", *Nature* **396**, 142–144 (1998).

[41] S. Wakatsuki *et al.*, "The nonexponential evolution of pulsar magnetic fields", *Astrophysical Journal* **392**, 628–636 (1992).

[42] R. Narayan and J.P. Ostriker, "Pulsar populations and their evolution", *Astrophysical Journal* **352**, 222–246 (1990).

[43] D.R. Lorimer *et al.*, "Pulsar statistics: the birthrate and inital spin periods of radio pulsars", *Monthly Notices of the Royal Astronomical Society* **263**, 403–415 (1993).

[44] W.D. Arnett, D.N. Schramm and J.W. Truran, "On relative supernova rates and nucleosynthesis roles", *Astrophysical Journal* **339**, L25–L27 (1989).

[45] K.U. Ratnatunga and S. van den Bergh, "The rate of stellar collapses in the galaxy", *Astrophysical Journal* **343**, 713–717 (1989).

[46] R.C. Kennicutt, "Constraints on the masses of supernova progenitors", *Astrophysical Journal* **277**, 361–366 (1984).

[47] P. Fouqué, J.M. Solanes, T. Sanchis and C. Balkowski, "Structure, mass and distance of the Virgo cluster from a Tolman-Bondi model", *astro-ph/0106261*, 2001.

[48] B.G. Marsden, "Supernova 1987A in the large magellanic cloud", *IAU circular #4316* (unpublished) February 24, 1987.

[49] J. Kristian *et al.*, "Submillisecond optical pulsar in supernova 1987A", *Nature* **338**, 234–236 (1989).

[50] J. Middleditch *et al.*, "A 2.14 ms candidate optical pulsar in SN1987A", *astro-ph/0010044 v2* (2000).

[51] K. Hirata *et al.*, "Observation of a neutrino burst from the supernova SN1987A", *Physical Review Letters* **58**, 1490–1493 (1987).

[52] K.S. Hirata *et al.*, "Observation in the Kamiokande-II detector of the neutrino burst from supernova SN1987A", *Physical Review* **D38**, 448–458 (1988).

[53] R.M. Bionta *et al.* "Observation of a neutrino burst in coincidence with supernova 1987A in the Large Magellanic Cloud", *Physical Review Letters* **58**, 1494–1496 (1987).

[54] E.N. Alekseev, L.N. Alekseeva, V.I. Volchenko and I.V. Krivosheina, "Possible detection of a neutrino signal on 23 February 1987 at the Baksan underground scintillation telescope of the Institute of Nuclear Research", *Journal of Experimental and Theoretical Physics Letters* **45**, 589–592 (1987).

[55] E.N. Alekseyev, L.N. Alexeyeva, I.V. Krivosheina and V.I. Volchenko, "Detection of the neutrino signal from SN 1987A in the LMC using the INR Baksan underground scintillation telescope", *Physics Letters* **B205**, 209–214 (1988).

[56] V.L. Dadykin *et al.*, "Detection of a rare event on 23 February 1987 by the neutrino radiation detector under Mont Blanc", *Journal of Experimental and Theoretical Physics Letters* **45** 593–595 (1987).

[57] M. Aglietta *et al.*, "On the event observed in the Mont Blanc Underground Neutrino Observatory during the occurrence of supernova 1987A", *Europhysics Letters* **3**, 1315–1320 (1987).

[58] D.N. Schramm and J.W. Truran, "New physics from supernova 1987A", *Physics Reports* **189**, 89–126 (1990).

[59] T. Totani, K. Sato, H.E. Dalhed and J.R. Wilson, "Future detection of supernova neutrino burst and explosion mechanism", *Astrophysical Journal* **496**, 216–225 (1998).

[60] A. Burrows, D. Klein, and R. Gandhi, "The future of supernova neutrino detection", *Physical Review* **D45**, 3361–3385 (1992).

[61] D.N. Spergel and J.N. Bahcall, "The mass of the electron neutrino: monte carlo studies of SN 1987A observations", *Physics Letters* **B200**, 366–372 (1988).

[62] T. Totani, "Electron neutrino mass measurement by supernova neutrino bursts and implications for hot dark matter", *Physical Review Letters* **80**, 2039–2042 (1998).

[63] J. Bonn *et al.* "The Mainz neutrino mass experiment", *Nuclear Physics Proceedings Supplement* **B91**, 273–279 (2001).

[64] V.M. Lobashev *et al.* "Direct search for neutrino mass and anomaly in the tritium beta-spectrum: status of 'Troitsk neutrino mass' experiment", *Nuclear Physics Proceedings Supplement* **B91**, 280–286 (2001).

[65] J.F. Beacom R.N. Boyd and A. Mezzacappa, "Black hole formation in core-collapse supernovae and time-of-flight measurements of the neutrino masses", *Physical Review* **D63**, 073011 (2001).

[66] S.E. Woosley, "SN 1987A: after the peak", *Astronomical Journal* **330** 218–253 (1988).

[67] T. Shigeyama, K. Nomoto, M. Hashimoto and D. Sugimoto, "Light-curve models for supernova 1987A in the Large Magellanic Cloud", *Nature* **328**, 320–323 (1987).

[68] S.E. Woosley, P.A. Pinto, P.G. Martin and T.A. Weaver, "Supernova 1987A in the Large Magellanic Cloud: the explosion of a $\sim$ 20 $M_\odot$ star which has experienced mass loss?", *Astronomical Journal* **318**, 664–673 (1987).

[69] J. Boger *et al.*, "The Sudbury Neutrino Observatory", *Nuclear Instruments and Methods* **A449**, 172–207 (2000).

[70] G. Ewan *et al.*, "Sudbury Neutrino Observatory proposal", *SNO Technical Report* **87–12**, (1987).

[71] P. Vogel and J.F. Beacom, "The angular distribution of the reaction $\overline{\nu}_e + p \to n + e^+$", *Physical Review* **D60**, 053003 (1999).

[72] T. Kuramoto, M. Fukugita, Y. Kohyama and K. Kubodera, "Neutrino-induced reaction cross sections at intermediate energies for chlorine and water detectors", *Nuclear Physics* **A512**, 711–736 (1989).

[73] K. Langanke, P. Vogel and E. Kolbe, "Signal for supernova ν_μ and ν_τ neutrinos in water Čerenkov detectors", *Physical Review Letters* **76**, 2629–2632 (1996).

[74] M. Choi *et al.*, "Scientific review of the SNO water systems", edited by A.J. Noble, *SNO Report*, April, 1996.

[75] T. Spreitzer, "Statistical analysis of detector performance as a function of compensation coil configuration in SNO", *SNO Analysis Report*, June, 2001.

[76] E.W. Beier *et al.*, "Performance of the electronics for the Sudbury Neutrino Observatory", *SNO Technical Report* **98–022**, (1998).

[77] M.R. Dragowski *et al.*, "The ^{16}N calibration source for the Sudbury Neutrino Observatory", *nucl-ex/0109011* (2001).

[78] A.W.P. Poon *et al.*, "A compact ^{3}H(p,γ)^{4}He 19.8-MeV gamma-ray source for energy calibration at the Sudbury Neutrino Observatory", *Nuclear Instruments and Methods* **A452**, 115 (2000).

[79] W.R. Nelson, H. Hirayama and D.W.O. Rogers, "The EGS4 code system", SLAC Report 265 (1985).

[80] "MCNP4A, a Monte Carlo n-particle transport code system", Radiation Shielding Center, Los Alamos National Laboratory, (unpublished) (1993).

[81] H.S. Ng, "Implementation of a supernova generator code for the Sudbury Neutrino Observatory monte carlo analysis software", B.Sc. Thesis (unpublished), University of British Columbia, 1997.

[82] H.-T. Janka and W. Hillebrandt, "Neutrino emission from type II supernovae: an analysis of the spectra", *Astronomy and Astrophysics* **224**, 49–56 (1989).

[83] S.A. Colgate and R.H. White, "The hydrodynamic behavior of supernovae explosions", *Astrophysical Journal* **143**, 626–681 (1966).

[84] I.V. Igumenshchev, R. Narayan, "Three-dimensional magnetohydrodynamic simulations of spherical accretion", *astro-ph/0105365* (2001).

[85] J.F. Beacom and P. Vogel, "Can a supernova be located by its neutrinos?", *Physical Review* **D60**, 033007 (1999).

[86] H.-T. Janka, in *Vulcano Workshop 1992: Frontier Objects in Astrophysics and Particle Physics*, edited by F. Giovannelli and G. Mannocchi (Italian Physical Society, Vulcano, 1993).

[87] S.E. Woosley *et al.*, "The r-process and neutrino-heated supernova ejecta", *Astrophysical Journal* **433**, 229–246 (1994).

[88] S.W. Bruenn, "Neutrinos from SN1987A and current models of stellar-core collapse", *Physical Review Letters* **59**, 938–941 (1987).

[89] E.S. Myra and A. Burrows, "Neutrinos from type II supernovae: the first 100 milliseconds", *Astrophysical Journal* **364**, 222–231 (1990).

[90] A. Burrows, "Supernova neutrinos", *Astrophysical Journal* **334**, 891–908 (1988).

[91] A. Burrows, *private communication* (2001).

[92] S.W. Bruenn, K.R. De Nisco and A. Mezzacappa, "General relativistic effects in the core collapse supernova mechanism", astro-ph/0101400 (2001).

[93] H.-T. Janka, "Flux-limited neutrino diffusion versus monte carlo neutrino transport", *Astronomy and Astrophysics* **256**, 452–458 (1992).

[94] M. Liebendörfer *et al.*, "Probing the gravitational well: no supernova explosion in spherical symmetry with general relativistic Boltzmann neutrino transport", *Physical Review* **D63**, 103004 (2001).

[95] C.H. Llewellyn Smith, "Neutrino reactions at accelerator energies", *Physics Reports* **3**, 261–379 (1972).

[96] L.A. Ahrens *et al.*, "Measurement of neutrino-proton and antineutrino-proton elastic scattering", *Physical Review* **D35**, 785–809 (1987).

[97] K. Kubodera and S. Nozawa, "Neutrino-nucleus reactions", *International Journal of Modern Physics* **E3**, 101–148 (1994).

[98] J.R. Klein, The `en_cc_neutron.for` and `dir_cc_neutron.for` SNOMAN routines, September, 1998.

[99] W.C. Haxton, "Nuclear response of water Cherenkov detectors to supernova and solar neutrinos", *Physical Review* **D36**, 2283–2292 (1987).

[100] J.R. Klein, The `en_nc.for` SNOMAN routine, October, 1995.

[101] J.F. Beacom and P. Vogel, "Mass signature of supernova ν_μ and ν_τ neutrinos in SuperKamiokande", *Physical Review* **D58**, 053010 (1998).

[102] J.N. Bahcall, "Neutrino Astrophysics", Cambridge University Press, Cambridge, 1989.

[103] F. Boehm and P. Vogel, "Physics of Massive Neutrinos", 2nd edition, Cambridge University Press, Cambridge, 1992.

[104] P.J. Doe, D. Earle, K.M. Heeger, N.A. Jelly and R.G.H. Robertson, "Systematics of the D_2O target in SNO", *SNO Analysis Report*, June, 2001.

[105] J.F. Beacom, *private communication* (2001).

[106] S.W. Bruenn, *private communication* (2001).

[107] M. Liebendörfer, *private communication* (2001).

[108] A. Burrows, D. Klein and R. Gandhi, "Supernova neutrino bursts, the SNO detector, and neutrino oscillations", in the Proceedings of the XV International Conference on Neutrino Physics and Astrophysics, *Nuclear Physics* **B31**, 408–412 (1993).

[109] Y.-Z. Qian and G.M. Fuller, "Signature of supernova flavor mixing in water Čerenkov detectors", *Physical Review* **D49**, 1762–1770 (1994).

[110] A.S. Dighe and A.Y. Smirnov, "Identifying the neutrino mass spectrum from a supernova neutrino burst", *Physical Review* **D62**, 033007 (2000).

[111] J.N. Bahcall and R.M. Soneira, "The universe at faint magnitudes", *Astrophysical Journal Supplement* **44**, 73–110 (1980).

[112] J.N. Bahcall and T. Piran, "Stellar collapses in the galaxy", *Astrophysical Journal* **267**, L77–L81 (1983).

[113] P. Wittich, "First measurement of the flux of solar neutrinos from the sun at the Sudbury Neutrino Observatory", Ph.D. Thesis (unpublished), University of Pennsylvania, 2000.

[114] J. Klein and V. Rusu, "Data cleaning: the qcluster cut", *SNO Analysis Report*, March, 2000.

[115] X. Chen, The `flt_fgc_cut.for` SNOMAN routine, March, 2000.

[116] J. Klein, "Data cleaning: the qvt cut", *SNO Analysis Report*, March, 2000.

[117] F. Duncan, "Dead tubes—updated", *SNO Detector Note*, May, 2001.

[118] M.S. Neubauer, "Data cleaning: the in-time channel (itc) cut", *SNO Analysis Report*, March, 2000.

[119] M.S. Neubauer, "Data cleaning: the fitterless time spread cut", *SNO Analysis Report*, November, 1999.

[120] N. McCauley, The `flt_crate_isotropy_cut.for` SNOMAN routine, April, 2000.

[121] J. Klein, "Data cleaning: an analog measurement board cut", *SNO Analysis Report*, August, 1999.

[122] N. McCauley, "Data cleaning: the neck cut", *SNO Analysis Report*, March, 2000.

[123] R. Van de Water, "Data cleaning: the q/nhit cut", *SNO Analysis Report*, April, 2000.

[124] D.L. Wark, The `flt_ring_of_fire_cut.for` SNOMAN routine, April, 2000.

[125] S.J. Brice, "The standard SNO rates", *SNO Analysis Report*, October, 1999.

[126] A.D. Marino, "Muon-induced spallation products in the SNO detector", *SNO Analysis Report*, May, 2000.

[127] K. Scholberg, "Supernova neutrino detection", in the Proceedings of the XIX International Conference on Neutrino Physics and Astrophysics, *Nuclear Physics* **B91**, 331–337 (2001).

[128] M.H. Schwendener, M.Sc. Thesis, Laurentian University (in progress).

[129] J. Heise, "SNO supernova monitoring and response procedure (v3.0)", *SNO Supernova Procedure*, July, 2001.

[130] J. Heise, "SNO supernova monitoring and response checklist (v3.0)", *SNO Supernova Procedure*, July, 2001.

[131] J. Sylvestre, "Dial-out alarm program", *SNO Technical Report* **97–028**, (1997).

[132] S.J. Brice, "The elastic fitter", *SNO Technical Report* **95–040**, (1995).

[133] P.D. Emond, "Determination of supernova stellar coordinates for the Sudbury Neutrino Observatory", B.Sc. Thesis (unpublished), Laurentian University, 2000.

[134] C. Pagnutti, "Report on xaview", *SNO Memo*, September, 2001.

[135] K. Scholberg, "SNEWS: the supernova early warning system", *in the Proceedings of the 3rd Amaldi Conference on Gravitational Waves*, Caltech, July 1999 (astro-ph/9911359).

[136] M. Aglietta *et al.*, "The most powerful scintillator supernovae detector: LVD", *Nuovo Cimento* **A105**, 1793–1804 (1992).

[137] Y. Fukuda *et al.*, "Measurements of the solar neutrino flux from Super-Kamiokande's first 300 days", *Physical Review Letters* **81**, 1158–1162 (1998).

[138] S. Ahlen *et al.*, "First supermodule of the MACRO detector at Gran Sasso", *Nuclear Instruments and Methods* **A324**, 337–362 (1993).

[139] N. McCauley for the SNO Data Selection Committee, "Final run list for the paper", *SNO Analysis Report*, April, 2001.

[140] Y.Z. Qian, P. Vogel and G.J. Wasserburg, "Diverse supernova sources for the r-process", *Astrophysical Journal* **494**, 285–296 (1998).

[141] F. James, "MINUIT—Function minimization and error analysis", *CERN Program Library* **D506**, 1998.

[142] G.J. Feldman and R.D. Cousins, "Unified approach to the classical statistical analysis of small signals", *Physical Review* **D57**, 3873–3889 (1998).

[143] K. Scholberg, "A search for neutrino from gravitational collapse with the MACRO experiment", Ph.D. Thesis (unpublished), California Institute of Technology, 1997.

[144] J. Ahrens *et al.*, "Search for supernova neutrino-bursts with the AMANDA detector", astro-ph/0105460, 2001.

[145] R.S. Miller *et al.*, "A search for astrophysical sources of low-energy neutrinos using the IMB detector", *Astrophysical Journal* **428**, 629–632 (1994).

[146] Y. Fukuda for the Super-Kamiokande Collaboration, "Observation of supernova neutrinos at Super-Kamiokande", bound photocopied transparencies of the *First International Workshop of the Supernova Early Alert Network* (unpublished), Boston University, 1998.

[147] E.N. Alekseev *et al.*, "Upper bound on the collapse rate of massive stars in the Milky Way given by neutrino observations with the Baksan underground telescope", *Journal of Experimental and Theoretical Physics* **77**, 339–347 (1993).

Appendix A

The Sudbury Neutrino Observatory Collaboration

Below is a complete list of the 227 SNO collaborators that have worked on the project as of June 2001. Since 1983, 16 institutions from 3 countries have been involved with the design and development of the Sudbury Neutrino Observatory.

Brookhaven National Laboratory, *Upton, NY, USA*

J. Boger, R.L. Hahn, J.K. Rowley, M. Yeh

Carleton University, *Ottawa, Ontario, Canada*

A.L. Carter, B. Hollebone, D. Kessler, N. Starinsky

Centre for Research in Particle Physics, *Ottawa, Ontario, Canada*

I. Blevis, F. Dalnoki-Veress, A. DeKok, J. Farine, D.R. Grant, C.K. Hargrove, G. Laberge, I. Levine, K. McFarlane, H. Mes, C. Mifflin, A.T. Noble, V.M. Novikov, M. O'Neill, M. Shatkay, C. Shewchuk, D. Sinclair

Chalk River Laboratories, *Chalk River, Ontario, Canada*

E.T.H. Clifford, R. Deal, E.D. Earle, E. Gaudette, G. Milton, B. Sur

Laurentian University, *Sudbury, Ontario, Canada*

J. Bigu, M. Braille, J.H.M. Cowan, D.L. Cluff, R.U. Haq, J. Hewett, J.G. Hykawy, G. Jonkmans, S. Luoma, R. Michaud, A. Roberge, J. Roberts, E. Saettler, M.H. Schwendener, H. Seifert, G. Shayer, D. Sweezey, R. Tafirout, C.J. Virtue

Lawrence Berkeley National Laboratory, *Berkeley, CA, USA*

D.N. Beck, Y.D. Chan, X. Chen, M.R. Dragowsky, F.W. Dycus, J. Gonzalez, M.C.P. Isaac, Y. Kajiyama, G.W. Koehler, K.T. Lesko, A.D. Marino, M.C. Moebus, E.B. Norman, C.E. Okada, A.W.P. Poon, P. Purgalis, A. Schuelke, A.R. Smith, R.G. Stokstad, S. Turner, I. Zlimen

Los Alamos National Laboratory, *Los Alamos, USA*

J.M. Anaya, T.J. Bowles, S.J. Brice, E-I. Esch, M.M. Fowler, A. Goldschmidt, A. Hime, K. Kirch, A.F. McGirt, G.G. Miller, W.A. Teasdale, J.B. Wilhelmy, J.M. Wouters

National Research Council of Canada, *Ottawa, Ontario, Canada*

J.D. Anglin, M. Bercovitch, W.F. Davidson, R.S. Storey

Oxford University, *Oxford, UK*

J.C. Barton, S. Biller, R.A. Black, R.J. Boardman, M.G. Bowler, J. Cameron, B. Cleveland, X. Dai, J. Dunmore, G. Doucas, H. Fergani, A.P. Ferraris, K. Frame, H. Heron, C. Howard, N.A. Jelley, A.B. Knox, M. Lay, W. Locke, J. Lyon, S. Majerus, N. McCauley, G. McGregor, M. Moorhead, M. Omori, N.W. Tanner, R.K. Taplin, M. Thorman, P.T. Trent, D.L. Wark, N. West, J. Wilson

Princeton University, *Princeton, NJ, USA*

R. Kouzes, M.M. Lowry

Queen's University, *Kingston, Ontario, Canada*

A.L. Bell, E. Bonvin, M. Boulay, M. Chen, Y. Dai, M. Dayon, F. Duncan, L.S. Erhardt, H.C. Evans, G.T. Ewan, R. Ford, A. Hallin, A. Hamer, P.M. Hart, P.J. Harvey, D. Haslip, C.A.W. Hearns, R. Heaton, J.D. Hepburn, C.J. Jillings, E.P. Korpach, H.W. Lee, J.R. Leslie, M.-Q. Liu, H.B. Mak, A.B. McDonald, J.D. MacArthur, W. McLatchie, B.A. Moffat, S. Noel, T.J. Radcliffe, B.C. Robertson, P. Skensved, R.L. Stevenson, X. Zhu

University of British Columbia, *Vancouver, BC, Canada*

S. Gil, J. Heise, R.L. Helmer, R.J. Komar, T. Kutter, C.W. Nally, H.S. Ng,
Y.I. Tserkovnyak, C.E. Waltham

University of California at Irvine, *Irvine, CA, USA*

R.C. Allen, G. Bühler, H.H. Chen

University of Guelph, *Guelph, Ontario, Canada*

G. Aardsma, T. Andersen, K. Cameron, M.C. Chon, R.H. Hanson, P. Jagam, J. Karn,
J. Law, I.T. Lawson, R.W. Ollerhead, J.J. Simpson, N. Tagg, J.-X. Wang

University of Pennsylvania, *Philadelphia, PA, USA*

C. Alexander, E.W. Beier, J.C. Cook, D.F. Cowen, E.D. Frank, W. Frati,
W.J. Heintzelman, P.T. Keener, J.R. Klein, C.C.M. Kyba, G. Mayers, D.S. McDonald,
M.S. Neubauer, F.M. Newcomer, S.M. Oser, R.J. Pearce, V.L. Rusu, R.G. Van de Water,
R. Van Berg, P. Wittich

University of Washington, *Seattle, WA, USA*

Q.R. Ahmad, J.M. Beck, M.C. Browne, T.V. Bullard, T.H. Burritt, G.A. Cox, P.J. Doe,
C.A. Duba, S.R. Elliott, J.E. Franklin, J.V. Germani, P. Green, A.A. Hamian,
R. Hazama, K.M. Heeger, M. Howe, R. Meijer Drees, A. Myers, J.L. Orrell,
R.G.H. Robertson, K.K. Schaffer, M.W.E. Smith, T.D. Steiger, T. Van Wechel,
J.F. Wilkerson

Appendix B

Using the Supernova Signal Formalism

For illustration purposes, the full calculation for the number of ν_e neutrinos expected to interact via the elastic scattering reaction in the D_2O volume of the detector:

$$\nu_e + e^- \rightarrow \nu_e + e^- \qquad (E_{thres} = 0 \text{ MeV}) \quad [D_2O] \tag{B.1}$$

at neutrino emission time $t_i = 0$ s and neutrino energy $E_\nu = 6$ MeV will be shown for the supernova model of Burrows *et al.* [60] at a distance $D = 10$ kpc.

As outlined in Chapter 5, the supernova neutrino signal at the source is described by Equation 5.1:

$$\frac{d^2 N_{src}}{dE_\nu dt_i} = F(t_i) f(E_\nu, t_i). \tag{B.2}$$

The number of neutrinos leaving the supernova source at $t_i = 0$ is obtained by using the neutrino luminosity and average energy spectra according to Equation 5.2:

$$\begin{aligned} F(0) &= \frac{L(0)}{\epsilon_\nu(0)} \qquad (B.3) \\ &= \frac{4.545 \times 10^{53} \frac{\text{ergs}}{\text{s}} \times \frac{10^{-7} \text{ J}}{\text{erg}} \times \frac{1 \text{ eV}}{1.602 \times 10^{-19} \text{ J}} \times \frac{1 \text{ MeV}}{10^6 \text{ eV}}}{15.123 \text{ MeV}} \\ &= 1.876 \times 10^{58} \text{ s}^{-1}. \end{aligned}$$

According to the Burrows model, the characteristic Fermi-Dirac parameters for ν_e neutrinos at $t_i = 0$ are $T_{\nu_e}(0) = 1.7$ MeV and $\eta_{\nu_e}(0) = 11.0$, indicating that the high-energy tail of this spectrum is very "pinched" relative to a Maxwell-Boltzmann distribution. Using

Equation 5.10 for a Fermi-Dirac distribution that includes a chemical potential factor, the spectrum at $t_i = 0$ is calculated to be:

$$\begin{aligned} f(6,0) &= \frac{1}{N_{FD}(0)} \left[\frac{E_\nu^2}{1 + e^{E_\nu/T_\nu(0) - \eta_\nu(0)}} \right] \\ &= \frac{1}{2357.529 \text{ MeV}^3} \left[\frac{(6.0 \text{ MeV})^2}{1 + e^{(6.0 \text{ MeV}/1.7 \text{ MeV} - 11.0)}} \right] \\ &= 0.0153 \text{ MeV}^{-1}, \end{aligned}$$

where the normalization, $N_{FD}(0)$, is determined using Equation 5.8:

$$\begin{aligned} N_{FD}(0) &= \int_0^\infty \left[\frac{E_\nu^2}{1 + e^{E_\nu/T_\nu(0) - \eta_\nu(0)}} \right] dE_\nu \\ &= \int_0^\infty \left[\frac{E_\nu^2}{1 + e^{(E_\nu/1.7 \text{ MeV} - 11.0)}} \right] dE_\nu \\ &= 2357.529 \text{ MeV}^3. \end{aligned}$$

Hence, the number of neutrinos leaving the collapsing star per unit energy per unit time is:

$$\begin{aligned} \left. \frac{d^2 N_{src}}{dE_\nu dt_i} \right|_{E_\nu = 6 \text{ MeV},\, t_i = 0 \text{ s}} &= F(0) f(6,0) \\ &= (1.876 \times 10^{58} \text{ s}^{-1})(0.0153 \text{ MeV}^{-1}) \\ &= 2.863 \times 10^{56} \text{ (MeV s)}^{-1}. \end{aligned}$$

The neutrino flux at the detector is described by Equation 5.11:

$$\frac{d^2 N_{det}}{dE_\nu dt} = N_t \, \sigma(E_\nu) \frac{1}{4\pi D^2} \frac{d^2 N_{src}}{dE_\nu dt_i} \tag{B.4}$$

For the example being considered, the number of neutrino counts in the D_2O volume per unit energy per unit time is:

$$\begin{aligned} \left. \frac{d^2 N_{det}}{dE_\nu dt} \right|_{E_\nu = 6 \text{ MeV},\, t_i = 0 \text{ s}} &= N_{e,\mathrm{D_2O}} \frac{\sigma(6)}{4\pi D^2} \left[\frac{d^2 N_{src}}{dE_\nu dt_i} \right]_{E_\nu = 6 \text{ MeV},\, t_i = 0 \text{ s}} \\ &= (30.173 \times 10^{31} \text{ e}^- \text{ in the } D_2O \text{ volume}) \\ &\quad \frac{5.418 \times 10^{-48} \text{ m}^2}{4\pi (10 \text{ kpc})^2} \left(\frac{1 \text{ kpc}}{3.086 \times 10^{19} \text{ m}} \right)^2 2.863 \times 10^{56} \text{ (MeV s)}^{-1} \\ &= 0.391 \text{ (MeV s)}^{-1}. \end{aligned} \tag{B.5}$$

Performing the integration over all energies yields the count rate for the time specified in this example:

$$\left.\frac{dN_{det}}{dt}\right|_{t_i = 0\,\mathrm{s}} = N_{e,\mathrm{D_2O}}\,\frac{1}{4\pi D^2}\int_0^\infty dE_\nu\,\sigma(E_\nu)\left[\frac{d^2N_{src}}{dE_\nu dt_i}\right]_{t_i = 0\,\mathrm{s}}$$
$$= 66.669\ \mathrm{s}^{-1}. \tag{B.6}$$

Finally, the total number of ν_e neutrinos that interact via the elastic scattering reaction in the D_2O volume is determined using Equation 5.12:

$$N_{det} = N_{e,\mathrm{D_2O}}\,\frac{1}{4\pi D^2}\int_0^\infty\int_0^\infty \sigma(E_\nu)\frac{d^2N_{src}}{dE_\nu dt_i}\,dE_\nu\,dt_i$$
$$= 8.523\ \text{counts}. \tag{B.7}$$

Appendix C

Estimate of the Observed Signal Due to Oxygen Reactions

While reactions involving oxygen are not fully specified in the supernova neutrino simulations performed, a reasonable estimate can be made. As outlined in Section 4.3, the signal due to interactions with the target oxygen molecules has contributions from both the charged-current channel:

$$\nu_e + \mathrm{O} \rightarrow \mathrm{F} + e^- \quad [\mathrm{D_2O}, \mathrm{H_2O}] \tag{C.1}$$

$$\overline{\nu}_e + \mathrm{O} \rightarrow \mathrm{N} + e^+ \quad [\mathrm{D_2O}, \mathrm{H_2O}] \tag{C.2}$$

and the neutral-current channel:

$$\nu_{\mu,\tau} + {}^{16}\mathrm{O} \rightarrow \nu_{\mu,\tau} + {}^{15}\mathrm{O} + n + \gamma \quad [\mathrm{D_2O}, \mathrm{H_2O}] \tag{C.3}$$

$$\overline{\nu}_{\mu,\tau} + {}^{16}\mathrm{O} \rightarrow \overline{\nu}_{\mu,\tau} + {}^{15}\mathrm{O} + n + \gamma \quad [\mathrm{D_2O}, \mathrm{H_2O}] \tag{C.4}$$

$$\nu_{\mu,\tau} + {}^{16}\mathrm{O} \rightarrow \nu_{\mu,\tau} + {}^{15}\mathrm{N} + p + \gamma \quad [\mathrm{D_2O}, \mathrm{H_2O}] \tag{C.5}$$

$$\overline{\nu}_{\mu,\tau} + {}^{16}\mathrm{O} \rightarrow \overline{\nu}_{\mu,\tau} + {}^{15}\mathrm{N} + p + \gamma \quad [\mathrm{D_2O}, \mathrm{H_2O}] \tag{C.6}$$

$$\nu_{\mu,\tau} + {}^{16}\mathrm{O} \rightarrow \nu_{\mu,\tau} + {}^{15}\mathrm{O} + n \quad [\mathrm{D_2O}] \tag{C.7}$$

$$\overline{\nu}_{\mu,\tau} + {}^{16}\mathrm{O} \rightarrow \overline{\nu}_{\mu,\tau} + {}^{15}\mathrm{O} + n \quad [\mathrm{D_2O}]. \tag{C.8}$$

The final state detectable particles from these reactions include electrons, positrons, gamma rays and neutrons. Neutrons in the $\mathrm{H_2O}$ region are not considered to be detectable because the energy of the γ ray produced in the neutron capture process is below practical detection thresholds.

C.1 Hardware Threshold

Since the energies are relatively high, the probability of detecting electrons and positrons from supernova neutrino charged-current interactions is very high. Monte Carlo simulations of supernova neutrinos show that typically ~97% of the electron and positron events are detected above the detector hardware threshold of 16 PMTs. Due to high energy threshold for the ^{16}O charged-current reactions, the average electron/positron energy is higher than other charged-current reactions[1]. Therefore the detection efficiency for electrons and positrons from oxygen charged-current reactions is expected to be slightly higher than 97%. However, for the purposes of estimation, the value of 97% is used.

Energies for the γ rays from the neutral-current excitation reactions are predicted to be in the range 5–10 MeV [73]. Monte Carlo simulations show that the detection efficiency for 5 MeV gamma rays is approximately 97% in the D_2O region and 80% in the H_2O region. For 10 MeV gamma rays, the efficiency is slightly higher at 98% in the D_2O region and 91% in the H_2O region. Average detection efficiency values of 97% (D_2O) and 85% (H_2O) are adopted to estimate the observed γ-ray signal due to interactions with oxygen.

As presented in Section 4.2.3, three distinct methods are proposed to detect neutrons in the SNO detector, and each technique has a different detection efficiency. The efficiency values obtained from Monte Carlo study are: $\epsilon = 37\%$ for pure D_2O, $\epsilon = 85\%$ using NaCl salt and $\epsilon = 55\%$ with the neutral current detectors in place.

The detection efficiencies discussed above are summarized in Table C.1. These values are used to estimate the contribution from reactions involving oxygen to the SNO supernova signal above the hardware detector threshold of 16 PMTs. The expected signal in the Beacom and Vogel model and in the Burrows model are discussed in the sections below.

[1] For average neutrino energy values according to the Beacom and Vogel model and the Burrows model, see Tables 6.2 and 6.6, respectively.

Particle	**Region**	**Detection Efficiency (hardware)**
$e^{\pm}$	D_2O	0.97
$e^{\pm}$	H_2O	0.97
γ	D_2O	0.97
(5 MeV)		*0.97*
(10 MeV)		*0.98*
γ	H_2O	0.85
(5 MeV)		*0.80*
(10 MeV)		*0.91*
n (D_2O)	D_2O	0.37
n (Salt)	D_2O	0.85
n (NCDs)	D_2O	0.55

Table C.1: SNO particle detection efficiencies above the detector hardware threshold of 16 PMTs for various final state particles. The three entries listed for γ rays indicate the average efficiency value used in the estimate as well as the efficiency values for the two energies investigated.

C.1.1 Beacom and Vogel Model

Neutrino count values presented in Table 6.1 for the Beacom and Vogel model indicate that 92 neutrino events from reactions with oxygen would yield a total of 13 electron and positron events, 59 γ-ray events and 24 neutron events in the final state. The results obtained by applying the detection efficiencies in Table C.1 indicate that 74 particles would be observed above the detector hardware energy threshold in the pure D_2O phase, 85 particles in the salt phase and 78 particles during the time that the neutral current detectors are in place. This corresponds to 13 electron/positron events, 52 gamma-ray events and between 9 and 20 neutron events, depending on the neutron detection method employed.

Regardless of the neutron detection method, a total of 8 electron/positron events and 33 γ-ray events are expected in the H_2O region in addition to the 410 positrons produced

via the inverse beta decay reaction and the 20 electrons produced through elastic scattering. Including the estimated contribution due to oxygen reactions, electron antineutrinos constitute 88% of the H_2O signal above the detector hardware threshold according to the Beacom and Vogel model.

C.1.2 Burrows *et al.* Model

According to Table 6.5, 13 neutrino events are expected from oxygen reactions using the Burrows model, which corresponds to 7 electron and positron events, 5 γ-ray events and 2 neutron events in the final state. Applying the particle detection efficiencies listed in Table C.1 results in the following total numbers of observed final state particles according to the Burrows model: 12 events during pure D_2O, 13 events during the salt phase and 12 events with the neutral current detectors. In other words, 7 electron/positron events, 4 gamma-ray events and 1–2 neutron events are expected.

Considering the supernova signal in the light-water region alone, a total of 4 electron/positron events and 3 γ-ray events are expected in addition to the 320 positrons produced via the $\overline{\nu}_e + p \rightarrow n + e^+$ reaction and the 20 electrons produced through the $\nu + e^- \rightarrow \nu + e^-$ reaction. Including the estimated contribution due to oxygen reactions, electron antineutrinos constitute 93% of the H_2O signal above the detector hardware threshold of 16 PMTs according to the Burrows model.

C.2 Analysis Threshold

In Chapter 8, the energy threshold appropriate for the analysis of a supernova burst during the pure D_2O and salt phases is determined to be 34 PMTs. The effect of applying this threshold to the signal resulting from interactions with oxygen is discussed below.

The probability of detecting electrons and positrons above the supernova analysis

threshold due to charged-current interactions remains relatively high. Monte Carlo simulations of reactions that do not involve oxygen show that approximately 90% of the electron and positron events are detected above the analysis threshold. As with the signal above the hardware threshold, the high energy threshold value for ^{16}O reactions means that the signal due to oxygen reactions remains relatively insensitive to an NHIT threshold even as high as 34 PMTs. In order to place a conservative lower limit on the number of counts expected from oxygen reactions an efficiency value of 90% is used.

Energies for the γ rays from the neutral-current excitation reactions are predicted to be in the range 5–10 MeV. In order to characterize the gamma-ray detection efficiency in the energy range 5–10 MeV, Monte Carlo simulations are performed in both the heavy- and light-water regions. The results indicate that the detection efficiency for 5 MeV gamma rays is approximately 48% in the D_2O region and only 24% in the H_2O region. The detection efficiency for 10 MeV gamma rays is considerably higher in both regions at 98% in the D_2O volume and 79% in the H_2O volume. In the absence of information regarding the exact distribution of γ-ray energies, average detection efficiency values are used to estimate the signal contribution from oxygen reactions. For the D_2O region, the average efficiency value is 73% and for the H_2O region the average efficiency value is 52%.

The neutron detection efficiency values obtained from Monte Carlo study for events above the analysis threshold are: $\epsilon = 27\%$ for pure D_2O and $\epsilon = 77\%$ using NaCl salt. The corresponding detection efficiency using the NCDs is not known at this time.

The detection efficiencies discussed above are summarized in Table C.2. These values are used to estimate the contribution from reactions involving oxygen to the SNO supernova signal above the supernova analysis threshold of 34 PMTs.

Particle	**Region**	**Detection Efficiency (analysis)**
$e^{\pm}$	D_2O	0.90
$e^{\pm}$	H_2O	0.90
γ	D_2O	0.73
(5 MeV)		*0.48*
(10 MeV)		*0.98*
γ	H_2O	0.52
(5 MeV)		*0.24*
(10 MeV)		*0.79*
n (D_2O)	D_2O	0.27
n (Salt)	D_2O	0.77

Table C.2: SNO detection efficiencies above the supernova analysis threshold of 34 PMTs for various final state particles. The three entries listed for γ rays indicate the average efficiency value used in the estimate as well as the efficiency values for the two energies investigated.

C.2.1 Beacom and Vogel Model

The results obtained by applying the detection efficiencies in Table C.2 indicate that 53 particles would be observed above the supernova analysis threshold in the pure D_2O phase and 65 in the salt phase. This corresponds to 12 electron/positron events, 35 gamma-ray events and between 6 and 18 neutron events, depending on whether neutron capture occurs in pure D_2O or in salt.

Regardless of the neutron detection method, a total of 8 electron/positron events and 20 γ-ray events are expected in the H_2O region in addition to the 392 positrons produced via the $\overline{\nu}_e + p \rightarrow n + e^+$ reaction and the 15 electrons produced through the $\nu + e^- \rightarrow \nu + e^-$ reaction. Including the estimated contribution due to oxygen reactions, electron antineutrinos constitute 92% of the H_2O signal above the supernova analysis threshold according to the Beacom and Vogel model.

C.2.2 Burrows *et al.* Model

The results obtained by applying the detection efficiencies in Table C.2 indicate that 10 particles would be observed above the supernova analysis threshold of 34 PMTs in the pure D_2O phase and 11 in the salt phase. This corresponds to 6 electron/positron events, 3 gamma-ray events and 1 neutron event (the number of neutrino events is sufficiently low that the neutron method does not make a significant difference).

Considering the H_2O region, a total of 4 electron/positron events and 2 γ-ray events are expected, in addition to the 296 positrons produced via the inverse beta decay reaction and the 13 electrons produced through elastic scattering reactions. Including the estimated contribution due to oxygen reactions, electron antineutrinos constitute 95% of the H_2O signal above the supernova analysis threshold according to the Burrows model.

C.3 Summary

Estimated contributions above both the hardware and analysis thresholds from the various reactions involving oxygen are summarized below for the two generic supernova models.

C.3.1 Beacom and Vogel Model

Between 75 and 85 events due to supernova neutrino reactions with oxygen are expected above the hardware threshold of 16 PMTs using the Beacom and Vogel model. Once the analysis threshold requiring 34 PMTs in coincidence is applied, the range of total events due to oxygen reactions becomes 53–65. Table C.3 provides a summary of the estimated contributions from the various oxygen reactions above both the hardware and analysis thresholds for the Beacom and Vogel model.

Oxygen Reaction	**Region**	**Counts (hardware)**			**Counts (analysis)**	
		D_2O	**Salt**	**NCDs**	**D_2O**	**Salt**
Charged Current:	*total*	*12.77*	*12.77*	*12.77*	*11.86*	*11.86*
$\nu_e + O \rightarrow F + e^-$	D_2O	0.98	0.98	0.98	0.91	0.91
$\overline{\nu}_e + O \rightarrow N + e^+$	D_2O	3.44	3.44	3.44	3.20	3.20
$\nu_e + O \rightarrow F + e^-$	H_2O	1.84	1.84	1.84	1.71	1.71
$\overline{\nu}_e + O \rightarrow N + e^+$	H_2O	6.51	6.51	6.51	6.04	6.04
Neutral Current:	*total*	*61.19*	*72.63*	*65.49*	*41.23*	*53.14*
$\nu_{\mu,\tau} + {}^{16}O \rightarrow \nu_{\mu,\tau} + {}^{15}O + n + \gamma$	D_2O	2.82	3.83	3.20	2.10	3.15
$\overline{\nu}_{\mu,\tau} + {}^{16}O \rightarrow \overline{\nu}_{\mu,\tau} + {}^{15}O + n + \gamma$	D_2O	2.80	3.81	3.18	2.09	3.14
$\nu_{\mu,\tau} + {}^{16}O \rightarrow \nu_{\mu,\tau} + {}^{15}N + p + \gamma$	D_2O	7.75	7.75	7.75	5.83	5.83
$\overline{\nu}_{\mu,\tau} + {}^{16}O \rightarrow \overline{\nu}_{\mu,\tau} + {}^{15}N + p + \gamma$	D_2O	7.90	7.90	7.90	5.94	5.94
$\nu_{\mu,\tau} + {}^{16}O \rightarrow \nu_{\mu,\tau} + {}^{15}O + n$	D_2O	3.69	8.48	5.49	2.69	7.68
$\overline{\nu}_{\mu,\tau} + {}^{16}O \rightarrow \overline{\nu}_{\mu,\tau} + {}^{15}O + n$	D_2O	3.56	8.19	5.30	2.60	7.42
$\nu_{\mu,\tau} + {}^{16}O \rightarrow \nu_{\mu,\tau} + {}^{15}O + n + \gamma$	H_2O	3.37	3.37	3.37	2.06	2.06
$\overline{\nu}_{\mu,\tau} + {}^{16}O \rightarrow \overline{\nu}_{\mu,\tau} + {}^{15}O + n + \gamma$	H_2O	3.36	3.36	3.36	2.05	2.05
$\nu_{\mu,\tau} + {}^{16}O \rightarrow \nu_{\mu,\tau} + {}^{15}N + p + \gamma$	H_2O	12.85	12.85	12.85	7.86	7.86
$\overline{\nu}_{\mu,\tau} + {}^{16}O \rightarrow \overline{\nu}_{\mu,\tau} + {}^{15}N + p + \gamma$	H_2O	13.09	13.09	13.09	8.01	8.01
Total SNO ν_e Events		2.82	2.82	2.82	2.62	2.62
Total SNO $\overline{\nu}_e$ Events		9.95	9.95	9.95	9.24	9.24
Total SNO "ν_μ" Events		61.19	72.63	65.49	41.23	53.14
Total SNO D_2O Events		32.94	44.38	37.24	25.36	37.27
Total SNO H_2O Events		41.02	41.02	41.02	27.73	27.73
Total SNO $e^\pm$ Events		12.77	12.77	12.77	11.86	11.86
Total SNO γ Events		52.39	52.39	52.39	34.81	34.81
Total SNO n Events		8.80	20.24	13.10	6.42	18.33
Total SNO Events		**73.96**	**85.40**	**78.26**	**53.09**	**65.00**

Table C.3: Summary of estimated contributions above both the hardware and analysis thresholds from reactions involving oxygen to the supernova signal using the Beacom and Vogel model.

C.3.2 Burrows *et al.* Model

Between 12 and 13 events due to supernova neutrino reactions with oxygen are expected above the hardware threshold of 16 PMTs using the Burrows model. Once the analysis threshold of 34 PMTs is applied, the range of total events due to oxygen reactions becomes

10–11. Table C.4 provides a summary of the estimated contributions from the various oxygen reactions above both the hardware and analysis thresholds for the Burrows model.

Oxygen Reaction	**Region**	**Counts (hardware)**			**Counts (analysis)**	
		D_2O	**Salt**	**NCDs**	**D_2O**	**Salt**
Charged Current:	*total*	*6.86*	*6.86*	*6.86*	*6.36*	*6.36*
$\nu_e + \mathrm{O} \rightarrow \mathrm{F} + e^-$	D_2O	1.05	1.05	1.05	0.97	0.97
$\overline{\nu}_e + \mathrm{O} \rightarrow \mathrm{N} + e^+$	D_2O	1.32	1.32	1.32	1.22	1.22
$\nu_e + \mathrm{O} \rightarrow \mathrm{F} + e^-$	H_2O	1.99	1.99	1.99	1.85	1.85
$\overline{\nu}_e + \mathrm{O} \rightarrow \mathrm{N} + e^+$	H_2O	2.50	2.50	2.50	2.32	2.32
Neutral Current:	*total*	*4.96*	*5.88*	*5.31*	*3.34*	*4.29*
$\nu_{\mu,\tau} + {}^{16}\mathrm{O} \rightarrow \nu_{\mu,\tau} + {}^{15}\mathrm{O} + n + \gamma$	D_2O	0.23	0.31	0.26	0.17	0.25
$\overline{\nu}_{\mu,\tau} + {}^{16}\mathrm{O} \rightarrow \overline{\nu}_{\mu,\tau} + {}^{15}\mathrm{O} + n + \gamma$	D_2O	0.23	0.31	0.26	0.17	0.25
$\nu_{\mu,\tau} + {}^{16}\mathrm{O} \rightarrow \nu_{\mu,\tau} + {}^{15}\mathrm{N} + p + \gamma$	D_2O	0.63	0.63	0.63	0.47	0.47
$\overline{\nu}_{\mu,\tau} + {}^{16}\mathrm{O} \rightarrow \overline{\nu}_{\mu,\tau} + {}^{15}\mathrm{N} + p + \gamma$	D_2O	0.64	0.64	0.64	0.48	0.48
$\nu_{\mu,\tau} + {}^{16}\mathrm{O} \rightarrow \nu_{\mu,\tau} + {}^{15}\mathrm{O} + n$	D_2O	0.30	0.69	0.45	0.22	0.62
$\overline{\nu}_{\mu,\tau} + {}^{16}\mathrm{O} \rightarrow \overline{\nu}_{\mu,\tau} + {}^{15}\mathrm{O} + n$	D_2O	0.29	0.66	0.43	0.21	0.60
$\nu_{\mu,\tau} + {}^{16}\mathrm{O} \rightarrow \nu_{\mu,\tau} + {}^{15}\mathrm{O} + n + \gamma$	H_2O	0.27	0.27	0.27	0.17	0.17
$\overline{\nu}_{\mu,\tau} + {}^{16}\mathrm{O} \rightarrow \overline{\nu}_{\mu,\tau} + {}^{15}\mathrm{O} + n + \gamma$	H_2O	0.27	0.27	0.27	0.17	0.17
$\nu_{\mu,\tau} + {}^{16}\mathrm{O} \rightarrow \nu_{\mu,\tau} + {}^{15}\mathrm{N} + p + \gamma$	H_2O	1.04	1.04	1.04	0.63	0.63
$\overline{\nu}_{\mu,\tau} + {}^{16}\mathrm{O} \rightarrow \overline{\nu}_{\mu,\tau} + {}^{15}\mathrm{N} + p + \gamma$	H_2O	1.06	1.06	1.06	0.65	0.65
Total SNO ν_e Events		3.04	3.04	3.04	2.82	2.82
Total SNO $\overline{\nu}_e$ Events		3.82	3.82	3.82	3.54	3.54
Total SNO "ν_μ" Events		4.96	5.88	5.31	3.34	4.29
Total SNO D_2O Events		4.69	4.95	5.10	3.67	4.62
Total SNO H_2O Events		7.13	7.13	7.13	5.79	5.79
Total SNO $e^{\pm}$ Events		6.86	6.86	6.86	6.36	6.36
Total SNO γ Events		4.25	4.25	4.25	2.81	2.81
Total SNO n Events		0.71	1.63	1.06	0.53	1.48
Total SNO Events		**11.82**	**12.74**	**12.17**	**9.70**	**10.65**

Table C.4: Summary of estimated contributions above both the hardware and analysis thresholds from reactions involving oxygen to the supernova signal using the Burrows model.

Appendix D

Online Analysis Using 100 Supernovae

The Level 3 summary histograms presented in Chapter 9 show a simulated supernova burst at 10 kpc according to the Burrows model. In those plots however, the underlying distribution is not readily apparent, so plots using simulated data from 100 supernovae at 10 kpc are presented in this Appendix.

The summary histograms for the events in the entire burst are shown in Figure D.1, whereas the analysis histograms for events in the D_2O and H_2O regions are shown in Figures D.2 and D.3, respectively. In each of the $\cos\theta_{SN}$ angular distributions, events from the forward-peaked elastic scattering interactions stand out above events from the other interaction types.

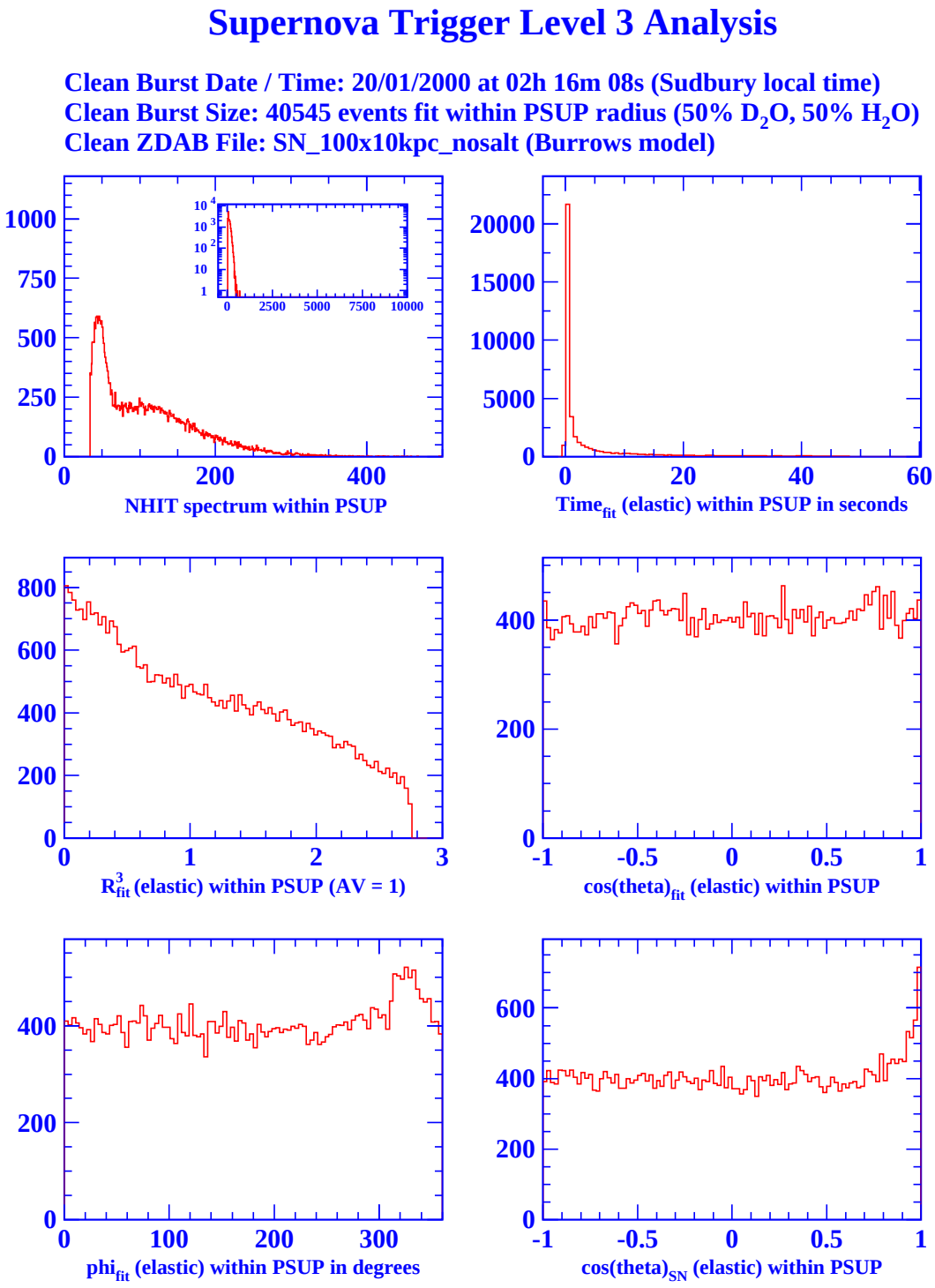

Figure D.1: Level 3 analysis summary histograms showing various distributions for all burst events that are reconstructed within the detector volume using events from 100 supernovae at 10 kpc simulated according to the Burrows supernova model.

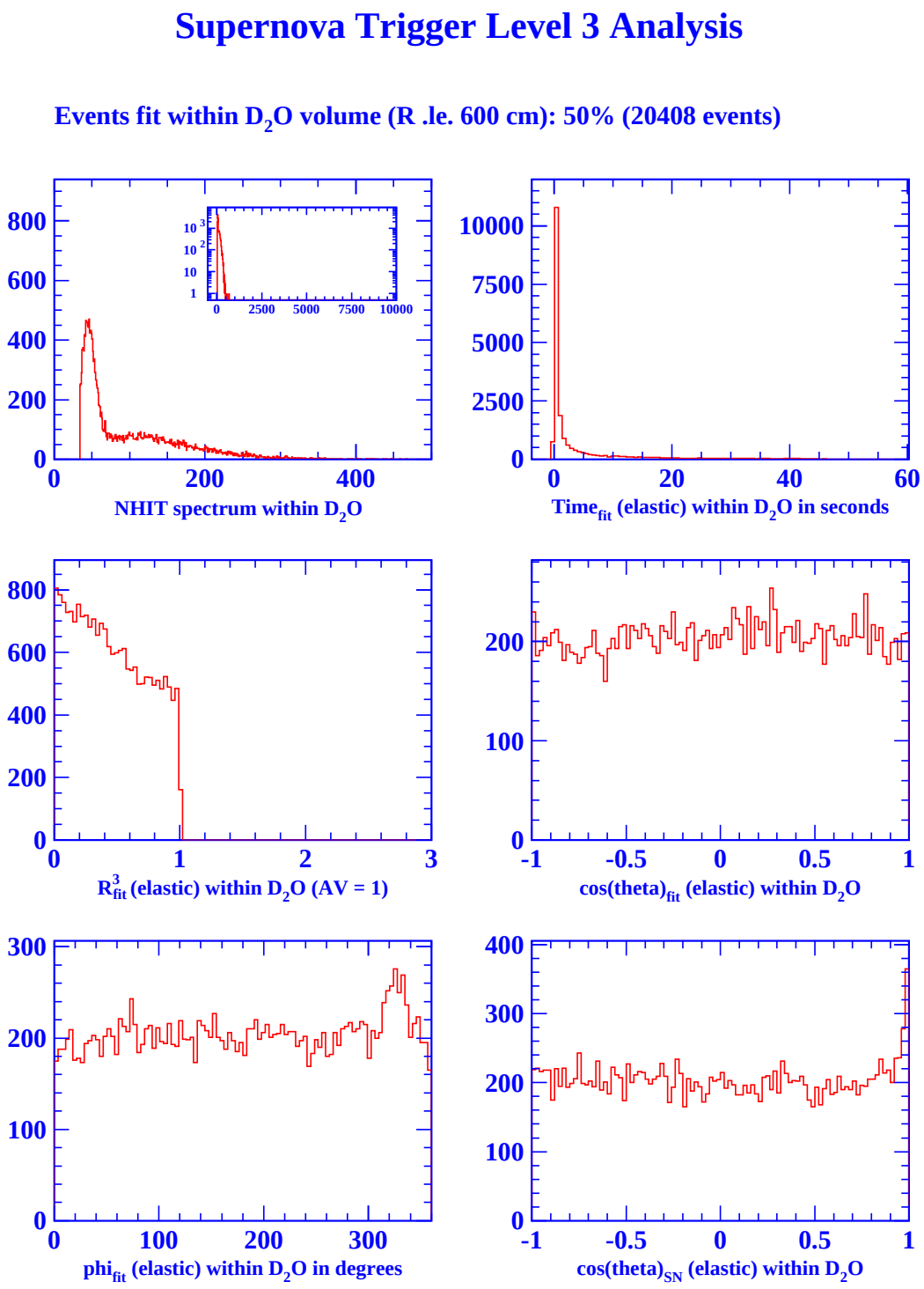

Figure D.2: Level 3 analysis summary histograms showing various distributions for burst events that are reconstructed within the D_2O region using events from 100 supernovae at 10 kpc simulated according to the Burrows supernova model.

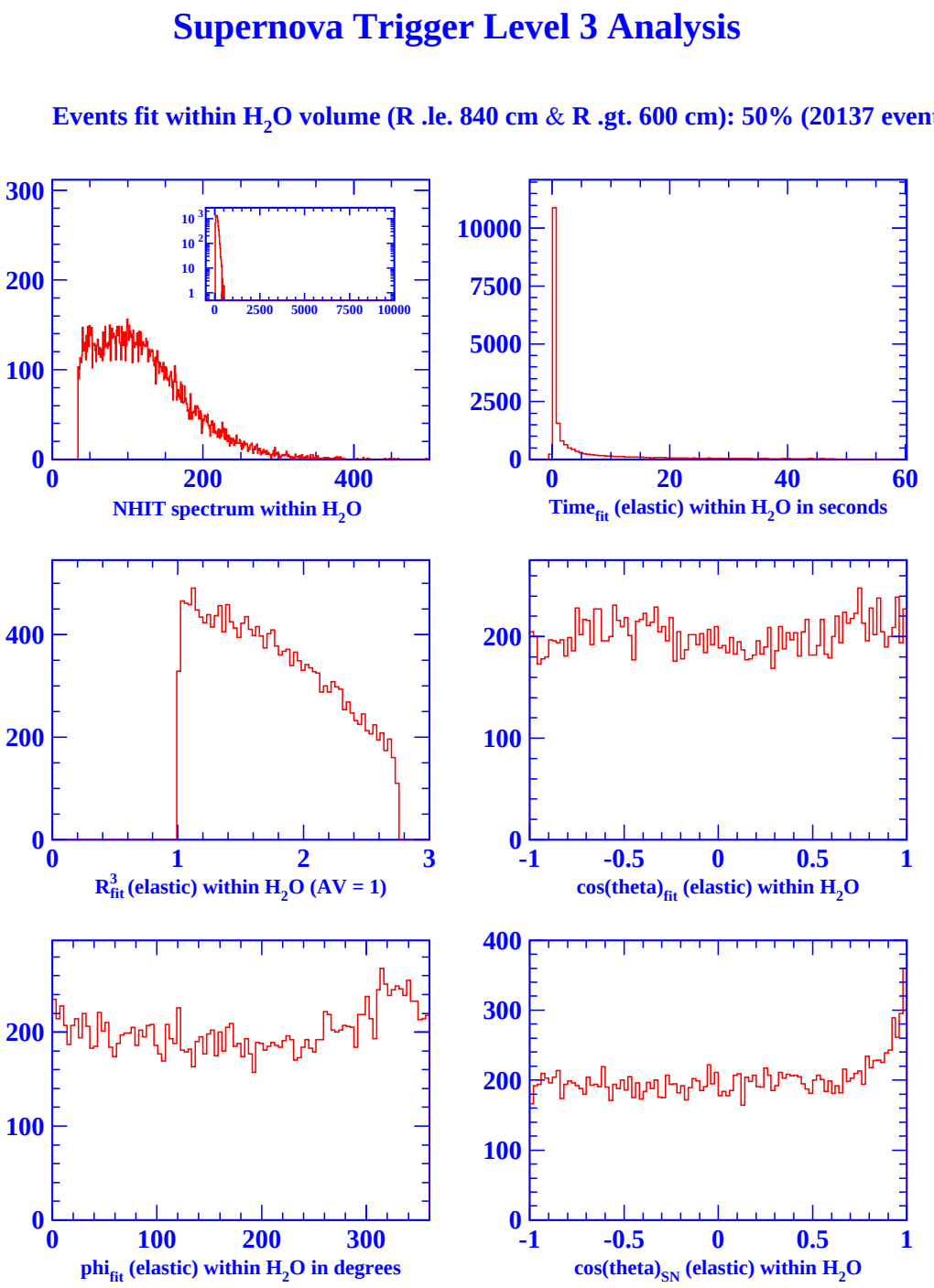

Figure D.3: Level 3 analysis summary histograms showing various distributions for burst events that are reconstructed within the H_2O region. using events from 100 supernovae at 10 kpc simulated according to the Burrows supernova model.

Appendix E

Milestones Relevant to SNO Supernova Monitoring

Work on the SNO supernova burst monitor began before the detector was filled with water in May 1999. The monitoring software evolved through testing and development stages both offline and online, and the most significant milestones are summarized in Table E.1. Prior to February 23, 2000, some small fraction of bursts were not being identified online due to a software bug in the event storage array. Once this bug was fixed, the online monitoring software was considered to be fully functional. Therefore, February 23, 2000 is taken to be the first day of online monitoring within SNO.

Date	**Significance**
May 1, 1999	SNO detector online (commissioning stage)
May 19, 1999	Burst monitor installed in online version of SNOSTREAM (bursts communicated via email to M.H. Schwendener) [$30 \leq$ NHIT ≤ 800, NEVENT $= 51$, TIME $= 2$ seconds]
August 9, 1999	Burst information communicated via email to Supernova Working Group [$50 \leq$ NHIT ≤ 800, NEVENT $= 51$, TIME $= 2$ seconds]
August 10, 1999	First spallation event seen online by trigger
November 2, 1999	Detector configuration frozen
December 16, 1999	Global trigger channel added to all events [NHIT ≥ 49, NEVENT $= 51$, TIME $= 2$ seconds]
December 20, 1999	Level 2 analysis installed online Detector operators receive burst email
February 17, 2000	Alert popup window activated for Level 1 bursts
February 23, 2000	Final algorithm bug fixed (burst event numbering) [NHIT ≥ 34, NEVENT $= 51$, TIME $= 2$ seconds]
April 19, 2000	Change event accounting within SNOSTREAM [NHIT ≥ 34, NEVENT $= 50$, TIME $= 2$ seconds]
August 8, 2000	Level 3 event reconstruction activate online
October 17, 2000	Author receives cell phone for supernova on-call support
December 21, 2000	Detector hardware threshold decreased from 18 to 16 PMTs
May 28, 2001	Salt added to D_2O region
May 30, 2001	Dial-out system commissioned
August 3, 2001	[NHIT ≥ 34, NEVENT $= 30$, TIME $= 2$ seconds]

Table E.1: Summary of milestones relevant to SNO supernova monitoring.